Department of Physics
Imperial College London

Quantum Detection
National Physical Laboratory

Graphene Optical and Microwave Molecular Sensing Platforms

Nicola Charlotte Grant Black

A thesis submitted to Imperial College London for the degree of
Doctor of Philosophy

Supervised by:

Professor Lesley F. Cohen
Professor Stefan A. Maier
Dr Ling Hao

December 2018

Declaration of Authorship

This thesis is the original work of the author with exception of help and guidance acknowledged in the text.

Collaborator Contributions

I'd like to acknowledge my collaborators for their respective contributions in this thesis: Dr Ivan Rungger for fitting the experimental adsorption sensor response data with the various theoretical 'Modified Langmuir' models in chapter 4 which we jointly developed. Dr Rodrigo Berte who helped design and ran the FDTD simulations of the SERS discs used in figure 3.1 of chapter 3. Dr Viktoryia Shautsova for the theoretical FDTD simulations of silicon with different oxide thickness used in figure 3.2 of chapter 3 and the transport measurements of the graphene samples in figure A.4 of the Appendix. Dr Viktoryia Shautsova and Dr Adam Gilbertson for the fabrication of the 'G-SERS samples' studied in this thesis. Dr Bing Li for his assistance in the graphene transfer of the 'Microwave samples' studied.

Copyright Declaration

Abstract

The unique electronic and physical structure of graphene is highly sensitive to its surroundings, producing a promising candidate for future sensor technologies. However, graphene responds equally to perturbations at both sides of its interface, such that tuning the chemical potential of the substrate at the graphene-solid interface impacts the sensor response at the graphene-gas/liquid interface. In this work, two distinct non-contact graphene sensing platforms are studied under various ambient conditions to assess their propensity towards molecular sensing.

The different spectral enhancement mechanisms of graphene surface enhanced Raman spectroscopy platforms are studied through interfacing graphene to differently treated gold nanodisc substrates. Using statistical Raman analysis, the influence of the chemical enhancement mechanism with respect to the graphene Raman peaks is assessed. Moreover, Kelvin force microscopy shows that the locally enhanced electromagnetic field can induce surface chemical reactions which are dependent upon the sensor environment. Explicitly, laser illumination in an air/nitrogen ambient, p-/n-dopes the graphene sheet by $\sim$ -0.87 ± 0.05 meV/$\sim$ +0.75 ± 0.07 meV.

By measuring the change of resistivity of graphene upon gas adsorption using a microwave dielectric resonator, a contactless non-invasive gas sensing platform is demonstrated. This large area graphene measurement platform allows evaluation of the real time sorption processes of NO_2 with graphene. Using a modified Langmuir adsorption model, the sticking coefficient is exponentially dependent upon NO_2 occupancy. Consequently, the possible variation of the NO_2 binding energy, which is frequently considered as the main parameter, plays only a secondary role compared to the rising adsorption energy barrier with increasing NO_2 coverage. Finally, through preliminary temperature and electrical gating measurements the charge transfer affinity of graphene based NO_2 sensors is explored. Interestingly, the sensor response can be hindered and/or enhanced by back gate control of the doping in graphene.

Acknowledgements

First and foremost I'd like to thank my 'plethora' of supervisors that enabled this collaborative PhD between Imperial College London and the National Physical Laboratory. Professor Lesley Cohen for her guidance, patience and enthusiasm throughout the course of the PhD, encouraging me to pursue my own ideas, while still challenging them and most importantly pulling me back and helping me see the bigger picture when I got lost in details. Dr Ling Hao at NPL who was always encouraging and trusted me to go down the 'chemistry' path while simultaneously giving me technical and general advice. Professor Stefan Maier, who recommended to me this PhD opportunity and despite a very busy schedule, always replied to my emails and concerns. Dr John Gallop, my unofficial supervisor, without his support, guidance, patience navigating microwave technologies and many enjoyable discussions I truly doubt the success of this PhD.

From NPL I'd like to thank Dr Ivan Rungger for his collaboration and our many late nights discussing adsorption models and like myself being more interested in the underlying physics of graphene gas sensors than simply measuring a response. I'd also like to thank Dr Andrew Pollard and Dr Cristina Giusca at NPL for letting me use their Raman systems.

A special thank you goes to Dr Viktoryia Shautsova, who it has been a pleasure working alongside. Who introduced me to the basics of graphene, helped integrate me with the Imperial group and always found time to discuss research and provide encouragement. To Dr Rob Maher for training me on the various Raman microscopes and our many discussions. To Dr Rodrigo Berte who collaborated on the COMSOL and FDTD simulations of the G-SERS platform. I really appreciate him sacrificing one of his server licenses and simulation time to enable me to run mine. A super thank you goes to Dr Bing Li who has the steadiest hand in the lab and helped me with the graphene transfer.

I'd like to thank the many researchers in Quantum Detection at NPL and the EXSS Group at Imperial who despite me appearing part time in each institute and being dubbed 'The Ghost' helped me navigate both institutions. To the 25+ office mates I've had between Imperial and NPL, you've all been wonderful to work alongside. I'd also like to thank the many students I've met through the Graphene Flagship conferences and studies, in such a fast competitive field my peers from other institutions inspired, encouraged me and reinvigored my passion. It has been a pleasure to meet so many passionate people. Moreover, I'd like to thank my ex-colleagues and friends from the University of Glasgow and CERN who have encouraged me all the way, and have been the Giant Shoulders I've been standing upon.

I'd like to thank all those non-academics and friends who have put up with me for the last few years and have kept me somewhat grounded. To Vicky Hall and Patrick Alkness for the sporadic phone calls and online messages whose friendship and support has been invaluable. I'd like to thank my parents and siblings, particularly my Father for his financial and emotional support. Finally I'd like to thank my partner Daniel Gómez Blanco who has been by my side through my Bachelor, Masters and now PhD thesis. Who has encouraged me to take breaks, eat healthily, meditate, exercise, go to the pub and financially supported me through the last 6 months of writing. Keep up the good work!

Querido Dani, esta tesis es para ti. Tu pobre inversión.

Contents

List of Publications

- Shautsova, V., Sidiropoulos, T., Gusken, N., Black, N., Gilbertson, A., Maier, S.,Oulton , R., Cohen, L., (2018) Plasmon induced thermoelectric effect in graphene. *Nature Communications*, 9(10), p.5190.
- Black, N.C.G., Rungger, I., Li, B., Maier, S.A., Cohen, L.F., Gallop, J.C. and Hao, L., (2018) Adsorption dynamics of CVD graphene investigated by a contactless microwave method. *2D Materials*, 5(3), p.035024.
- Black, N., Lui, CG., Pearce, R., Li, B., Maier, S., Cohen, L., Gallop, J., and Hao, L. (2017) Graphene Gas Sensing Using a Non-Contact Microwave Method. *Nanotechnology*, 28(39), 395501.
- Ma, L., Lu, Z., Tan, J., Liu, J., Ding, X., Black, N., Li, T., Gallop, J., and Hao, L. (2017) Transparent Conducting Graphene Hybrid Films to Improve Electromagnetic Interference (EMI) Shielding Performance of Graphene. *ACS Applied Materials and Interfaces*. 9(39), 34221-9.
- Shautsova, V., Gilbertson, A., Black, N., Maier, S. and Cohen, L. (2016) Hexagonal Boron Nitride Assisted Transfer and Encapsulation of Large Area CVD Graphene. *Scientific Reports*. 6, 30210.

List of Figures

List of Tables

List of Abbreviations

AFM	atomic force microscopy.
AuND	gold nanodisc.
CVD	chemical vapour (deposition) deposited.
EM	electromagnetic mechanism.
FDTD	finite difference time domain.
FTIR	Fourier transform infra red.
FWHM	full width at half maximum.
GERS	graphene enhanced Raman spectroscopy.
G-FET	graphene field effect transistor.
G-SERS	graphene surface enhanced Raman spectroscopy.
h-BN	hexagonal boron nitride.
HOMO	highest occupied molecular orbital.
HOPG	Highly ordered pyrolytic graphite.
ITO	indium tin oxide.
KFM	Kelvin force microscopy.
KPFM	Kelvin peak force microscopy.
LED	light emitting diode.
LSF	Least Squares Method.
LUMO	lowest unoccupied molecular orbital.
MDS	minimum discernible signal.
N_2	nitrogen.
NO_2	nitrogen dioxide.
O_2	oxygen.
PMMA	polymethylmethacrylate.
Pos	peak position.
ppb	parts per billion.
ppm	parts per million.
SEM	scanning electron microscope.

SERS Surfaced Enhanced Raman Spectroscopy/Scattering.

SiO_2/Si silicon dioxide/silicon.

SMU source measure unit.

SPM scanning probe microscopy.

TE Transverse Electric.

TM Transverse Magnetic.

TST transition state theory.

UV ultra violet.

VNA vector network analyzer.

Chapter 1

Introduction

Sensor technologies are becoming increasingly ubiquitous, with the common goal to improve measurement precision and sensitivity. Molecular sensing is a broad term encompassing a large range of spectroscopies, chromatographies, microscopies and electrical platforms spanning the macro- and nanoscales down to single molecular detection [1, 2]. Although single molecular sensing platforms provide the ability to detect rare stochastic processes, that would otherwise be burried within the noise, leading to insights into chemical reaction mechanisms [3, 4, 5]; quantitative analysis requires the measurement of a large number of events requiring the process of large quantities of data [6]. Indeed emerging smart sensors look at integration with computational processes to account for this emerging demand [7, 8, 9]. With this in mind, macroscopic sensing is still vital in certain applications. For example, cheap chemiluminescent nitrogen dioxide (NO_2) gas sensors loose their efficiency at higher concentrations [10]. As a result, monitoring realistic city pollution levels or in laboratory environments at concentrations of detrimental toxicological impact [11, 12] suggests the need for highly sensitive accumulative gas sensors.

Graphene is an interesting platform, both for ultra-sensitive spectroscopic Raman based sensing and chemo-restive type accumulative sensing applications. The former provides chemical identification of the measurand species, although is limited to the nanoscale and requires specialist equipment. Whereas the latter provides simple, fast and real time cumulative molecular detection via simple electrical resistance measurements;

although chemical disambiguation is still a challenge. However, this versatility of graphene, specifically its ability to integrate with multiple sensing technologies potentially provides a way to maximise the benefits of each sensing technology while hopefully minimising their respective shortfalls. Indeed, graphene has shown promise for a large range of sensing platforms [13, 14, 15, 16, 17, 18, 19].

Graphene is comprised of carbon atoms arranged in a two dimensional honeycomb lattice with a single delocalized electron per atom. Remarkably, this arrangement gives rise to a band structure with a linear dispersion around the K points of the Bouillon Zone Boundary - from which all its unique properties arise [20, 21]. As a consequence, the charge carriers of graphene, known as Dirac Fermions, are highly sensitive to modulations of the carrier density [20]. Therefore, external perturbations to the crystal structure or carrier distribution can be directly probed and/or measured; which is especially desirable for quantitative analysis of measurands [14].

Of particular importance for gas sensing, graphene exhibits: unique optical properties, which include broadband light interaction and a particularly high Raman cross section [22, 23]; high tunable electrical conductivity [24, 25], which is perturbed in the presence of adsorbate species [26]; high thermal conductivity [27, 28], which furthers the robustness of nanoparticle based surface enhanced Raman spectroscopy platforms [29, 30, 31] and; sensitivity to mechanical stress and flexibility, which enables integration to a wide range of nano-patterned substrates [32].

Therefore, the work in this thesis focuses on two distinct, non-contact graphene sensing platforms: a graphene surface enhanced Raman spectroscopy (G-SERS) platform, which is a highly sensitive Raman based spectroscopic sensor comprised of graphene integrated with a periodic gold nanodisc array; and the development of a novel graphene coupled microwave dielectric cavity gas sensing platform, which is shown to be a highly sensitive accumulative gas sensing technique based on the measurement of electrical sheet resistance. Although the G-SERS platform can be used as a molecular sensor in aqueous solutions, the discussion in this thesis will be framed in terms of ambient gas sensing. In short, it is the nanoscale interactions at the graphene interfaces which is the common focus of this work. In both platforms, the graphene charge density is modulated either through graphene substrate treatments, electric field effects and the adsorption of environmental gases. Interestingly, the relative doping of the graphene surface is shown to enhance and/or hinder certain aspects of the sensor response which is shown to be potentially pivotal in designing selective graphene sensors.

1.1 Gas Sensing Technology Overview

Gas sensors technologies are used in all walks of life including research and development, industry, environmental monitoring, earth observation and health and monitoring toxicological hazards [33, 34, 35, 36]. However, the diverse range of applications requires sensors capable of gas detection at various concentration ranges and the importance of sensor properties such as sensitivity, selectivity, detection limits, recovery and response times depend upon the application. Metal oxide semiconductors rely on redox reactions of gases at the surface to facilitate a charge transfer and produce an electrical signal [34, 37]. This signal can be detected as a change in capacitance, work function, optically or thermally depending on the metal oxide sensor. Although some metal oxide sensors have the benefit of miniaturisation, they also typically require high operation temperatures [37]. Alternative chemiresistive gas sensors which overcome this shortfall include polymer, carbon nanotube based and graphene sensors which don't require high operating temperatures [38]. Moreover, polymer sensors are compatible with chemical species that can degrade metal oxide sensor performances

[34].

Optical based gas sensors depend upon the measurement of absorption at particular wavelengths, where the absorption frequencies in the UV/Vis and IR correspond to electronic excitations and molecular vibrations respectively [39]. Interestingly, optical cavities provide some of the most chemical selective and sensitive gas sensors, since the path length is so large and the measurement relies upon the the chemical specific electronic excitation being stimulated using a monochromatic source [40]. On the other hand, gas chromatography techniques are more widely used for analytical measurements of gas mixtures. Gravimetric gas chromatography is widely used for accurate measurements and chemiluminescent sensors measure the ratio of the target gas with a reference upon illumination, which are useful for low cost NO_2 pollution monitoring [41, 42].

Recently, there has been a driving trend to scale down current sensor technology and design light, flexible and wearable sensors [7, 18, 43, 44, 45]. Furthermore, the incorporation of nanostructures is ideal for improving the surface to volume ratio in gas sensors. Moreover, metallic and dielectric nanoparticles are easily functionalised adding selectivity to gas sensing performance [3, 46, 47], which is a problem for most electronic based sensor arrays [48]. As a result, two dimensional materials such as graphene are particularly suited in the development in the next generation of sensor technology, since they are integrable with nanophotonic and nanoelectronic devices enabling multi-functional capabilities [43, 49, 50].

1.2 Graphene Gas Sensors Overview

In recent years there has been a development of a wide range of gas sensing platforms that rely on the unique properties of graphene [13, 14, 15, 16, 43]. Most graphene gas sensors function by measuring a change in electrical conductivity induced by gas adsorption. Upon adsorption, a p-type (n-type) gas will donate holes (electrons) to the graphene sheet, which modulates the charge carrier density and dopes the graphene which can be electrically detected via traditional DC measurements [26, 51, 52, 53, 54, 55, 56, 57, 58, 59]. Even nanomechanical pressure sensors rely upon measuring the change in electrical resistivity due to strain on suspended graphene nanodrums [60, 61, 62].

Consequently, graphene molecular sensors have fast response times and high sensitivity, with the potential for single molecular detection [26, 54], and have been shown to be capable of distinguishing chemically similar gas species by analysing these response times; explicitly the overall magnitude, gradient and shape of the sorption sensor response curves are dependent upon characteristic graphene–molecule interactions [63, 64]. Indeed there are a number of studies that discuss improving graphene responses by functionalising it [65, 66, 67, 68, 69, 70, 71, 72], optimising the graphene carrier density through field effect transistor devices [73, 74, 75, 76, 77], introducing defects [65, 71, 78, 79, 80, 81], and by studying the binding affinities of graphene and graphene derived 2D materials [78, 82, 83, 84, 85, 86, 87].

Interestingly, due to the gapless nature of the graphene band structure, graphene is a poor light emitter [22] despite having a relatively high optical absorbance (2.3% of white light) considering graphene is an atom thick material [23]. As a result, only light emission via phonon mode scattering or rather Raman spectroscopy is widely studied.

Table 1.1: Overview of gas sensing technologies used for NO_2 detection. The limit of detection (LOD), typical concentration ranges and typical measurement response times for the range indicated for NO_2 detection is compared. A brief overview of their advantages and disadvantages are also compared.

	Technology	**LOD***	**Range**	**Response Time**	**Advantages**	**Disadvantages**	**Ref.**
Electrical Response	Graphene Microwave Method	~87 ppb	0.1-100 ppm	5 mins	Contactless large area measurement, real time accumulation, easy fabrication	Long recovery time, no specificity or selectivity, need high resistivity substrate.	[88, 89]
	Graphene DC Transport	0.158 ppt	0.1-100 ppm	5 mins	Integrable with nanoscale electronics, potential ppt sensitivity, real time accumulative	Costly fabrication, no specificity or selectivity	[16, 15, 90]
	Metal Oxide Semiconductors	10.6 ppb	10 ppb to 100 ppm	<5 mins	Low cost, readily available	Incompatible with corrosive gases, poor selectivity, high operating temperatures	[91, 92, 93, 94]
	Ampeoteric	6 ppb	5-500 ppb	1 min	Well established, portable, low cost, Conmpatible with a large range of gases including VOCs**	Liquid electrolyte, Failures modes are not revealed unless advanced monitoring technique used.	[33, 94, 95]
Optical Response	SERS	Potentially single molecule	0.1 - 3 ppm	3 to 5 mins	Spectroscopic determination	Specialist equipment, dependent on overlap of plasmon mode with vibrational mode	[33, 96]
	Chemi-luminescent	18.6 ppb	18.6 - 50 ppb	5 mins	cheap, portable	Measurement relies on ratio of NO/Nox so looses sensitivity at higher concentrations	[41, 42]
	Optical Techniques	75 ppt	75 ppt to 100 ppm	1-120 s	Highly sensitive and specific detection	Expensive, specialised and bulky equipment	[39]

* LOD = Limit of Detection reported in literature so far

** VOCs = Volatile Organic Compounds

Indeed the Raman spectroscopy of graphene is highly sensitive to perturbations in its carrier density and lattice structure which is discussed in detail in chapters 2 and 3. To overcome the weak coupling to electromagnetic waves, the graphene dimensions are either reduced such that it can sustain optical surface plasmons [97, 98, 99, 100, 101] or integrated with plasmonic nanostructures [102, 103, 104]. It should be noted that graphene sustains long lived plasmons in the terahertz and the mid-IR [105, 106] which can be used to detect molecular vibrational spectra [107]. Interestingly, graphene nanostructure hybrid devices have shown promise as spectroscopic gas sensors. Either due to the change in graphene conductivity facilitating a change in the refractive index [108, 109, 110, 111, 112], or large enhancements of the electric near field of the nanostructures enabling spectroscopic molecular detection [113, 114, 115, 116]. The latter Surfaced Enhanced Raman Spectroscopy/Scattering (SERS) active graphene hybrid devices is the focus of chapter 3.

For context table 1.1 provides a useful general overview of similar gas sensing technologies to the gas sensing platforms explored in this thesis. Namely gas sensing methods based on electrical variation upon NO_2 adsorption and spectroscopic optical methods.

1.3 Thesis Overview

Since two distinct graphene gas sensing platforms are discussed in this thesis, the thesis structure is kept modular such that the core concepts and theory relevant for each chapter is self contained as much as possible. With this in mind, **Chapter 2** discuss the experimental techniques, apparatus and core concepts used to characterise the various graphene devices.

Chapter 3 focuses on a G-SERS platform consisting of chemical vapour (deposition) deposited (CVD) graphene transferred onto a gold nanodisc decorated substrate. In this chapter, the propensity of chemically doping the graphene through substrate interactions is shown to influence the enhancement factor of the graphene Raman signal. In addition to perturbations of the spectroscopic signature of graphene, it is shown through Kelvin force microscopy (KFM) and statistical Raman analysis, that the intense enhancement of the electric field in the vicinity of the nanostructures, upon resonant illumination, can induce surface chemical reactions with the environment. Graphene is permanently either doped by $\sim -0.87 \pm 0.05$ meV or $\sim +0.75 \pm 0.07$ meV depending on whether the sample is exposed to laser irradiation in an air or nitrogen ambient respectively. This work provides insight into how the graphene platform itself interacts with the SERS active nanostructures, which provides a necessary baseline for the interpretation of G-SERS platforms for targeted molecular sensing applications.

In contrast, **chapters 4 and 5** follow the development of graphene coupled to a microwave dielectric cavity to form a novel gas sensing platform. **Chapter 4** discusses a ‘Microwave Method’ which uses microwaves to probe the AC conductivity of the graphene charge carriers such that no electrical contacts are required. This enables a study of the fundamental graphene–gas surface interaction since contacts are known to perturb the measured electrical response [117, 118, 119, 120, 121]. This sensing platform is shown to detect nitrogen dioxide concentrations spanning 3 orders of magnitude. Moreover, the fundamental adsorption interactions are explored using a modified Langmuir adsorption model, where it is shown that the sticking probability is exponentially dependent upon the adsorbate surface coverage.

Chapter 5 records the preliminary measurements following the work from chapter 4. An open cavity design is developed as an alternative gas sensing platform, enabling high temperature measurements and electrostatic gating. This platform is designed to explore the charge transfer affinity between graphene and NO_2 adsorbates, which impacts the sensor response. As a result, the temperature measurements provide preliminary information on the NO_2 sorption energy barrier at equilibrium conditions, and the graphene field effect transistor device shows that modulating the charge carrier density can promote or hinder the sorption process. Remarkably, in some cases prevent sorption entirely.

Chapter 6 presents some general conclusions of the work in this thesis. Followed by **chapter 7** which suggests future work including and beyond gas sensing of both sensing platforms studied.

Chapter 2

Experimental Techniques

The aim of this chapter is to introduce the experimental techniques, methodology and the necessary concepts used to characterise the graphene samples studied in this work. To begin the wet transfer graphene sample fabrication process is described after a brief discussion of alternate transfer techniques. A detailed section in Raman spectroscopy is included, which is a standard characterisation tool of graphene and also forms the basis of surface enhanced Raman spectroscopy; which is explored as a molecular sensing platform in chapter 3. The other 'standard' characterisation techniques include scanning probe microscopy, Fourier transform infra red spectroscopy, electrical gating measurements and scanning electron microscopy. The two graphene coupled microwave dielectric resonator platforms are discussed in detail in chapters 4 and 5. This is because their design and development as gas sensing platforms is integral to the novel work of this thesis.

2.1 Graphene Fabrication

The first knowingly fabricated graphene sample was achieved using the mechanical exfoliation technique using Scotch tape [122]. Since then a variety of other methods ranging from chemical vapour deposition (CVD), mechanical exfoliation, liquid exfoliation, epitaxial growth and methods involving chemical precursors are used to prepare not only graphene, but a wide range of other 2D crystals[123, 124, 125, 20, 126].

Moreover, synthesis of functionalised graphene materials [127, 128, 129, 130, 131] is a rapidly expanding subfield of graphene where chemical control of the functional groups is a desired goal [132, 133, 134, 135]. Although some of the highest quality devices are fabricated using mechanical exfoliation methods [136] and chemical precursors [137, 138, 139, 140]; CVD graphene has the benefit of being grown large scale and consequently more easily integrable into the industrial environment [141, 142]. As a results, CVD graphene is widely commercially available and through the transfer procedure, can be integrated with a wide variety of substrates.

2.1.1 CVD Graphene Transfer

CVD graphene and h-BN grown on copper are bought from Graphenea and Graphene Supermarket respectively. The goal of the transfer method is to remove the graphene from the metal substrate and transfer it onto a desired substrate. Although recent progress has been made in non-polymer assisted transfer methods [143, 144, 145], the “wet” and “dry” graphene transfer procedures are two commonly utilised polymer assisted graphene transfer methods [146, 147, 148, 149, 150]. In this work a standard wet transfer procedure is predominately used to transfer graphene onto different treated silicon based substrates.

Figure 2.1 is a schematic representation of the wet graphene transfer procedure. First a thin protective layer of polymethyl methacrylate A4 495 (PMMA) is deposited on top of the graphene sheet using a spin coater at 1000 rpm for 30 s; resulting in an approximately 200 nm thick film. The polymer protected stack is then oxygen plasma ashed for 2 minutes at 100 W to remove the unwanted graphene layer on the unprotected backside of the copper foil. If necessary, in order to improve mechanical support, a Kapton tape frame is pressed on top of the PMMA layer (figure 2.1b). The copper is then etched in a 0.1 M aqueous solution of ammonium persulfate overnight

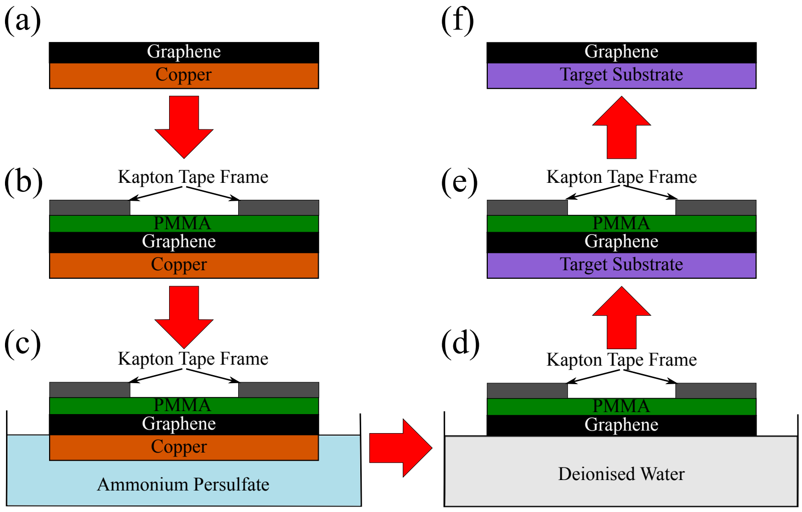

Figure 2.1: Schematic of the step by step process of the graphene transfer procedure. This process is equivalent for any 2D material that can be grown on an etchable metal foil.

(figure 2.1c). Once the copper has been fully dissolved into the acidic aqueous solution, the kapton/PMMA/graphene floating stack is transferred to a beaker of deionised (DI) water to remove any excess ions (figure 2.1d). A target substrate is then used to "scoop" the floating graphene stack out of the water (figure 2.1e). The sample is left to dry completely before annealing the sample at 180°C for 30 minutes. This step allows the PMMA to re-flow and improve graphene-target substrate adhesion. Once cool, the sample is immersed in acetone for 8 hours to dissolve the PMMA coating. Normally the acetone is refreshed at least once during this time. Finally, the sample is immersed in isopropyl alcohol (IPA) for 15 minutes to prevent acetone residue from building up on the surface and left to dry (figure 2.1f).

During a dry transfer procedure, after the sample has been rinsed in DI water it is removed from the water and placed (PMMA side down) on a glass slide. The graphene sample is dried on a hot plate at 60°C for an hour before transferring onto the target substrate. At this point, similar to the wet transfer procedure, the sample is annealed at 180°C before removing the PMMA in acetone and rinsing in IPA. During the wet transfer procedure it is not necessary to have a thick PMMA protective layer or the additional kapton frame support. Whereas during the dry transfer it is important that the graphene is fully supported, otherwise the film can collapse. The main benefit of the dry transfer procedure is that it removes p-dopant water molecules from the graphene substrate interface and the heating step relaxes the PMMA reducing graphene wrinkle formation. In general the quality of dry transferred graphene is better than that of wet transferred graphene [151]. However, the dry transfer procedure is technically more difficult, graphene is more damaged in the vicinity of the Kapton frame and the process is not scalable for large area industrial applications.

2.1.2 Target Substrate Preparation

In this work, graphene is transferred onto a variety of target substrates. The substrate properties along with the quality of graphene post transfer are summarised in table 2.1. A full discussion about the interpretation of graphene Raman statistics, which better describes the graphene quality, can be found in chapter 3 section 3.3.2. The "SERS" substrates (of chapter 3) are first decorated with plasmonically active gold nanostructures before the graphene is wet transferred. Gold nanodisc box arrays of dimensions 40 x 40μm on silicon are fabricated using e-beam lithography, thermal evaporation (40 nm gold) and lift-off. A variety of nanodisc arrays are fabricated with nanodisc radii ranging from 25 to 125 nm and periodicities of 200 to 1000 nm. After nanodisc fabrication, three graphene gold nanodisc hybrid devices are fabricated as shown in figure 2.1. For the first sample, graphene is wet transferred onto the nanodisc substrate following the process described above. For the second sample, the substrate is first oxygen plasma treated to improve graphene-substrate adhesion and increase doping prior to a dry graphene transfer. The third nanodisc substrate is first oxygen plasma treated, followed by the dry transfer of monolayer h-BN and

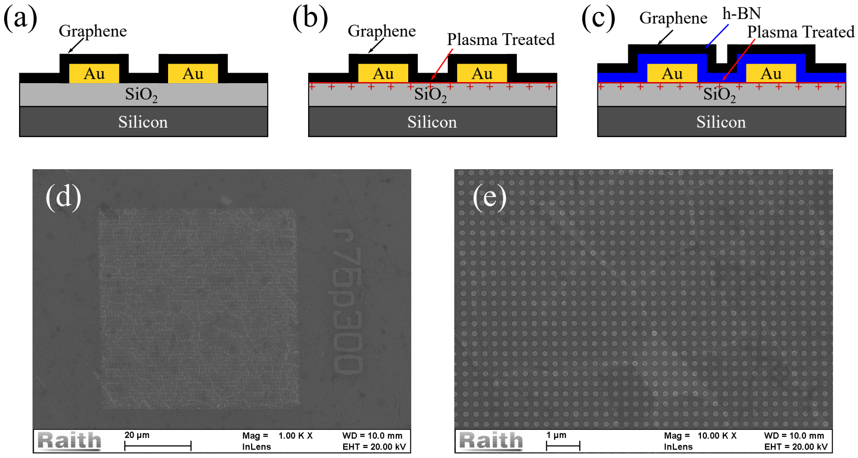

Figure 2.2: Graphene gold nanodisc hybrid devices where (a) is wet transferred graphene, (b) the substrate is oxygen plasma treated prior to dry graphene transfer and (c) the substrate is oxygen plasma treated prior to the sequential dry transfer of monolayer h-BN and graphene. SEM micrigraphs of the gold nanoparticles of radii 75 nm and periodicity 300 nm of sample (a) at (d) 1 kx magnification showing full array structure and (e) 10 kx magnification showing nanoparticles.

then the dry transfer of graphene. The h-BN provides a Van der Waals interface for graphene to adhere to and also passivates the highly doped silicon substrate. In this way three optically active graphene gold nanodisc hybrids are fabricated; the oxygen plasma treated sample, the wet transferred sample and the h-BN pacified sample, with decreasing magnitude of p-doping respectively (see figure 2.2).

The “Microwave Samples” substrates consisted of low doped (high resistivity) silicon, each with varying thermally grown oxide thickness. The high resistive nature was necessary to be compatible with the microwave measurement. The graphene was wet transferred onto all of these highly insulating substrates using the wet transfer process. From these samples, the lightly doped silicon substrate with the native oxide is utilised for the microwave gas sensing measurements described in chapter 4. Whereas the other samples consisted of various thermally grown oxides that are designed to be compatible with graphene field effect transistor type measurements as shown in chapter 5.

Table 2.1: Summary of the substrate properties and graphene transfer details of the various samples fabricated. Silicon wafers are bought from Graphene Supermarket, CrysTec GmbH and Inseto (UK) Ltd. The CVD graphene used in this work was purchased from Graphenea. The quality of graphene is quantified using Raman spectroscopy measurements and DC transport measurements[*]. Only areas of graphene in the absence of gold nanodiscs (AuNDs) are considered for the SERS sampels.

	Substrate	**Substrate Oxide**	**Substrate Resistivity (Ω.cm)**	**Substrate Doping**	**Transfer**	**Graphene Quality (AuNDs Absent)**
SERS Samples[**]	AuNP/SiO_2/Si	90 nm	0.001-0.005	P	Wet Transfer	**Moderately p-doped and strained** $I(G/2D)_{mean} = 1.026 \pm 0.004$ $PosG_{mean} = 1593.9 \pm 0.043$ cm^{-1} $Pos2D_{mean} = 2651.8 \pm 0.069$ cm $^{-1}$ 2.3% of area has a D peak
	AuNP/SiO_2/Si	300 nm	∼ 0.001-0.005	P	Dry Transfer After Oxygen Plasma Treatment	**Highly p-doped and strained** $I(G/2D)_{mean} = 1.447 \pm 0.003$ $PosG_{mean} = 1601.0 \pm 0.075$cm^{-1} $Pos2D_{mean} = 2653.0 \pm 0.0138$ cm $^{-1}$ 50-80% of area has a D peak where: $I(D/G)_{mean} = 0.6381 \pm 0.004$
	AuNP/SiO_2/Si	300 nm	∼0.001-0.005	P	Dry Transfer After Oxygen Plasma h-BN Transfer	**Lightly doped and strained** $I(G/2D)_{mean} = 0.668 \pm 0.003$ $PosG_{mean} = 1583.6 \pm 0.022$ cm^{-1} $Pos2D_{mean} = 2642.1 \pm 0.043$ cm $^{-1}$ 28.7% of area has a D peak where: $I(D/G)_{mean} = 0.956 \pm 0.006$
Microwave Samples	Undoped Si[†]	Native	>500	I	Wet Transfer	**Lightly doped, no significant strain** $I(G/2D)_{mean} = 0.427 \pm 0.001$ $PosG_{mean} = 1586.6 \pm 0.0464$ cm^{-1} $Pos2D_{mean} = 2691.8 \pm 0.0520$ cm $^{-1}$ 23.0% of area has a D peak where: $I(D/G)_{mean} = 0.3714 \pm 0.002$
	SiO_2/Si[‡]	50 nm	>2000	N	Wet Transfer	**Lightly p-doped** Dirac Point $\sim 2.5 - 10V$ Hole Mobility ∼ 3.62355 cm^{2}V^{-2}s^{-1} Electron Mobility ∼ 1.88433 cm^{2}V^{-2}s^{-1}
	SiO_2/Si[§]	100 nm	>10 000	P	Wet Transfer	**Lightly p-doped** Dirac Point $\sim 11.5 - 13.5$ V Hole Mobility ∼ 46.73 cm^{2}V^{-2}s^{-1} Electron Mobility ∼ 10.94 cm^{2}V^{-2}s^{-1}
	SiO_2/Si	300 nm	>6000	P	Wet Transfer	NA

[*] The DC transport data was calculated using equation (2.9).

[**] The Raman data used for the quality analysis of graphene transferred onto the SERS samples is discussed fully in chapter 3.

[†] The Raman data used for the quality analysis used for the undoped silicon sample is discussed fully in chapter 4.

[‡] The transport measurement for this sample is shown in appendix figure A.6.

[§] The transport measurement for this sample is discussed in chapter 5

2.2 Raman Spectroscopy

Raman spectroscopy in its simplest description is the measurement of the inelastic scattering of light with a material [152, 153]. When an intense laser light of frequency ω_0 impinges a Raman active surface, light will either scatter elastically (Rayleigh scattering) or inelastically (Raman scattering). The inelastically scattered photons can either loose energy though the emission of phonons into a lattice, Stokes emission, or gain energy via molecular vibrations in the lattice producing a photon with a higher frequency, Anti-Stokes emission. Semi-classically this process is described by the absorption of a photon which excites an electron to a virtual state, followed by the emission of a photon which has gained or lost energy by a discreet amount dependent upon molecular vibrations (see Fig. 2.3 [154]). A more complete description of Raman scattering involves the interaction of photons, electrons and phonons. Phonons like photons are both massless particles. Where photons are the quantum description of electromagnetic radiation, phonons are a description of lattice vibrations/lattice waves. Raman scattering is then described as being comprised of three real transitions: the absorption of an incident photon, the emission or absorption of phonons and the emission of the scattered photon. The virtual transition involves the creation of an exciton, whereupon it is scattered via exciton-phonon interactions and ultimately destroyed, returning the system to the ground state [155]. The real transitions can occur in any order. Figure 2.3 schematically shows the first order Raman process both semi-classically and quantum mechanically using a Feynman diagram.

In short, Raman spectroscopy provides a wealth of information about a material's crystal structure. It is a technique that is dependent upon the inter-molecular vibrations of atoms in a lattice and therefore is highly sensitive to chemical and physical properties of a material. As a consequence, Raman spectra can provide information about a

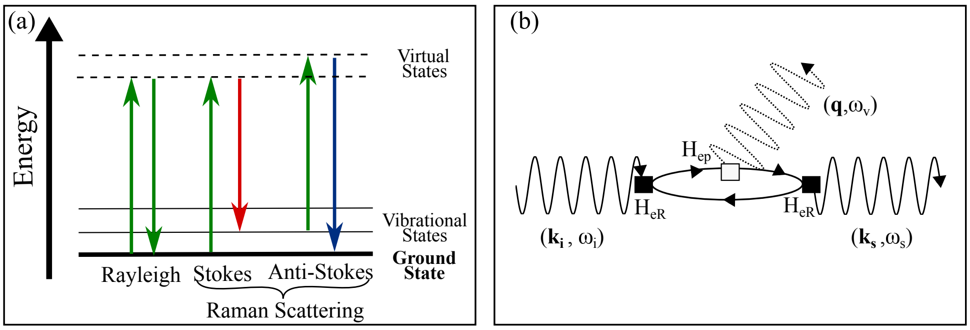

Figure 2.3: Two schematics of a first order Raman scattering interaction. (a) Semi-classical depiction of Raman scattering emphasising the origin of the Stokes and Anti-Stokes shift due to optical transitions to a virtual state. (b) Feynman diagram describing a first order Raman scattering process. The vertices indicate a particle interaction described by H_{eR} and H_{ep} which are the operators for the electron-light radiation and the electron-phonon interaction respectively.

material's physical crystal structure, temperature, chemical environment molecular arrangement and functional groups, purity and stress or strain in the system [154, 156, 157, 158, 159]. A detailed overview of the Raman scattering process is described in appendix A.1.

2.2.1 Raman Apparatus

The Raman measurements reported are performed on a variety of Raman systems (see table for specs). All Raman systems used were of a confocal set up and equipped with a piezo scanning stage enabling 100 nm step sizes. The three major parts of the Raman apparatus are the excitation source, the microscope and the spectrum analyser. The laser beam passes through a beam splitter and is focused on the sample as shown in figure 2.4. The scattered light is then collected through the microscope and using a beam splitter directed towards the spectrometer. The light is then diffracted via a diffraction grating and focused onto a CCD camera. Obviously the higher the frequency of scattered light the smaller the magnitude of diffraction. This allows the different frequencies to be distinguished laterally and converts the photon signal into

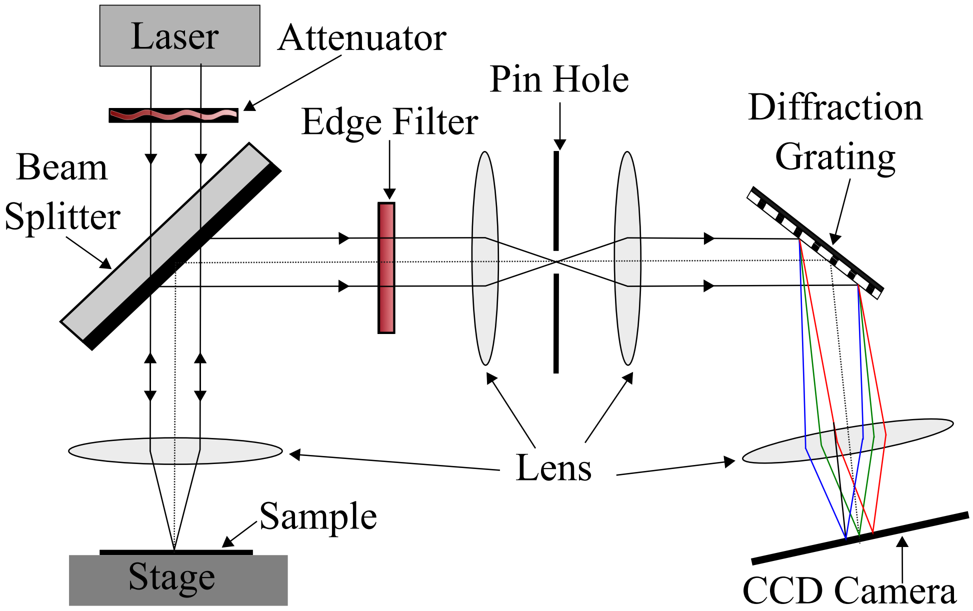

Figure 2.4: Schematic layout of a typical confocal microscope Raman system.

an electrical signal. The higher the density of lines present in the grating improves the spectral resolution. The confocal set-up in conjunction with a pin hole prevents unfocused light from entering the spectrometer improving the spatial resolution. One of the most important optical components scattered lights beam path is the edge filter. The edge filter is chosen such that all Rayleigh scattered/reflected light at the same energy as the excitation source is adsorbed by the filter and does not reach the spectrometer. Otherwise the elastic Rayleigh scattered light would dominate the signal masking the less quantum efficient Raman scattered light and potentially damaging the spectrometer through over saturation. Most microscopes stages are integrated with XYZ piezo stages enabling Raman mapping. For the gas sensing measurements the Jobin-Yvon Raman system was integrated with a Linkam THMS600 stage. The atmospheric environment inside the Linkam stage can be controlled by flushing a gas into the stage and the temperature varied from -196°C to 600°C.

Table 2.2: Table of specifications of the various Raman microscopes used.

Raman Microscope	**Laser Source (nm)**	**Grating l/mm**	**Stage**
WiTec	532, 633, 785	600, 1800	Piezo
Renishaw	488, 514, 633, 780, 830	1800, 2400 †	Static
Jobin-Yvon LabRam	514 , 633	600, 1800	Linkam Stage and Piezo
Renishaw Invia	514, 633	1800, 2400	Piezo
Renishaw G4L12	532, 633		Piezo

†Has an additional grating at 1200 l/mm is compatible for $\lambda = 633$ nm, 780 nm).

2.2.2 Raman Power Density Calculation from Beam Waist

Typically the spot size of a Gaussian beam can be calculated by measuring the intensity profile, P, of the beam along a knife edge and fitting the result to equation (2.1) [160, 161, 162]:

$$P = P_0 + \frac{P_{max}}{2}\left(1 - erf\left(\frac{\sqrt{2}(x-x_0)}{w}\right)\right), \qquad \text{with} \quad erf(z) = \frac{2}{\sqrt{\pi}}\int_0^z e^{-x^2}dx \tag{2.1}$$

where P_0 and P_{max} are the minimum and maximum measured intensity of the profile, x_0 an offset, w the beam waist and $erf(z)$ is the Gaussian error function.

A typical way to measure the focal spot size of a laser beam is to scan the focused beam across the edge of a silicon sample edge, while continually sampling the intensity. In

Table 2.3: Properties of the 633 nm laser during the environmental measurements using a 50x long working distance objective lens. The average power density between the high power and low power measurements is (2.95±0.19)x10^5 Wcm^{-2} and (3.43±1.22)x10^4 Wcm^{-2} respectively

Ambient	Power (mW)	Waist (μm)	Power Density (Wcm^{-2})
Air	4.55	0.831	2.09x10^5
Air	1.14	1.565	1.48x10^4
Nitrogen	4.55	0.920	1.71x10^5
Nitrogen	1.14	0.962	3.91x10^4

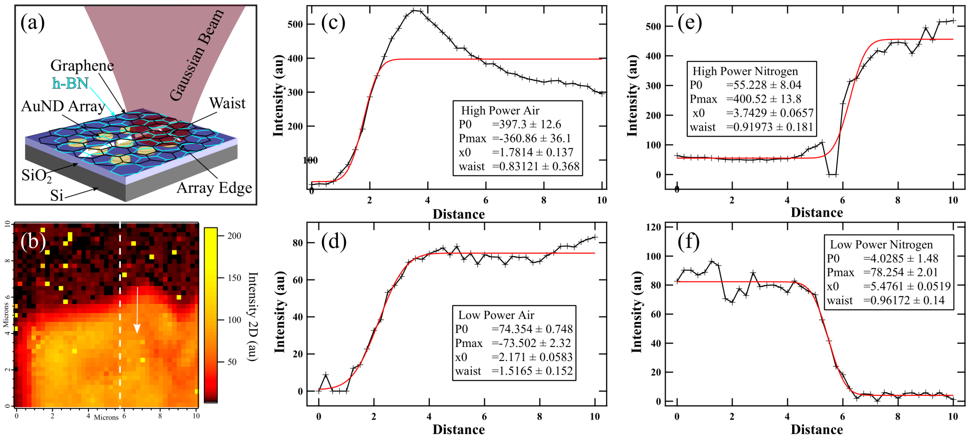

Figure 2.5: (a) Schematic of the Gaussian beam being scanned across the AuND array boundary of the G-SERS sample. The dashed white line shows the direction of travel. (b) The Raman intensity map of the 2D peak acquired during the low laser power measurement in the nitrogen ambient. The extracted intensity profile of the 2D Raman peak crossing the AuND array boundary during the (c) high and (d) low power air ambient and the (e) high and (f) low power nitrogen ambient measurements. Each profile is fitted using equation (2.1). The dashed white line of (b) corresponds to (f) the low power nitrogen ambient.

Table 2.4: Properties of the 633 nm laser during the G-SERS substrate treatment comparison study using a 100x objective. The average power density in this measurement configuration is (1.42±0.46)x10^5.

Sample	Power (mW)	Waist (μm)	Power Density (Wcm^{-2})
h-BN Spacer	3.05	0.62	2.52x10^5
Wet Transfer	3.05	1.32	5.56x10^4
Oxygen Plasma	3.05	0.912	1.17x10^5
Mean	3.05	0.95±0.20	1.42 ± 0.46x10^5

this way, the silicon sample edge is analogous to the knife edge. In this experiment, the AuND array itself is used as another type of edge. By taking a line profile of the measured intensity of the 2D peak Raman map, the change in intensity of the peak due to the SERS enhancement produces a similar knife edge profile. This is possible since the EM enhancement falls off within nanometers of the disc edge (see figure 3.1 of chapter 3), whereas the beam waist itself is in the order of microns. Figure 2.5 shows (a) a schematic of the measurement, (b) an representative graphene 2D Raman intensity map used to extract the intensity profile and (c-f) the extracted intensity profiles of all environmental Raman measurements. Since the beam waist extracted from each fitted profile is equivalent to the laser spot radius when focused, the power densities for each environmental measurement is reported in table 2.3. As a result the average power density of the high and low power measurements is (2.95±0.19)x10^5 Wcm^{-2} and (3.43±1.22)x10^4 Wcm^{-2} respectively. Similarly, table 2.4 shows the results of the beam properties of the G-SERS comparison study where the exact same procedure is used. In this experimental set up the power density is (1.42±0.46)x10^5 Wcm^{-2}.

2.2.3 Raman Spectroscopy of Graphene

A typical graphene Raman spectrum obtained from the wet transfer procedure is shown in figure 2.6a. The characteristic G and 2D peaks of pristine graphene in addition to a D peak is clearly shown at $\sim$ 1580, 2675 and 1340 cm^{-1} respectively. As with all scattering processes, both energy and momenta must be conserved. Interestingly, the G peak is the only spectral peak arising from a first order process and has the phonon wave vector $\mathbf{q} = 0$, such that it satisfies $\mathbf{q} = \mathbf{k}_i - \mathbf{k}_s$, where $\mathbf{k}_i$ and $\mathbf{k}_s$ are the incident and scattered phonon wave vectors. From the phonon dispersion in figure 2.6b $\mathbf{q} = 0$ can only be satisfied at the Γ point at the center of the Brillouin zone. Moreover, only electrons close to the Dirac point (K point of the Brillouin zone) can be excited at optical frequencies as highlighted in figure 2.6c by the blue region. On the other hand, the 2D peak is a two phonon scattering process where the phonons have opposite wave vectors ($\mathbf{q}$ and $-\mathbf{q}$) to conserve momentum (and $\mathbf{q} \simeq 2\mathbf{k}$). In addition to these fundamental graphene peaks, other spectral peaks become activated in the presence of defects such as the D' and D peak which are intravalley and intervalley scattering process respectively.

---

[*] For clarity, in Raman spectroscopy the terminology "red shift" corresponds to the phonon frequencies interacting with light have decreased. In other words, the scattered 2D photon is red shifted with respect to the G scattered photon however the 2D band phonons are blue shifted with respect to the G band

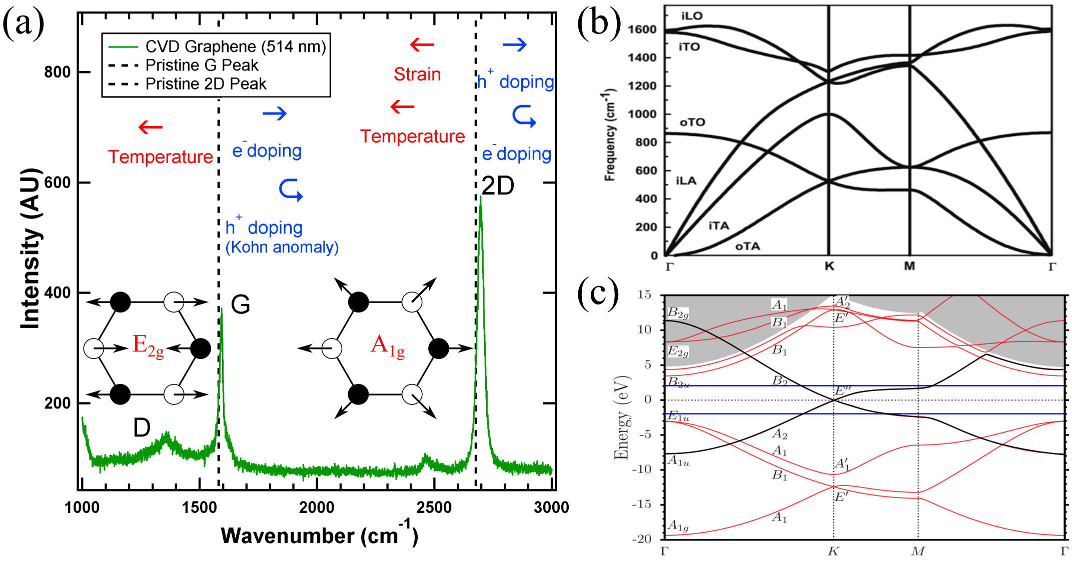

Figure 2.6: (a) Typical Raman spectrum of wet transferred CVD graphene/SiO_2/Si obtained using a 514 nm excitation source. Dashed lines correspond to the location of the G and 2D peaks of pristine graphene [163]*. A visualisation of the atomic displacements in the graphene lattice (where the white and black atoms correspond to the two graphene sublattices) and their resultant vibrational modes responsible for G (E_{2g}) and D/2D (A_{1g}) Raman peaks are shown inset. The arrows show the general peak shift trends upon charge doping, heating and straining the lattice. (b) The phonon branches of graphene reprinted with permission from [164]. Note that i denotes “in-plane” vibrations, o “out of plane” vibrations, L longnitudinal, T transverse, O optical and A acoustic phonons. (c) The band structure of graphene reprinted with permission from [165]. The black (red) bands correspond to the Π (σ) bands. The blue lines indicate the approximate energy range accessible with visible light such that phonons can only interact with electrons in this energy region.

Figure 2.7 summarises these process schematically on the electron dispersion around the Dirac point [158, 166, 164, 167]. Using the G peak as an example, the process is as follows: first the absorption of a photon of energy, $\hbar\omega_i$ facilitates the transition $|i\rangle \rightarrow |n\rangle$ forming an electron-hole pair; then the excited electron with momentum $\mathbf{k}$ and energy $E_m(\mathbf{k})$ interacts with a phonon of momentum $\mathbf{q}$ and energy $\hbar\omega_{ph(G)}$ corresponding to the transition from $|m\rangle$ to the virtual state $|n\rangle$; finally the electron-hole pair recombine emitting a photon of energy, $\hbar\omega_{s(G)}$ corresponding to $|n\rangle \rightarrow |f\rangle$ where $|f\rangle$ is the final

---

phonons.

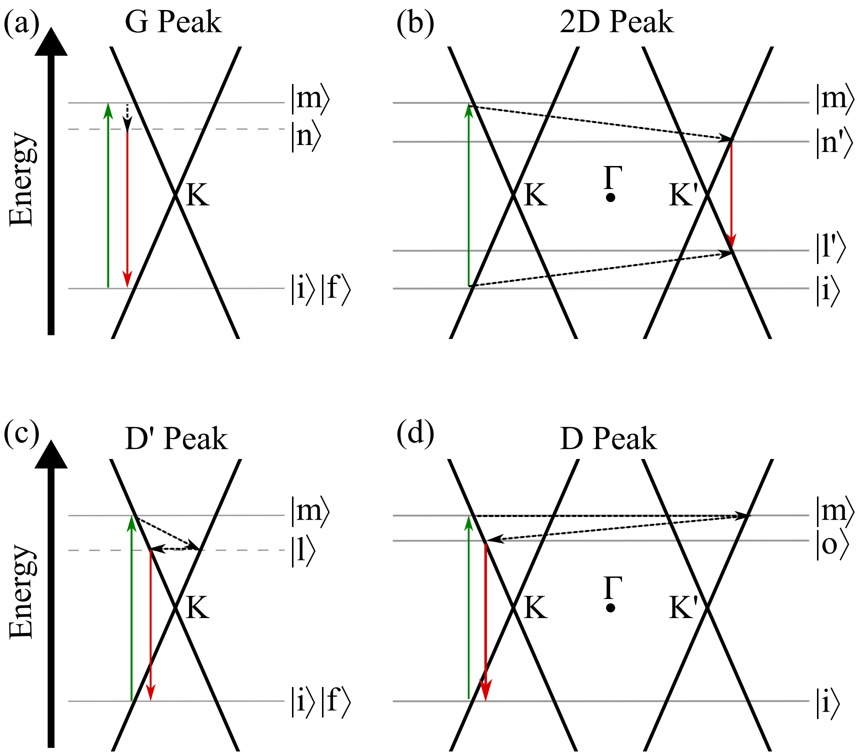

Figure 2.7: Examples of prominent Raman scattering processes in graphene adapted from [166, 164]. The solid black lines show the electron dispersion around the K (and K') point(s). (a) First order G peak process involves the electron scattering with the $q = 0$ phonon. (b) Second order 2D peak process where the scattering involves two iTO phonons with equal but opposite momentum in k-space. Defect activated processes (dashed horizontal arrows) give rise to the (c) D' peak and (d) the D peak. Grey lines are a guide for the eyes to show the energy states of the system. The solid gray lines indicate real energy states and the dashed gray lines indicate virtual states. Therefore all optical transitions between solid gray lines indicate are resonant processes whereas transitions from dashed line are not.

energy state of the process. Clearly for energy conservation purposes the incident and final states must be equal, i.e. $|f\rangle = |i\rangle$ [158, 168]. Similar logic can be used to construct the processes of the other Raman peaks of graphene as shown in figure 2.7. Due to the linear dispersion around the K point all vertical transitions from and to a solid grey line are real at optical frequencies. A corollary of this is that, provided the graphene isn't doped beyond 2E$_F$ which will result in Pauli blocking, all optical frequencies are resonant. Moreover, the two phonon process contain two resonant process which results in the 2D peak being twice the height of the G peak (See appendix A.1.3 for more details).

2.2.4 Interpretation of Graphene Raman Spectra

Like the electron dispersion, the phonon dispersion of graphene is derived from its honeycomb crystal lattice structure. As a result, perturbations in the crystal lattice due to thermal expansion, stress/strain, carrier density and environmental conditions perturb the Raman signal. In general the G and 2D phonon modes blue shift upon electron and hole doping and redshift upon increasing temperature and tensile strain [166, 169, 170, 163] as summarised in figure 2.6. Interestingly, due to the highly symmetric nature of the graphene branch structure at the Γ and K points, the phonon modes soften (decrease) in what is called a Kohn Anomaly [171, 172, 164, 173]. As a result hole (electron) doping of the G (2D) band can lead to a small redshift before a blueshift [163, 169]. Moreover, the relative intensity of the peaks are dependent on good phonon-electron coupling, such that strong doping and strain perturbations decreases the intensity of the G band and 2D band due to increasing scattering probabilities [170, 169], where the exact origin is complex since the density of states of the band and branches is needed [174]. The two phonon double resonance process also results in the wavelength dependence of the 2D band (and D band). Further to this, the 2D band broadens significantly in the presence of high doping and interactions with other aromatic chemical species including another graphene layer [175, 176]. Finally, the presence of the D and D'peaks (where the D' peak is located as a sharp shoulder on the G peak at around ~ 1590 cm^{-1}) are indicative of disorder/defects in the lattice [177, 164, 166]. Obviously, the appearance of sharp additional peaks, in addition to the perturbation of the graphene peak shapes, imply that an external molecular source is interacting with graphene and has its own Raman spectrum convolved with the graphene spectrum. However, not all molecular species have strong Raman cross sections, and will not produced a signal without some form of enhancement mechanism. For example 4-aminothiophenol and 4-nitrothiophenol require a SERS type of enhancement to be observed, but they do perturb the graphene signal.

2.2.5 Spectral Processing

Clearly there are a lot of factors that change graphene peak shape and location. Moreover, it is rare that a single spectrum is truly representative of the overall properties of the graphene sample. Instead, it is more useful to compare the graphene properties over a sample area and build up statistics of the spectral peak properties associated with the sample. In this thesis all spectral maps are analysed using Igor Pro version 6.37 regardless of the Raman microscope used to collect the spectral data. This has the added benefit of consistent analysis between different Raman instrumentation, being in full control of background removal procedures, the processing of convolved peaks and enabling quality control checks within the analysis. Typically, after the spectral data is acquired, any background slope convoluted with the spectral peak is removed (see appendix A.3) and the individual peak is fitted either with a Gaussian or Lorentzian peak shape using an Levenberg-Marquardt algorithm, which is a non-linear least-squares fitting procedure, as follows:

$$f_{Gauss}(x) = y_0 + A\left\{exp - \left(\frac{x - x_0}{width}\right)^2\right\} \tag{2.2}$$

$$f_{Lor}(x) = y_0 + \frac{A}{(x - x_0)^2 + B} \tag{2.3}$$

where A is the peak amplitude (intensity), x_0 is the peak position and y_0 an offset. The FWHM from the Gaussian peak from is $2\sqrt{ln(2)}width$ and from the Lorentzian is $2\sqrt{B}$.

2.3 Scanning Probe Microscopy

Scanning probe microscopy (SPM) instruments consist of a probe, with an atomically sharp tip, which is scanned across a surface while maintaining a constant force or force gradient by a feedback loop. As the probe is drawn across a surface, it interacts with the interatomic forces between the surface and the tip, which are topographically dependent and can be measured [178]. A Dimension 3100 and Brucker's ICON scanning probe microscopy instruments are used predominantly to measure the height profile and surface potential profile using atomic force microscopy and kelvin force microscopy.

2.3.1 Atomic Force Microscopy Apparatus

In AFM the attractive and repulsive (Van der Waals) forces between the probe and the surface are investigated using a probe, which consists of an atomically sharp tip attached to a reflective cantilever, which is mounted onto a piezoelectric actuator and a position sensitive photodiode detector (figure 2.8a). A laser beam is reflected from the end of the cantilever onto the photodetector accurately measuring the movements of the tip. An electrical current proportional to the beam movement is generated at the detector which can then be converted to a voltage signal. This voltage is then compared to a desired 'set point' value and the error between the two is used to force the tip back to the desired position of the cantilever in an automated feedback procedure [179, 180].

As the tip approaches a surface it is initially attracted by the surface predominantly through van der Waals forces [182]. These attractions increase the closer the probe gets to the surface until the atoms of the tip become very close to the atoms of the surface and the orbital electrons begin to repel (figure 2.8b). There are three typical

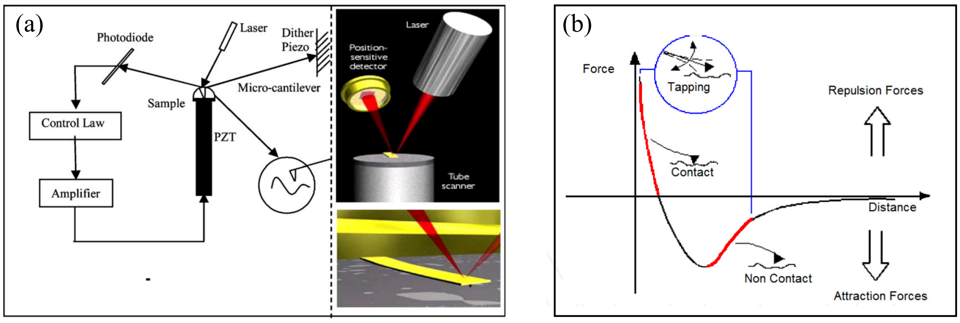

Figure 2.8: (a) Generalised schematic of an AFM where the inset is of the cantilever components reproduced with permission from [179]. (b) Typical force curve of an SPM tip as it approaches the surface [181].

AFM modes commonly used to probe these forces: contact, non-contact and tapping mode. Contact mode is where the tip is brought into direct contact with the surface and interacts with the repulsive forces as it is dragged across the surface. Non-contact AFM probes the attractive forces by oscillating at the cantilever's resonant frequency a distance above the surface. Tapping mode AFM, like non-contact mode, oscillates above the surface but is intermittently brought into contact with the surface. As the oscillating tip is brought into contact, force interactions cause a shift in the oscillation resonant frequency thus measuring the change in amplitude or frequency gives information on the interatomic forces and a surfaces topography. In other words, the deflection of the laser beam mechanically induced oscillation of the cantilever is dependent upon the surface forces that interact with the tip.

2.3.2 Kelvin Force Microscopy

Kelvin Force Microscopy (KFM) is an extension of AFM but instead probes the electrostatic forces between the tip and the surface. In KFM a conducting tip, with work function ϕ_t, is brought into contact with an electrically grounded surface, with work

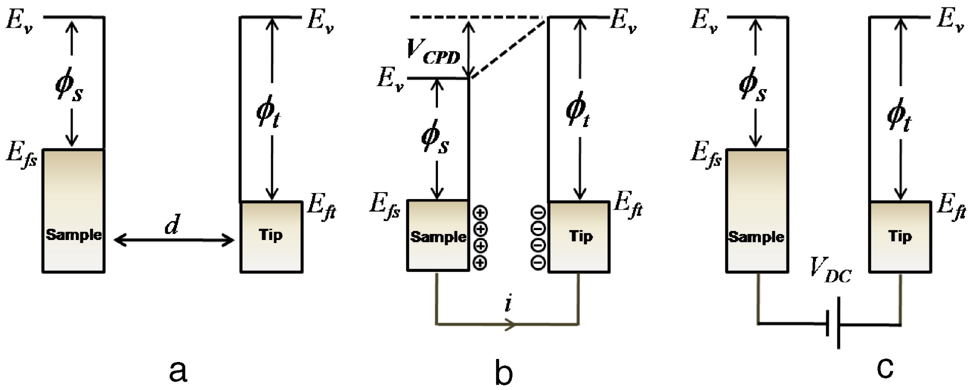

Figure 2.9: The electronic energy levels of the sample and the tip (a) when the tip is not interacting with the surface and they are a large distance apart, (b) brought close to the surface and the Fermi Levels align and (c) an external voltage applied at V_{CPD} to restore the Fermi Levels back to the original state. Figure reprinted with permission from [183].

function ϕ_s creating a contact potential difference (CPD) V_{CPD}:[†]

$$V_{CPD} = \frac{(\phi_t - \phi_s)}{\pm e}. \tag{2.4}$$

Initially, before contact (figure 2.9a), both the tip and the sample are aligned with identical vacuum energies a distance d apart. As the tip is moved closer to the surface, it is brought into electrical contact. The electrons then migrate from the material with the lower work function to the material with the higher work function (figure 2.9b this is from the sample to the tip). At equilibrium an electrical force is generated between the tip and the sample surface due to their respective Fermi levels aligning creating a contact potential difference V_{CPD}. The contact potential difference (CPD) can be nullified by applying an external bias V_{DC} until the electrical force disappears (figure 2.9c).

To measure the V_{CPD}, a two pass method is used. On the first pass the surface topography is measured using tapping mode AFM. On the second pass, the probe scans the same

---

[†] The ± e term in equation (2.4) depends on how the apparatus is biased.

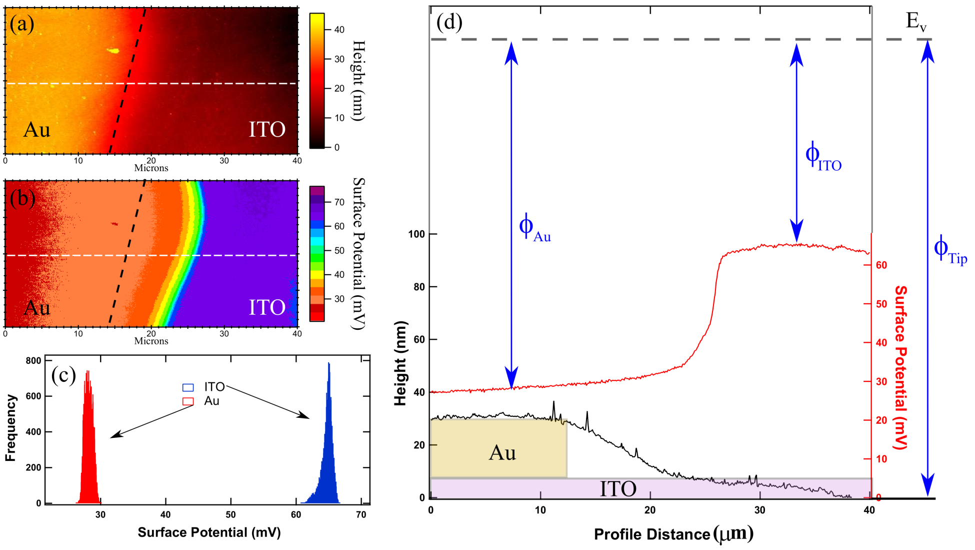

Figure 2.10: (a) AFM and (b) KFM micrographs across a Au-ITO step. The dashed black lines roughly show the gold step boundary where the diffuse edges are due to the tip curvature. (c) KFM histograms of the surface potential distribution on the gold and ITO surface. (d) The AFM (black) and KFM (red) surface profiles of the white dashed lines from (a) and (b) respectively. Overlaid on this image is a schematic of the Au-ITO step and the relative magnitude of the measured work functions of the Au, ITO and PtIr tip where E_V is some vacuum energy level. From this measurement it is confirmed that the machine is biased such that equation (2.4) is $eV_{CPD} = \phi_{tip} - \phi_s$.

area except held at the same distance above the surface. During this second pass, an oscillating voltage is applied to the tip $V_{ac} = V\cos(\omega t)$ such that the tip is attracted and repulsed by the charge at the surface, which induces a mechanical oscillation that can be measured by laser deflection as before. Considering the tip-sample system to be a capacitor, the electrostatic force on the tip can be described as follows:

$$F_{el} = -\frac{1}{2}\frac{dC}{dZ}(V_{dc} - V_{CPD} + V_{ac}\cos\omega t)^2, \tag{2.5}$$

Where dC/dZ is the differential capacitance between the surface and the tip [182]. Therefore, to measure the magnitude of the voltage induced deflection, a compensating dc-voltage, V_{dc}, between the tip and the sample is applied such that when the V_{ac} reaches a minimum and V_{dc} is equal to the contact potential Voltage.

Equation (2.4) is dependent upon the biasing of the KFM apparatus. It is unclear how the machine is internally biased and if the software is designed to compensate for it. Therefore a simple experiment measuring the potential step across a physical gold - indium tin oxide (ITO) step confirms the biasing. Figure 2.10 displays representative measurements of (a) the topography, (b) the surface potential, (c) surface potential histograms over each material and (d) line profiles across the AFM and KFM maps across the Au-ITO step. In ultra high vacuum, the work function of gold and ITO are ∼5.2 and 4.5 eV [184, 185] such that $\phi_{Au} > \phi_{ITO}$. Therefore, the potential step measurement of figure 2.10d is only consistent when $eV_{CPD} = \phi_{tip} - \phi_{Au}$; where the platinum iridium tip purchased from Windsor Scientific Ltd has a high work function ∼5.7-6.3 eV. It should be noted, that the lack of a sharp interface at the step is due to a combination of: the gold deposited material having a diffuse edge and the lateral KFM and AFM resolution being limited by the probe geometry [186, 187].

Kelivn Peak Force Tapping

Brucker's ICON scanning probe microscope has the additional functionality of peak force tapping. During the AFM tapping scan, this instrument simultaneously measures a force curve similar to figure 2.8b, at every point scanned as the tip approaches and is withdrawn. A force set point is chosen during the AFM scan, which has the benefit in preventing the tip from crashing into the surface and allows soft and hard surfaces to be measured reliably without risking the tip integrity. Moreover, since a force curve is measured at every point, nano-mechanical information such as tip-surface adhesion and dissipation is measured simultaneously as the height information. After the peak force informed surface topography is measured in the AFM scan, the probe is brought to a fixed height above the surface as before and surface potential is measured in Kelvin pass.

2.3.3 KFM Tip Calibration Reference Sample

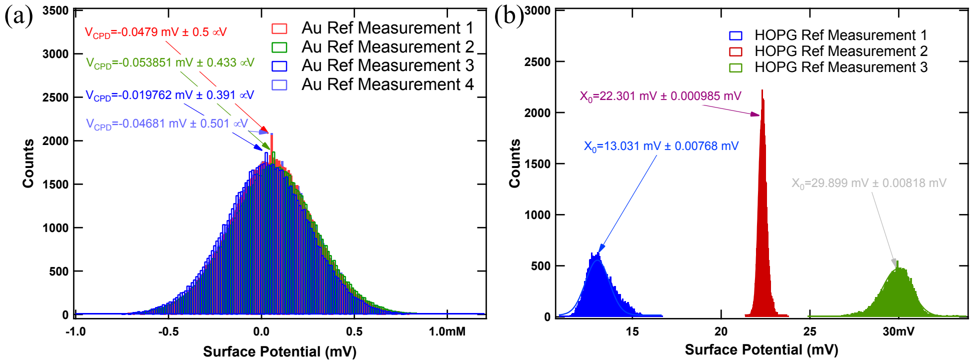

Figure 2.11: Repeated measurements of the surface potential of different areas on (a) gold and (b) HOPG reference samples. The measurements between 2 and 3 on the gold reference were on a different samples showing that the tip didn't degrade much during this particular measurement. Conversely there is a lot of variation between HOPG regions making gold a better reference material due to its consistency.

The work function is defined as the minimum energy required to remove an electron from a material such that $\phi = V_{Vacuum} - E_F$, where V_{Vacuum} is the vacuum potential and E_F is the materials Fermi energy. This is particularly useful in graphene characterisation, since a change in the Fermi energy of graphene results in large changes of its electrical properties [188, 189]. As are result KFM is an invaluable tool in assessing spatial doping variations due to wrinkles [190], nano device geometry [191], multilayer regions [192, 193, 194], strain [195], substrate material variation [196] and molecular dopants [197, 74]. To determine the work function of the graphene surface, the work function of the SPM tip is calculated using equation (2.4) where ϕ_s is the work function of a known reference sample. Highly ordered pyrolytic graphite (HOPG) and gold were both tested as reference sample candidates. The widely accepted work function of gold at $\sim$ 5.1 eV holds only in vacuum conditions. The moment the gold sample is brought into ambient conditions, atmospheric gases adsorb onto the surface and alter the work function[184, 197, 198]. On the other hand HOPG, upon mechanical exfoliation of a graphitic layer, a fresh surface can be measured before an appreciable number of adsorbates contaminate the surface [184]. Figure 2.11 both reference samples are tested and the gold reference sample is more stable. In practice, cleaving the HOPG sample created terraces of graphitic layers with varying degrees of surface adhesion which made it an inconsistent reference sample. Moreover, HOPG had a tendency to containate the surface of the tip. Therefore, despite an absolute workfunction of the gold reference sample being unknown in the lab ambient conditions, the consistency of the surface potential distribution regardless of where the tip is located on the sample, made it a more reliable calibration source.

2.3.4 Work Function Determination of G-SERS platform.

Figure 2.12 compares the 60 x 60 μm AFM and KFM images acquired after different environmental laser exposures. Although the SPM tip is calculated against a gold reference sample, its work function inevitably alters between measurements due to tapping induced blunting or interaction with contaminant residues on the graphene surface. Moreover, it is difficult to bring the SPM tip into 'contact' at the same interaction distance (a problem resolved using KPFM). As such, the gold calibrated SPM tip is used to measure the entire graphene coated AuND array to determine the deviations in surface work function. From this, sequential measurements using a fresh SPM tip is calibrated against an unperturbed part of the graphene sample. Although higher resolution images are obtained of the regions of interest, comparing the whole array provides a more accurate work function determination to measure gas induced changes.

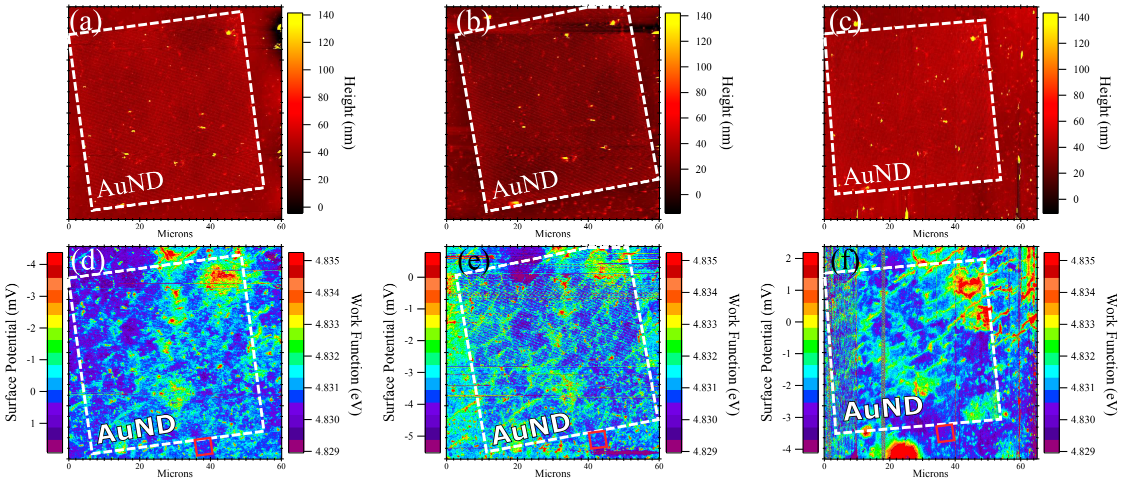

Figure 2.12: AFM images (a) before laser illumination, (b) after laser illumination in a N_2 gas environment and (c) after laser illumination after compressed air environment where (d-f) are the corresponding KFM measurements. After the first tip calibration, the graphene in the red box region is used to calibrate the work function of sequential tips.

2.4 Scanning Electron Microscopy

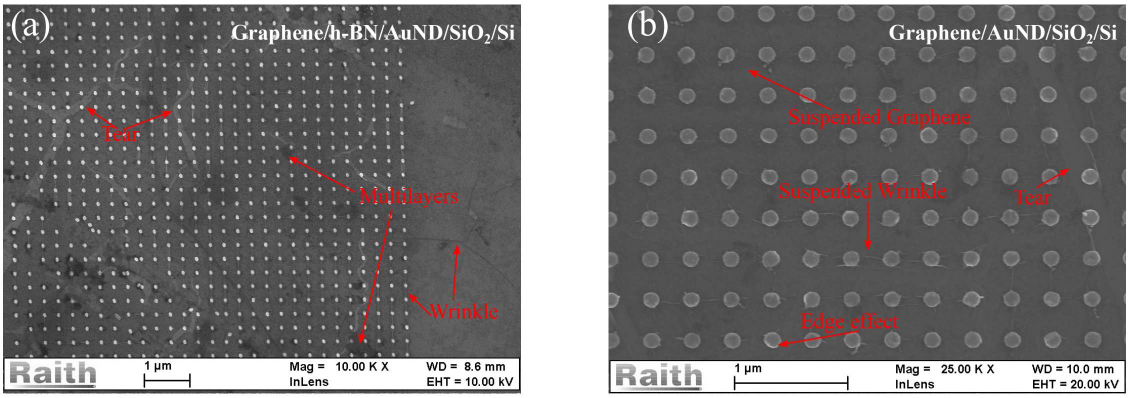

Figure 2.13: Scanning electron micrographs of (a) dry transferred graphene and h-BN, and (b) wet transferred graphene on gold nanodisc arrays. Surface adhesion and defects such as tears and wrinkles can be viewed using SEM.

All scanning electron microscope (SEM) images are taken using a Raith e-Line electron lithography system. The main components of any SEM is the electron source, the column the electrons are accelerated through, the electron detector and the sample chamber. The beam of electrons interact with the material which emits secondary electrons, where the intensity of the collected emitted electrons build an image of a surface. In this work, images are taken using 10 kV drop from the beam column resulting in a 30 μm focusing beam aperture and 10 mm working distance. Although graphene is conductive, the energy of impacting electrons is enough to defect and dope the graphene sheet. Therefore after an image is taken the electron beam is immediately capped to prevent overtly damaging the film. Due to the two dimensional nature of graphene, there is little variation in the secondary electrons of pristine graphene. Instead, multilayer, defects, boundaries, tears and wrinkles are easily viewed using SEM [199, 200].

Figure 2.13 are typical SEM images of (a) graphene and h-BN dry transferred and (b) graphene wet transferred onto a gold nanodisc SERS array. The periodic array is clearly visible and have a brighter contrast due to a nanoparticle edge effect. Graphene wrinkles and multilayers typically have a darker contrast, whereas tears in the graphene brighter die to underlying insulating substrate charging up upon electron beam exposure. Interestingly, although SEM enables high resolution images of graphene, due to the atomic flatness of 2D materials it is difficult to determine much more about 2D heterostructure interactions. Instead Haigh et AL. [201] demonstrate that the individual layers of a 2D heterostructure can be imaged using transmission electron microscopy of a sample cross section.

2.5 FTIR

Fourier transform infrared spectroscopy is a widely used technique to study the light-matter interaction at near, mid and far infrared frequencies. As the source light impinges the surface, the light will either transmit, adsorb or scatter resulting in a characteristic

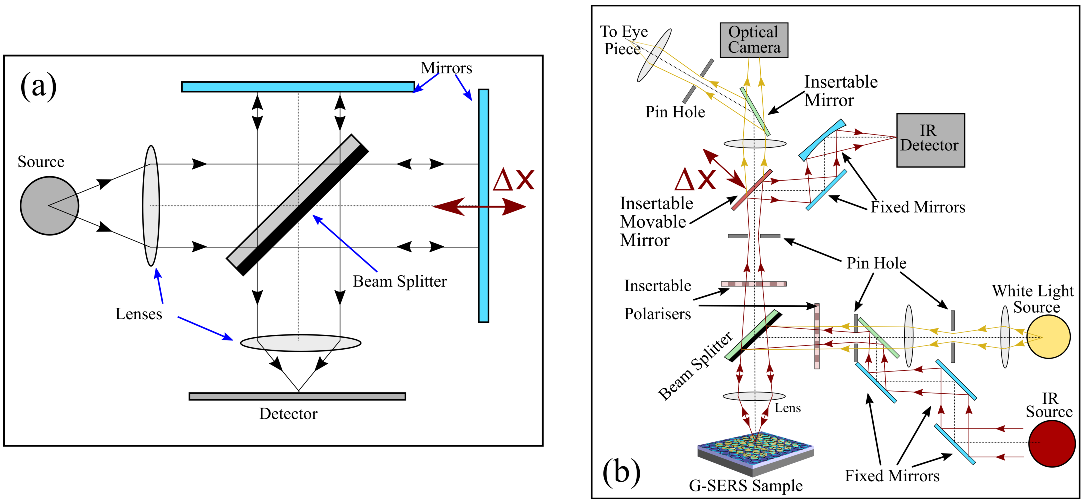

Figure 2.14: (a) Beam path in a Michelson interferometer, where the path of one of the split beams can be modulated by a distance of Δx using a movable mirror. (b) The beam path based on a Hyperion 3000 FTIR microscope in the reflection mode. The multiple movable mirrors in place enable switching between the IR and white light beam paths and the insertable movable mirror is necessary to achieve an interferogram of the light reflected from the target G-SERS sample.

spectrum of the material's properties. The spectral response is acquired by using a Michelson interferometer component to generate an interferogram in conjunction with the use of discrete Fourier transforms to convert the spatial signal into a frequency signal. A Michelson interferometer (figure 2.14a) splits a source beam through a partially reflective beam splitter, whereupon one of the split beams is reflected from a mirror, a distance L from the beam splitter, towards the detector. The other split beam is also reflected back towards the detector using a movable mirror that can be moved precisely by Δx around L, such that as the reflected light approaches the detector, it will interfere with the other light [202]. As a result, a monochromatic light source will result in a typical interference pattern and a polychromatic light source an interferogram dependent on the value of x. The intensity of the combined wave trains is a function of x such that $I(x) = S(\nu)cos(2\pi\nu x)$, where $S(\nu)$ is intensity of the the monochromatic line located at wavenumber ν. The interferogram is sampled by moving the mirror through N discrete equidistant steps and converted the real space domain to the frequency domain using a discrete Fourier transform as follows [203]:

$$S(k \cdot \Delta \nu) = \sum_{n=0}^{N-1} I(n\Delta x) exp\left(\frac{i2\pi nk}{N}\right), \tag{2.6}$$

where the $\Delta \nu$ spacing in reciprocal space is related to real space Δx by $\Delta \nu = 1/(N \cdot \Delta x)$. In addition to this method achieving high wavenumber accuracy, the acquisition of spectral data is limited by the speed at which the mirror can moved, making it significantly faster than the monochromatic equivalent.

Placing a sample in the beam path will perturb the interferogram, as shown in figure 2.14b. Since silicon isn't transparent in the near and mid IR, measurements of the G-SERS samples were acquired using the 'reflection' mode. As a result, to deconvolve the perturbed spectral signal from the source, the interferogram of the source signal is obtained by placing a gold mirror in the place of the sample. All measurements were acquired using a Bruker Hyperion 2000 microscope. Depending on the spectral range, silicon and InGaAs (indium gallium arsenide) detectors are used in the near and mid IR regions respectively (see figure 3.2 in chapter 3). The gold nanodiscs typically resonate in the near IR/visible region, as such most measurements are taken using the silicon detector.

2.6 Electrical Measurements

2.6.1 DC Transport Measurements

Both traditional DC and non-traditional microwave AC measurements investigate the electrical properties of graphene. Since the development of the microwave measurements is an extensive part of chapters 4 and 5, only a brief explanation of standard DC

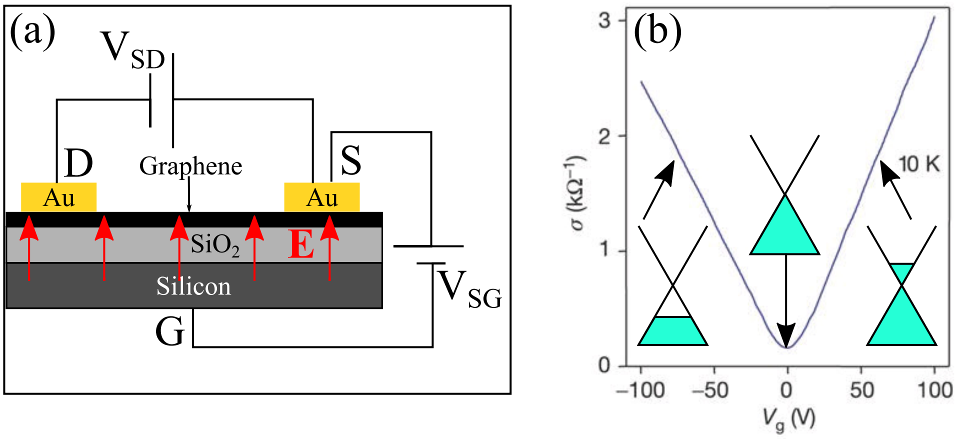

Figure 2.15: (a) Two terminal geometry for G-FET characterisation. (b) Typical conductivity response of graphene adapted from [204], showing ambipolar behaviour. Upon increasing (decreasing) the gate voltage from the charge neutrality point at $V_G = 0$, the electron (hole) concentration and conductivity increases.

graphene transport measurements is described here. Graphene field effect transistor (G-FET) devices allow fast characterisation of the electrical properties of graphene [24, 205, 206]. Indeed this measurement (using a four terminal configuration) confirmed the presence of graphene in Novoselov and Geim's seminal work [122]. Figure 2.15a shows how the source/drain and source/gate biases are applied in this G-FET configuration; where the silicon dioxide layer functions as the gate dielectric. A voltage, V_{SG}, is dropped across the oxide causing charge to build up at the interface. The graphene electrons then 'reorganise' to minimise the effect from the charged silicon dioxide interface, ultimately inducing an electric field across the interface forming a parallel plate capacitor system. The mobility of such a system can be described as follows:

$$\mu = \frac{\sigma}{ne} = \frac{\sigma}{Q} = \frac{\sigma}{C_g V_g}, \tag{2.7}$$

where the gate capacitance $C_g = \epsilon' \epsilon_0 A / t_{ox}$ and A, t_{ox} and ϵ' correspond to the area, thickness and permittivity of the dielectric layer.

Now, the sheet conductivity of a material is described by:

$$\sigma_S = \frac{L}{R_S W}, \tag{2.8}$$

where L and W are the length and width of the graphene channel and R_S the sheet resistance. By combining equations 2.7 and 2.8 and using Ohms Law the graphene mobility can be described as follows:

$$\mu = \frac{\partial \sigma}{\partial V_g} \frac{1}{C_g} = \frac{\partial I_{SD}}{\partial V_g} \frac{L}{W} \frac{1}{C_g V_{SD}}. \tag{2.9}$$

Using a Keithley dual source measure unit (SMU), the source drain current, I_{SD}, is measured during a gate voltage, V_{SG}, sweep while keeping the source drain voltage V_{SD} constant. In this way the hole and electron mobilities can be calculated using equation (2.9) by fitting the gradient of the measured curve at either sides of the Dirac point. A consequence of equation (2.9) is that the length and width of the measurement channel greatly effect mobility result. Explicitly, since the mobility is limited by intravalley scattering processes [207, 208], smaller measurement channels result in higher mobilities. In this work, the length of the measurement channel is in the order of centimeters whereas typical graphene devices are in the order of micrometers or less.

2.6.2 Microwave Dielectric Resonators

Electromagnetic microwave resonance is a phenomenon exhibited by conducting cavities or free standing dielectric structures or a combination of the two geometries. The common feature of these resonators is that electromagnetic standing waves can be set up at certain frequencies. The values of these resonant frequencies are set by the size, geometry and relative permittivity of the enclosed materials. Ignoring any microwave dissipation processes the resonant frequencies would be infinitely sharp but in real resonators there will be loss processes (such as ohmic dissipation in the conducting walls of the cavity, dielectric losses in the dielectric materials and external losses representing the microwave radiation coupled out of any feed structures). As a result of finite losses from these processes, real resonators have finite linewidths associated with each resonance. This leads to their wide use as filters and other microwave frequency selectors – typically between 300 MHz-300 GHz – making them integral components in oscillators, amplifiers and tuners for microwave circuits [209, 210, 211]. Resonance in a dielectric resonator is analogous to hollow metallic cavities, except that the boundary conditions are defined by the large change in permittivity at the dielectric material's interfacing surface, instead of the interface of a conductor. As a result, the resonant modes are dependent upon the geometry and the relative permittivity of the dielectric material [209].

A useful figure of merit for a resonator is its quality factor, Q, which describes a resonators capability to store electromagnetic energy and is the ratio between the maximum energy stored and the maximum energy dissipated per cycle - where dissipation typically occurs through heat losses. More quantitatively, the Q factor can be derived to approximate the ratio between the resonant frequency and its associated linewidth such that [210]:

$$Q = \frac{f_0}{\omega_0}, \tag{2.10}$$

where f_0 and ω_0 correspond to the resonant frequency and its linewidth respectively.

In this thesis, a frequency domain transmission technique is used to measure the Q of a resonator. This involves inserting the resonator into a metal enclosure and using two coaxial probes connected to a vector network analyzer (VNA) to source and measure the input and output microwave signals [210, 212]. The resultant transmission curve of a resonant mode is of a Lorentzian lineshape in the frequency domain where the central frequency is f_0 and its full width at half maximum or linewidth is ω_0.

The overall losses in the resonator are additive and the observed linewidth ω_0 is related to the individual losses arising from several sources according to the relationship [213, 214]:

$$\frac{\omega_0}{f_0} = \frac{R_h}{G_h} + \frac{R_g}{G_g} + \tan\left(\frac{\delta}{g_d}\right), \tag{2.11}$$

The first two terms represent conduction losses, arising from the walls of the resonator (having sheet resistance R_h) and from any other conducting material included within the resonator housing (in this case the graphene film which is being measured, having sheet resistance R_g). The third term represents losses in the dielectric resonator structure itself, where $\tan\delta$ is the loss tangent δ of the dielectric, defined as the ratio of the imaginary to real parts of the permittivity. The constants G_h and G_g are geometric factors which relate to the electromagnetic energy density at the resonator and graphene respectively, normalised by the energy stored in the cavity. Similarly, g_d is a geometry factor related to energy stored within the dielectric. The coupling losses are ignored since these may be made arbitrarily small. Additionally, the loss in the substrate on which the graphene sample is supported, is also small enough to disregard, as well as remaining constant.

It is the simple additivity of these losses, combined with the accuracy of frequency measurement, which makes the dielectric resonator method a powerful means to characterise the sheet resistance R_g. The housing losses can be made small so that changes in R_g, in response to chemical or electric field doping or temperature can be accurately measured if the graphene film is brought into the evanescent field region which surrounds the dielectric resonator.

In practice, the additive contributions to the overall resonator linewidth ω_0 means that the quality factor of a loaded resonator system (Q_L). In any mode of operation, this can be expressed in terms of quality factors associated with each of the individual loss mechanisms leading to the formula:

$$\frac{1}{Q_L} = \frac{1}{Q_d} + \frac{1}{Q_c} + \frac{1}{Q_r} + \frac{1}{Q_{cpl}}, \tag{2.12}$$

where Q_d, Q_c, Q_r and Q_{cpl} are dielectric, conductive, radiative and coupling losses respectively.

Surface impedance measurements typically use $\mathrm{TE}_{01\delta}$ resonant modes since the intrinsic quality factor can be high (as there is very low dissipation in the housing for this mode geometry). The dominant dissipation of energy is then due to the evanescent electric fields interacting with conduction electrons in the graphene surface. Provided the presence of the graphene and its substrate do not perturb the frequency of the resonator too much, first order perturbation theory is applicable and equation (2.12) may be applied and the perturbation of Q_L allows the evaluation of sheet resistivity, provided the geometry facotrs are known or can be measured. A particular case for measuring the sheet resistivity of graphene is derived in chapter 4 section 4.2. However, more complete descriptions of dielectric resonator mediated surface impedance measurements can be found here [213, 214, 215, 216].

2.6.3 Determining the Resonant Frequency and Linewidth in the Microwave Measurements

From the previous section, the measurement of Q is an integral component for the measurement of the graphene conductivity. In this work two resonant peak fitting procedures are used. The first of which is the '3 dB method'. This method simply relies on the in-built analysis software in the Anritsu series 37XXXC vector network analyzer

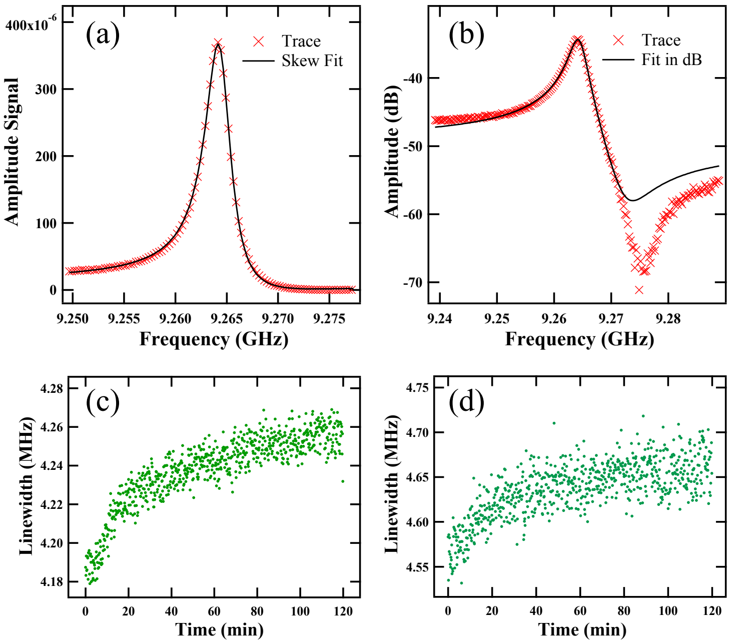

Figure 2.16: Resonant mode fitted with the skewed Lorentzian curve using (a) a linear scale and (b) a logarithmic scale. The sensor response at 3 ppm NO_2 using the (c) LSF and (d) 3dB method to fit the resonant mode.

(VNA). The Anritsu VNA, which works in the logarithmic scale, calculates the resonant frequency by reading the maximum value in the pre-programmed data range. The two linewidth points are calculated by subtracting 3 dB units from this maximum value. If the resonant peak does not have a background slope this method accurately measures the resonant frequency and the linewidth. This is the case in chapter 4 where the graphene sample is enclosed by the copper housing. However, using the open cavity configuration as shown in chapter 5, the resonant mode is located on a slight slope. As a result, the maximum value is not the resonant frequency, instead it is slightly offset. Secondly the two points to calculate the linewidth are clearly offset upon visual inspection with the VNA as the 3dB method cannot compensate for the slope. The origin of this slope is suspected to be due to convolution of the resonant signal with a destructive interference mode due to microwave cable length.

To compensate for this slope, the resonant data is converted to the linear scale ($linear =$

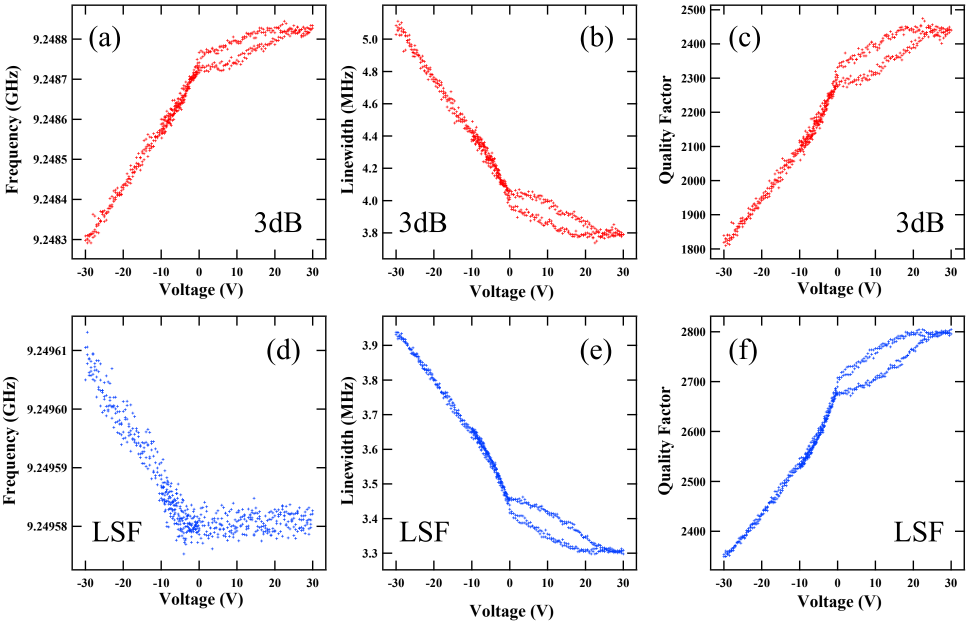

Figure 2.17: Comparison of the measurement of frequency, linewidth and quality factor of the resonant using the (a-c) 3dB method and (e-f) LSF method respectively.

$10^{dB/10}$) and fitted using a least squared fitting procedure (‘LSF method’) of a skewed Lorentzian curve described as follows:

$$y(x) = \frac{af_0 + s(x - f_0)}{(x^2 - f_0^2)^2 + (\omega^2 x^2)^{\frac{1}{2}}} + c, \tag{2.13}$$

where f_0 and ω are the resonant frequency and linewidth respectively, a is the amplitude, s defines the skew and c is an offset value.

Figure 2.16a shows an example of a trace of the empty cavity resonant mode being fitted to equation (2.13) where figure 2.16b is the same data converted to the logarithmic scale. Clearly, the fit describes the main properties of the resonant mode and is less successful in capturing the lossy mode. Figure 2.16c and d follow the change in linewidth upon exposure to 3 ppm NO_2 evaluated using the ‘LSF method’ and the ‘3dB method’ respectively. The linewidth calculated using the LSF method is sharper and less noisy than the 3 dB method.

The deviation between these two fitting procedures is most pronounced during the applied electric field measurements of the graphene. Figure 2.17a-c and d-f compare the resonant frequency, linewidth and quality factor of the same measurement analysed using the 3 db and LSF methods respectively when sweeping an applied voltage. The most pronounced difference is in the measurement of the resonant frequency which is shown to increase (decrease) upon increasing gate voltage using the 3 dB (LSF) method. As the linewidth sharpens upon increasing gate voltage, the skew becomes more pronounced and the maximum frequency value is more offset from the resonant frequency. Interestingly, the LSF measured frequency in the region of the Dirac point is consistent, indicative of the loss of precision of the microwave measurement as the graphene sheet reduces in conductivity. Although the LSF reduces the maximum change measured, the reduced noise in the linewidth and gas measurements is significant making it the more reliable measurement.

2.7 Finite Difference Time Domain Calculations

Finite difference time domain calculations are performed using Lumerical FDTD Solutions software. The sample material and geometry is first imputed into the software. Of importance is the inputting of the complex permittivity range of the material being modeled in the frequency range calculated. Then the system is meshed into discrete Cartesian cells of dimensions Δx, Δy and Δz. By solving Maxwell's equations at discreet time interval steps, Δt, at the boundaries of each cell. The calculation is started by injecting a plane wave source above the structure. The new field components at Δt are then calculated sing the finite difference between the previous spatial boundary points based at the values at the previous time interval. This is continued until steady state conditions are met. The frequency values are then extracted using Fourier transform.

To model the response of a AuND array, a single gold nanodisc monomer unit with periodic boundary conditions is simulated as an approximation. Additional boundary conditions involve the use of perfectly matching layers (PML) to prevent stray reflections from interfering with the calculation (e.g. at the base of a silicon substrate). Specifically, a plane wave source is used to illuminate the modeled surface. The reflected waves are monitored with a detector placed above the structure (see figure 3.2 from chapter 3). The near field components of nanostructures are assessed by placing monitors at the xy and xz axis cutting through the nanodiscs (see figure 3.1c and d of chapter 3). The average electric field above a nanodisc is achieved by calculating the mean value of the full xy plane of the monomer unit as seen in figure 3.1e of chapter 3.

Chapter 3

G-SERS Platforms for Enhanced Optical Sensing

3.1 Introduction to Chapter

SERS is a powerful analytical technique that provides fast real time ultra sensitive molecular detection; providing a chemical finger print of the species detected [217, 218]. Graphene metal nanoparticle hybrid devices present promising molecular sensing platforms. Through the combination of spectral enhancements originating from the nanoparticle decorated substrate, in a typical SERS response [217, 219, 220], and meV the graphene itself, in what is aptly names graphene enhanced Raman spectroscopy (GERS) [116, 221, 222]. These hybrid devices are named G-SERS platforms [113, 115, 29, 223, 224, 225]. In addition to spectral enhancements mediated through the traditional electromagnetic and chemical mechanisms, G-SERS platforms quench unwanted fluorescence from 'probe' molecules [224, 226], provide an atomically flat surface [29] and the overall enhancement can be improved via electrically tuning the graphene Fermi level [227, 228, 229]. As a consequence, G-SERS platforms have the potential to not only selectively enhance trace molecules, but also simultaneously evaluate the quality of the graphene through its characteristic Raman spectrum. However, the Raman spectrum of graphene itself changes upon doping [169, 170].

Although there are a variety of studies correlating the local doping variation in graphene through kelvin probe microscopy and its Raman spectrum [189, 192, 194, 196, 230, 231], a detailed study of the doping variation of graphene induced from the substrate is still in its infancy. This is particularly important since G-SERS platforms typically consist of highly periodic nanoparticle arrays providing a highly modulated topological graphene surface with respect to strain and doping around the nanoparticle.

In this work, graphene is interfaced with a SERS active substrate. The SERS substrate consits of gold nanodisc (AuND) particles arranged in a periodic pattern on a silicon substrate. Section 3.2 introduces the main spectral enhancement mechanisms relevant for the AuND platform. A primary focus is on the electromagnetic mechanism (EM) of enhancement followed by Fabrey Perot enhancements and the a short discussion of the chemical enhancement mechanism. Following this, section 3.4 follows a comparison study using Raman spectroscopy on three differently prepared G-SERS substrates. As a result, the interfacing graphene is either highly doped (oxygen plasma treated substrate), moderately doped (normal wet transferred graphene) and a lightly doped (h-BN pacified) by oxygen plasma treating the substrate prior to a dry graphene transfer, transferring graphene using the wet transfer method and incorporating a h-BN spacer layer prior to a dry graphene transfer respectively. First a detailed evaluation of the graphene spectrum in the presence and absence is compared highlighting the difference in doping induced by the treated substrates and the AuNDs. Secondly a rigorous statistical analysis is performed on these samples with the aim to show how to reliably characterise large area CVD graphene devices and better highlight the doping variation which arises from engineering the solid-graphene interface. Finally section 3.4 moves on to look at optically induced doping at the graphene-gas interface. In an effort to correlate the doping dependence of the enhancement factor, it was found that intense electric field enhancement facilitated by the AuNDs is sufficient to irreversibly dope the graphene. An effort to understand the mechanism of this doping resulted in a methodology whereupon the graphene sheet can be selectively p or n doped depending upon the gaseous environment graphene resides in prior to optical excitation. This doping is quantified using KFM where a p-doping (n-doping) shift of $\sim -0.87 \pm 0.05$ meV ($\sim +0.75 \pm 0.07$ meV) is stimulated in a compressed air (nitrogen) environment. A discussion on whether this change in graphene surface chemistry is optically or thermally induced concludes this section.

3.2 Hybrid Graphene Gold Nanodisc Platforms

The following section provides a description of the enhancement mechanisms relevant for the graphene gold nanodisc hybrid devices. This section will first briefly summarise the key concepts behind the electromagnetic enhancement mechanism and the origin of the fourth power enhancement of the electric field in the Raman measurement. Following this, the electric field distribution of the gold nanodiscs platform is simulated and it is shown how the rapidly decaying electric field profile upon increasing height above the nanodiscs make two dimensional materials ideal for integration. With this in mind, the different magnitudes of enhancement experienced by the different Raman scattered graphene peaks are compared and other mechanisms contributing towards spectral enhancement, namely a Fabrey Perot type enhancement and the chemical enhancement mechanism.

3.2.1 The Electromagnetic SERS Mechanism

SERS is primarily driven by an electromagnetic mechanism (EM), whereupon the intensity of the Raman spectral peaks of a molecule is enhanced via the interaction of light with the resultant electric field of the molecule and its environment. The first SERS spectrum observed by Fleischmann et al. [232] was of pyridine molecules adsorbed on a roughened silver electrode. However it wasn't until later that the works of Jeanmaire et al. [233] and Albrecht et al. [234] that an adequate explanation of the physics behind the observed spectral enhancement mechanism was first proposed. Finally, work by Moskovits [235] proposed a model which attributed the observed spectral enhancement to a "bumpy" metallic surface. This rough surface caused a local enhancement of the electric field. Since then, SERS active substrates have been tailored to optimize the "bumpiness" of the metallic surface. As a result, metallic nanoparticles in colloidal dispersions, anchored to a surface, or nanostrucutres directly fabricated onto a substrate have become standard SERS platforms [236, 237].

The SERS enhancement factor, G, is defined as the ratio of the Raman signals from a known number of molecules in the presence and absence of a plasmonically active nanostructure [217, 238]. Briefly, a plasmon is a quazi-paritcle arising from the collective oscillations of free electrons in matter. These oscillations are typically arise in dipolar moments due to resonant coupling with the electromagnetic radiation [239]. The average enhancement factor is around 10^6, but can be higher when the probe molecules are localised around a nanostructure [218, 240, 241]. Enhancements as large as 10^{14} and 10^{15} have been reported on SERS platforms capable of single molecular detection [242]. Upon illumination with a plane wave at the plasma frequency of a nanoparticle, ω_p, an electromagnetic resonance with time dependent dipole symmetry occurs [220, 239, 241, 243] (see figure 3.1c). The origin of the augmented SERS spectrum intensity, is routed in the enhancement of the electric field at the surface of a nanoparticle such that $\mathbf{E}_s = g\mathbf{E}_0$; where $\mathbf{E}_0$ is the incident electric field and g the field enhancement. Adsorbed molecules at the nanoparticle surface are enhanced by the $\mathbf{E}_s$. As a result, the electric field experienced by the Raman scattered light produced by the molecule will be $\mathbf{E}_r \propto \alpha_R g \mathbf{E}_0$, where α_R is the Raman polarizability tensor (see appendix A.1). In addition to this, the Raman scattered light can be further enhanced by a factor g' via the exact same mechanism the incident light experienced. However, the scattered light must also coincide with the frequency distribution of the resonant plasmon. Typically these requirements are met since the plasmon distribution is broad. As a result, the total enhancement of the SERS electric field $\mathbf{E}_{SERS} = \alpha_R g' g \mathbf{E}_0$. Finally, since the intensity of the scattered light is proportional to the square of the modulus of the electric field, the intensity of the SERS light is

$$I_{SERS} \propto \alpha_R^2 |g' g|^2 I_0, \tag{3.1}$$

where I_0 is the intensity of the incident field.

Therefore for low wavenumber bands $g' \sim g$, the SERS intensity will be enhanced by a factor proportional to the fourth power of the incident near field where $|\mathbf{E}_i|^4 = |g|^4$. As such, the total SERS enhancement factor can be described as

$$G = \left|\frac{\alpha_R}{\alpha_{R0}}\right| |g g'|^2, \tag{3.2}$$

where α_{R0} is the Raman polarizability of the isolated molecule. A more rigorous derivation of the above can be found in the work of Moskovits [241], Stiles et al. [218] and Ru et al. [244].

3.2.2 Gold Nanodisc Arrays as a Platform for SERS

Metallic nanoparticles can be considered SERS active if their dimensions are smaller than the wavelength of the incident light but are still big enough to sustain surface plasmons [241]. From the Drude model[239, 241], the dielectric function of a metal can be described as

$$\epsilon(\omega) = 1 - \frac{\omega_p^2}{\omega^2 + i\gamma\omega}, \tag{3.3}$$

where γ is the collision frequency of the charge carriers. The plasma frequency of a free electron gas is defined as $\omega_p^2 = (ne^2)/(\epsilon_0 m)$, where n is the number density of electrons with charge e and effective optical mass m. Explicitly, ϵ_0 is the permittivity of free space.

The SERS active nanoparticle platform in this study comprised of gold nanodisc arrays. Each with different radial dimensions and spacing periodicity. Figure 3.1a is a SEM image of the G-SERS platform studied. The dark line across the image shows a tear in the graphene such that the insulating silicon dioxide layer starts to charge up and provides good contrast. The high resolution image shows that graphene contours the nanoparticles well and the graphene isn't prone to suspension across the nanodiscs. The inset is a schematic of a monomer unit of a single gold nanodisc of radius $r = 50$ nm and periodicity $p = 300$ nm deposited on a silicon dioxide/silicon (SiO_2/Si) substrate.

As stated previously, the SERS electric field is proportional to the polarization of the gold nanodisc which is described as follows [245]:

$$\alpha(\omega) = \frac{4\pi a^2 b}{3} \frac{\epsilon(\omega) - 1}{1 + L\big(\epsilon(\omega) - 1\big)}. \tag{3.4}$$

This is dependent upon $\epsilon(\omega)$ where a and b are the dimensions of the long and short axis of the discs and L is a geometric depolarization factor.

Zorić et al. [245] showed that the localised surface plasmon can be described simply in terms of the nanodiscs dimensions such that,

$$\omega_{lsp}^2 = \frac{L3c^2}{ab}, \tag{3.5}$$

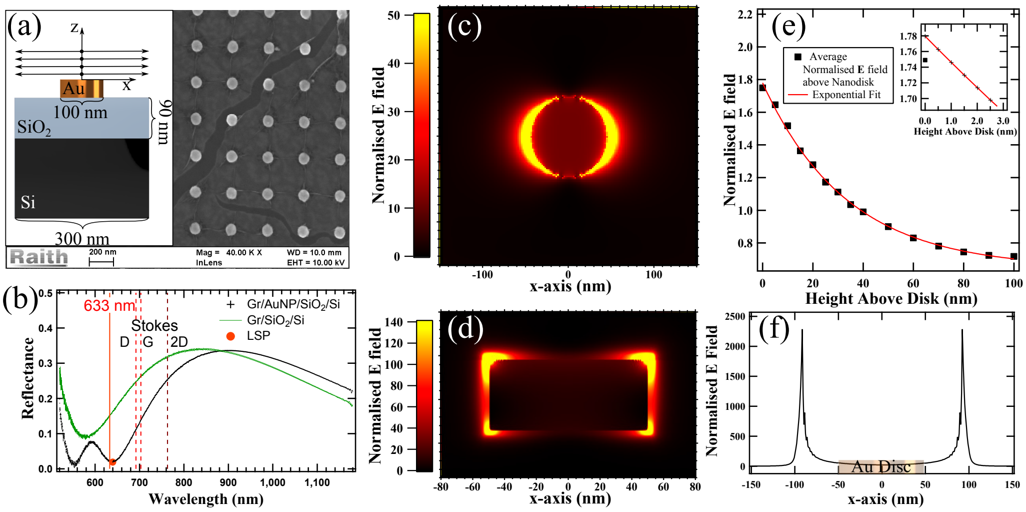

Figure 3.1: (a) SEM micrograph of graphene a gold nanodisc array of radius 50 nm and periodicity of 300 nm. Inset shows schematic of device monomer unit. (b) FTIR response of the array showing a resonance around 620 nm. The solid red line corresponds to the 633 nm Raman laser and the dashed lines correspond to typical graphene Raman peaks. The solid red point indicates the localised surface plasmon band of the nanoparticle array. The lumerical FDTD simulation of the normalilised electric field distribution ($|\mathbf{E}|^2/|\mathbf{E_0}|^2$) of (c) xy and (d) xz plane of the gold nanodisc unit. (e) The average electromagnetic field integrated over the full monomer unit xy plane as a function of increasing z height above the nanodisc. (f) A cross section of (d) at $y = 0$.

where c is the speed of light.

From equations (3.3) to (3.5), it is clear that the plasmon properties are dependent upon the disc dimensions and the optical properties of the nanoparticle material. Aside from the alkali metals, only the group 11 transition metals have a resonant frequency at visible wavelengths [246]. Therefore, the SERS platforms studied were comprised of gold nanoparticles arranged in a periodic array.

Figure 3.1b compares the optical response of the graphene-AuND hybrid platform and the graphene using Fourier transform infra red (FTIR) spectroscopy. The Raman laser line at 633 nm is shown to excite at the plasmon resonance mode - which is the minimum of the at $\sim$ 620 nm annotated with the red circle. The dashed lines show the Stokes Raman peaks typical of CVD graphene, indicating their relative positions with respect to the plasmon distribution. Interestingly, the Raman scattered peaks of graphene are far away from the nanodiscs resonant mode where $g \neq g'$. As a result the peaks will experience non-uniform enhancement. Explicitly, the 2D peak will experience a smaller g' compared to the G and D peaks.

To visualise the near field distribution around the gold nanodisc, a finite difference time domain (FDTD) lumerical method is used. (see chapter 2 section 2.7 for details). Figures 3.1c and d show the resultant normalised electric field distribution generated around a gold nanodisc upon plane wave excitation at $\lambda = 633$ nm in the xy and xz direction respectively. $|\mathbf{E}|^2/|\mathbf{E_0}|^2$ describes the calculated electric field divided by the source electric field, where the modulus squared is proportional to the intensity. The characteristic dipole distribution of the enhanced electric field is clearly seen where the highest enhancements are located at the nanoparticle edge. More practically, figure 3.1e shows the average field enhancement of the whole monomer surface (figures 3.1c and d) upon increasing height above the nanodisc. Clearly, the average **E** field decays exponentially as a function of distance from the nanoparticle. Interestingly, the inset of figure 3.1c is the same calculation using a finer mesh to better capture the physics at distances closer to nanoparticle surface - i.e. the distances relevant for interfacing 2D materials. Finally, figure 3.1f plots the normalised electric field profile through the center of the nanodisc of figure 3.1d. The characteristic sharp intense **E** field at the disc edge which exponentially decays as a function of distance is clearly seen.

From these theoretical simulations, the calculated electric field enhancement is orders of magnitude reduced when compared to the typical 10^6 order of magnitude reported in literature [218, 240, 241]. Normally these measured enhancement factors include a geometric scaling factor that improves the result. Following this, the consequent work in this thesis is focused on the enhancement of the graphene spectrum itself, which requires calculating the full substrate area and is not limited by a single point which is commonly used to describe the enhancement of a single molecule. Fortunately, the measured graphene enhancement factors discussed further in this chapter (table 3.2) are of the same order of magnitude instilling confidence to this model. Regardless, it is clear that 2D materials, due to their low dimensionality, are ideal candidates for coupling to optically active nanostructures. The exponentially decreasing electric field distribution is optimally coupled to graphene as close to its maximum enhancement as physically possible. Moreover, Van der Waals heterostructures, such as graphene on hexagonal boron nitride (h-BN), are still thin enough to interact with the enhanced electric field with minimal loss, providing an excellent optically active sensing platform. Table 3.3 estimates typical interlayer distances of graphene and graphene/h-BN on a AuND and is discussed in section 3.3 with respect to the G-SERS platforms studied.

3.2.3 Other Spectral Enhancement Mechanisms

Although the electromagnetic enhancement mechanism is the dominant mechanism contributing to the SERS enhancement, electromagnetic calculations alone do not account for the total enhancement observed experimentally. The chemical enhancement mechanism and constructive interference effects at the silicon dioxide/silicon layer provide non-trivial spectral enhancements [247, 248]. The chemical mechanism facilitates spectral enhancement via interactions between the metal nanoparticle and the typically adsorbed probe molecule [249, 250, 251]. The change in polarisability of the metal nanoparticle/graphene surface induced by the adsorbed species alters Raman spectral intensity according equation (3.1). Additionally, this results in enhanced molecular vibrations, leading to electrons tunneling to other vibrational states, charge transfer and resonant process. All in all, these slight perturbations in the electrons energy state ultimately relax selection rules [159].

Graphene itself is a proven spectral enhancing platform and has given rise to what are named GERS platforms [221, 29, 252, 253]. The GERS mechanism is facilitated via chemical enhancement processes. It has been shown that maximum enhancements of GERS platforms occur when the highest occupied molecular orbital (HOMO) and lowest unoccupied molecular orbital (LUMO) bands of the probe molecule are located close the graphene Fermi level [221, 222, 227, 228, 253]. As a result spectral enhancement is dependent upon the relative degree of doping in graphene. In general, the GERS enhancement, which is measured as the ratio of the spectral intensity of a probe molecule in the presence absence of graphene, is in the range of 10-10^2. Although the chemical mechanism prevalent in GERS platforms provide significantly smaller enhancements than metal particle graphene hybrid platforms, EM enhancement contributions of G-SERS platforms are confined to the local vicinity of the plasmonic nanoparticles. In contrast, the chemical mechanism provides enhancement throughout the whole graphene sheet. Moreover, GERS platforms provide an atomically smooth homogeneous surface, despite underlying substrate fluctuations, such that probe molecules can adsorb to the surface in a more predictable way [226]. A further benefit is that the aromatic band system of graphene can quench the fluorescence response of most aromatic probe molecules, effectively reducing unwanted background effects and improving the signal to noise ratio [102, 224]. As a consequence, despite the chemical enhancements facilitated through graphene being considerably smaller than the electromagnetically facilitated enhancement from the gold nanoparticles, it is still an important contribution towards spectral enhancements.

Finally, the substrate the graphene is placed upon can play a role in enhancing the electric field that interacts with 2D materials. In the case of silicon with a thermally grown oxide layer, light will interfere between the two layers such that the enhancement depends upon the thickness of the oxide layer - a Fabry-Perot interference affect. The

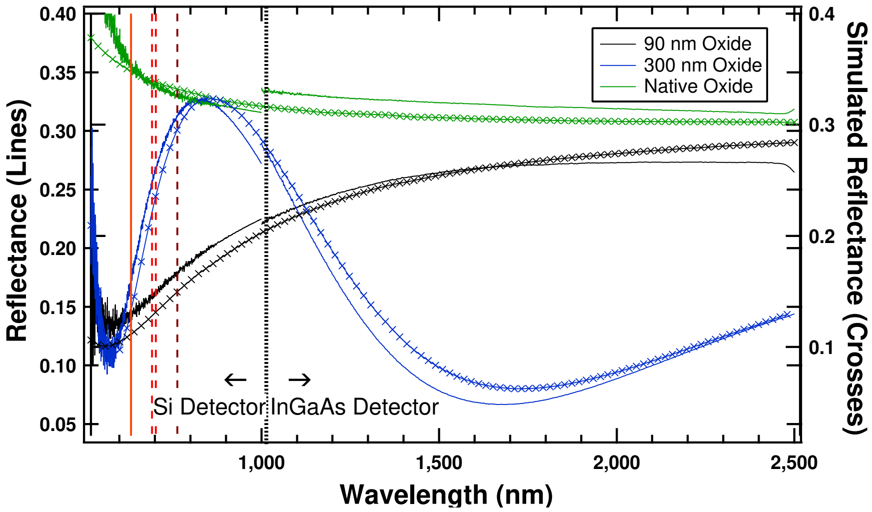

Figure 3.2: FTIR measured and lumerical simulated reflectance of silicon with a native (green), 90 nm (black) and 300 nm (blue) oxide layer. The solid line corresponds to the 633 nm laser pump and the dashed lines correspond to the Stokes Raman peaks of graphene. To cover the full wavelength range a silicon (InGaAS) detector measured the experimental data as left (right) of the black dashed line.

resultant enhancement factors can be as high as 30 [247]. It should be noted that this is the mechanism that provides optical contrast allowing graphene to be detected with the naked eye on silicon dioxide\silicon (SiO_2\Si) substrates [254]. Figure 3.2 compares the reflectance of light of silicon wafers with a native, 90 nm and 300 nm oxide layer. The solid red line corresponds to the 633 nm laser pump and the dashed lines correspond to the D, G and 2D peak. Although this enhancement is small in comparison to both the EM and chemical mechanism, it is clear that the characteristic Raman scattered bands of graphene are not necessarily enhanced to the same degree.

To summarise, spectral enhancements considered in this work are facilitated by EM of the gold nanodiscs, chemical interactions induced from the graphene itself and finally interference affects from the substrate. Each enhancement mechanism does not uniformly influence a wide spectral range. The EM enhancement is maximised around the plasmon distribution and the interference related enhancements are consistent across the wafer although not the whole spectrum. By contrast, chemically mediated mechanisms are less easy to quantify since they are molecular/quantum process. Moreover, graphene is highly sensitive to perturbations in its charge carrier density due to chemical interactions with its substrate and its environment. Fortunately, despite a plethora of mechanisms resulting in various types of spectral enhancements, the Raman response of graphene is fairly well understood. As a result, the following work aims to understand how different degrees of doping of the graphene itself influence the spectral enhancements of G-SERS sensing platforms.

3.3 Optimising the Enhancement Factor by Interfacial Engineering of the Graphene Substrate.

As introduced above, there are a variety of parameters that result in spectral enhancements in G-SERS platforms. Namely the thickness and permittivity of the substrate material/s, the nano-particle geometry, and the unique electronic configuration of graphene itself. Fortunately, being a solid state device the fabrication of the nanoparticle decorated substrate is easily controlled and predictable. On the other hand, the integration of CVD graphene into the device is less controlled. The transfer technique introduces impurities and dopants from the water and polymethylmethacrylate (PMMA) used in the fabrication procedure. In addition to this, there are a variety of defects such as grain boundaries, wrinkles and point defects in the graphene itself that result in local variation of the graphene properties, in particular its doping characteristics.

Despite this, one of the key strengths of a G-SERS platform is the ability to reference the measured enhanced signal against the characteristic graphene spectrum. This is particularly important since, the doping of graphene does not only enhance or weaken the spectra of the probe molecule, but also the characteristic graphene Raman peaks.

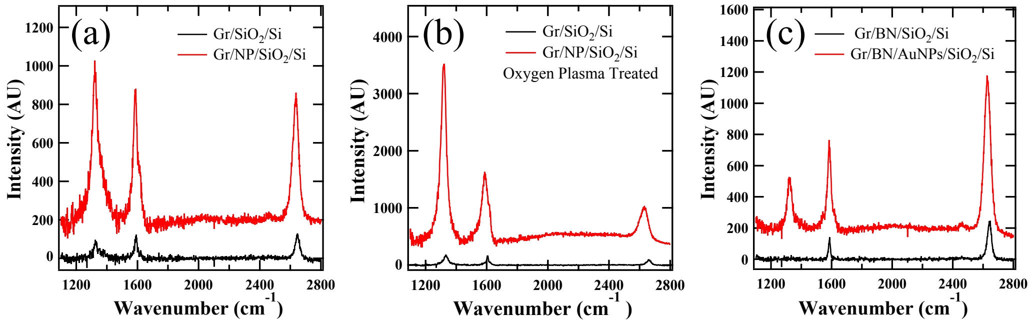

Figure 3.3: Representative Raman spectra of graphene in the presence (red spectra) and absence (black spectra) of the gold nanodisc array for (a) graphene wet transferred onto silicon, (b) oxygen plasma treated substrate with dry transferred graphene and (c) oxygen plasma treated substrate with dry transferred h-BN followed by dry transferred graphene. (See Appendix A.3 for details on the background removal).

Bearing in mind that the different enhancement processes discussed in the previous section do not enhance equally, the importance of referencing the enhanced graphene spectrum while simultaneously detecting molecular species becomes invaluable. Interestingly, the combination of doping induced enhancement coupled with plasmonic nanostructures is still in its infancy. Therefore, the work in this section aims to address how chemically doping the graphene influences the graphene spectrum of AuND G-SERS platforms.

To discern the doping induced spectral enhancements of G-SERS platforms, graphene is interfaced with three distinct AuND patterned and surface treated substrates. Fortunately, although there is a large degree of local variation of the graphene properties arising from the transfer procedure. The mean of the doping distribution can be controlled through careful preparation of the interfacing substrate [197, 255, 256, 257, 258]. Figure 3.3a-c compares the typical Raman spectrum of graphene in the presence (red spectra) and absence (black spectra) of AuNDs of (a) an untreated substrate whereupon graphene was transferred using a standard wet transfer method, (b) a substrate that was oxygen plasma treated prior to a dry graphene transfer and (c) a substrate where a h-BN spacer layer was dry transferred onto an oxygen plasma treated surface prior to a dry graphene transfer. A comparison of the graphene quality through analysis of the Raman peaks of figure 3.3 and more rigorously via statistical analysis of Raman maps is presented in sections 3.3.1 and 3.3.2 respectively. From this, it is shown that graphene is highly (oxygen plasma treated), moderately (wet transfer) or lightly (h-BN pacified) p-doped depending on the substrate interface. For full details of the sample fabrication see section 2.1.1 of chapter 2.

3.3.1 Overview of the Raman Spectra of Differently Prepared Substrates.

The discussion of the Raman spectra in this section introduces key concepts that will recur throughout this thesis chapter. Table 3.1 summaries the peak position, full width and half maximum and peak ratios of each representative spectrum of figure 3.3. For comparison the peak properties of 'pristine' graphene [163, 259, 260] are also tabulated. Interestingly, all the G and 2D peak phonon modes are blue shifted with respect to pristine graphene. The increase in wavenumber of the G and 2D bands are attributed to hole doping facilitated by the PMMA [261, 262] used in the transfer process, water trapped underneath the graphene in the wet transfer [148] sample and

Table 3.1: Raman peak properties from figure 3.3. The peaks are fitted to a Lorentzian function except for the peaks marked with the superscript* which are fitted to a Gaussian function. (Appendix A.4 shows the peak fitted spectra in detail). The data for pristine graphene excited at 633 nm were collected from references [163, 259, 260]

Fabrication Method	AuND	Peak Position (cm^{-1})			FWHM (cm^{-1})			Ratio	
		D	G	2D	D	G	2D	D/G	G/2D
Wet Transfer	No	1329.3	1590.6	2646.4	48.52	23.41	30.36	0.68	0.86
	Yes	1324.6	1585.8	2635.2	57.58	29.61	43.93	1.08	1.03
Oxygen Plasma	No	1332.6	1605.6	2659.9	36.69	18.19	30.48	1.12	1.61
	Yes	1318.2	1587.4*	2625.3*	39.21	50.76*	67.41*	3.02	2.03
h-BN Spacer Layer	No	NA	1585.7	2642.1	NA	12.87	28.15	NA	0.54
	Yes	1322.7*	1584.3	2628.3*	42.933*	27.60	52.463*	0.56	0.57
Pristine Graphene	NA	NA	$\sim$1581	$\sim$2625	NA	$\sim$13.5	$\sim$23	NA	0.5

dangling bonds generated on the silicon dioxide surface after oxygen plasma treatment [263]. Appendix A.5 compares transport measurements of equivalently fabricated samples without AuNDs which verifies that all samples are p-doped.

Unsurprisingly, the G and 2D bands are shifted the most in the oxygen plasma treated substrate, followed by the wet transferred graphene and then the h-BN pacified sample, which confirms the order of doping since larger wave numbers correspond to higher concentrations of charge carriers [169]. Interestingly, the G band shift is smaller in the presence of the AuNDs due to the graphene in contact with the nanoparticles being decoupled from the p-doping substrate and AuNDs n-doping the graphene upon optical excitation [264]. Consequently, the AuND facilitated n-doping brings the originally p-doped graphene closer to the charge neutrality point. In contrast, the 2D band position decreases when the graphene lattice is strained [163], which is the case for the graphene contoured around the gold nanoparticles. Clearly, h-BN is good at pacifying the graphene from substrate induced doping, such that there is hardly any change in the G peak position in the presence or absence of the AuNDs. The discrepancy in the 2D peak positions are due to strain. This strain and doping relationship is explored further in the next section and figure 3.7.

The G/2D intensity ratio is typically 0.5 for monolayer graphene in the absense of strong doping effects [164, 166]; which is clearly the case for h-BN pacified graphene in the presence and absence on AuNDs and the standard wet transferred graphene sample in the absence of AuNDs. However since the spectral peak intensities are greatly affected by charge doping, the oxygen plasma treated and the unpacified interaction between graphene and the gold nanodiscs provide enough doping such that this ratio will change even in the presence of monolayer graphene. In particular, a decrease in intensity of the 2D peak is expected [229, 265]. Further to this, due to the near field enhancement being the strongest for the D band and the weakest for the 2D band, it is expected that the ratio of the enhanced peaks is higher than those absent of the gold nanoparticles, which is consistent with what is observed.

In the absence of the AuNDs the D band which arises due to disorder (see chapter 2) in the graphene structure or if close to the edges is absent only in the h-BN pacified sample. The slight disorder in the crystal structure of the wet transfered sample is caused by the polymer used in the transfer procedure and the evaporation of water trapped under the graphene sheet which breaks through the membrane causing cracks [143, 148, 266]. The D peak is more intense in the oxygen plasma sample due to extreme substrate treatment inducing surface charges in the silicon creating defects in the graphene crystal. To better quantitatively assess the number of defects present if the graphene sheet, the intensity of the D/G peak ratio is used. A D/G ratio >1, as is the case for the oxygen plasma treated graphene, is indicative of large crystal disorder. Which is consistent with its harsh treatment of the substrate surface. Whereas the D/G intensity ratio <1 suggests less impurities, as is the case of the wet transferred graphene. However, the D band is expected when measuring graphene integrated with nanostructures since graphene contours the nanoparticles well (as shown in the SEM image of figure 3.1a) which introduces abrupt transverse discontinuities-"artificial edges" [164, 224, 267]. This is clearly shown in figure 3.10 of section 3.3.2 which shows 10 x 20 μm Raman maps of the D peak properties of the same samples studied. Consequently, the presence of the AuNDs always activate a D peak, therefore defect concentration evaluation is impossible in the presence of AuNDs only.

Interestingly, for all enhanced spectra, when graphene is in the vicinity of the AuNDs, the enhanced G peaks exhibit a slight shoulder at $\sim$ 1618 cm^{-2} at the D' band location. The D' band is due to disorder in the graphene lattice due to restructuring forming nanocrystaline domains [166]. Interestingly, since the D' band is absent in the h-BN pacified sample, it is likely that the increase in defected graphene is substrate mediated. Further to this, in general a sharp full width at half maximum (FWHM) of the Raman bands coincide with less doping and impurities in the crystal lattice. Therefore in the absence of the AuNDs it is clear that h-BN is the best quality graphene whereas the oxygen plasma treated is highly doped with a lesser quality. However, the electromagnetic enhancement in the vicinity of the AuNDs broadens the spectral peaks making it difficult to evaluate the quality control of the material.

To summarise, hole doping is most prominent for the oxygen plasma treated substrate due to the the formation of silanol functional groups at the silicon dioxide surface. As a result, the plasma treated surface is positively charged which significantly p-dopes the graphene. Conversely, the h-BN pacified surface shows very little doping compared to the "pristine" suspended graphene, has a G/2D intensity ratio of ∼0.57 and there is no evidence of a D band; demonstrating good quality. This is unsurprising since h-BN is an atomically flat 2D insulator, with similar crystal spacing as graphene and is free from charge impurities which provides a good surface for graphene to adhere to via Van der Waals bonds [268]. However, not only does the presence of the AuNDs dope and strain the graphene, the non-uniform spectral enhancement of the graphene itself affects interpretation of the graphene properties. As a consequence, when preparing the G-SERS platform it is important to have a region free of nanostructures as a quality control reference.

Doping and Enhancement Factor Comparison

To conclude this section, table 3.2 compares the measured enhancement factors of the main graphene Raman peaks from figure 3.3. Since there are many mechanisms that results in spectral enhancements, all the samples were fabricated on substrates with 300 nm oxide. However, the wet transferred sample was transferred onto a wafer from a different batch from the others and from FTIR measurements (figure 3.4a)

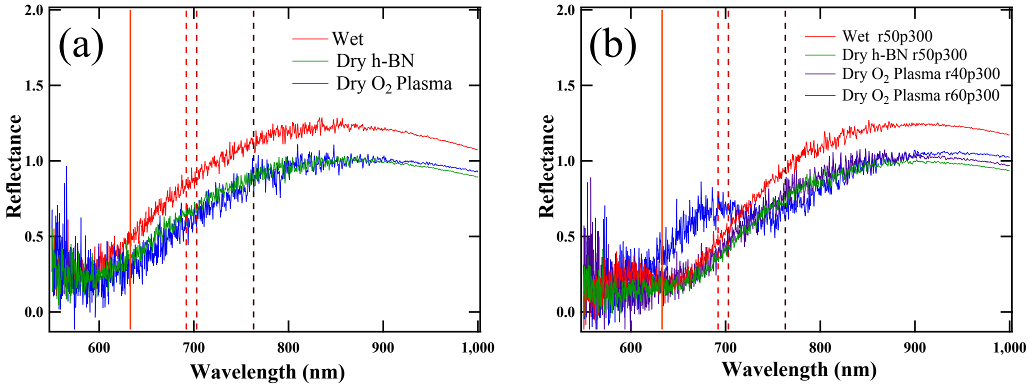

Figure 3.4: FTIR reflectance of wet transferred graphene, graphene dry transferred into an oxygen plasma treated substrate and graphene dry transferred onto a h-BN pacified sample in the (a) absence and (b) presence of gold nanodiscs. Discs with radii at 50 nm and periodicity 300 nm were were fabricated on the wet transferred and h-BN sample. Discs with radii at 40 nm and 60 nm with the same periodicity were studied on the oxygen plasma treated substrate.

it is clear that the oxide thickness are not exactly identical. Unfortunately, identical AuND geometries were not possible for the oxygen plasma treated sample. Instead the nanodisc array consisted of a radius of 60 nm and periodicity of 300 nm which shifts the resonance as shown in figure 3.4b. An additional array with smaller nanoparticle radii of 40 nm is also compared which is of relevance for section 3.3.2.

Another factor to consider is the lateral height where the gold–graphene distance of the h-BN pacified sample is larger than the other samples. Since the EM of enhancement is the prominent mechanism, at least at frequencies corresponding to the D and G bands, the calculated average normalized electric field from the inset of figure 3.1e is compared at relevant interlayer distances as shown in table 3.3. The interlayer spacing d_{int} values of table 3.3 are idealised assuming Van der Waals type interactions obtained from literature. In reality, the interlayer separation distances can vary depending on defects and crystal stacking orientation and therefore are guideline values [269, 270, 271]. The calculated electric field distribution is the result of the average electric field enhancement of a full nanodisc unit as shown in figure 3.1a. Interestingly, the simulated

Table 3.2: G-SERS enhancement factors for different substrate treatments.

Fabrication Method	Enhancement Factors D	G	2D
Wet Transfer	10.05	6.32	5.32
Oxygen Plasma	19.14	7.08	5.64
h-BN Layer	NA	3.92	3.69

Table 3.3: Normalised electric field at relevant interlayer separations distances.

Material Interface	d_{int} (Å)	$\|\mathbf{E}\|^2/\|\mathbf{E_0}\|^2$
Au – Gr	3.31 [118]	1.67
Au – h-BN	2.48 [269]	1.69
h-BN – Gr	3.20 [271]	NA
Au – h-BN – Gr	5.68	1.60

enhancement factors underestimates the enhancement factors measured. Potential reasons for this include the use of no filling factors and ignoring light matter interactions with the 2D materials themselves, which are doping dependent. Ignoring these two parameters are non-trivial particularly since graphene/h-BN/gold structures have been shown to have remarkable light confinement properties [272].

Regardless, the enhancement factors are largest from D, G and then the 2D band, since the lower wavenumbers are located closer to the plasma frequency of the AuNDs. Although work by Schedin et al. [113] correlate the enhancement factor using assuming $|\mathbf{E}|^4$ from FTIR measurements, it is clear that scattered Raman peaks are too far away for this relationship to be accurate. From table 3.3 there is an estimated 5% decrease in electric field magnitude in the graphene of the h-BN pacified sample due to the increased distance at excitation frequency. Since the D peak intensity naturally increases due to the 'artifical edge effect' the enhancement factor is not reliable. Interestingly, there is less distinction between the enhancement factors of the G and 2D band of the h-BN pacified sample compared to the other two. Implying one of two things, first that the lack of doping dampens the enhancement of the G peak, or secondly the approximate 2.37 Å extra graphene—gold distance is sufficient to reduce the local enhancement. However, the 2D bands of all samples should be mostly decoupled from the plasmon enhancement. With this in mind, the large increase in enhancement factor of the G peak compared to the 2D peak suggests that the increased p-doping enhances the peak. To conclude, despite EM enhancement contributions dwarfing those of the chemical mediated mechanism, the psuedo-large area of carbon atoms being probed optically (i.e. all the carbon atoms illuminated under the laser spot) shows that global charge doping isn't negligible.

3.3.2 Statistical Raman Analysis of Doping

From the previous section it is clear that a wealth of information can be extracted from the Raman spectra of figure 3.3. However, the properties of a typical graphene surface vary spatially. Therefore, Raman spectroscopy maps of dimensions 10x20 μm are compared to investigate the local spectral variation across the various graphene samples. Figures 3.5 and 3.6 compares the peak position, full width at half maximum and enhancement factors spatially for both the G and 2D peaks respectively. The dashed lines show the interface between the graphene in the presence (right) and absence (left) of the AuND array. Clearly, each sample shows local variations within the graphene irrespective of the AuNDs.

Interestingly, there is a clear contrast between the graphene peak properties in the presence or absence of the AuND array. With the exception of the G peak position, which is invariant across the h-BN pacified interface. This indicates that the main source of doping for the other samples is due to graphene—substrate interactions. This confirms the initial single spectrum assessment of figure 3.3 showing that the addition of the AuNDs dopes and strains the graphene membrane. This is more easily visualized in figure 3.7 where the Raman peak data is displayed in a 2D histogram format. Here the invariance of the G peak position of the h-BN interfaced layer is in stark contrast to the other samples, which shows a distinct doping shift in the presence and absence of the AuNDs. Similarly, the difference in AuND induced strain on the graphene becomes more

Figure 3.5: Raman maps of the local varation of the G peak properties.

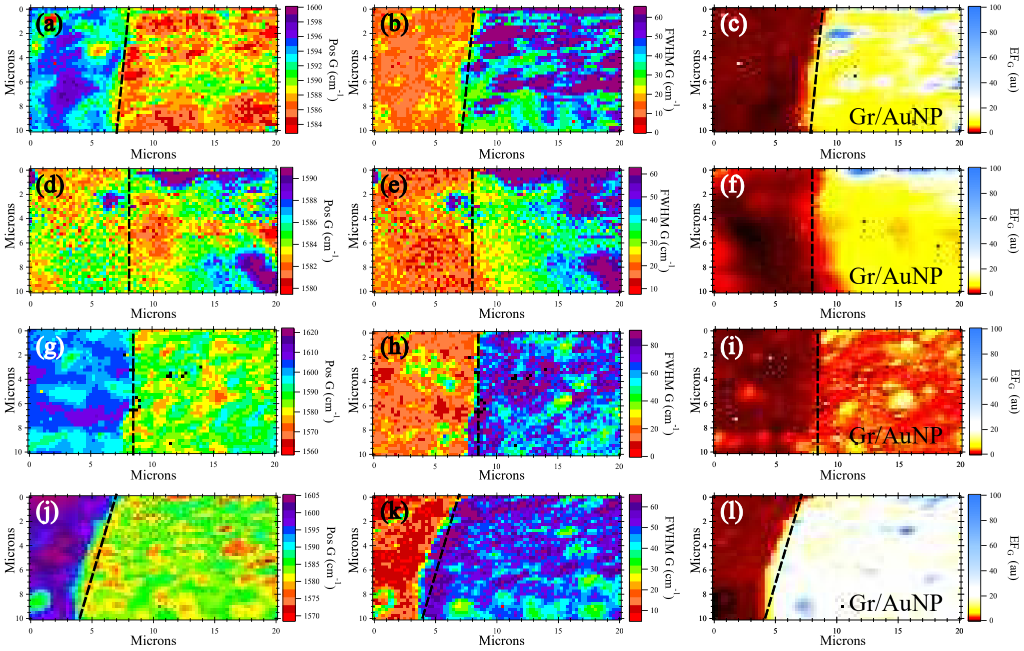

Figure 3.6: Raman maps of the local varation of the 2D peak properties.

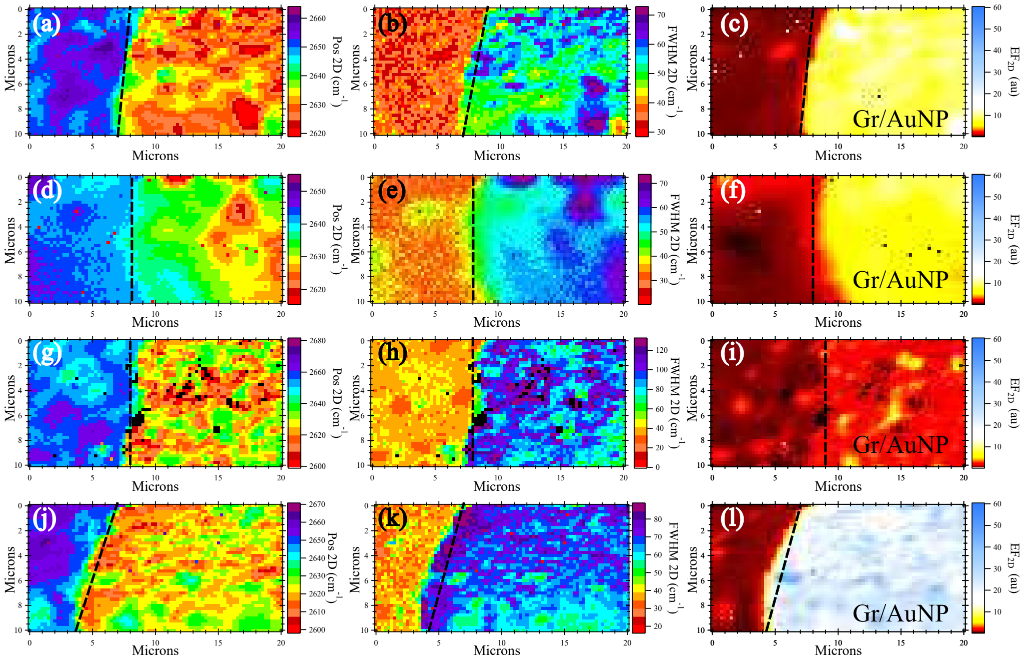

The above Raman maps show the peak position (Pos), FWHM and Intensity for (a-c) standard wet transferred graphene on gold nanodiscs r50p300 (d-f) h-BN protected substrate on gold nanodiscs r50p300 and oxygen plasma treated substrate on (g-i) r40p300 gold nanodiscs and (j-l) r60p300 gold nanodiscs for G and 2D peak maps, figures 3.5 and 3.6 respectively. Each map was imaged at the nanoparticle array edge such that the pixels left (right) of the dashed line correspond to the graphene Raman signal in absence (presence) of the AuNDs.

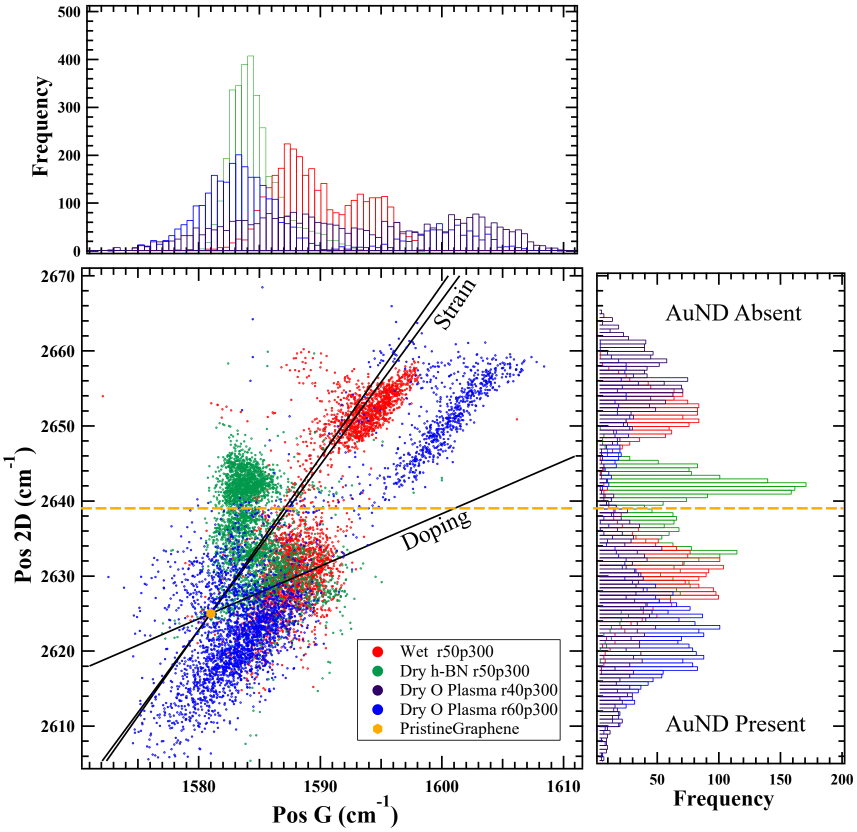

Figure 3.7: 2D scatter plot comparing G and 2D peak position on and off gold nano particle arrays on graphene transferred via different methods. Red hexagon corresponds to pristine graphene at (1581, 2625) as observed by Berciaud et al. [259] under 633 nm laser illumination. The black solid lines correspond to vectors in Pos 2D-Pos G space associate with tensile strain and doping. The strain contribution is split into two gradients dependent upon whether the 2D inter valley scattering process involves the inner or outer cone [273]. The dashed orange lines show a clear distinction between the Raman response of graphene in the presence and absence of AuNDs.

apparent by following the large shift in 2D peak wavenumber along the strain vector guide line - where decreasing (increasing) wave numbers corresponds to increasing tensile (compressive) strain. Moreover, the distributions clearly show that the oxygen plasma treated samples are the most doped, followed by the wet transferred sample and finally the h-BN pacified layer and the AuND-interfaced graphene. Interestingly, in the presence of the AuNDs, the peak position distributions broaden; including in the h-BN pacified sample. As a result, the presence of the AuNDs not only reduces

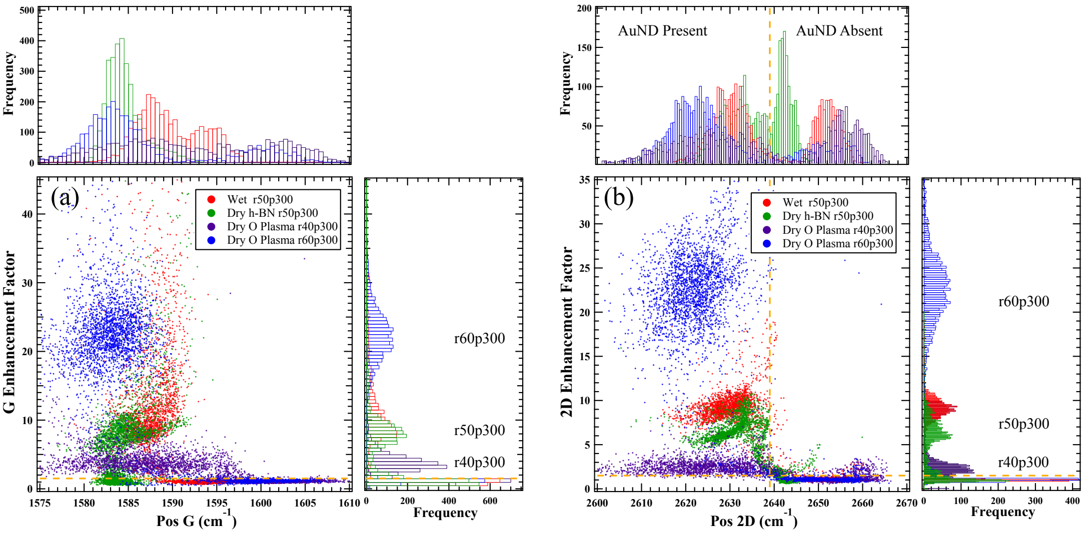

Figure 3.8: 2D scatter plots of the (a) G and (b) 2D peak enhancement factor vs peak position. Corresponding 1D histograms are plotted at the corresponding axis as a guide to the eye. Above (below) the horizontal dashed lines mark a clear separation between the Raman spectra influenced (uninfluenced) by AuNDs. Similarly left (right) of the vertical dashed line in (b) shows spectra influenced (uninfluenced) by the AuNDs due to strain.

the p-doping influence of the substrate, but also increases the micron scale doping variation.

To elucidate the role of nanoparticle size on the enhancement factor, similar 2D histograms were constructed as shown in figure 3.8 corresponding to the (a) G peak and (b) 2D peak. The EF was calculated by dividing the total intensity data set by the mean peak intensity in the absence of nanoparticles. In both cases the corresponding 1D histograms clearly show a positive correlation between the nanoparticle size and the EF. From the FTIR result in figure 3.4b, better coupling the of the scattered photons to the resonant mode as shown in figure 3.4b certainly contributes to this response. Interestingly, although the EM enhancement mechanism/nano particle size influences the enhancement factor the most, comparing the lightly doped h-BN pacified sample with the moderately doped wet transferred graphene shows an increased overall enhancement of the moderately doped wet transferred sample. Strikingly, the EF of

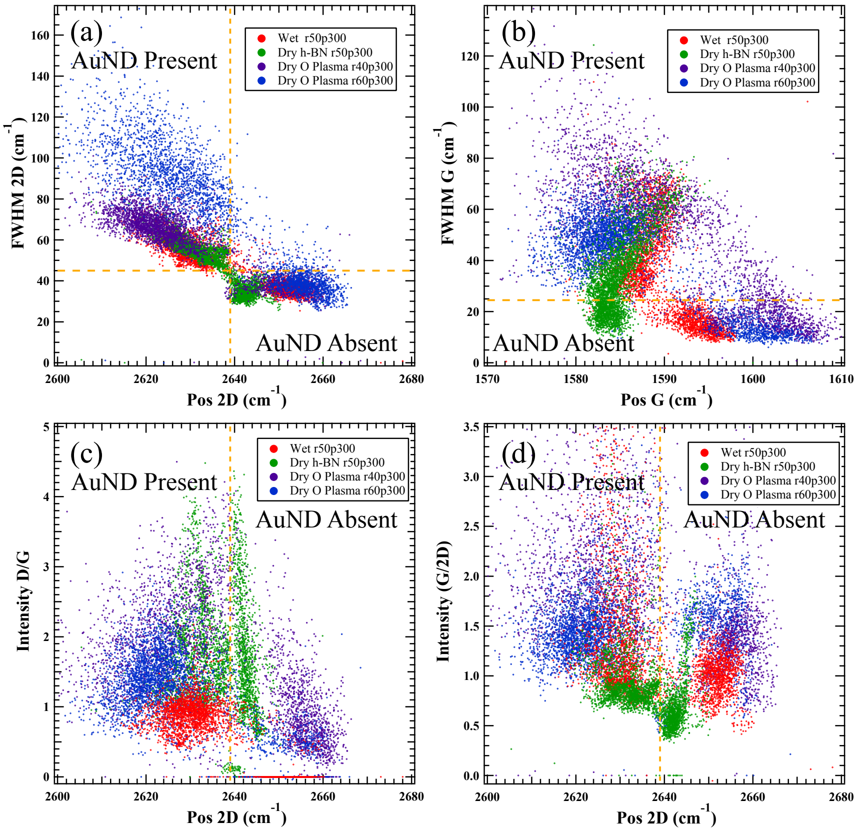

Figure 3.9: 2D scatter plots of the (a) G and (b) 2D peak FWHM vs position. The intensity ratio of the (c) D/G and (d) G/2D vs 2D peak position. The dashed lines show a clear distinction between the data in the presence and absence of AuND.

the 2D peak of the wet transferred sample compared to the h-BN pacified sample is obviously larger than the G peak. This is particularly important since the 2D peak is largely decoupled from the plasmon resonant mode. However, upon comparison with figure 3.4b, it is unclear whether or not the prominent factor is substrate induced doping or interference induced enhancements at the oxide interfaces.

For completeness, figure 3.9 compares the other spectral peak properties. Figure 3.9a plots the 2D FWHM against the 2D peak position. The increased strain and line broadening of the graphene peak induced by the AuNDs is easily distinguishable, as marked by the dashed orange lines. Figure 3.9b compares the G peak FWHM against the G peak position. The smearing of the distributions in the presence of the AuNDs is

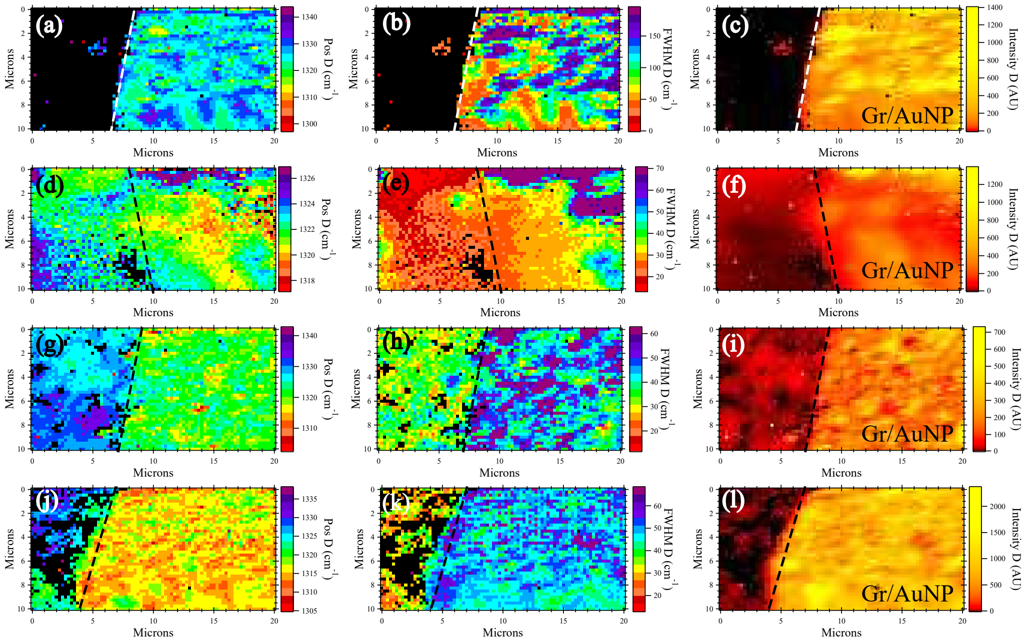

Figure 3.10: Raman maps of the D peak properties showing the spatial variation of the Pos, FWHM and Intensity for (a-c) standard wet transferred graphene on gold nanodiscs r50p300 (d-f) h-BN protected substrate on gold nanodiscs r50p300 and oxygen plasma treated substrate on (g-i) r40p300 gold nanodiscs and (j-l) r60p300 gold nanodiscs. Each map was imaged at the nanoparticle array edge such that the pixels left (right) of the dashed line correspond to the graphene Raman signal in absence (presence) of the AuNDs.

clearly evident. Unlike the broadening of the 2D peak, the G peak broadening is more pronounced in the presence of the AuNDs. With the exception of the h-BN pacified sample which is broadened but the distribution less smeared, possibly due to the h-BN providing a more homogeneous surface for the graphene to adhere.

Finally, the the D/G and G/2D intensity ratios are compared against the strain sensitive 2D peak position in figures 3.9c and d respectively. The large shift in 2D peak position separates the graphene response in the presence and absence of AuNDs. Overall in the presence of AuNDs the D/G ratio distribution spreads and increases. However, the distribution is more consistent regardless of the AuNDs for the h-BN pacified sample. The points at zero are attributed to regions of graphene without an appreciable D peak, indicating that the wet transferred sample contains fewer defects. This is more clearly shown in figure 3.10 from the 2D maps of the D peak where the black pixels correspond to regions of graphene where there is no detectable D peak. Interestingly, in the absence of AuNDs, the wet transferred method produces the least defected graphene and the oxygen plasma treated substrate produces the most defected graphene. This is quantitatively summarised in table 2.1 of chapter 2. This is unsurprising since the oxygen plasma treated substrate introduces more defects into the graphene lattice and the graphene/h-BN sample requires two PMMA mediated consecutive transfers. Strikingly, the concentration of D peak increases in the presence of the AuNDs. As stated previously, this is due in part to the presence of defects in the graphene lattice and in part due abrupt transverse discontinuities caused by the AUNDs creating "artificial edges" [164, 224, 267]. Finally, the G/2D intensity ratio distribution also spreads in the vicinity of AuNDs. For graphene in the absence of AuND the statistical mean of the G/2D ratio is between 0.5 - 1. Interestingly this mean ratio increases in the presence of AuNDs which is consistent with the EM enhancement being stronger for the G than the 2D peak.

To conclude this section, the statistical analysis of the Graphene Raman data provides a more robust and comprehensive characterisation of the G-SERS platform. From figure 3.8, it is clear that in addition to improving the electric field—graphene coupling by choice of specific nanoparticle geometry, substrate interference effects and increased p-doping in particular augments G peak enhancement [170] by 30%. The statistical analysis of the Graphene Raman data allowed for unambiguous distinction between the graphene properties influenced by the AuNDs, doping and strain effects. More interestingly, the Raman maps of graphene show increased sensitivity in the vicinity of the AuNDs as evidenced by a ‘smearing’ of the spectral distribution statistics. This smearing of graphene properties in the presence of the AuNDs implies: that either the G-SERS platform is sensitive to the spatial doping variations in the graphene that cannot be measured in the absence of the AuNDs; or the AuNDs themselves are enhancing doping mechanisms within the graphene, since the AuNDs reduce p-doping by counter n-doping mechanisms. In short, the influence of “chemical” doping of the graphene via substrate engineering is not entirely masked by the EM facilitated nanoparticle enhanced spectra, nor the AuND decoupling of substrate effects. Despite this, G-SERS platforms provide a promising platform for spectroscopic sensing. Through continual analysis of the baseline graphene properties, the presence of the probe molecules unique spectroscopic signature is potentially not the only information that can be attained from G-SERS sensors. Since the graphene Raman spectrum is sensitive to perturbations in doping and strain of the crystal lattice, the graphene spectrum itself can provide additional facets of information that SERS sensors alone cannot. However, the interpretation and understanding of the various enhancement effects that are necessary in order to determine the baseline for the optimisation of reliable future G-SERS molecular sensing platforms.

3.4 Optically Induced Environmental Doping of Graphene

From the previous section, the Raman maps of graphene across the AuND interface show local variation of spectral properties in addition to their enhancement. Initially KFM measurements were undertaken to correlate regions of high doping with regions of high Raman spectral enhancement. However, through imaging the surface potential of the graphene gold nanodisc arrays, it became clear that regions of nanoparticle decorated sample exposed to the laser became permanently doped. This effect did not occur in regions where there were non nanoparticles. This effect is clearly shown in Figure 3.11 where the (a) AFM and corresponding KFM (b) before and (c) after Raman

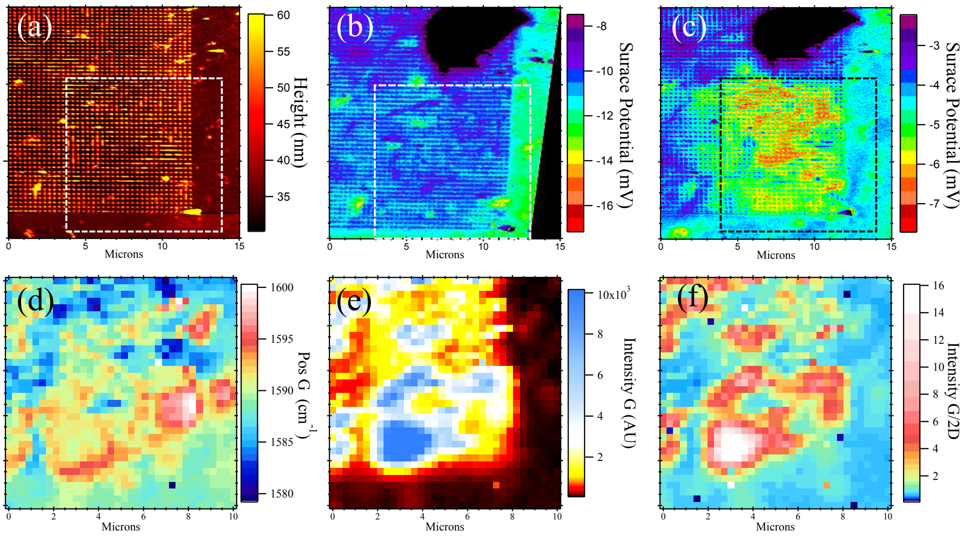

Figure 3.11: (a) AFM image and corresponding KFM images of graphene/h-BN sample (b) before and (c) after laser illumination at at 633 nm at ∼ 2.5 mW. The black spot in the KFM images corresponds to a hole in the 2D materials such that the non-conductive substrate is exposed and charging the tip. Raman maps of the G Peak (d) position and (e) intensity, and (f) the G/2D intensity ratio. Logarithmic false colour scales are used for (d) and (e) since the electromagnetic enhancement is too large to view variations on and off the nanodisc array clearly. The dashed boxes on the SPM images mark the regions illuminated for the Raman measurements.

illumination of graphene on h-BN at the AuND (radius of 50 nm and periodicity of 300 nm) interface. Appendix A.6 is the KFM measurements of an equivalent substrate without a h-BN pacified layer. The surface potential of the illuminated area (dashed box) is clearly changed before and after laser illumination. KFM measures the surface potential, which is the difference between the work function of the SPM tip and the material being probed (see chapter 2 section 2.3.2). From the biasing set up of the scanning probe microscope, an increasing surface potential corresponds to increasing the p-doping of graphene. Therefore, from the KFM measurements, it is immediately apparent that the total region illuminated where discs were present is irreversibly p-doped. Moreover, this laser induced doping in the vicinity of the AuNDs is not uniform across the graphene, however KFM resolution is limited by the probe geometry.

Corresponding Raman maps of the laser doped region of the G peak position, intensity and G/2D ratio are shown in figures 3.11d-f respectively. The G peak position is most sensitive to doping variation, indicating regions of highly p-doped graphene (∼1600 cm^{-1}) over the AuND region. In general, these highly doped regions correspond to areas with the largest enhancement above the AuNDs, as shown by the G peak intensity map. Interestingly, the G/2D ratio shows that for the most part, is similar across the imaged array except at locations of highly p-doped graphene. Although from the SPM micrographs there are clear areas of PMMA residues that could contribute to the p-doping, these regions do not obviously correlate with the Raman maps. This in part is due to the mismatch of resolution between the scanning probe microscope, limited by tip curvature in the order of nanometers; and the spot size of the Raman laser, in the order of about a micron.

The following work aims to elucidate this permanent doping mechanism. Regions of graphene at the AuND interface were measured using KFM before and after laser illumination at different laser intensities and environmental conditions - namely air and nitrogen at atmospheric pressure. During laser illumination, the Raman signal of graphene was continuously measured. Surprisingly, the‘inert’ nitrogen gas environmental conditions, n-doped the illuminated graphene whereas an air environment p-doped the AuND regions of the sample. Through analysis of the KFM micrographs and the corresponding Raman maps, the graphene is shown to be selectively doped by ± 1 meV via optical excitation mediated predominately via the AuNDs depending on the environmental conditions.

3.4.1 Optically Induced Environmental Doping of Graphene

Background

The doping of nanoparticle decorated graphene can only occur via an interaction at the interface, in other words the doping is either induced from the substrate or from the gaseous environment at the exposed surface. Under illumination at nanoparticle resonance, the electrons in graphene are excited either optically [274] or thermally [275, 276]. It has been shown that thermal annealing of graphene irreversibly dopes graphene by decreasing the graphene—substrate bond distance which increases the interlayer coupling [277, 278]. As a consequence, to minimize doping from the G-SERS substrate a h-BN pacifying layer was introduced prior to the graphene transfer. As a result, the only doping pathway is via the exposed surface. As such, optical excitation is performed in two different ambients; an air environment, achieved using a compressed air cylinder such that nitrogen, oxygen and trace amounts of water is expected; and a nitrogen environment.

Laser induced doping has been shown to reversibly [279, 280, 281] and irreversibly [282, 283, 284, 285, 286] dope the graphene surface. Laser doping of graphene on a SiO_2 substrate is achieved by the laser inducing charge trap defects on the SiO_2 surface [282]- this process is irreversible. In contrast, the laser induced doping of graphene on a h-BN substrate is mediated through the defect states in the band structure arising from nitrogen vacancies and carbon defects - this process is reversible [280, 281]. Laser induced annealing of graphene/SiO_2 facilitates the transition from 'pristine' graphene to nanocrystalline graphene by breaking C—C bonds and induce sp^3 hybridisation [284, 286] at laser powers as low as 1 mW upon continuous exposure. Interestingly, Huang et al. [285] showed that a 3 mm beam diameter with an irradiance as low as 60 W cm^{-2} increased the induced amorphization of the carbon lattice. However, temperatures as high as 1100°C were measured implying it was a global thermal effect; particularly since a typical 1 mW Raman measurement for a 1 μm beam diameter has an irradiance of 2.55x10^5 Wcm^{-2}. In all laser induced annealing measurements p-doping of graphene was observed due to either the ambient environment or oxygen and water species trapped at the surface. Therefore, altering the molecular environment should change the magnitudeof the doping.

Further to this, thermal annealing of graphene in different ambient conditions influences the doping. Indeed, it is well established that thermal annealing in oxygen environments induces defects in the graphene lattice and ultimately p-dopes the sheet [261]. Similarly, annealing *in situ* followed by oxygen exposure will reversibly p-dope the graphene unless water is present, where the p-doping becomes irreversable [278, 287]. In addition to this, measurements have also shown reversible oxygen/air doping post annealing *in situ* and nitrogen environments [288, 289], where nitrogen is assumed to be inert at room temperature. However, annealing in nitrogen environments has been shown to reduce the p-doping character [290] and produce n-type graphene [291]. However it is unclear if this is due to nitrogen actively n-doping the sheet, the lack of O_2/H_2O in the vicinity or other fabrication conditions.

Interestingly, despite the emergence of G-SERS platforms, environmentally dependent optically induced doping of graphene gold hybrid devices has not been previously investigated. Further investigation into this effect is important since G-SERS platforms provides such a promising sensing platform, whereupon a key strength includes that of high thermal dissipation through the graphene which protects the integrity of the optically active nanostructures [29, 30, 31]. Moreover, reversible optically induced doping has been reported in graphene [264, 292, 293] where hot electron chemistry is an emerging field [292, 294, 295, 296]. As such, understanding and ultimately controlling the behaviour of G-SERS platforms in different environmental conditions is of paramount importance.

3.4.2 KFM Determination of Optical Doping of G-SERS Platform

To discern between substrate, environmental thermal and optically induced doping, graphene transferred onto a gold nanodisc decorated sample (radius = 75 nm and periodicity = 400 nm) is pacified by an h-BN spacer layer, to reduced substrate induced doping. The graphene is measured using KFM before and after laser exposure. To investigate thermal effects, laser irradiation of the sample is achieved using a 633 nm Raman system where 10x10 μm maps at either at a high and low laser power at 4.55 mW and 1.14 mW respectively. The corresponding power densities are $(2.95\pm0.19)\text{x}10^5$ Wcm^{-2} and $(3.43\pm1.22)\text{x}10^4$ Wcm^{-2} respectively for a measured beam diameter of 1.07 ± 0.17 μm (see chapter 2 section 2.2.2 for details). The maps were taken at a AuND array boundary to distinguish between effects induced by the nanoparticles and the graphene itself. To understand the origin of the doping, the illumination was carried out in both a nitrogen and air ambient. To achieve the different ambients, the G-SERS sample is placed into a Linkam stage and flushed with nitrogen to remove any moisture in the stage. During this procedure the stage is not heated to avoid any unwanted thermal effects. After the purging procedure, the target environmental gas (N_2 or compressed air) is introduced to the stage at 1 atm and sealed. During all Raman measurements the stage was kept at at 25°C. During laser illumination Raman spectra are continually recorded. It should be noted that all KFM measurements were made in an ambient of lab air.

Figures 3.12 and 3.13 compare the laser induced doping effects at high power in an air and nitrogen environment respectively where: (a) is an AFM micrograph of the region of interest where (b) shows the same region with an overlaying Raman map of the 2D peak position, confirming the location of the illuminated region due to graphene strain

Figure 3.12: High Power Laser Illumination in Air Ambient

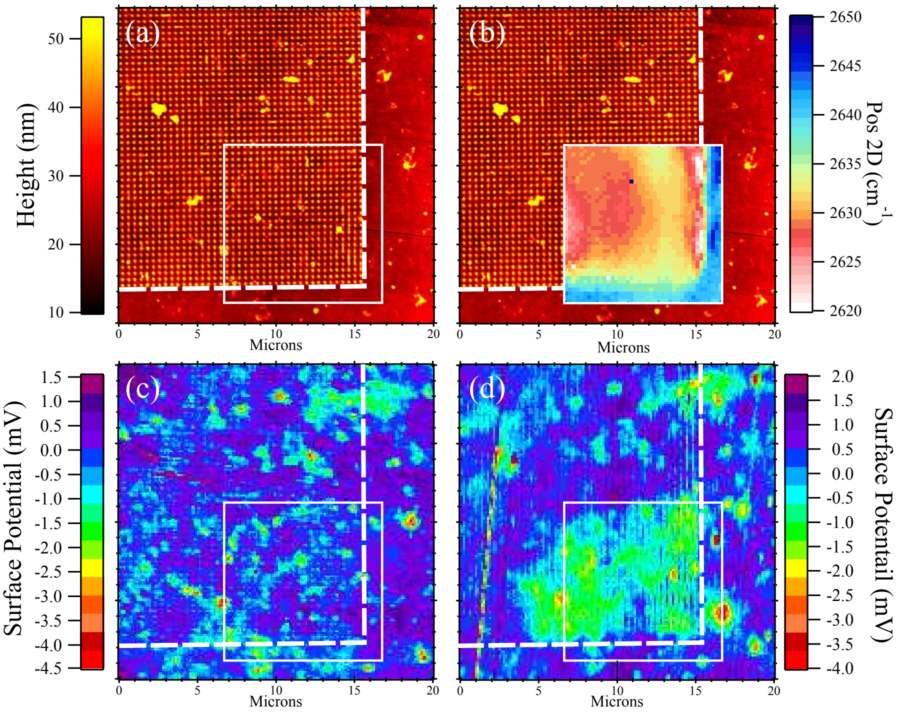

Figure 3.13: High Power Laser Illumination in Nitrogen Ambient

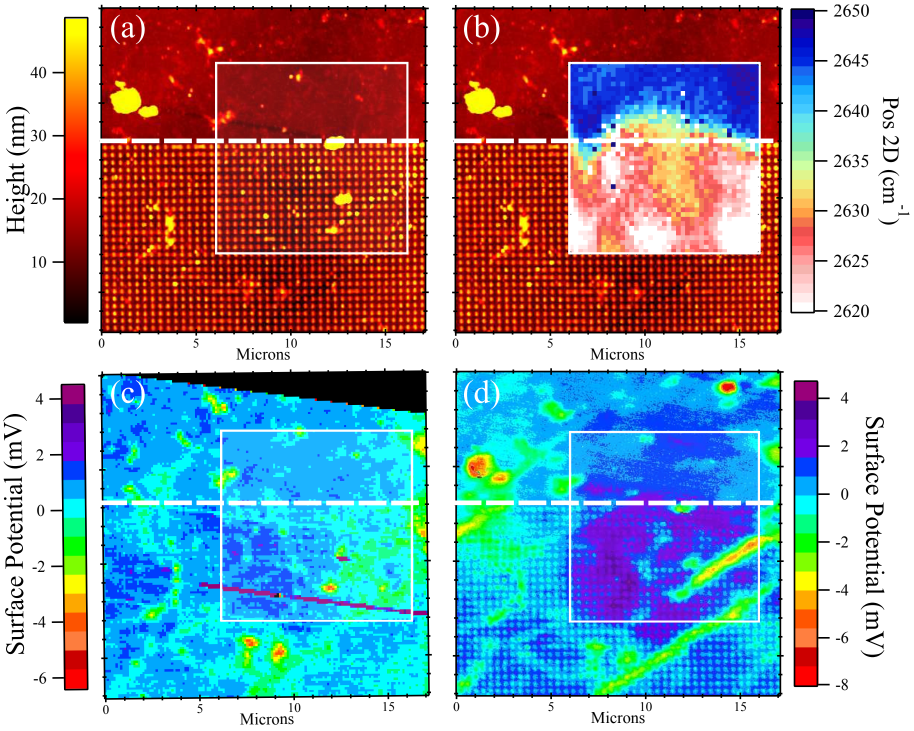

(a) AFM image (b) Raman map acquired laser illumination of the graphene 2D peak for localisation purposes and KFM images (c) before and (d) after 633 nm laser illumination at 4.55 mW in air and N_2 environments at 1 bar. Dashed line indicates gold nanodisc array edge.

Figure 3.14: Low Power Laser Illumination in Air Ambient

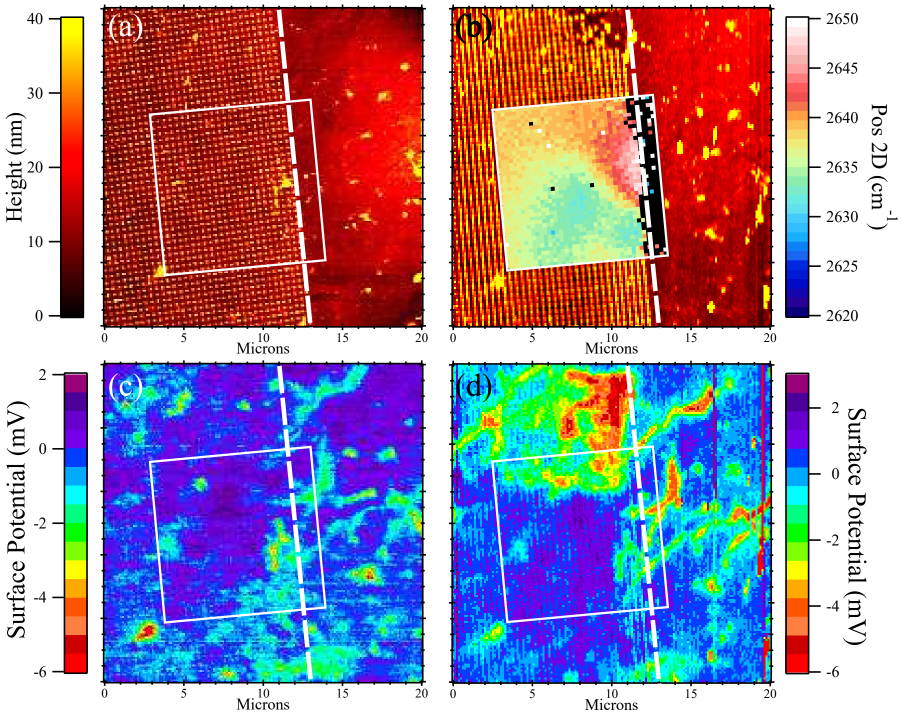

Figure 3.15: Low Power Laser Illumination in Nitrogen Ambient

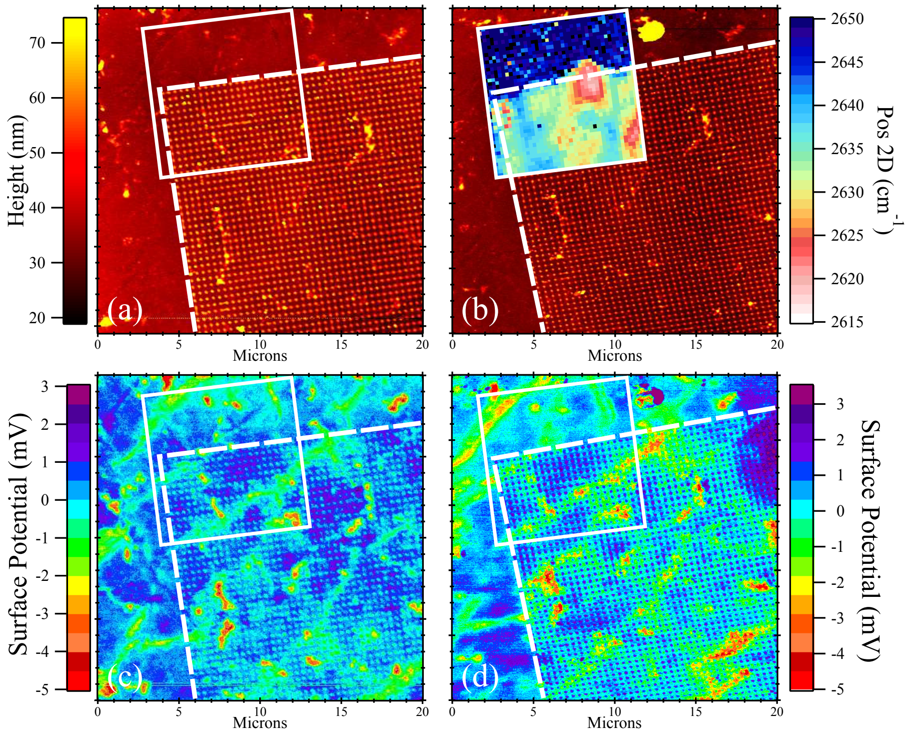

(a) AFM image (b) Raman map acquired laser illumination of the graphene 2D peak for localisation purposes and KFM images (c) before and (d) after 633 nm laser illumination at 1.14 mW in air and N_2 environments at 1 bar. Dashed line indicates gold nanodisc array edge.

induced by the AuNDs shifting the peak position. The corresponding KFM images (c) before and (d) after laser illumination are compared. The dashed white lines marks the AuND array boundary and the solid white box mark the region illuminated by the laser. KFM measures the potential difference between the work function of the scanning probe microscopy (SPM) tip and the graphene surface. As a result, variations at the surface correspond to changes in the work function of graphene. Explicitly, an increase in surface potential corresponds to a decrease in the work function and Fermi energy. Prior to laser exposure, green-red regions at low surface potential values on the KFM micrographs correspond to p-doping PMMA and graphene wrinkles [190, 297]. Of consequence, upon comparison with graphene directly transferred unto the AuND/SiO_2/Si substrate, the h-BN spacer layer clearly screens the graphene from doping interacting from the substrate (See Appendix A.6 for KFM image of an equivalent substrate without h-BN showing substrate interactions). However, the AuNDs are discernible as pale blue dots on the KFM micrographs due to the increased strain on the graphene [190, 195] at the interface.

Interestingly, the most striking difference between KFM micrographs before and after laser illumination is the local increase in p-type and n-type doping in the air and nitrogen environments respectively. The enhanced regions of p-doping in figure 3.12d are most prominent around deposits of PMMA and in regions of suspended or cracked graphene. However, the graphene regions in the absence of the AuNDs do not show an obvious increase in p-doping, indicating that the increased p-doping after laser illumination is more prominent in the presence of AuNDs. Conversely, figure 3.13d shows the experiment in a nitrogen environment results in n-doping of the graphene. Moreover, the region illuminated in the absence of AuNDs is also altered which is certainly not the case in the air illuminated experiment.

As a control, both measurement procedures were repeated at different regions of the

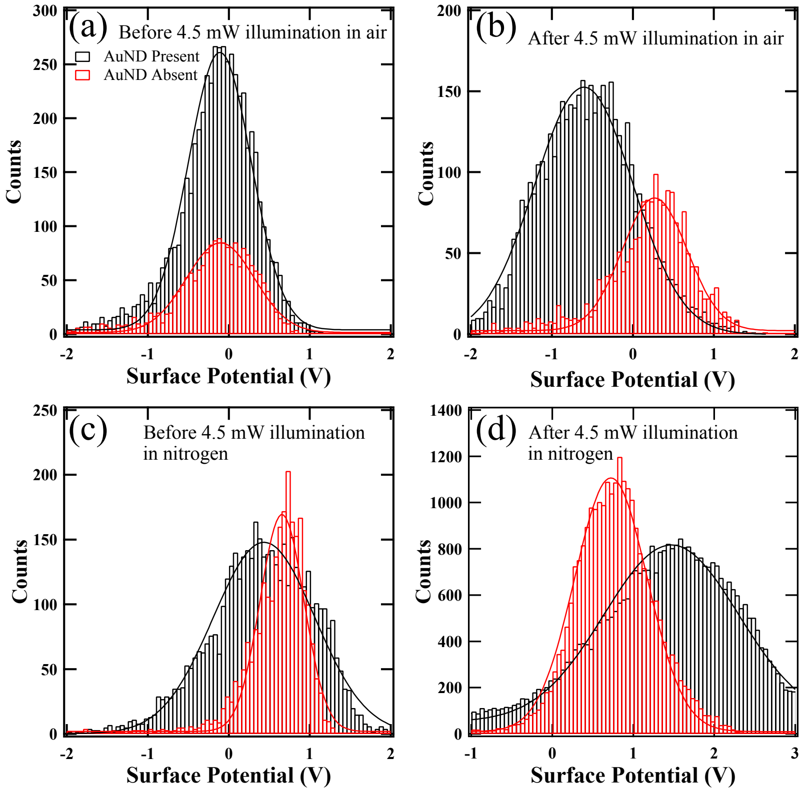

Figure 3.16: KFM histograms comparing the surface potential of graphene in contact with h-BN/SiO_2/Si (red) and h-BN/AuNP/SiO_2/Si (black) (a) before and (b) after 633 nm laser illumination in air at 4.55 mW. Similarly (c) is before and (d) after 633 nm laser illumination at 4.55 mW in nitrogen. The relative number of counts is dependent upon the resolution of the SPM imaging which was not the same for all measurements.

sample, at a lower laser power of 1.14 mW in the air and nitrogen environments as shown in figures 3.14 and 3.15 respectively. Unfortunately, the sample above the region of interest in figure 3.14 is slightly damaged between KFM measurements. Also, each Raman spectrum acquired in air, consisted of the summation of two spectra acquired at half the integration time as those acquired in nitrogen ambients. This was done to minimise saturation effects in the high power measurements in the presence of the AuNDs. Unfortunately, in the absence of AuNDs at low power, these conditions prevented accumulation of a satisfactory signal. Irrespective of this, all laser exposures were acquired during identical periods of time and does not adversely impact the laser induced doping effect. Regardless, the KFM measurements in the irradiated regions of both environments show no obvious doping effects.

To quantify the change in doping in the high power measurements, figure 3.16 compares the surface potential histograms in the presence and absence of AuNDs. Each KFM micrograph is measured either using different SPM tip, or at least a day has passed between measurements such that the work function of the SPM tip is altered between measurements. Therefore, only the relevant shift in surface potential magnitude between features of the same micrograph are comparable. Figures 3.16a and b compare the histogram distributions before and after high power laser illumination in air. A gaussian curve is fitted to each histogram as a guide for the eye. Before illumination in air, there is little difference between the surface potential of graphene in the presence or absence of the AuNDs. However after illumination, not only is there a striking reduction in the surface potential of graphene in the presence of the AuNDs, indicative of p-doping, but also a broadening of the statistical distribution. Similarly, in the nitrogen environment there is a relative shift in the surface potential in the presence of the AuNDs and statistical broadening. However, this shift corresponds to a relative increase in surface potential or n-doping of the graphene.

The measured surface potential is equal to the difference in work functions between the graphene surface and the SPM tip such that $\phi_G r = \phi_{tip} - eV_{CPD}$. The first tip used was calibrated against a gold reference sample, immediately afterwards a 60 μm KFM image encompassing the total nanoparticle array was measured. The work function of the gold reference sample was taken from a literature value of 4.75 since values of gold in air range from 4.7-4.8 eV [184, 197, 198]. To avoid tip degradation of sequential measurements, the new tips used are calibrated against the same untampered part of the graphene sample (see chapter 2 section 2.3.4 for details). As such, figure 3.17 compares the change in work function in (a) air and (b) nitrogen. From this it is clear that the graphene in the presence of the AuND array (solid lines) experiences

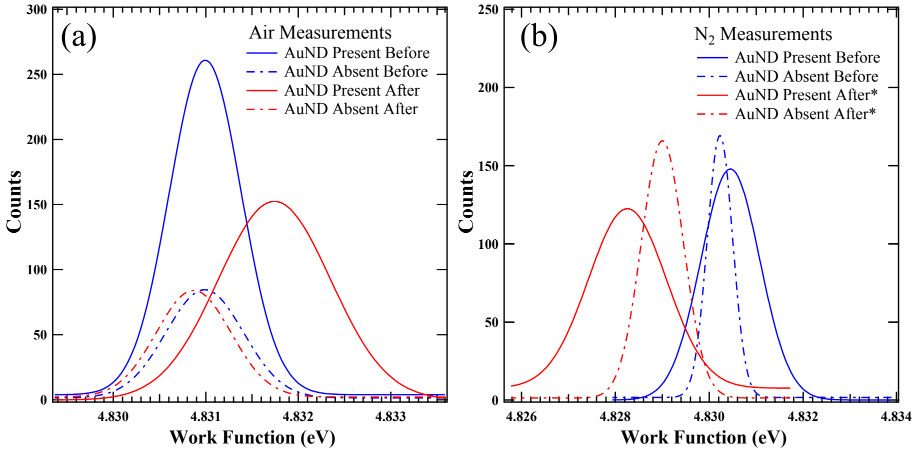

Figure 3.17: Work function histogram distributions of measurements in (a) air and (b) nitrogen environments. The blue (red) curves correspond to graphene before (after) laser illumination at 4.55 mW. The solid (dashed) lines correspond to KFM measurements in the presence (absence) of the gold nanoparticles. The N_2 measurement after laser exposure is 0.15 x magnified for easy visual comparative purposes.

a much larger shift than the graphene in the absence of AuNDs. The Fermi level is related to the work function as $\phi = E_{vac} - E_F$, where E_{vac} is the vacuum potential. Therefore, an increase (decrease) in the work function corresponds to p-doping (n-doping) of the graphene sheet. As such, the air environment promotes p-doping and the nitrogen rich environment promotes n-doping. It should be noted that the use of a three significant figures from the literature value for the work function of gold leads to a systematic error, since the measured changes in work function are just under a millivolt. Fortunately, the change in surface potential is equivalent to the change in work function, so improved work function determination is not necessary. Table 3.4 compares the statistical mean of each distribution and the relative difference of the graphene surface potential influenced by the AuNDs. In air the shift is $\sim$ -0.87 ± 0.05 mV (m eV) and in nitrogen $\sim$ +0.75 ± 0.07 mV (m eV). However, in the nitrogen environment from figure 3.13d the illuminated graphene region in the absence of AuNDs also shows slight n-doping when compared the equivalent non-illuminted region. In other words, the absolute effect could be larger. Finally, since the doping is permanent, and dependent

Table 3.4: Statistics from the Gaussian fitted surface potential histograms consisting of the mean ± the standard error of the mean.

AuND	Distribution Mean ± Standard Error (mV)			
	High Power Air		High Power N2	
	Before	After	Before	After
Present	-0.10993±0.02741	-0.60401±0.04291	0.43572±0.04440	1.4702±0.05878
Absent	-0.10323±0.02960	0.26953±0.02847	0.65724±0.01911	0.72476±0.03162
$\Delta_{(Present-Absent)}$	-0.0067±0.04035	-0.87354±0.05150	-0.22152±0.04833	+0.74544±0.06674

upon the environment the graphene surface is exposed to, it is likely that the irradiated graphene changes the surface chemistry on the surface.

To summarise, graphene in the region of AuNDs is either p-doped or n-doped by approximately ± 1 meV upon laser illumination; where the sign of the doping is dependent upon the environmental conditions. Since the graphene is decoupled from doping contributions arising from the substrate and gold nanoparticles, this effect is most likely due to surface chemical effects occurring at the exposed graphene surface. However, it is still unclear whether this effect is optically or thermally driven. At resonance the graphene electrons can be excited [274], which could lead to the observation of this effect being more prominent in the vicinity of the AuNDs. However, the AuNDs also enhance the heat absorption of heat from the laser [275, 276], which would also lead to the observed effect being prominent in the vicinity of the AuNDs (See appendix A.7 for a brief discussion of this). Interestingly, due to the high thermal conductivity of graphene and potentially the high lateral conductivity of h-BN, graphene is also effective at dissipating heat from plasmonic hot spots [30, 298]. Regardless, in both cases the interaction with the laser induces a surface chemical reaction with molecular species at the interface. However, from these measurements alone it is difficult to resolve a mechanism. Therefore, the following subsection discusses the measured Raman response in terms of temperature and doping effects.

3.4.3 Temperature Considerations

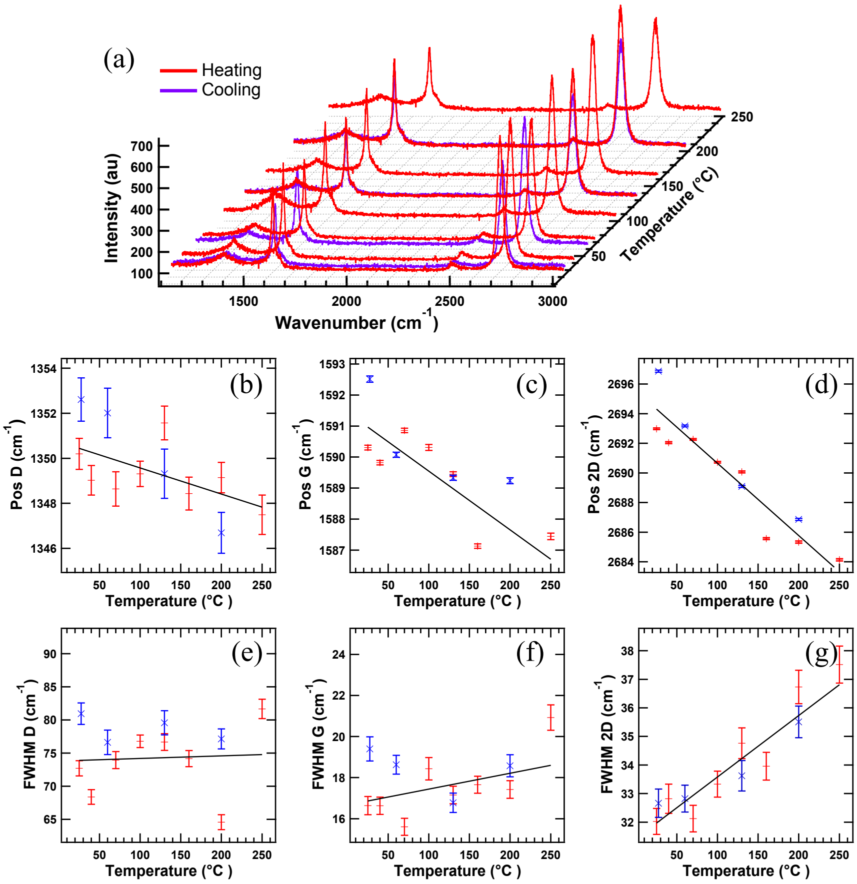

Figure 3.18: (a) Evolution of the graphene Raman spectra upon heating (red) and cooling (blue) acquired using 514 nm laser (at 4.55 mW using the 50x long working distance objective inside the Linkam stage). The average (b-c) peak position and (e-g) FWHM of graphene spectra taken at various temperatures.

Before comparing the Raman statistics acquired during laser illumination of the environmental experiments, for context figure 3.18a shows the evolution of the characteristic Raman spectrum properties of wet transferred CVD graphene on silicon upon heating. The sample was measured after annealing at 300°C for at least 20 minutes. It should be noted that although thermal annealing improves the graphene adhesion to the substrate, it also promotes further doping and strain [163, 299], which is detrimental to the high mobility properties of graphene [300]. Consistent with previously reported literature [301], as the temperature increases, the frequency of the characteristic

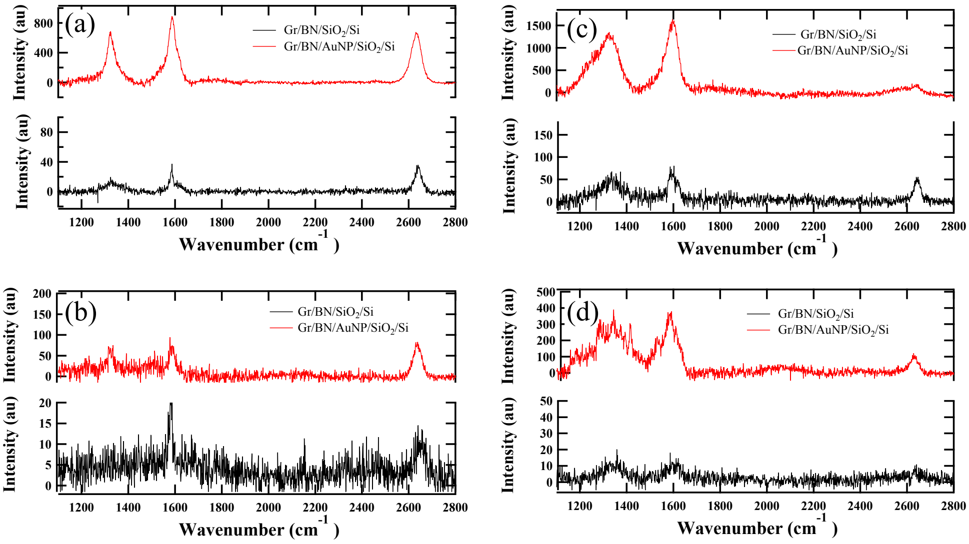

Figure 3.19: Representative Raman spectra during laser exposure at (a) high and (b) low power in air and (c) high and (d) low power in nitrogen. The black lines correspond to spectra measured off the AuNP array are 10 x magnified with respect to the equivalent measurement of graphene in contact with AuNP (red spectra).

graphene peak positions decreases. This is due to thermal lattice expansion as shown in figures 3.18b-d. Interestingly, the FWHM temperature dependencies of figures 3.18e-g, show that the peak broadening of the 2D band is also a reliable metric. Although a 532 nm laser (opposed to a 633 nm) was used to excite this Raman response, only the G peak position being a non-resonant process is invariant to the excitation laser frequency. Although the peak position and FWHM of the resonant D and 2D processes are pump frequency dependent, their relative trends are the same, providing a good reference.

Figure 3.19 compares some representative graphene Raman spectra in the presence (red) and absence (black) of the AuNDs from each environmental measurement. Interestingly, upon visual inspection of the general peak shapes acquired during the four measurement conditions, it became clear during the nitrogen ambient measurements at low power, that many of the Raman spectra exhibited miscellaneous sharp peaks around 1100 - 1800 cm^{-1} - the prominent enhancement region of the AuNDs. Moreover,

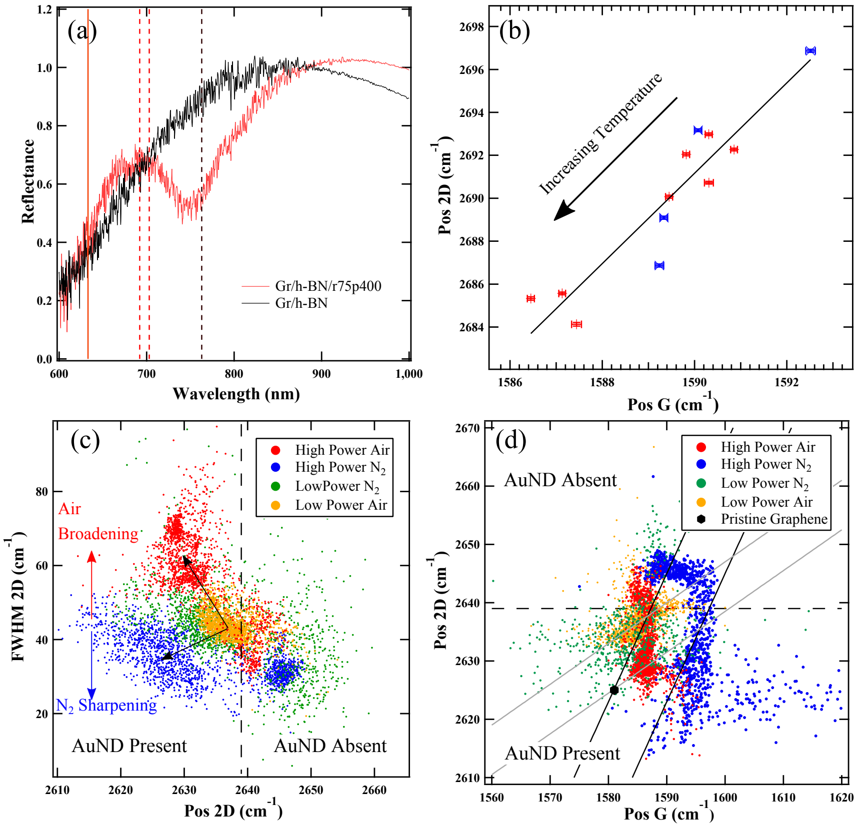

Figure 3.20: (a) The FTIR response of graphene/h-BN on the nanodisc array (radius 75 nm and periodicity 400 nm) and the silicon substrate. Although the pump at 633 nm is not strongly resonant the 2D peak is. (b) The temperature data from figure 3.18 in Pos 2D vs Pos G vector space (note that these measurements taken with a 514 nm laser). The Raman statistics comparing the (b) the 2D peak FWHM vs its position of the various experimental conditions and (c) peak position of the 2D and G peak.

there is a distinct dampening of the 2D mode. In contrast, both the high and low power air ambient conditions show well defined peaks, with expected peak broadening and shifts in the presence of the AuNDs.

For context figure 3.20a is the FTIR response of the G-SERS platform studied showing the main resonance coincide with the 2D mode. Unsurprisingly, there is a broadening of the 2D linewidth in the presence of the AuNDs as shown in figure 3.20c. A dashed black line roughly separates the Raman signal from the graphene in the presence and absence of the AuNDs; since it is more useful to compare the G-SERS response separately from the graphene response. Interestingly, as shown by the black arrows, the 2D peak distribution measured at high power in air (nitrogen) is broader (sharper) than the low power measurement in the vicinity of the AuNDs. The peaks sharpening during the high power nitrogen ambient measurements is particularly interesting, since figure 3.18g shows that typically the graphene peaks broaden as the temperature increases. Therefore, thermal effects alone cannot produce this effect. Furthermore, the low wavenumber enhancement of adsorbed aromatic molecules ha been reported by Xu et al. [302], where they use a similar G-SERS substrate and attribute this enhancement to $\pi-\pi$ interactions of the aromatic probe molecule and the graphene. With this in mind, the observed appearance of the miscellaneous peaks at low wavenumber could be due to resonant, $\pi-\pi$ interactions between graphene and a transient N_2 adsorbate species. Moreover, the reduction in the 2D peak typically caused by interaction between aromatic planes or more gerenally charge doping [164, 166, 170, 175]. Although molecular nitrogen isn't aromatic, it does have a $\pi-\pi^*$ system, where the π^* orbitals are vacant prior to optical excitation. Moreover, the transient nature of these additional peaks could be alluded to physisorption interactions at the graphene surface.

By plotting the Raman data in the Pos2D vs PosG vector space [163] as shown in figure 3.20d, the strain and doping effects can be be separated. From this, the low power measurements follow the grey doping vector, as is typical of CVD graphene samples. However, the high power measurements follow the black strain vector lines suggestive of thermally induced strain. Interestingly, in the vicinity of the AuNDs in the nitrogen ambient, there is an approximate 10 cm^{-1} blue shift of the G phonon mode between the Raman response of graphene at low power and high power. Conversely, the air measurements do not show a significant shift of the G peak between high and low power in the vicinity of AuNDs, despite clearly measuring p-doping through the KFM. In addition to this, where there is a clear distinction between the graphene in the presence and absence of AuNDs during the high power nitrogen ambient measurements, this distinction is not as clear for the air ambient measurements. This could be due to the logarithmic phonon anomaly [163, 173]. Since the h-BN pacified graphene is lightly doped and following the 'pristine' graphene strain vector, hole doping can occur via a red shift of the G band phonon before blue shifting as expected. If this is the case, air ambient doping effects could be screened during high power Raman measurements. Finally, for comparison, figure 3.20d correlates the temperature trend from figure 3.18 in the Pos2D vs PosG vector space where the red (blue) crosses correspond to heating (cooling). From comparison of the relative distributions during the low and high power measurements, the gradient trend does not fit well with the observed measurements. Although thermal induced annealing is the likely mechanism behind the observed strain, it is unclear what magnitude of temperature is required to do this. From Lee et al. [163] an upper limit estimate of 100°C is consistent with the observed measurements.

Although it is not possible to do a defect analysis before and after illumination, since the Raman data is being obtained during laser illumination. However, figures 3.20c and d indicate that graphene in the presence of AuNDs exposed to low power laser illumination is hardly perturbed. With this in mind, figure 3.21 shows histograms of the intensity ratios of the D and G peaks in the presence of AuNDs during all environmental measurements. Each histogram is fitted with a Gaussian distribution where the mean $(\mathrm{I(D/G)})_{mean}$) and standard error of the mean (σ_{SEM}) are tabulated in table 3.5. Of the total number spectra measured ($N_{tot} = 1681$), only data points pertaining to the Gaussian distributions fitted are used to calculate the standard error. Clearly, Raman spectra corresponding to graphene in the absence of the AuNDs, which do not have a D peak or where the enhanced signal was too strong which saturated the detector are not included. As a result, the high power nitrogen measurements in particular are missing

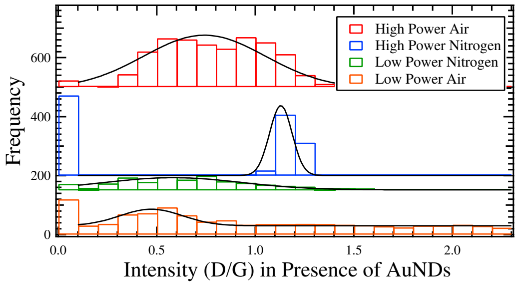

Figure 3.21: Raman histograms of the D/G peak intensity in the presence of AuNDs during different measurement conditions fitted with Gaussian distributions which are linearly offset for clarity

Measurement	AuNDs Present Only		
Conditions	$I(D/G)_{mean}$	σ_{SEM}	N
High Power Air	0.742	0.012	320
High Power Nitrogen	1.130	0.002	346
Low Power Air	0.473	0.005	533
Low Power Nitrogen	0.584	0.026	91

Table 3.5: The resultant statistics of the distributions in figure 3.21 where $I(D/G)_{mean}$, σ_{SEM} and N are the mean, standard error of the mean and number of data points.

data points due to detector saturation. Regardless, these statistics are indicative of a slight increase in defect peaks in both the nitrogen and air high power measurements which is likely to be due to strain than any severe degradation of the crystal structure.

To conclude, from the combination of KFM and Raman analysis of the four experimental procedures, it is clear that laser illumination of graphene at high power causes environmentally induced doping. Interestingly, this effect is more pronounced in the vicinity of the AuNDs. However, in addition to enhancing the electric field via the electromagnetic enhancement mechanism of SERS, gold nanoparticles also heat up via the enhanced absorption cross section. Therefore, both electronic and thermal excitation effects are considered. From the Raman measurements at high power (figure 3.20c), there is a distinct increase of strain in the graphene contoured to the nanoparticles suggestive of thermal heating effects. Consequently, any thermally induced interactions of residues such as PMMA or any other surface contaminants should be present irrespective of ambient conditions. It should be noted, that the upper limit temperature estimate of 100°C in the vicinity of the AuNDs suggests that ablation is unlikely. Therefore, the increased p-doping of the graphene in the air ambient can be attributed to the interaction with oxygen and water. Whereas, the presence of transient peaks during the low power nitrogen measurements, implies molecular nitrogen plays an active role in the doping of graphene. As a result, molecular nitrogen ambients are not necessarily ‘inert’. As a consequence, the environmental dependent optical doping of G-SERS platforms presents a simple method to fabricate interesting doping domains. This could potentially have applications in selectively enhancing particular molecular species, making G-SERS devices attractive sensing platforms.

3.5 Chapter Conclusion

To conclude, the G-SERS gold nanodisc platforms facilitated spectral enhancement via a variety of mechanisms. The nanodiscs provided the largest enhancement via an electromagnetic mechanism, the graphene itself facilitated GERS enhancement through chemical mechanisms, the substrate oxide layer provided enhancement through interference effects and the doping of the graphene itself modified the enhancement. Each of these enhancement mechanisms have unique and limited spectral range with the potential of high tunable optically active substrates. By interfacing graphene with a variety of differently treated substrates, the chemical induced doping was assessed and compared via a statistical Raman analysis. Oxygen plasma treatment of the substrate induced heavy p-doping in the graphene sheet, whereas hexagonal boron nitride provided an effective substrate pacification layer resulting in high quality graphene. Despite the h-BN inclusion increasing the distance between graphene and the AuNDs, the graphene still coupled well to the **E** field hot spot. As a result, it is shown to fully analyse the global properties of graphene, the highly sensitive Raman spectrum of graphene is best characterised by combining the analysis of the overall spectral peak characteristics and single spectra.

Interestingly, by incorporating Kelvin force microscopy with the surface characterisation of graphene, not only is the local surface potential properties of graphene assessed, but it is clear that Raman spectroscopy is not a non-invasive tool in the presence of the gold nanodiscs. More interestingly, laser irradiation of the different arrays in air and nitrogen ambients doped the array by $\sim -0.87 \pm 0.05$ meV and $\sim +0.75 \pm 0.07$ meV respectively corresponding to p and n-doping - as measured with respect to a platinum iridium tip calibrate against a gold reference sample. The effect is most pronounced in the vicinity of the gold nanodiscs. However, it is clear that there is a laser induced annealing effect since the Raman analysis shows increased strain of the graphene in the vicinity of the AuNDs. Moreover, even at low laser power, where there are no obvious laser induced strain signatures in the graphene in the presence of the AuNDs, there is an increased scattering in the presence of the nitrogen ambient in the prominent enhancement region of the AuNDs. This is suggestive of optical excitation and some transient chemical interaction of the nitrogen gas molecules and graphene. Interestingly, from examination of the before and after laser irradiation KFM micrographs at high power, there is no obvious laser ablation of surface contaminants nor distortion of the AuNDs themselves. As such, large area surface composition restructuring is unlikely to contribute to the doping change. Instead, the permanency of the optical induced doping of graphene, such that the KFM measurements show doping weeks after the irradiation, indicate a change in the surface chemistry of graphene. It is likely both optical and thermal effects lead to excitation of the graphene electrons which perturbs the graphene surface chemistry. Indeed future measurements could include an evaluation of G-SERS heating, the optoelectronic properties of the environmentally doped arrays and more interestingly, the fabrication of two dimensional doping domains of graphene for novel optoelectronic devices and the investigation of topological systems.

Chapter 4

Graphene Gas Sensing using a Microwave Method

4.1 Contactless Gas Sensing Motivation

Typical graphene based gas sensors depend upon the measurement of the change in the electrical properties of graphene upon gas adsorption [26]. These sensors are highly sensitive with fast response times arising from the unique intrinsic properties of graphene - namely high charge carrier 104 mobilities [25] that are ambipolar and particularly sensitive to perturbations of the graphene electronic structure [24, 188, 197]. Upon the adsorption of p-type (n-type) dopant gas molecules onto the graphene surface, holes (electrons) are donated to the graphene surface changing the sheet conductivity [51, 52, 53, 54, 55, 26, 56, 57].

Currently used graphene gas sensors require the deposition of metal contacts to probe the conductivity, and it is not clear to date whether the DC electrical signals reported are entirely due to gases perturbing the conductivity of graphene itself, or whether there are large contributions from the metal contacts locally doping the graphene [117, 118, 119] and/or from metal—gas adsorbate charge transfer interactions [120, 121]. To overcome this limitation a high Q microwave dielectric resonator perturbation technique [88, 303, 215], where the sheet resistance and conductivity of graphene can be determined without the need for invasive contacts.

As a consequence, the absence of metal contacts indicates that the signal measured from this contactless technique originates entirely from the graphene—gas adsorbate interaction-providing a unique platform to probe the fundamental adsorption interactions at the graphene surface. In this work CVD graphene transferred onto a high resistance silicon substrate is exposed to different concentrations of NO_2 - a p-doping gas. The time-dependent conductivity measurement is determinded by the rate of adsorption and desorption dynamics of NO_2 on graphene. For low NO_2 concentrations the underlying kinetics of such processes on graphene and carbon nanotubes have been previously studied using Langmuir models [304, 305], where it was shown that for low concentrations the NO_2 coverage is dominated by the binding energy at discrete types of adsorption sites [306, 304, 307]. However, these models fail to describe the adsorption dynamics at higher concentrations.

In this chapter the contactless microwave measurement technique of graphene is explained and its extrapolation into a unique gas sensing platform is described. To understand the characteristic shape of the conductivity signal upon NO_2 gas exposure (the sensor response lineshape), statistical analysis of Raman spectroscopy and Kelvin peak force microscopy (KPFM), which describes the surface properties of graphene, informs a modified Langmuir model that describes the underlying adsorption physics of the empirically fit data. This modified Langmuir model describes the adsorption interaction of NO_2 concentrations spanning concentrations from 300 parts per billion (ppb) to 100 parts per million (ppm). A key result of this work shows that in addition to the binding energy of NO_2 on graphene, the time dependence of the signal is largely determined by the energy barrier for adsorption, which we find to increase continuously with increasing NO_2 coverage rather than having a discrete set of constant values.

The work in this chapter was published in the IOP journals *Nanotechnology* [88] and *2D Materials* [89]. As such a large proportion of the figures (although slightly modified) in this chapter are used thanks to the permission of IOP publishing.

4.2 The Microwave Method

Microwave dielectric resonators have historically provided a contactless method of probing the surface electrical properties of a range of materials [308, 309] and more recently graphene [310, 311, 312]. The "Microwave Method", a term coined by Hao et al. [303, 313], is a methodology that allows for large area measurements of the sheet resistance of graphene by comparing three simple measurements. The method relies on measuring the perturbation of the resonant frequency and linewidth of the TE_{011} mode of a dielectric resonator in a cavity due to the presence of graphene and its supporting substrate.

When microwaves interact with a dielectric material, in this case a cylindrical sapphire puck (see figure 4.1a), standing waves are formed. There are two types of mode, Transverse Electric (TE) and Transverse Magnetic (TM), referring to the direction orhogonal to the axis of the cylinder. For conductivity measurements on graphene samples which are parallel to this direction it is important to choose TE modes for measurement, so that the frequency and linewidth perturbations arise from the same field profiles. Of interest for the microwave method is the TE mode of a cylindrical dielectric resonator with radius R and height L where the resonant frequency modes depend upon the geometry and material properties of the dielectric as follows:

$$f_{mnp} = \frac{c}{2\pi\sqrt{\mu_r \epsilon_r}} \sqrt{\left(\frac{X'_{m,n}}{R}\right)^2 + \left(\frac{p\pi}{L}\right)^2} \ , \tag{4.1}$$

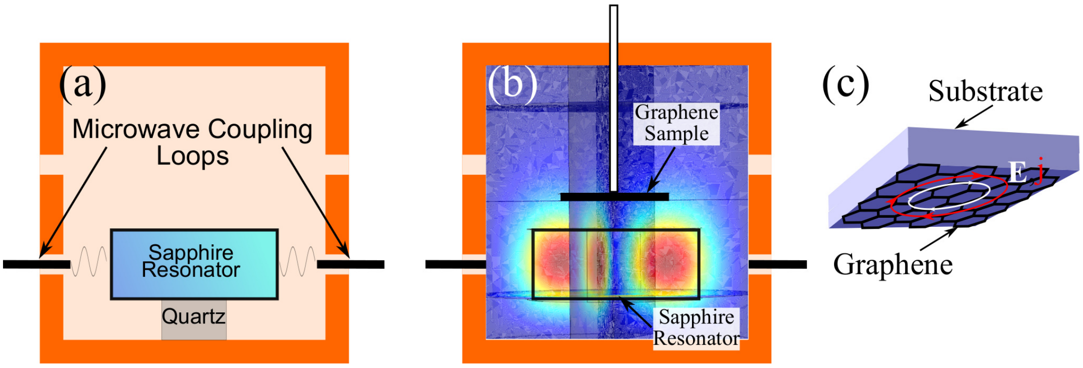

Figure 4.1: (a) Schematic of the microwave dielectric resonator inside a copper cavity housing. (b) Comsol electric field distribution indicating how the graphene sample is positioned to interact with the evanescent electric field. (c) A schematic showing the current and electric field distribution at the graphene sample surface.

where c is the speed of light, μ_r and ϵ_r are the permeability and the permittivity of the dielectric material, p is an integer and $X'_{m,n}$ is the n^{th} zero of the derivative of the m^{th} Bessel function [210].

Using the TE_{011} mode, when a sample of large area graphene on a low loss dielectric substrate is brought into a fixed position above the dielectric puck resonator, the graphene electrons will interact with the azimuthal electric field as shown in figure 4.1b, which will drive current loops in the graphene sheet, as shown in figure 4.1c, creating ohmic losses that will broaden the resonance lineshape. Unlike metals and semiconductors where only the surface conductivity can be probed non-invasively in this manner [309], since the electromagnetic skin depth of graphene, δ, is far greater than the thickness of a few layers of graphene in the microwave frequencies ($\delta \approx 10$ μm [313]) the presence of graphene will not screen the electromagnetic fields. Now if the same dielectric substrate (without graphene) is brought to the same position above the resonator, the shift in resonance frequency and linewidth due to the substrate can be measured as shown in figure 4.2. This shift in the resonant frequency in the presence of a bare substrate, Δf_s, and the linewidth, $\Delta\omega_s$ can be described using first order perturbation theory where the complex substrate and graphene permittivity

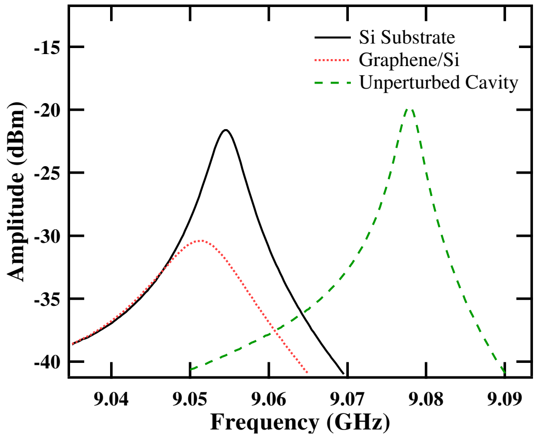

Figure 4.2: The shift in resonances of the TE_{011} in the three measurement configurations of the “Microwave Method” necessary to calculate the sheet resistivity of graphene. The resonances are measured with a VNA (Anritsu series 37XXXC) at ≈ 10.6 GHz in the presence of a 10 x 10 mm graphene on high resistivity silicon substrate.

is described as $\epsilon_s' + i\epsilon_s''$ and $\epsilon_g' + i\epsilon_g''$ respectively; provided the quality factor of the resonator is high enough compared to the losses introduced by the substrate. The quality factor is the ratio between the energy stored in the resonator and the energy lost to the cavity per cycle. In the presence of a bare substrate, the quality factor is related to the ratio of resonant frequencies and linewidths where $Q = f_0/\omega_0$ (see chapter 2 section 2.6.2). Therefore, the frequency shift can be described as:

$$\Delta f_s = f_0 \left(\frac{(\epsilon_s' - 1) \int \mathbf{E}^2 dV}{W} \right), \tag{4.2}$$

where W is the total microwave energy stored by the cavity and $\int \mathbf{E} dV$ is the electric field within the volume of the substrate, V. Similarly, the frequency shift due to graphene, Δf_g, can be described as follows:

$$\Delta f_g = f_0 \left(\frac{(\epsilon_s' - 1) \int \mathbf{E}^2 dV + (\epsilon_g' - 1) \int \mathbf{E}^2 dv}{W} \right), \tag{4.3}$$

where the second term of the numerator describes the energy graphene and v the graphene volume. Now, since the graphene volume will always be so much smaller than the substrate volume, the second term can reasonably be ignored.

Similar expressions can be used to describe the shift in linewidth of the substrate and the graphene ($\Delta\omega_g$),

$$\Delta\omega_s = 2f_0\left(\frac{(\epsilon_s'')\int \mathbf{E}^2 dV}{W}\right) \tag{4.4}$$

and

$$\Delta\omega_g = 2f_0\left(\frac{(\epsilon_s'')\int \mathbf{E}^2 dV + (\epsilon_g'')\int \mathbf{E}^2 dv}{W}\right). \tag{4.5}$$

Unlike the frequency shift, the shift in linewidth due to graphene is not negligible despite the v«V since graphene has high conductivity comparable to that of a metal such that ω_g'' »ω_s''. As a result, by combining equations (4.2) to (4.5) a simplified relationship of the easily measurable quantities Δf_s and $(\Delta\omega_g - \Delta\omega_s)$ is obtained where

$$\Delta\omega_g - \Delta\omega_s = 2f_0\left(\frac{\epsilon_g''\int \mathbf{E}^2 dv}{W}\right) = \epsilon_g''\frac{2\Delta f_s t_g}{(\epsilon_s' - 1)t_s}, \tag{4.6}$$

using the assumption that the ratio of energy stored in each material is equivalent to the thicknesses $\int \mathbf{E}^2 dv / \int \mathbf{E}^2 dV \approx \; t_g/t_s$ where t_g and t_s in the graphene and substrate thicknesses respectively.

Since the 3D conductivity can be expressed simply in terms of the imaginary part of the complex permittivity equation (4.6) can be expressed in terms of conductivity as follows

$$\sigma = 2\pi f_0\epsilon_0\epsilon_g'' = \frac{\pi f_0\epsilon_0(\Delta\omega_g - \Delta\omega_s)(\epsilon_s' - 1)t_s}{\Delta f_s t_g}. \tag{4.7}$$

Finally since graphene is a 2D material, the 3D conductivity can be converted to a 2D sheet resisitance, R_s using the following expression $\sigma = t_g/R_s$ such that

$$R_s = \frac{\Delta f_s}{\pi f_0\epsilon_0(\Delta\omega_g - \Delta\omega_s)(\epsilon_s' - 1)t_s}. \tag{4.8}$$

4.3 Graphene Gas Sensing using the Microwave Method

As discussed in section 4.1, there are a range of graphene based gas senors that function by measuring the change in electrical properties of graphene upon adsorption of gas molecules. Therefore, since resonance broadening is dependent upon the graphene sheet resistivity, the doping of the graphene sheet due to gas adsorption can be measured non-invasively using the Microwave Method. To facilitate gas sensing, a graphene coupled - dielectric resonator microwave cavity is inserted into an isolated chamber where different gases can be leaked and mixed with synthetic air (80% nitrogen and 20% oxygen) through an injection line as shown in figure 4.3a. A more extensive description of the measurement apparatus is given in section 2. In this study, different concentrations of NO_2 are diffused through small holes in the copper housing, that are big enough to enable gas diffusion yet small enough such that there is no microwave leakage.

From equation (4.8) the graphene sheet resistance is inversely proportional to the perturbed resonators linewidth. Therefore, during a gas sensing measurement the change of linewidth (or equally Q) of the perturbed graphene coupled dielectric resonator system is followed, which is indicative of a resistivity change in the graphene due to adsorption of gas molecules donating a charge carrier into the graphene sheet. Figure 4.3b is an example of the change of linewidth of the dielectric resonator upon exposure to 50 ppm of NO_2. After 5 minutes, the PID of the temperature controller is stabilized and then 50 ppm of NO_2 gas is diffused into the sensing chamber. The graphene, which is already slightly p-doped due to the wet transfer procedure, donates electrons to the NO_2 molecules as they adsorb onto the sheet. As a result, the hole conductivity of the graphene sample increases as a function of time which results in a broadening of the resonant lineshape. Using the Microwave Method described above,

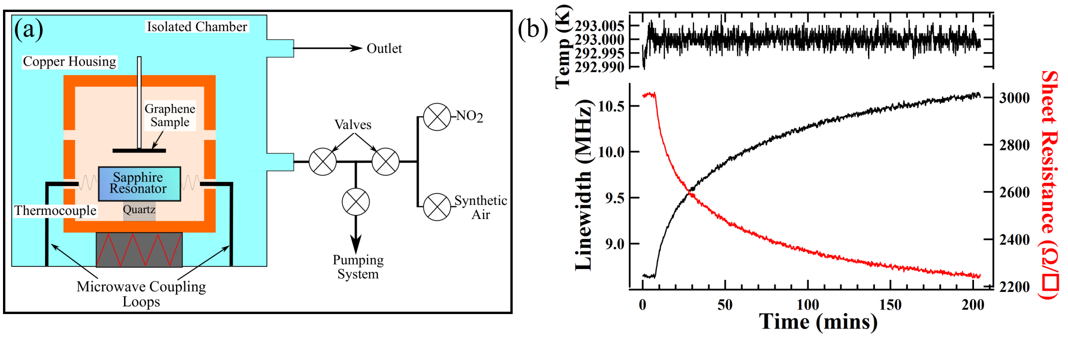

Figure 4.3: (a) Schematic of the measurement apparatus for gas sensing measurements and (b) an example of a sensor response measurement acquisition of 50 ppm NO_2 in synthetic air. The linewidth and temperature are continually measured and the sheet resistance is calculated according to equation (4.1).

the corresponding sheet resistance can be calculated using equation (4.8) which is convenient when comparing the sensor response to traditional electrical based graphene gas sensors.

Traditional graphene electrical based gas sensors utilize the concept of sensor response which is defined as the change in sensor resistivity divided by the initial resistivity. In an analogous way the sensor response can be defined in terms of the change in linewidth such that

$$S(t) = \frac{\omega(t) - \omega_0}{\omega_0}, \tag{4.9}$$

where ω_0 and $\omega(t)$ corresponds to the initial linewidth and the linewidth at some time t. This is a useful concept for comparative measurements, however, ω_0 must be consistent. This is due to the graphene resisitivity being directly dependent upon the number NO_2 molecules adsorbed on the surface. These molecules are capable of facilitating charge transfer and ultimately environmentally doping the graphene sheet. Therefore, a consistent choice of ω_0 ensures that the initial doping state of the surface being investigated is consistent.

To illustrate the importance of this, figure 4.4 compares five adsorption measurements,

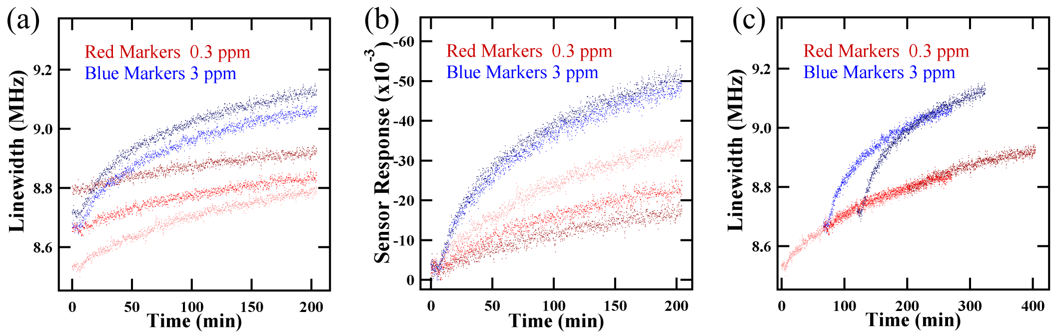

Figure 4.4: (a) Change in linewidth during gas exposure when starting at different initial linewidth values, and (b) the resulting sensor response curves. (c) Offsetting the linewidth data along the x-axis clearly shows that the sensor responses are dependent on occupancy of the graphene surface.

three exposed to 0.3 ppm of NO_2 and two exposed to 3 ppm where each measurement has a different ω_0 value as shown in figure 4.4a. The corresponding sensor response curves are shown in figure 4.4b. The measurements at 3 ppm, that have a similar ω_0, have similar sensor response curves. In contrast, the 0.3 ppm measurements, that have largely different ω_0 values, have decisively different sensor response slopes. Interestingly, an overarching response trend becomes apparent when offsetting the measurements of figure 4.4a as shown in figure 4.4c. By overlapping the shallower part of the sensor response slopes, a general adsorption trend becomes apparent that has a rate dependency upon the initial doping state of graphene. This is easily seen on the low surface coverage 0.3 ppm measurements. The 3 ppm measurements show two distinct responses that are indicative of two distinct kinetic regimes where the “slow" regime has an overall doping dependent character whereas the “fast" regime becomes limited by this doping dependent order in the system. A full discussion on the kinetic regimes of gas adsorption will be discussed in section 4.4.

To recover the graphene sensor after an adsorption measurement, the NO_2 injection line was isolated and the graphene sensor allowed the NO_2 molecules to desorb and diffuse out of the system. Interestingly, while the NO_2 adsorption response is in the

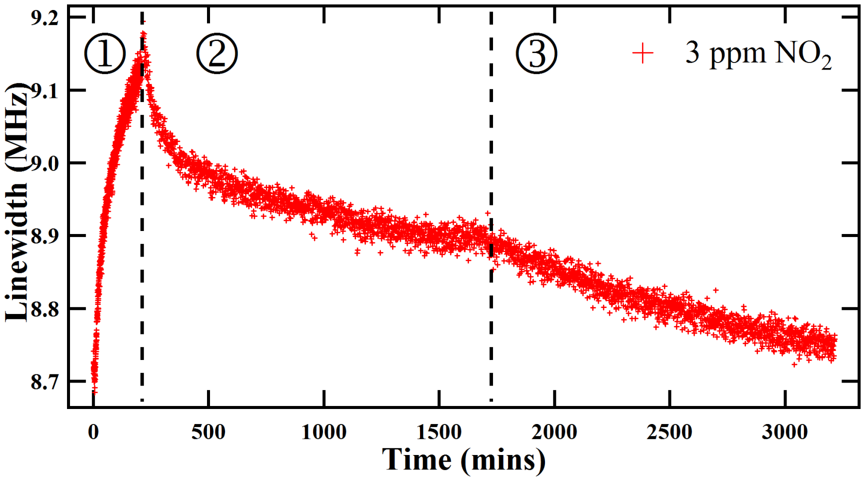

Figure 4.5: The full sensor response and recovery for 3 ppm NO_2. In region 1 NO_2 is flowed through the sensor. In region 2, the valves are closed and the samples is left to desorb NO_2. In region 3 air is then flowed into the system to promote further desorption of NO_2.

orders of hours, the desorption timescale is in the order of days. Figure 4.5 shows an example of a full adsorption and desorption measurement acquisition at 3 ppm NO_2. In region 1 the sensor is exposed to 3 ppm NO_2 gas where the increase in linewidth is due to the adsorption of NO_2 molecules. In region 2 the NO_2/synthetic air mixture inlet valve is closed, enabling the gas to desorb and diffuse through the system and exit through the outlet valve. However, after a day the desorption rate slows even further. This is due to the measurement apparatus functioning in “static” conditions, in other words, there is no air flow promoting the desorption of NO_2. Therefore, in region 3, air is flowed through the system enhancing the removal of NO_2 through the outlet.

It has been shown that rate of desorption and therefore sensor recovery can be enhanced by increasing the temperature [314, 315, 316, 317], exposure to ultra violet (UV) light [57, 318] and pumping down the system to a rough vacuum [26, 64, 289]. However these treatments can be harsh and degrade the graphene surface. For example, UV exposure provides the adsorbate molecules enough energy to cleave bonds and desorb from the surface. Unfortunately, this very same process promotes the cleavage of the

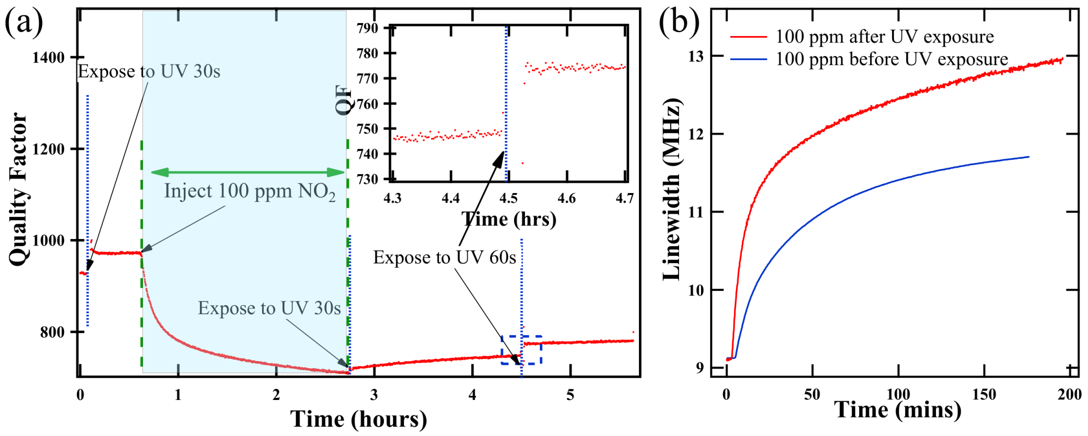

Figure 4.6: (a) A full UV measurement run following the quality factor of the resonator ($Q \propto 1/\omega$)The blue dashed lines indicate regions exposed to a UV LED for at 6.5 V at 26 mA the region of blue background bordered by green dashed lines is where NO_2 gas was injected into the system. Clearly between 1-40 minutes the signal is stable. After gas adsorption the sample is clearly desorbing the gas molecules. The inset is a zoomed in region depicted by the blue dashed box. (b) Compares the gas adsorption affinity of the same graphene sample before and after UV stimulated desorption treatments where the graphene surface is irreversibly altered after UV treatments.

sp^2 hybridised graphene bonds, forming free radical species which ultimately promote sp^3 bond formation or, in other words, increase the concentration of defects present [81]. Figure 4.6a shows such an experimental run. Initially the sensor is at some equilibrium position, after UV illumination the Q increases (ω decreases) indicative of a decrease in conductivity. This new conductivity state of graphene is stable for around 40 minutes. After which the sample is exposed 100 ppm NO_2 for approximately 3 hours whereupon the Q drops, indicating an increase in hole conductivity. During desorption the sample is exposed to UV immediately after the NO_2 exposure and again after 2 hours recovery. The inset graph shows a zoom in of the blue box clearly showing the before and after response of UV exposure. Unfortunately the sample was removed from the cavity to perform UV illumination as such continuous measurements were impossible in this particular cavity design. Figure 4.6b then shows the degradation of the sample before and after UV treatments, where it is clear that graphene becomes defected and more “sticky” after a UV treatment which can be described to the formation of defects.

Consequently, the graphene surface before and after UV illumination is altered and the graphene molecles binding affinity is altered such that the graphene surface is no longer comparable to its previous pre-illuminated state. As a study for future work, it is possible to incorporate a UV light emitting diode (LED) into the copper housing without perturbing the microwave resonator properties. This modification would allow for UV exposure without changing the gas environment and so could lead to new information about the energy involved in the ond breaking processes. Similarly, an extensive study to see how the sensor recovers after repetitive thermal treatments is intended for future work, since thermal annealing is a known occurrence at high temperatures. Consequently, for this study ambient desorption was the preferred recovery method.

Figure 4.7a shows the sensor response spanning three orders of magnitude of NO_2 concentrations: 0.3, 1, 3, 10 50 and 100 ppm. After each adsorption measurement the sample is recovered such that the linewidth $\omega_0 = 8.7$ MHz was obtained. In figure 4.7b the maximum change in linewidth was plotted against NO_2 concentration on a natural log-log plot. As a matter of notation the square brackets indicate the concentration of the gas species they contain. A linear line of best fit was extrapolated to the noise floor/ minimum discernible signal (MDS) of the measurement system. From this, the long term sensitivity limit of the system is approximately 90 ppb. However, it should be noted that this value can be significantly improved upon by reducing the insertion loss and optimising the graphene—resonator coupling which will minimise the noise in the system.

To determine the fastest detection timescale capable of NO_2 concentration differentiation, the sensor responses at times ($t = 30$s, 1, 5, 10 and 30 minutes as indicated by the dashed blue lines of figure 4.7a) were extracted and plotted on a log-log plot similar to figure 4.7b. Upon fitting with a straight line, figure 4.7c shows that it is impossible to distinguish the different NO_2 concentrations before 5 minutes of gas exposure as there

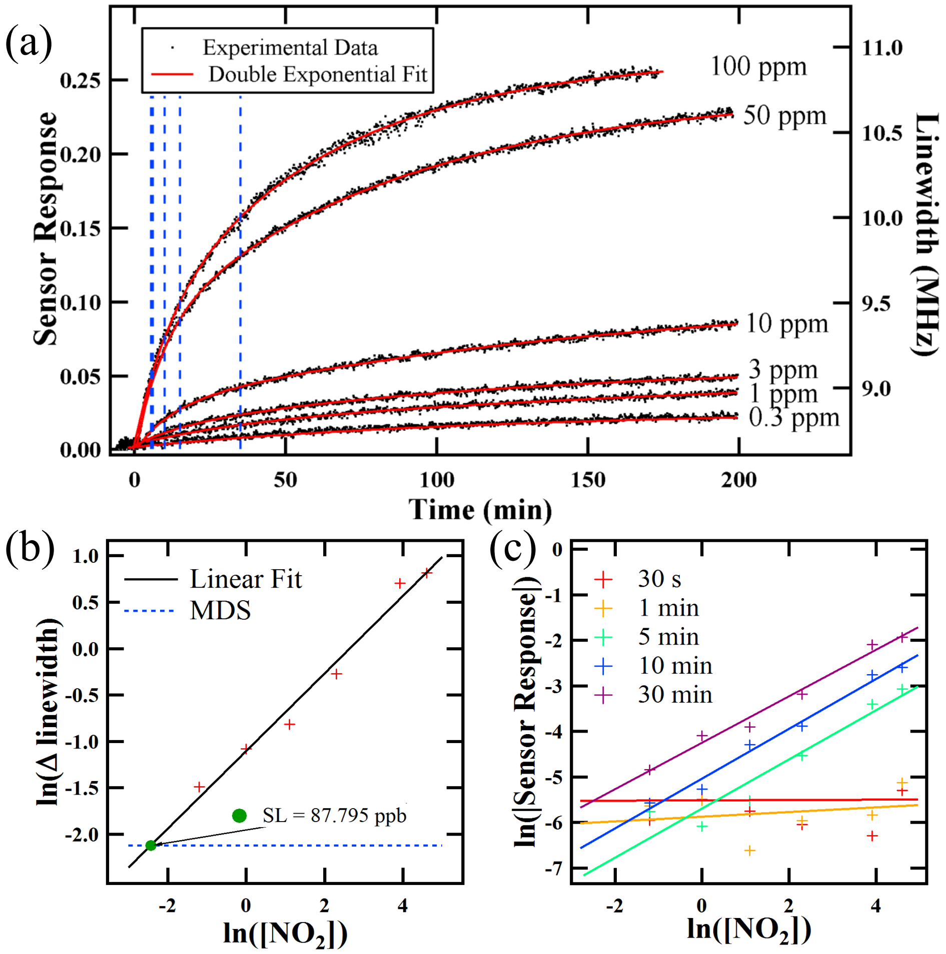

Figure 4.7: (a) Graphene sensor response for NO_2 adsorption and corresponding resonant linewidth at various concentrations. NO_2 gas is injected into the system at time $t = 0$. Blue dashed lines corresponds to the times t=30 seconds, 1, 5, 10 and 30 minutes after initial gas injection. Note that the t=30 seconds and the t =1 minute blue dashed lines on the far left of the graph partly overlap, so that they appear as a single thick dashed line. (b) The long time exposure sensor sensitivity limit is determined by extrapolating the maximum measured change in linewidth, Δ linewidth, to lower NO_2 concentrations, and comparing this with the noise floor of the measurement system (horizontal blue dashed line). (c) Sensor responses at various times (corresponding to the vertical blue dashed lines of (a)) indicate that the fastest response time occurs around 5 minutes of exposure, since for shorter exposure times there is no systematic increase in the sensor response for increasing NO_2 concentrations. Note that the value of $\omega_0 = 8.7$ MHz was used.

is no appreciable gradient to the fitted line. However, after 5 minutes of exposure, the linear fits have an appreciable gradient whereupon the various concentrations can clearly be distinguished.

4.4 Adsorption dynamics at the graphene surface

From the previous section, a graphene—coupled microwave dielectric resonator platform provides an alternative gas sensing platform capable of gas sensing through 3 orders of magnitude of NO_2 gas concentrations. However, from literature graphene-gas sensing studies [26, 63] and the results of figures 4.4 and 4.5 it is clear that the rate of the sensor response and its lineshape is dependent upon a few crucial properties. Namely the type of gases present and their molecular electron affinities, the gas concentration the sensor is exposed to, the relative doping of the graphene sheet and the local surface properties of the graphene sheet. As a first approach to understand the interaction between graphene and NO_2, figure 4.7a, shows that every surface response concentration can be fitted using a double exponential equation of the following form

$$S(t) = S_e\left(1-(1-\alpha)\exp\left\{-\frac{t}{\tau_1}\right\}-\alpha\exp\left\{-\frac{t}{\tau_2}\right\}\right), \tag{4.10}$$

where S_e is the sensor response at equilibrium ($t \to \infty$), α determines the relative weight of the two exponents, and $\tau_{1/2}$ are the associated time constants where $\tau_1 \leq \tau_2$, so that τ_1 (τ_2) corresponds to the fast (slow) component of the sensor response.

Figure 4.8 shows the values of the parameters in equation (4.10) fitted to the experimentally measured NO_2 concentrations, n_G. For increasing n_G the value of S_e increases, and the time constants $\tau_{1/2}$ decrease. The value of α is about 1 for small n_G, and decreases for larger concentrations, which shows that while for small n_G the data has

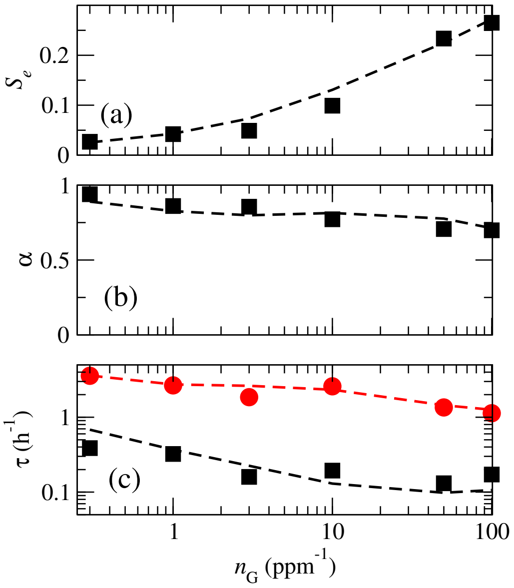

Figure 4.8: Parameters in equation (4.10) fitted to the experimental data in figure 4.7a: (a) equilibrium sensor response, S_e, (b) relative weight of the two exponentials, α, and (c) time constants τ_1 (black squares) and τ_2 (red circles). Solid points indicate the parameters fitted to the experimental data directly, while the dashed lines correspond to fits to the theoretical model.

predominantly single-exponential behavior, for larger n_G the second exponent plays an increasingly important role. Note that while equation (4.10) fits the data well, the underlying relation between this equation and the corresponding parameters with the microscopic kinetic processes of NO_2 adsorption and desorption on graphene is not clear.

In figure 4.7a it can be seen that the difference in the slopes of the curves at various concentrations decreases as time progresses. This slope corresponds to the rate of adsorbate formation, which is approximately proportional to the time derivative of the sensor response. The reaction scheme for the adsorption of NO_2 on graphene is as follows:

$$NO_2(g) + Gr^* \longrightarrow NO_2\text{–}Gr(ads), \tag{4.11}$$

where Gr^* represents a free graphene binding site and the (g) and (ads) denote whether the NO_2 is in the gas phase or an adsorbate species on graphene. The rate of adsorption is related to the sensor response such that

$$\frac{dS(t)}{dt} = k(t)\,[\mathrm{NO_2}]^{y(t)}\,[\mathrm{Gr}^*]^{z(t)}, \tag{4.12}$$

where denotes $k(t)$ as the effective time-dependent rate constant, and $y(t)$ and $z(t)$ as the partial time-dependent reaction orders. Knowledge of the partial reaction orders in chemical kinetics is useful in determining how reactants interact and determining the chemical adsorption mechanism. For NO_2 gas sensing the value of the time-dependent effective reaction order with respect to $[\mathrm{NO_2}]$, $y(t)$, indicates how responsive the sensor is to changes in NO_2 concentrations, where larger values indicate better sensitivity. The value of $y(t)$ is obtained by taking the natural logarithms of the rate equation

$$\ln\frac{dS(t)}{dt} = \ln k(t) + z(t)\,\ln[\mathrm{Gr}^*] + y(t)\,ln[\mathrm{NO_2}], \tag{4.13}$$

and extracting the time derivative of the sensor response at each time step. Note that, to obtain a smooth result, the experimental data is empirically fitted with the double exponential expression (equation (4.10) and figure 4.7a). For every time-step t the logarithm of these results as a function of $\ln[\mathrm{NO_2}]$ is plotted (figure 4.9a), so that according to equation (4.13) the slope of the linearised curve is then equal to $y(t)$. As can be seen from figure 4.9a, for each time-step the resulting logarithm of the rate increases approximately linearly as a function of $\ln[\mathrm{NO_2}]$, indicating the validity of the above equation. The resulting time-dependent $y(t)$ is shown in figure 4.9b, where it can be seen that for the initial adsorption, the effective reaction order is about 0.7. To put it in context, a reaction order of 1 defines a system where the rate is proportional to the concentration of NO_2, such that doubling the amount of NO_2

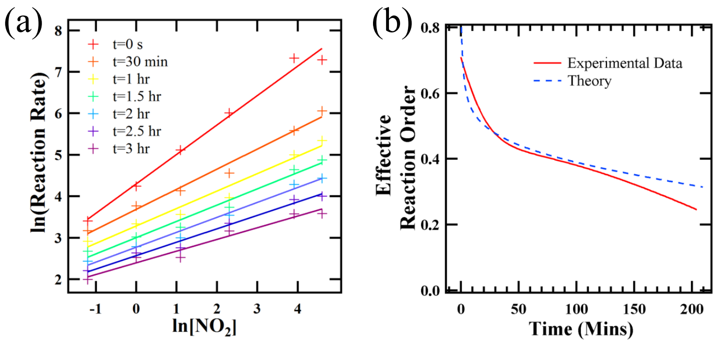

Figure 4.9: (a) Logarithm of the sensor response rate, $\ln(dS/dt)$, as function of $\ln[\mathrm{NO_2}]$ for different exposure times. At each exposure time the data points are interpolated with a straight line. Following equation (4.13) the slope of these lines correspond to the effective reaction order at a specific time, $y(t)$. (b) The resulting $y(t)$ indicates two distinct adsorption regimes on either side of the “knee-bend" shape. The theoretical model based on equation (4.17) is in good agreement with experiment.

molecules also doubles the rate. In contrast, a partial reaction order with respect to NO_2 of 0 implies that the rate is independent of the NO_2 concentration. According to figure 4.9b, after approximately 35 minutes the reaction order is significantly reduced. Thus indicating an initial rapid adsorption of NO_2 followed by a slower adsorption regime. In other words, as the adsorption reaction proceeds, the probability to adsorb further NO_2 molecules is decreased for increasing surface coverage. This result highlights a fundamental kinetic limitation due to the nature of the $N0_2$ interaction at the graphene surface - that there are two distinct regimes an initial fast adsorpiton regime followed by a slower adsorption regime. In contrast, the sensitivity limitation of $\approx$ 90 ppb and a 5 minute minimum detection time as a result from analysis of figure 4.7 can be improved upon by reducing the insertion loss of the cavity and better graphene resonator coupling geometry. Whereas the chemistry limitation at the surface cannot be overcome, instead it can be managed and improved by studying the thermodynamics of the system. However, from the results of figure 4.7 and 4.9 the current graphene sensor studied is capable of reliably distinguishing the NO_2 concentration within 5-35 minutes, which occurs during the initial rapid adsorption phase.

Further to this, the observed double exponential behavior with two time constants typically describes an adsorption process that requires an initial fast adsorption event, followed by a slow adsorption event, which can be due to the presence of two distinct types of adsorption sites on the surface [319] or due to a system limited by interparticle diffusion [320, 321]. Although it should not be too surprising that a double a exponential fitting results in a reaction order with two distinct adsorption regimes. The same result can be achieved using different fittings. Interestingly, aside from the low concentration curve at 0.3 ppm where a single exponential expression is sufficient to fit the data (figure 4.10a), all other response curves required a minimum of two exponentials (figure 4.10b). With this in mind, a single exponential description at low concentrations implies that either there is not enough NO_2 present to hinder the adsorption of subsequent NO_2 molecules or that only the preferential adsorption sites are being occupied. Further to this, large area wet transferred CVD graphene has grain boundaries, regions of multilayer regions, wrinkles and polymer residues due to the transfer process. As a result, it is unlikely that only two distinct adsorption sites are present. Instead, a surface with many adsorption sites becomes a more realistic model. Therefore a stretched exponential, $S_t = S_e - K \exp\{-t/\tau_s\}^{\beta}$, also known as a Kohlrausch function, which is an approximation of a sum of many exponentials, would better describe the graphene surface [322, 323]. Here S_t is the linewidth at time t, S_e is the value at equilibrium, K is an amplitude coefficient, τ_s is the time constant associated with the exponential term and β is an exponent such that $0<\beta \leq 1$. Figure 4.10c compares the fitting of a double exponential and a stretched exponential of 50 ppm NO_2 and both are equivalent descriptions. Figure 4.10d then compares the reaction order with respect to NO_2 of the data fitted to both the Kohlrausch function and the double exponential equation. Although the slope is a lot steeper, it also shows two distinct regimes where the “knee-bend” arising after approximately 35 minutes.

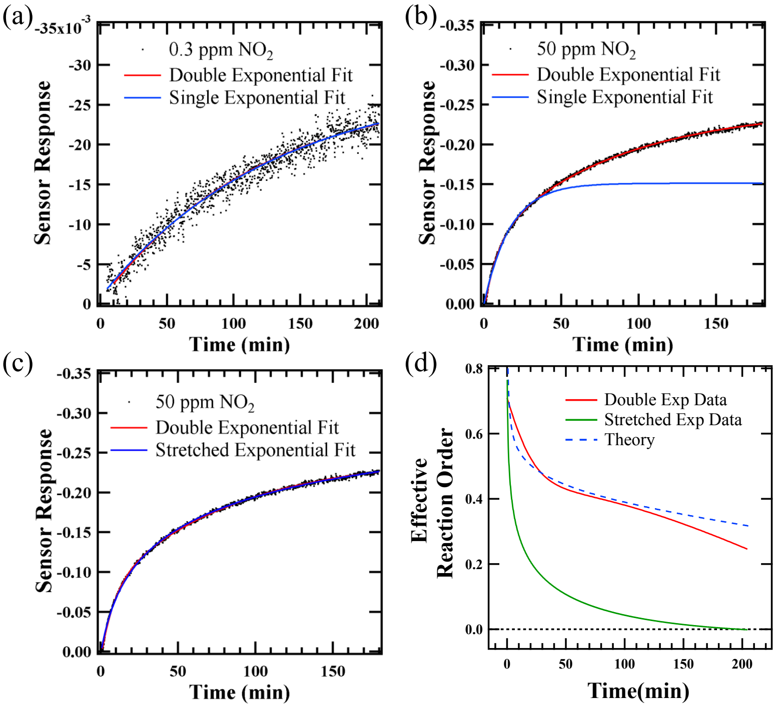

Figure 4.10: (a) Fitting the 0.3 ppm sensor to both a single and a double exponential expression. (b) The 50 ppm sensor response cannot be fitted with both a single exponential and a double exponential expression for comparison purposes. (c) The stretched and the double exponential expressions fit the 50 ppm data equally well.

However, a drawback of the stretched exponential function is that for $\beta < 1$, which is the regime required to the experimental data, it has an unphysical infinite slope at $t = 0$, while the experimental data always starts with a finite slope. Furthermore, figure 4.10d suggests that at around 200 minutes the rate of adsorption is independent of NO_2 concentration, since the effective reaction order equals zero, which is not what is observed experimentally. In addition to this, the fast time constant (τ_1) of equation (4.10) is about an order of magnitude smaller than the slow time constant (τ_2). Moreover, if three or four exponential expressions are used to fit the same data, their contribution to the time constants are insignificant and amount only to overfitting. For these reasons, the two exponential expression is used instead for the fitting, as they avoid this unphysical behavior, and also allow for more flexibility in the functional form. Regardless, both functions are ultimately empirical fits to the experimental data and although they both show two distinct adsorption regimes, they provide no physical explanation as to what is happening at the surface.

4.4.1 Surface characterisation

To investigate the adsorption mechanism with graphene, and the possibility of two discrete adsorption site model, the graphene sensor is characterised using KPFM and Raman spectroscopy measurements. Figure 4.11a shows a typical CVD graphene Raman spectrum of the graphene sensor studied. The inset is a map of the G/2D peak intensity, where a value slightly less than 0.5 is indicative of monolayer graphene.[164] This can be seen clearly in the histograms of figure 4.11c and d. Figure 4.11b utilizes the vector analysis method described by Lee et al. [163]. Here the red line and orange line are vectors in the Pos G-Pos 2D space associated with tensile strain and doping effects respectively. Note that the term 'Pos' is used to indicate Raman peak position. The sample studied is shown to be slightly strained compared to pristine graphene (green marker [163]) but more interestingly the distribution aligns better with the doping vector. This is attributed to residual NO_2 molecules on the surface and PMMA residue from the wet transfer fabrication procedure p-doping the graphene. Fortunately, PMMA is a low loss material present at an unchanging low surface coverage. As such, its presence does not overtly influence the microwave measurement. However, its presence does p-dope graphene in the local vicinity which will affect the graphene conductivity. Fortuitously, any enhanced NO_2 adsorption on graphene in the vicinity of PMMA residues is pacified by ensuring that the initial linewidth of the sensor is consistent for every measurement, as it is assumed such a defected adsorption site is permanently poisoned with NO_2 after the first NO_2 exposure. Figure 4.11c correlates the FWHM of the 2D peak with its corresponding G/2D peak ratio. This co-localisation method shows that the majority of the monolayer graphene pixels measured correspond to graphene with a FWHM less than 40, which can be indicative of good quality graphene.[300] It should be noted that narrow Lorentzian shaped 2D peaks can also be confused with few layer turbostratic graphene[166]. Therefore, it is important to analyze FWHM of the 2D peak in the context of regions of monolayer graphene. [300]. The G/2D peak intensity histogram (figure 4.11d), in conjunction with the 2D histogram of figure 4.11c, clearly shows a continuous distribution, where the average G/2D peak intensity ratio is slightly less than 0.5. This is attributed to the sample being slightly p-doped, as charge doping is known to enhance (decrease) the G (2D) peak intensity such that the G/2D peak is still indicative of monolayer graphene[170, 324]. Similarly, the D/G intensity histogram (figure 4.11e) also shows a continuous distribution around 0.35 indicative of low defect concentration [164]. In the same way, the G peak position histogram (figure 4.11f) displays a continuous distribution, where the G peak position is sensitive to doping [164, 166].

For completeness, figure 4.12 shows the full set of Raman maps of the sample better illustrating the local variation of the Raman properties of graphene. Raman maps of the D, G and 2D peak show the peak intensity (figure 4.12a-c), FWHM (figure 4.12e-g) and peak position (figure 4.12h-j) variation over the 10 x 20 μm area. The large quantity of black pixels present in the D maps correspond to unsuccessful fitting of the D peak due to a lack of spectral intensity. Consequently, since the D peak is nominally present at the edges, boundaries or defected regions of graphene, the inability for the curve fit procedure to distinguish a Raman peak from the baseline noise is indicative of a low defect concentration. Histograms comparing the intensity, position and full width at half maximum of the D, G and 2D Raman peaks are shown in figures 4.12j-l respectively. As part of the peak fit procedure, if the peak fit fails the value is set to zero which is clearly shown in the histogram data. To conclude, there is no obvious bimodal behaviour present in any of the Raman map distributions, instead there is

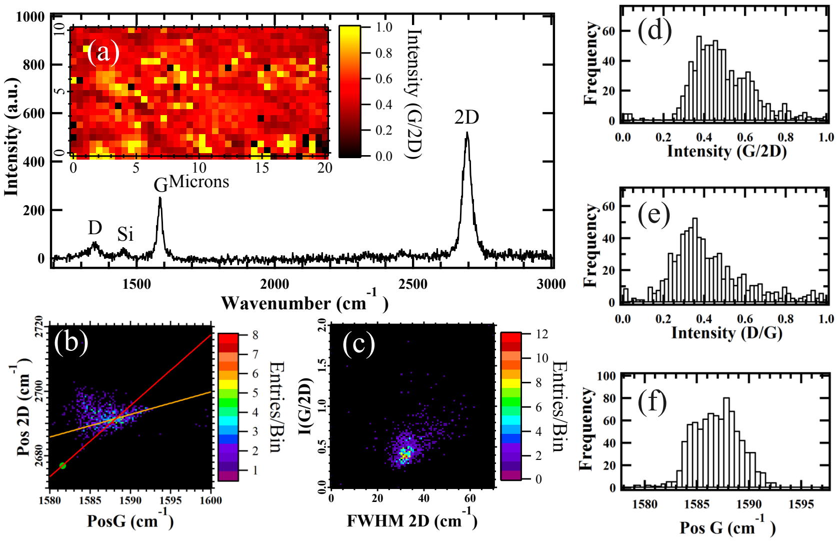

Figure 4.11: Surface characterisation of CVD graphene wet transferred onto a silicon substrate. (a) Representative graphene spectrum, inset 20 x 10 μm Raman intensity map of the G/2D peaks. 2D histograms of (b) the 2D vs G peak position and (c) the G/2D intensity ratio vs the 2D peak full width at half maximum. The green marker at (1581.6, 2676.9 cm^{-1}) is the value reported for suspended exfoliated graphene [163] showing only a slight increase in doping and strain of the graphene sheet which is expected for large scale wet transferred CVD graphene. 1D histograms of the (d) G/2D ratio (e) D/G ratio and (f) G peak position.

always a continuous distribution of properties.

Further to this, atomic force microscopy (AFM) maps of both monolayer graphene and a bilayer graphene region of the sample (figure 4.13a and c) show, despite minor amounts of PMMA residues (yellow blobs), that the transferred graphene is continuous. The tip adhesion and surface potential maps of the monolayer graphene (figures 4.13b and c) and the monolayer with multilayer graphene (figures 4.13f and g) clearly distinguishes the multilayer from the single layer. This is due to the weaker graphene—graphene Van der Waals bond compared to a graphene—substrate bond and to the charge screening effect preventing the substrate from influencing the top graphene film in the multilayer region as strongly as the monolayer region [194]. The surface potential map of monolayer graphene and the corresponding histogram (figures 4.13c and d) show, that

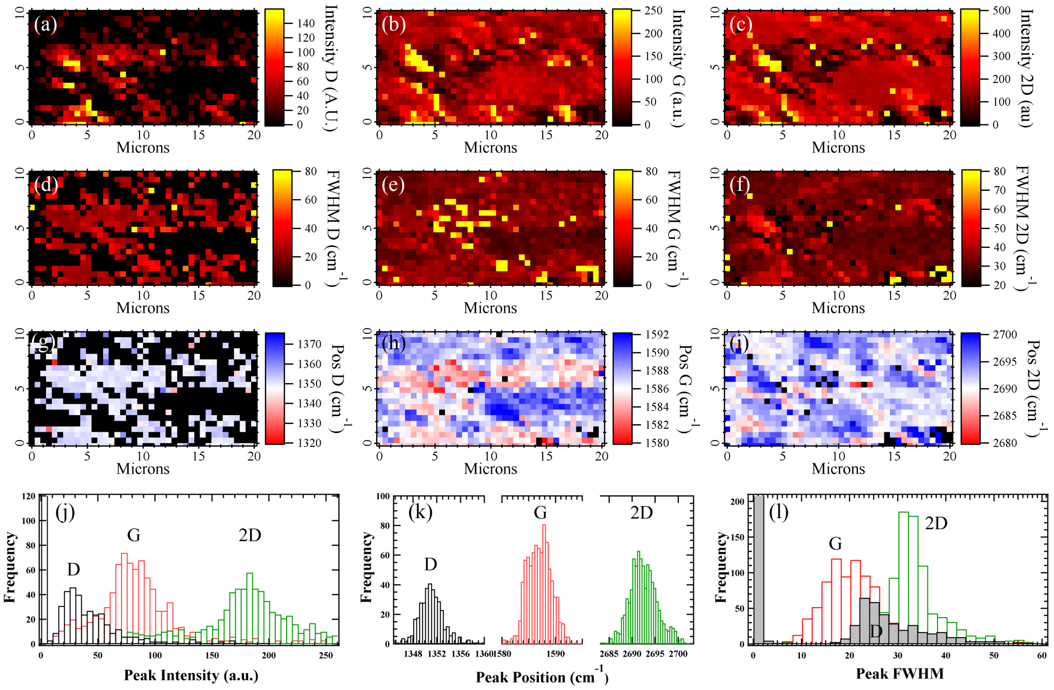

Figure 4.12: Raman maps of graphene the D, G and 2D Raman peaks with respect to peak (a-c) intensity, (d-f) full width at half maximum and (g-i) position. Corresponding histograms (j-l) compare the D, G and 2D Raman peak intensity, full width half maximum and position data. The D peak histogram data of (l) was shaded black as a visual guide. Raman peaks that were unsuccessfully fitted were set to zero. Note that the D peak histogram data has 1213 counts in the zero value bin which is not shown in the graph.

despite domains of graphene of different work function, the overall distribution of states is continuous. Naturally, defects/discontinuities in monolayer graphene coverage only broaden the distribution of energy states available on the graphene surface. Interestingly, the equivalent measurements of the multilayer regions of graphene (figures 4.13g and h) are less doped due to interactions with the substrate. Although there are two distinct regions associated with monolayer and multilayer graphene, it is clear that the overall distribution of energy states is still continuous, although slightly skewed from the normal distribution. Moreover, regions of multilayers are not prevalent on the surface.

To summarise, the surface characterisation results show no obvious bimodal behaviour

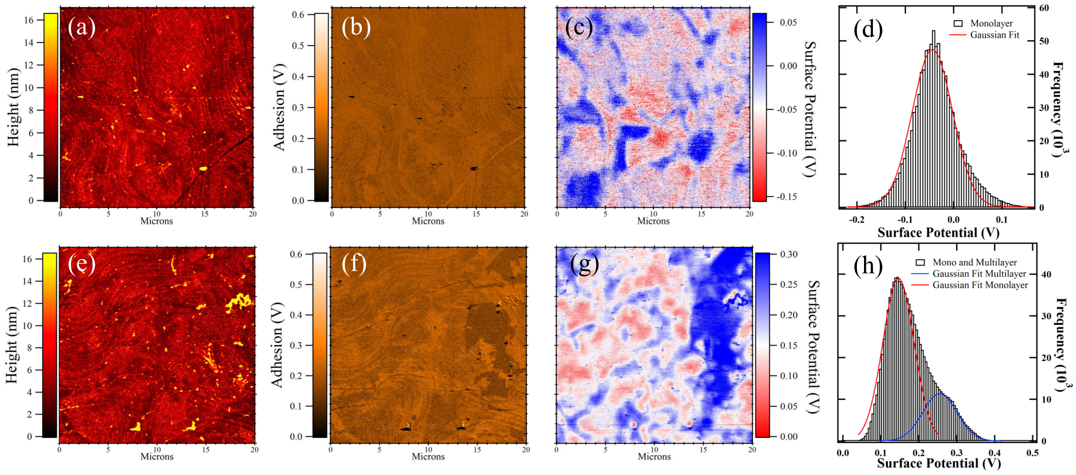

Figure 4.13: AFM, KFM, tip adhesion, and histogram of total KFM maps of (a-d) graphene and (e-h) monolayer graphene with a multilayer island.

indicating two distinct adsorption sites, but rather a continuous variation of properties across the surfaces. Therefore, these findings do not support the interpretation that the double exponential fit of the sensor responses (equation 4.10 and figure 4.7a) are due to two discrete types of adsorption sites.

4.4.2 Modified Langmuir Adsorption Model

To elucidate the graphene—NO_2 interaction and understand the origins of the sensor response, a modified Langmuir model is used to describe the adsorption at the surface. Traditionally, the Langmuir adsorption model [325, 326, 327] describes the changes in the adsorbate concentration as a dynamical process determined by the adsorption and desorption of molecules. The sticking coefficient is a key parameter, which describes the probability of an impinging molecule sticking to a surface. For an ideal Langmuir surface the sticking coefficient, k_A, is 1 for empty adsorption sites or 0 for filled adsorption sites. Explicitly, the adsorption is dependent upon the surface coverage. Further to this, it is assumed in such an ‘ideal’ system that: the surface is homogeneous i.e. containing only one type of adsorption site, that adsorption stops once all the adsorption sites are filled

- forming a monolayer on the surface, and the adsorbates are non interacting [327]. In reality very few adsorption systems are 'ideal', however, the Langmuir adsorption isotherm provides a strong basis upon which more sophisticated adsorption models can be developed.

With this in mind, to describe the adsorption of NO_2 on the graphene sensor, first it is assumed that NO_2 molecules remain intact upon adsorption, and denote the total number of available binding sites on the graphene surface as N_S, and the total number of bound NO_2 molecules as N such that the adsorbate concentration $n = N/N_S$. Time $t = 0$ is set to the instant where the NO_2 is added to the gas flow. In the same way that ω_0 does not correlate to an adsorbate free surface, but rather a reproducible surface, $t = 0$ is not a surface completely free from NO_2 molecules. Instead it is expected that there will be some NO_2 molecules bound to very strong binding sites corresponding to surface defects. As such these adsorption sites are effectively inert, and it is assumed that the NO_2 molecules do not desorb from these sites therefore are not a part of the available N_S sites nor the total number of adsorbed molecules N. Now if the sensor is exposed for a given time to air with a set concentration of NO_2 molecules, n_G, then the rate of adsorbate formation is

$$\frac{dn}{dt} = n_G\, k_A(1-n) - k_D\, n. \tag{4.14}$$

The first term on the right-hand side describes the NO_2 adsorption rate on an available Gr* sites, and is proportional to n_G and to the probability of finding a free Gr* site, given by $1-n$. The sticking coefficient, k_A, includes the probability of a gas phase molecule hitting the graphene surface in a given time-interval, and all the subsequent physical processes that NO_2 undergoes upon adsorption, which can be described with their effective adsorption barrier, E_A, so that $k_A \propto e^{-E_A/k_B T}$ [328]. Here k_B is the Boltzmann constant and T is the temperature. Similarly, the desorption rate is proportional to the number of adsorbed NO_2 molecules, and the proportionality factor is the desorption coefficient, k_D, which includes all physical processes that NO_2 undergoes upon desorption, and which are described by the energy barrier E_D, so that $k_\mathrm{D} \propto e^{-E_D/k_B T}$. For a pristine graphene surface E_A is approximately zero, and E_D is equal to the binding energy, E_B.

Finally, since all experiments were measured in ambient conditions, the effective adsorption reaction scheme of equation (4.11) implicitly includes the displacement reactions of any pre-adsorbed species such as oxygen (O_2) and nitrogen (N_2) occupying a Gr* with NO_2:

$$\mathrm{NO_2(g) + Gr{-}O_2(ads) \longrightarrow O_2(g) + NO_2{-}Gr(ads)} \tag{4.15}$$

$$\mathrm{NO_2(g) + Gr{-}N_2(ads) \longrightarrow N_2(g) + NO_2{-}Gr(ads).} \tag{4.16}$$

Since the binding affinity of NO_2 is larger than that of O_2 and N_2 [329], such a replacement reaction is thermodynamically favored. As a consequence, unlike adsorption at a Van der Waals interface which experiences either a small or non-existent adsorption barrier, to displace pre-adsorbed species it is necessary to overcome a non-trivial activation barrier E_A , as illustrated schematically in figure 4.14.

The sensor response signal, S, mainly depends on the number of NO_2 adsorbates on the surface, and on the probability of these NO_2 molecules accepting a graphene electron. For a given n, S in general, can be written in terms as $S(n) = c(n)\, n$, where $c(n)$ is the function that determines how much the linewidth changes for a given NO_2 surface coverage. This is determined by the changes in graphene carrier density due to the charge transfer from each NO_2 molecule, as well as by the related changes in mobility. Since these quantities are not yet directly accessible in the microwave

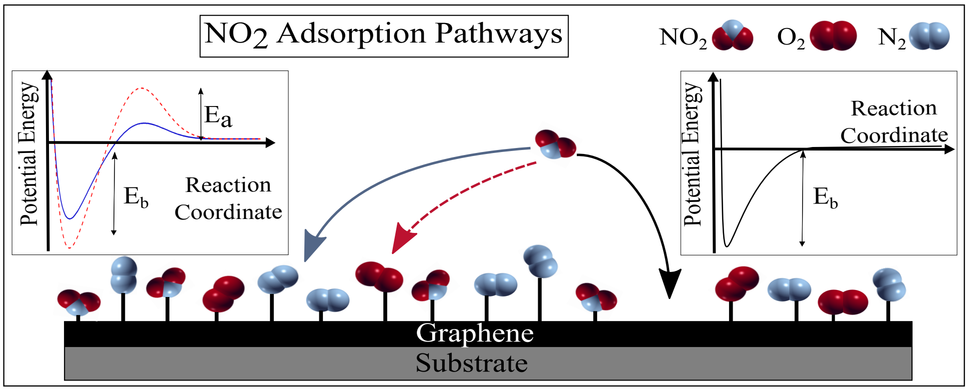

Figure 4.14: (a) Schematic representation of the possible NO$_2$ adsorption pathways, emphasizing a graphene surface with a range of different adsorption activation energy barriers to be overcome for successful molecular adsorption.

contactless experiments, the function $c(n)$ is unknown. However, is the motivation of chapter 5. Therefore, the theoretical model to describe the time-dependent sensor response needs to be formulated directly in terms of S rather than n. In the general case $S(t) = c(n(t))n(t)$. Choosing $c(n(t))$ to be an arbitrary monatomic function $c(n)$ equation (4.14) becomes

$$\frac{dS}{dt} = n_G\, k_{\mathrm{A,S}}(1-S) - k_{\mathrm{D,S}}\, S, \tag{4.17}$$

by replacing the molecular sticking and desorption coefficients with effective S-dependent coefficients. Equation (4.19) can be solved analytically to give

$$S(t) = n(t) = S_\infty\left(1 - e^{-\left(n_G k_{\mathrm{A,S}} + k_{\mathrm{D,S}}\right)t}\right), \qquad \text{with} \quad S_\infty = \frac{n_G k_{\mathrm{A,S}}}{n_G k_{\mathrm{A,S}} + k_{\mathrm{D,S}}}. \tag{4.18}$$

The experimental concentrations at $n_G = 0.3$ ppm and 100 ppm are used as the training data sets to obtain values for $k_{\mathrm{A,S}}$ and $k_{\mathrm{D,S}}$ upon fitting to equation (4.18). The quality of the these values is tested against the remaining sensor response curves. The resulting values are shown in figure 4.15a and compared to the experiment 4.15f showing a poor fit. To better describe the experiment, two models are explored, *CASE I* position dependent adsorption and desorption and *CASE II* surface coverage dependent adsorption and desorption.

***CASE I*: Position Dependent Adsorption and Desorption Coefficients.**
To investigate a system where the graphene surface was comprised with non-equivalent adsorption sites, the total number of active adsorption sites were divided into i_{max} smaller subsets, $N_{S,i}$, so that $\sum_{i=1}^{i_{max}} N_{S,i} = N_S$.The relative weight of each subset, w_i, is defined as $w_i = N_{S,i}/N_S$, so that $\sum_{i=1}^{i_{max}} w_i = 1$. We can then generalize equation (4.17) as

$$\frac{dS}{dt} = \sum_{i=1}^{i_{max}} w_i \left[n_G k_{\mathrm{A,S},i} (1 - S_i) - k_{\mathrm{D,S},i} S_i \right], \qquad \text{with } S = \sum_{i=1}^{i_{max}} w_i S_i, \tag{4.19}$$

where $k_{\mathrm{A,S},i}$ ($k_{\mathrm{D,S},i}$) is the sticking (desorption) coefficient for the subset with index i.

In this way the graphene surface is described as having i distinct regions with different properties, so that each has its own adsorption and desorption coefficient. The analytic solution for each $S_i(t) = n_i(t)$ has analogous form to the one given in equation (4.17). When comparing the model to the experiment, subdividing k_D in smaller subsets does not significantly improve the agreement with experiment, therefore a constant value for k_D is used. In general this shows that the adsorption process is dominated by variations in the sticking rate rather than the desorption rate.

Without loss of generality, the subsets can be ordered in such a way that $k_{\mathrm{A,S},i+1} \leq k_{\mathrm{A,S},i}$. We now introduce the variable $x \in [0, 1]$, and write the sticking rate as function of this variable as

$$k_{\mathrm{A,S}}(x) = \begin{cases} k_{\mathrm{A,S},1} & 0 \leq x < w_1 \\ k_{\mathrm{A,S},2} & w_1 \leq x < w_1 + w_2 \\ k_{\mathrm{A,S},3} & w_1 + w_2 \leq x < w_1 + w_2 + w_3 \\ \vdots & \\ k_{\mathrm{A,S},i_{max}} & 1 - w_{i_{max}} \leq x \leq 1 \end{cases}, \tag{4.20}$$

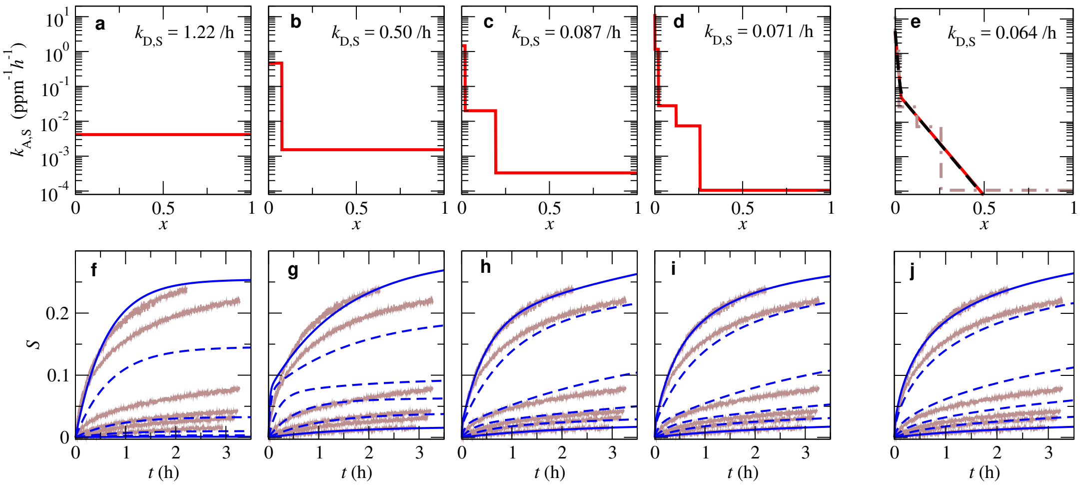

Figure 4.15: (a-e) The effective rate of adsorption $k_{\text{A,S}}/\gamma_D$ as a function of effective surface position, x, and the resultant theoretical sensor responses (f-j). The theoretical fittings (blue curves) are superimposed on top of the experimental data (brown curves). The theoretical parameters are obtained by fitting the theoretical model to the 0.3 and 100 ppm NO_2 data (solid blue curves). The dashed blue curves are the theoretical sensor response for the other NO_2 gas phase concentrations, not used for the fitting, which therefore correspond to the test set for the validity of the model. The step-wise curves in (a-d) are calculated with equation (4.21) (1 step for a, 2 for b, 3 for c, and 5 for d), the continuous red curve in e is calculated with equation (4.25), and the black dash curve with equation (4.27). The dash-dotted brown curve in 3 is a copy of the curve in d, and shows that the continuous functions smoothly average the step-wise functions.

or in a more compact notation

$$k_{\text{A,S}}(x) = \sum_{i=1}^{i_{max}} k_{\text{A,S},i} \left[\theta(x - x_i) - \theta(x - x_i - w_i)\right], \qquad \text{with} \quad x_i = \sum_{j=1}^{i-1} w_j, \tag{4.21}$$

where $\theta(x)$ is the Heaviside step function. This corresponds to a step-wise monotonically decreasing function, where the value at each step is equal to a given $k_{\text{A,S},i}$, and the width of the step is equal to w_i. From this, x corresponds to an effective variable describing different positions of the graphene surface, and write the position dependent occupation probability in analogous form as

$$S_x(x) = n_x(x) = \sum_{i=1}^{i_{max}} S_i \left[\theta(x - x_i) - \theta(x - x_i - w_i)\right], \quad \text{with} \quad x_i = \sum_{j=1}^{i-1} w_j. \tag{4.22}$$

This allows us to write equation (4.19) in an equivalent integral form as

$$\frac{dS}{dt} = \frac{dn}{dt} = \int_0^1 \left[n_G k_{\mathrm{A,S}}(x)(1 - S_x(x)) - k_{\mathrm{D,S}} S_x(x)\right] dx, \qquad \text{with } S = \int_0^1 S_x(x) dx, \tag{4.23}$$

which has the analytic solution

$$S(t) = n(t) = \int_0^1 S_\infty(x)\left(1 - e^{-\left(n_G k_{\mathrm{A,S}}(x) + k_{\mathrm{D,S}}\right)t}\right) dx, \quad \text{with} \quad S_\infty(x) = \frac{n_G k_{\mathrm{A,S}}(x)}{n_G k_{\mathrm{A,S}}(x) + k_{\mathrm{D,S}}}. \tag{4.24}$$

Instead of a sum over discrete values $S(t)$ is expressed as an integral over the effective position variable x. The advantage is that this integral form is valid for any arbitrary $k_{\mathrm{A,S}}(x)$, not only for the stepwise decaying function discussed so far.

First consider the results for $i_{max} = 2$ in figure 4.15bg, which models a surface with two distinct adsorption sites. Interestingly, $k_{\mathrm{A,S},1}$ is about two orders of magnitude larger than $k_{\mathrm{A,S},2}$, and the weight of the first region is much smaller than the one of the second region. While the agreement with experiment is improved compared to using only one region (figures4.14a and f), it is still rather poor. This shows that while for each individual value of n_G one can fit the experimental data well with two exponentials, since the fitting parameters for a each n_G are independent of the ones at a different n_G, to have a physically consistent model across varying n_G (equation (4.24)) two exponentials are not enough.

In contrast, the agreement between theory and experiment becomes reasonable for $i_{max} = 3$ (4.15ch), and becomes eventually rather good for $i_{max} = 5$ (4.15di). Interestingly, in these cases the values of the $k_{\mathrm{A,S},i}$ decrease on an exponential scale as x increases, and the weights become progressively larger as $k_{\mathrm{A,S},i}$ decrease. For small x the function $k_{\mathrm{A,S}}(x)$ therefore exhibits exponentially decreasing behavior. For large x the value of $k_{\mathrm{A,S}}(x)$ is very small, so that the model function does not significantly change when replacing the value with zero.

Having determined that the general $k_{\mathrm{A,S}}(x)$ needs to be an exponentially decaying function, we can replace the step functions with continuous exponential functions with piecewise linear variation of the exponents as

$$k_{\mathrm{A,S}}(x) = k_{\mathrm{A,S,0}}\, e^{\sum_{i=1}^{i_{max}} [f_i - \alpha_i (x - x_i)][\theta(x - x_i) - \theta(x - x_i - w_i)]} \left[\theta(x) - \theta(x-1)\right], \tag{4.25}$$

with

$$x_i = \sum_{j=1}^{i-1} w_j, \quad \text{and} \quad \alpha_i = \frac{f_i - f_{i+1}}{w_i}, \tag{4.26}$$

where $f_1 = 1$, and $k_{\mathrm{A,S,0}}$, f_i, and w_i are arbitrary parameters. Note that this function is zero outside the range $x \in [0, 1]$. We then obtain $n(t)$ by numerically evaluating equation (4.24). While this function is now continuous, it still has discontinuous derivatives. An alternative exponentially decreasing function with continuous derivatives can be obtained adding up exponential terms with different exponents, which gives the simpler form

$$k_{\mathrm{A,S}}(S) = \sum_{i=1}^{i_{max}} \bar{k}_{\mathrm{A,S},i}\, e^{-\bar{\alpha}_i x}, \tag{4.27}$$

with $\bar{k}_{\mathrm{A,S},i}$ and $\bar{\alpha}_i$ the i_{max} parameters to be fitted to the experimental training data set. For $k_{\mathrm{D,S}}(S)$ on the other hand we find that its exact functional form is not critical for these experiments.

To illustrate this we present the results for a constant $k_{\mathrm{D,S}}(S)$, as well as for a monotonically increasing trial function $k_{\mathrm{D,S}}(S) = k_{\mathrm{D,S,0}} + k_{\mathrm{D,S,1}}\left(1 - e^{-\beta_1 S}\right)$, with parameters

$k_{\mathrm{D,S,0/1}}$ and β_1, and show that the resulting $S(t)$ is largely identical.

When fitting equation (4.27) to experiment for $i_{max} = 1$ the agreement is not very good. For $i_{max} = 2$ on the other hand the agreement is already excellent (figure 4.15ej). The required number of parameters for the exponentially decreasing continuous $k_{A,x}(x)$, 5 for $i_{\mathrm{max}} = 2$, is therefore much smaller then the one required for a good agreement with experiment for the stepwise function considered earlier, where $i_{\mathrm{max}} \geq 5$ is required (figure 4.15). This further confirms that the exponentially decaying functional form is a good representation of the underlying physical processes. For $n_G = \{0.3, 1.0, 100.0\}$ ppm the agreement is essentially perfect. For $n_G = \{3.0, 10.0, 50.0\}$ the agreement is still good, and can be brought into perfect overlap with experiment when rescaling the function by a constant, or evaluating it at a slightly shifted n_G. This is attributed to slightly varying experimental conditions across the experimental runs for different n_G. For example, one can see that the experimental curves for 1 and 3 ppm are very close to each other, while one would expect the spacing to be more similar to the one between 0.3 and 1 ppm. Indeed the model predicts such a larger spacing. For larger i_{max} the agreement with experiment does not improve significantly, which shows that the true shape of $k_A(x)$ is well captured with two exponentials.

In general the adsorbed NO_2 molecules interact with each other, for example due to electrostatic repulsion of these negatively charged molecules, so that the activation barrier is expected to increase with increasing coverage, even for a perfectly homogeneous graphene surface. Moreover, the charge transfer per NO_2 molecule will generally decrease for increasing coverage due to electrostatic interactions, and the change in mobility for a given adsorbed molecule can also vary with coverage. The extracted $k_{\mathrm{A,S}}(x)$ in figure 4.15e therefore is a universal function, which includes the variation of the activation barrier due to an inhomogeneous surface, and implicitly also due to the inter-molecular interactions, as well as the changes of charge transfer and mobility

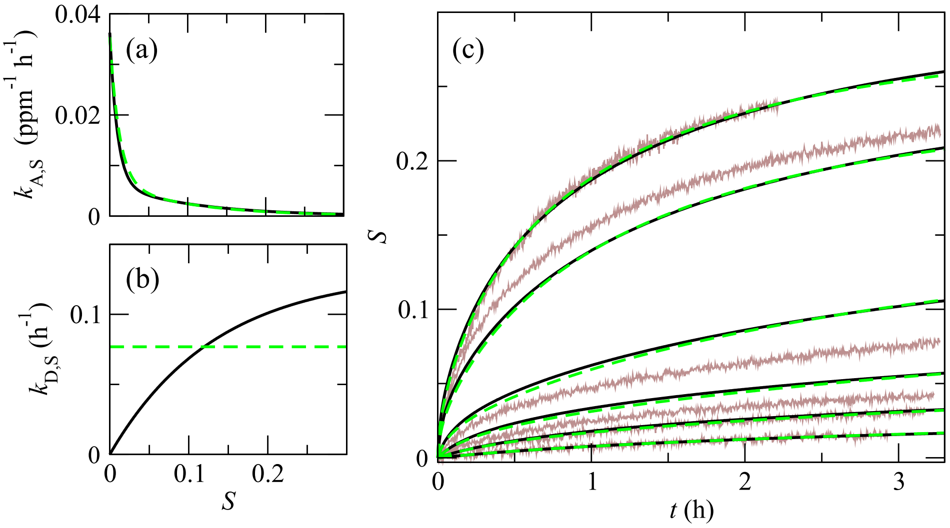

Figure 4.16: (a) Sticking and (b) desorption coefficients obtained by fitting the experimental sensor response at 0.3 and 100 ppm to equation (4.17). (c) Comparison of the resulting theoretical $S(t)$ (equation (4.17)) with the experimental results for all measured NO_2 concentrations. Solid black curves are for non-constant $k_{D,S}(S)$, while dashed green lines are for a constant $k_{D,S}(S)$. The light brown lines correspond to the experimental data, and are in good agreement with the theoretical results for all considered NO_2 concentrations.

with coverage.

CASE II: Surface Coverage Dependent Adsorption and Desorption

As an alternative/equivalent way, instead of expanding the sticking coefficient as a function of position, x, it can be expanded as a function of surface coverage, n, or equivalently of S, since we assume that $S = n$. This describes a system were the sticking and desorption coefficents are dependent on the surface coverage of adsorbates. Therefore, describing a system were the NO_2 adsorption affinity is dependent on the number of adsorbates pre-adsorbed on the surface. The variations of the sticking coefficient with $S = n$ includes both the effects due to molecule-molecule interactions, but also implicitly the graphene surface inhomogeneities. In analogy to equation (4.27) we can write this dependence as a sum of exponentially decaying functions

$$k_{\mathrm{A,S}}(S) = \sum_{i=1}^{i_{max}} \bar{k}_{\mathrm{A,S},i}\, e^{-\bar{\alpha}_i S}, \tag{4.28}$$

with parameters $\bar{k}_{\mathrm{A,S},i}$ and $\bar{\alpha}_i$.

Then $S(t)$ is obtained by numerically solving the differential equation

$$\frac{\partial}{dt} = n_G\ k_{A,S}(S)\,(1-S) - k_{D,S}(S)\, S. \tag{4.29}$$

As before $\bar{k}_{\mathrm{A,S},i}$ and $\bar{\alpha}_i$ the i_{max} parameters is determined by fitting the experimental training data set. For $i_{\mathrm{max}} = 2$, as shown in figure 4.16. The quality of the fit is similar for both the constant $k_{\mathrm{D,S}}(S)$ as well as well as for the monotonically increasing function. The agreement is slightly improved in this second case, but the difference is too small to determine the exact shape of $k_{\mathrm{D,S}}(S)$. We note that during the experimental desorption process, where NO_2 admixing into the air flow is stopped, it is found that the desorption of NO_2 is initially fast, and then proceeds at a much lower rate (figure 4.5), which is indicative of $k_{\mathrm{D,S}}(S)$ going towards 0 as S goes to 0, as demonstrated for the non-constant $k_{\mathrm{D,S}}(S)$ (black curve in figure 4.16). Overall, these results show that the adsorption behavior is dominated by the exponentially decreasing $k_{\mathrm{A,D}}(S)$, while $k_{\mathrm{D,S}}(S)$ plays a secondary role.

Comparison of *CASE I* and *CASE II*.

To conclude, despite both models describing different physics, when the sticking coefficient is described as continuously decaying exponential equations (4.27) and (4.28) and plugged into equations (4.24) and (4.29) for the position dependent and surface occupation dependent processes respectively, the theory is in good agreement with the experiment. In essence the function $k_{\mathrm{A,S}}(S)$ (and equivalently $k_{\mathrm{A,S}}(x)$), in the decaying exponential form, effectively take into account that the sticking coefficient depends both on coverage, n, and of the position on the graphene surface, which is described by the effective one dimensional variable, x. Indeed both approaches (*CASE I* and *CASE II*) include the effects of surface inhomogeneities as well as effective interactions between adsorbed molecules in the single effective variable. Both $k_{\mathrm{A,S}}(x)$ and $k_{\mathrm{A,S}}(S)$ are exponentially decaying functions of x and S respectively, showing that both models reflect the same underlying physical phenomenon.

Upon closer inspection of the position dependent model of *CASE I*, figure 4.15 shows that the initial curvature of the slopes do not quite match as nicely as the equivalent results of *CASE II*, the surface occupation model, as in figure 4.16c. However, the position dependent model clearly shows that the adsorption process is not dominated by a small number of adsorption sites with distinct and constant properties, but rather that the properties of the adsorption sites are continuously varying over the surface and with increasing coverage. This agrees with the experimental surface characterization results showing a continuous distribution of properties.

In the surface occupation model (*CASE II*) figure 4.16 shows for n_{G}=3, 10 and 50 ppm there are minor deviations of up to about 25% between theory and experiment, which we ascribe to the slightly varying experimental graphene sheet conditions across the different measurement runs. This is attributed to slight deviations in molecular coverage of the graphene surface at $t = 0$ for each initial NO_2 concentration. For each measurement, the initially present NO_2 molecules are expected to be bound to different random initial binding sites. Moreover, since O_2 is also a p-doping gas [329], the relative initial ratio of adsorbed O_2 and NO_2 molecules can vary even for the constant initial resistance that we use, and this variability in the ratio will slightly influence the measured time-dependent sensor response. Figure 4.17 compares each concentration measurement to the solution of equation (4.29) using the experimental n_G mixture

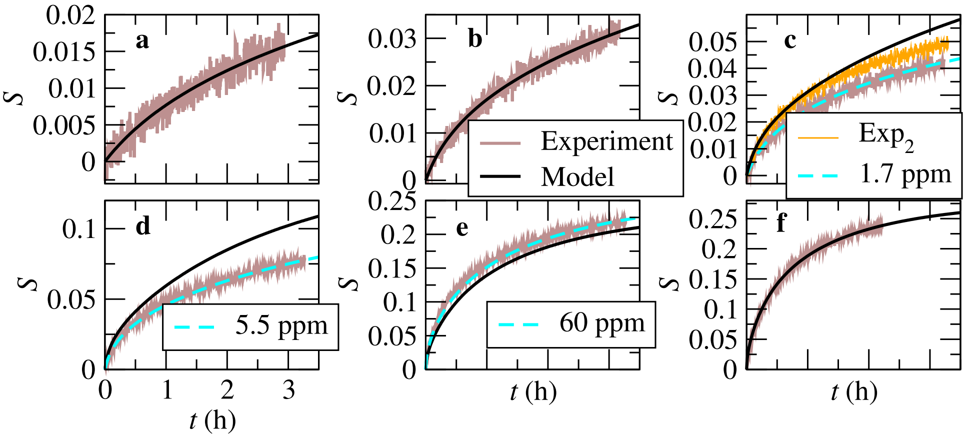

Figure 4.17: Time dependent sensor response for all the measured NO_2 concentrations: (a) 0.3 ppm, (b) 1 ppm, (c) 3 ppm, (d) 10 ppm, (e) 50 ppm, and (f) 100 ppm. Brown curves are the experimental data, black curves the theoretical results, obtained using equation (4.29) for constant $k_{D,S}$. The fitted $k_{A/D,S}(S)$ are shown as green dashed curves in figure 4.16. The agreement between theory and experiment is rather good for all curves. For the fitting sets (0.3 ppm and 100ppm, also denoted as training sets) the agreement is essentially perfect, and also for the test set in (b). For the test sets in (c-e) there are some quantitative deviations between experiment and theory. Theory and experiment can be brought to essentially perfect overlap also for these cases if the calculations are performed for concentrations that slightly differ from the nominal experimental values (dashed cyan curves). We therefore attribute the quantitative deviations in the test sets to slightly different experimental conditions for each measurement run. For example, the orange curves in (c) are for a second experimental run at 3 ppm, and these are significantly closer to the theoretical model, indicating the range of variability in the experimental measurements.

(black lines) to concentrations that are slightly deviated from the experimental conditions for each run (dashed cyan lines). As shown in figure 4.4 the initial surface conditions need to be consistent otherwise the sensor response can be greatly perturbed despite the same concentration. Consequently, figure 4.17c shows two near equivalent experimental responses for 3 ppm NO_2 exposure. The orange curve is significantly closer to the theoretical model which suggests that the initial surface state (measured as ω_0) is not consistent due to competing p-doping gases in atmosphere. Regardless, based on this comparison with the ideal model data we can therefore estimate the variations in the experimental sensor response for a specified amount of NO_2 to be below about 25%.

Finally, the proposed physical origin of the found exponential decrease of the effective sticking coefficient with increasing NO_2 coverage is understood in the context of transition state theory (TST). Within TST chemical reactants must have sufficient energy to overcome an energy barrier to become a product. Therefore, for a NO_2 molecule to bind to the graphene surface, the impinging molecule must have enough thermal energy to overcome the activation energy of binding, E_A, so that one has $k_{A,S} \propto \exp\{-E_\mathrm{A}/k_\mathrm{B}T\}$ [328, 330, 331, 332], where k_B is the Boltzmann constant and T the temperature. In general E_A can depend on n, and with respect to the lowest order one can assume a piece-wise linear dependence such that $E_\mathrm{A}(n) = E_0^* + \alpha n$, as described by the Elovich equation [330]

$$\frac{dn}{dt} = Af(n)P\exp\left(\frac{-E_0^* + \alpha n}{k_B T}\right) \tag{4.30}$$

where A is a pre-exponential factor, $f(n)$ describes the surface coverage term which for the proposed model is $(1-n)$ and P is the collision probability.

Therefore, the observed exponentially large reduction in $k_\mathrm{A,S}$ is attributed with increasing NO_2 concentrations to gradual increases in E_A. This increase of the average E_A with increasing n, and equivalently S, has a number of origins. Since NO_2 molecules are negatively charged upon adsorption on graphene, they repel each other, which is expected to lead to an increase E_A with increasing n. Furthermore, after the initial exposure to NO_2 the binding sites with small activation barriers are statistically more likely to be occupied first (black reaction co-ordinate in figure 4.14), while as time progresses more binding sites with increasingly large E_A need to be occupied. Therefore, the activation barriers for the displacement of O_2 and N_2 shown in figure 4.14 will become bigger as more NO_2 adsorbates 'poison' the graphene surface.

By applying equation (4.10) to the result of the surface coverage model's theoretical results for $S(t)$ with a double exponential, there is good agreement of the fitted S_e, α, and $\tau_{1/2}$ with the ones obtained when the fit is done directly to the experimental data (figure 4.8). Similarly, the effective reaction order (equation (4.13)) resulting from the theoretical $S(t)$ also agrees well with experiment (figure 4.9). This shows that the surface coverage model leads to the experimentally observed time dependent sensor response of seemingly double-exponential form, but that the underlying physical origin is not due to the presence of two distinct adsorption sites with constant properties, but that it is mainly due to the fact that the sticking coefficient decreases exponentially with increasing coverage in a continuous way.

4.5 Chapter Summary and Conclusions

To conclude this chapter, it is shown that a graphene coupled dielectric resonator platform provides a unique gas sensing platform. Using the Microwave Method the graphene sheet resistivity can be measured and compared to other electrical based graphene gas sensors. Moreover, since the use of microwaves is a measurement that does not require electrical contacts, it is possible to directly probe the adsorption of NO_2 molecules on graphene without ambiguity from metal—gas interactions.

From figure 4.9 the NO_2 adsorption occurs in two distinct regimes, a fast initial adsorption followed by a slower process. This, combined with the extrapolation of the sensitivity limit of this particular graphene gas sensor (figure 4.7), results in the most effective operation window for gas sensing measurements is found for 5-35 minutes of exposure. The upper exposure sensing limit is determined by the adsorption kinetics, while the sensitivity and minimum sensing time are determined by the noise in the system and by the graphene—resonator coupling; which can be improved by future optimisation.

A comparison of various fitting procedures and Langmuir based adsorption models were compared, where the surface occupation model relates well the sensors response to the adsorption and desorption kinetics of NO_2 on graphene. The key finding is that the molecular sticking probability decreases exponentially upon increasing NO_2 surface occupation, which is ascribed to an increase of the adsorption energy barrier with increased NO_2 surface coverage. Consequently, the properties of the binding sites vary continuously on the graphene surface, rather than being clustered around discrete values, which is in good agreement with the surface characterisation results.

Of particular importance is the conclusion that the often found double exponential behavior in the sensor response (equation 4.10 and figure 4.8) is usually ascribed to the existence of two chemically different binding environments, which is in contrast to our results for the graphene surface. Indeed most Langmuirian based studies of graphene gas adsorption set k_{A} equal to either a single discrete value (when the concentrations are so low that the surface adsorbates are effectively non-interacting) or to a few distinct values, which vary with gas concentration [304, 305, 306, 307].

To conclude, these findings describe a model which encompasses NO_2 concentrations spanning three orders of magnitude. As such these findings are of benefit for the whole sensor field, and represent an important step in the understanding of the microscopic mechanism of graphene based gas sensing.

Chapter 5

The Open Microwave Cavity: Preliminary Experiments

5.1 Chapter Motivation

In the previous chapter an alternative gas sensing platform that uses microwaves to probe the change in conductivity upon gas adsorption is introduced. Since the microwave method is a large area measurement and does not require contacts, it provides a unique platform for the measurement of fundamental graphene-gas interactions. However, the previous work does not provide any insight upon molecular binding energies nor the form of the charge transfer affinity function $C(n)$. Moreover, the previous microwave gas sensing platform did not allow high temperature measurements nor applying an electric field in a graphene field effect transistor (G-FET) configuration. Therefore, this chapter shows the preliminary measurements associated with an alternative cavity design that allows for temperature and electric field manipulation of the graphene charge carrier density.

First the open cavity gas sensing platform is introduced and shown to be capable of measuring the conductive properties of graphene. Moreover, it demonstrates success as a gas sensor where the adsorption and desorption characteristics of NO_2 are monitored. Using standard rate laws, as shown in this chapter, the energy for an NO_2 molecule to overcome a sorption energy barrier at equilibrium conditions is found to be ~ 0.19 eV from preliminary temperature dependent gas sensing measurements. This result is more remarkable since it is arrived at using separate first approximation models for both the adsorption and desorption data. Unsurprisingly, these models do not adequately reflect the rapid initial sorption processes, however a strategy to model the initial sensor response is described and proposed as a future work activity.

Similarly, graphene samples with a functioning back gate that are designed to be compatible with the microwave measurement described. Moreover, the initial IV curves confirm Dirac behavior. It is shown that by tuning the graphene work function through electrical gating, the adsorption and desorption can be enhanced. Although electric field induced graphene doping and environmental doping of graphene are two distinctly different mechanisms, this preliminary work provides evidence that the charge transfer affinity is dependent upon the doping level of graphene. However, future work is necessary to understand how the electric field interacts with adsorbing gas molecules and distinguish the subtilities between environmental and gate induced doping of graphene. Regardless, it is clear that the sorption can be enhanced and a discussion on how to elucidate the mechanism is discussed.

5.2 Alternative Cavity Design

The gas sensing apparatus described in chapter 4 is designed such that the graphene sample is brought close to the resonator using a low loss plastic holder. Having the sapphire puck and graphene sample enclosed in the copper housing reduces microwave leakage and losses. However, due to the plastic sample holder outgassing at relatively low temperatures, gas sensing measurements at high temperatures were impossible to conduct reliably. Moreover, from the previous section, the relationship between

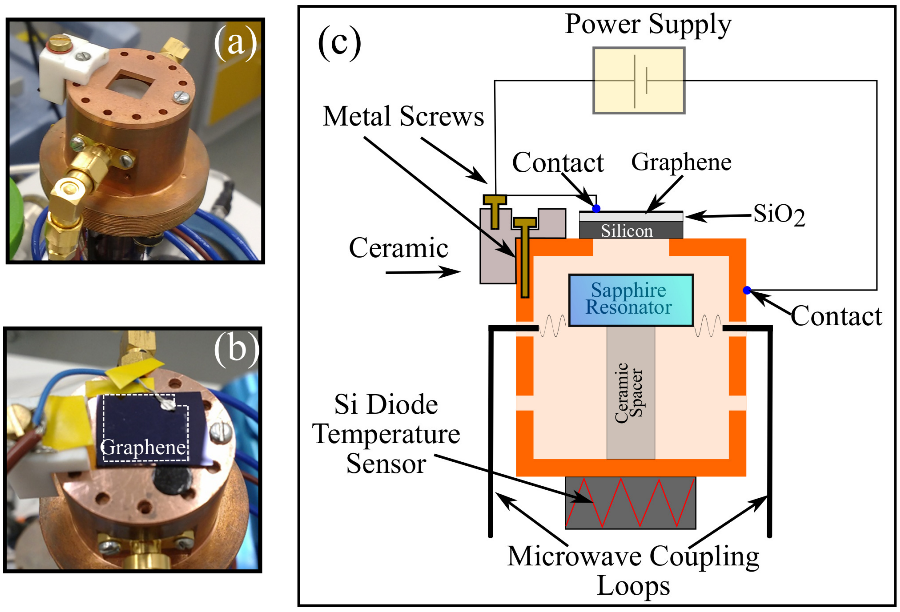

Figure 5.1: The open cavity resonator in the (a) empty and (b) graphene coupled configuration. The white dashed lines highlight the location of 13 x 13 mm wet transferred graphene sample. The sample has been secured to the copper lid using carbon tape and a single silver paint contact connects the graphene surface to the power supply. Electrical tape is used to ensure that there are no accidental shorting between the graphene contact wire and the copper housing. (c) Is a detailed schematic showing the open cavity resonator design, capable of gating simply by securing the silicon substrate to the lid of the copper housing, which in turn is connected to the power supply.

the sensor response and the charge transfer affinity is defined as $S(n) = c(n)n$, where c(n) is assumed to be a monotonic function (this is discussed further in section 5.4). However, the true nature is likely to depend upon the degree of doping of the graphene sheet, which for environmental sensing depends upon the surface coverage of adsorbate species. Previous studies have shown that charge transfer is improved when the graphene work function is located close to the HOMO/LUMO molecular orbitals [252] and indeed the work function of graphene itself impacts the sensor responsivity [74, 333]. To summarise, the work function of graphene can be altered through substrate induced doping [194, 257, 258], environmental doping [26, 334], chemical functionalisation [127, 335, 336] and via the electric field effect [188].

Therefore, to investigate the relationship between the sensor response of graphene and the charge transfer affinity, electrical gating is used in addition to environmental doping to assess the graphene character. To achieve this, an open cavity resonator design, where the graphene sample is strategically placed over a square hole in the center of the copper cavity lid is adopted [215, 337]. As a result, the graphene still interacts with the same resonant mode as the previous cavity resonator. An additional benefit of this configuration is the removal of the plastic sample holder, which enables measurements at higher temperatures.

The graphene sample is comprised of CVD graphene transferred onto high resistance (>10 kΩ) silicon with a thermally grown oxide of 100 nm purchased from Inseto (UK) Limited. Figures 5.1a and b show the open resonator system with and without graphene positioned over the square hole respectively. Figure 5.1c is a schematic illustrating the key components of the new geometry. The high resistivity silicon substrate is brought into contact with the copper housing, which is connected to a Rigol DP32A power supply forming the back gate connection. Gating is achieved by dropping a voltage across the SiO_2 dielectric. To prevent shorts, a ceramic piece is screwed to the lid which electrically isolates the graphene contact from the copper housing. To ensure the graphene is still coupled to the microwave mode, the sapphire resonator is raised using a ceramic spacer. In this configuration the backside of the substrate, not the graphene surface, interacts with the most intense portion of the evanescent field. This is to minimise the electrical contact surface area with graphene, since electrically gating such a large graphene area is more prone to dielectric breakdown. This is explained in detail in appendix A.8.

To experimentally evaluate the quality of the graphene—resonator coupling, ceramic spacers of lengths 10, 12 and 14 mm (with a resonator to lid gap of 6, 4 and 2 mm respectively) were compared by evaluating the linewidth and frequency shifts of the

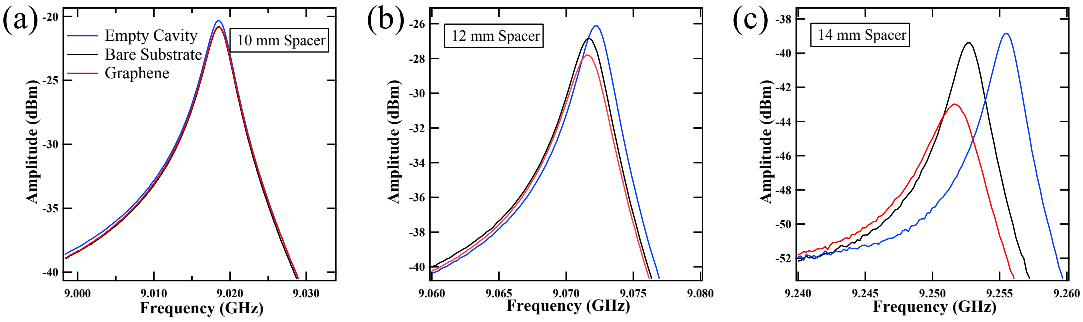

Figure 5.2: Comparison of the microwave measurements in the open cavity configuration using different spacer lengths at (a) 10 mm (b) 12 mm and (c) 14 mm. Although insertion loss increases as the resonator is positioned closer to the copper lid, the graphene—resonator coupling improves.

three Microwave Method configurations (see section 4.2 of chapter 4). Unsurprisingly, figure 5.2a shows that the resonator is too far away from the graphene when the 10 mm resonator is used, since there is no frequency shift observed. In other words, the dielectric substrate barely interacts with the resonant electric field. The 12 mm and 14 mm spacers (figures 5.2b and c) shows continued improvement such that the substrate (graphene) perturbs the frequency (linewidth) by a significant amount. Although decreasing the resonator—sample distance improves coupling, unfortunately the increased proximity to the hole worsens the insertion loss due to increased microwave leakage through the sample. Therefore the 14 mm ceramic spacer resulting in figure 5.2c is used in the following measurements because of the increased sensitivity to the broadening peak shape in the presence of graphene.

Figure 5.3 measured the change of (a) frequency and (b) linewidth of the resonant TE_{011} mode of the open cavity and the open cavity loaded with a graphene sample. To preserve the sample which was fixed to the lid of the resonator, a spare copper lid of equal dimensions is used to measure the empty cavity response resulting in a slight offset in the resonant mode as shown in figure 5.3c. Regardless, both the resonant frequency of the empty and loaded cavity decreases as the temperature

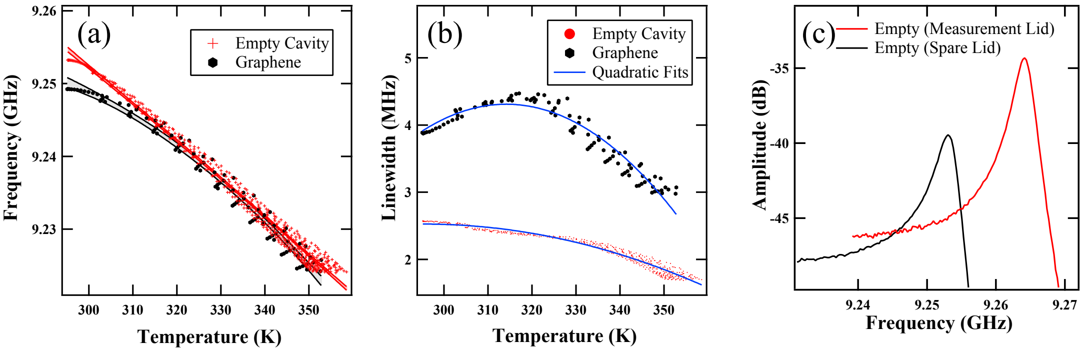

Figure 5.3: The resonant (a) frequency and (b) linewidth of the open dielectric resonator upon increasing temperature. (c) The trace of the copper lid used for each measurement showing slight deviation without the graphene sample.

increases. Figure 5.3a shows both curves are fitted using a quadratic polynomial with the confidence bands of the fit plotted alongside, although this fit is more a guide for the eye. It should be noted that the 'jump' in data sets is due to the PID of the Conductus LTC20 temperature controller, gently oscillating around the target value. This is due to the temperature controller being designed for room temperature and cryogenic measurements, such that high temperature measurements are at the limit of this sensors capabilities. There are many contributions for the resonant frequency response with temperature; including the relative movement of the sapphire puck to the copper housing due to thermal expansion. In addition to this, the temperature coefficient of the resonant cavity are dependent upon the thermal lattice, dielectric and permeability constants [338] where the dominant contribution arises from the change in permittivity with temperature [339, 340]. The additional frequency shift at low temperatures of the graphene loaded cavity, may arise from the change in silicon conductivity changing the microwave skin depth rather than the graphene itself which due to its atomically flat nature shouldn't perturb the frequency greatly [215, 313].

Interestingly, the temperature variation of the resonant linewidth of the graphene sample is much more pronounced than the empty resonator. The broadening of the graphene linewidth before sharpening can be attributed to the thermal excitation of the

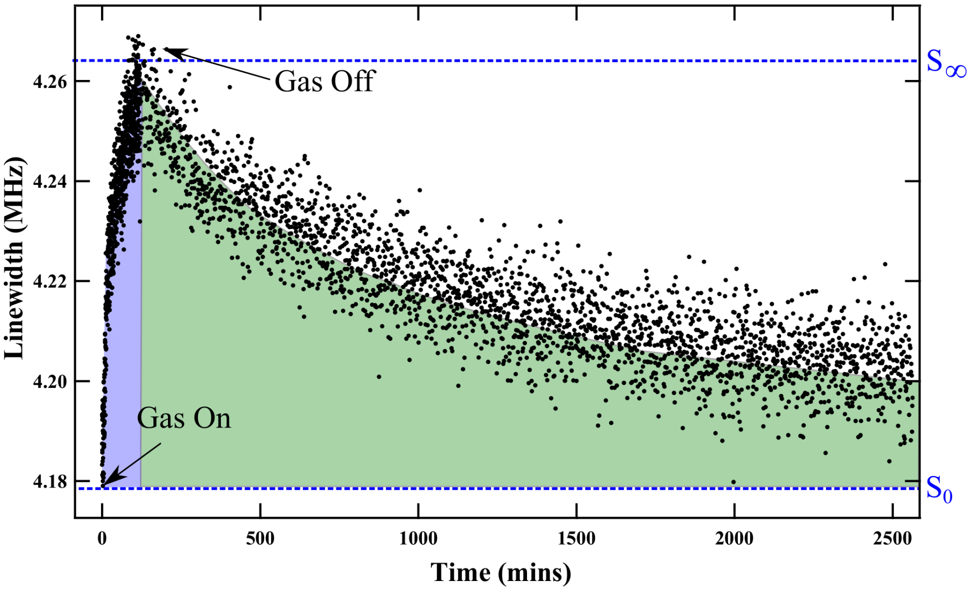

Figure 5.4: The adsorption (blue area) and desorption (green area) of 3 ppm NO_2 measured using the open cavity configuration at 295 K. The blue dashed lines estimate where the location of S_∞ and S_0 upon converted to sensor response terms.

charge carriers increasing conductivity, followed by the increased probability of scattering with other carriers and excited phonon modes due to the high temperature and graphene substrate interactions [341, 342]. This is similar to the typical conductivity response of semi-conducting metal oxide devices [343].

Finally, figure 5.4 demonstrates the applicability of the open cavity design as a gas sensor upon exposure to 3 ppm NO_2 gas kept at 295 K. The characteristic lineshape of both the adsorption (blue region) and desorption (green region) is highlighted and clearly distinguishable. As before in the previous enclosed cavity gas sensing measurements, the cavity is isolated in a chamber that is kept at a consistent temperature and NO_2 is introduced into the system as before. Explicitly, the gas diffuses into the chamber, interacts with the graphene and diffuses through the outlet. Due to the long desorption timescales, after the adsoprtion measurement is complete, the NO_2 gas valve is closed and the system is flushed with synthetic air for 10-15 minutes (at the same flow rate) before the system is exposed to lab air.

Using this alternative methodology and cavity configuration, the sequential sections investigate the combined adsorption and desorption behaviour at different temperatures and chemical potentials of graphene through electrical gating. As a result, the following work demonstrates the preliminary measurements elucidating the role of the desorption coefficient and an estimation of the lower and upper limits of the binding and activation energies involved with the sorption kinetics of NO_2 and graphene respectively. By varying the work function/ chemical potential of graphene through gating, enhanced desorption timescales is achieved and, more fundamentally, the importance of the charge transfer probability function (assumed to be 1 in the previous section) is discussed.

5.3 Adsorption and Desorption Temperature Variation

Utilizing the open cavity configuration, the adsorption and desorption of 3 ppm NO_2 gas is measured at 295, 313 and 353 K. After each temperature is reached, it is kept constant for at least five minutes to allow the system to reach thermal equilibrium. Once the temperature and PID is stable, 3 ppm of NO_2 gas is flowed through the system for 2 hours. From chapter 4 (figure 4.9) it is clear that the rapid adsorption regime lasts for approximately 30 minutes, therefore two hours is considered a sufficient length of time for gas exposure to efficiently capture the sorption characteristics. Figures 5.5a and b compare the change in linewidth with respect to the adsorption and desorption of NO_2. Interestingly, as the temperature increases both the rate of adsorption and desorption increase. This is consistent with previously measured temperature dependent graphene gas sensors [315, 344, 345, 346]. More broadly, thin film metal oxide gas sensors exhibit similar behaviour, whereupon increasing temperature first increases then decreases the sensor responsivity. This is partially due to increased absorption of the gases into the thin film material and the more dominant sorption processes and kinetic limitations [343]. It is assumed that graphene sensors only rely on surface sorption interactions. This is a reasonable assumption since graphene has been shown to be impermeable to lithium ions [347]. Consequently, it is unlikely that NO_2 can permeate through the graphene even if it dissociates into its constituent atomic species.

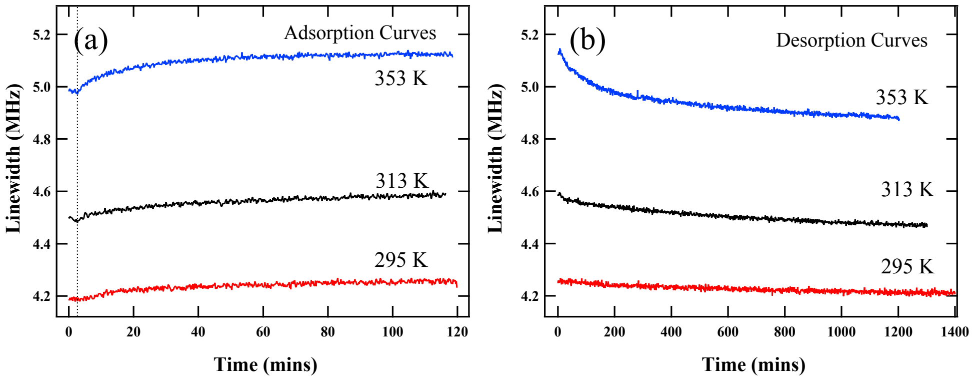

Figure 5.5: The change in linewidth during (a) adsorption and (b) desorption of 3 ppm NO_2 gas at 295, 313 and 353 K. Measured using the Least Squares Method (LSF) method. The dashed line corresponds to the time the inlet valve is opened to NO_2.

During each measurement, the graphene sensor is exposed to gas immediately upon reaching the target temperature. As a consequence, aside from the 295 K measurement, the high temperature measurements do not start with the system in sorption equilibrium with its initial surroundings. However, the benefit of exposing the system immediately to gas once temperature is reached, ensures that the initial surface coverage of NO_2 molecules is similar for each measurement. Therefore, a unique ω_0 value is established for each temperature using equation (4.9) to define the sensor response ($S(t) = (\omega_0 - \omega(t))/\omega_0$). This differs from chapter 4 where ω_0 is an easily reproducible value which is kept constant throughout all the concentration measurements. Therefore, for the high temperature measurements, ω_0 is determined such that the sensor response at sorption equilibrium in the absence of NO_2 is zero - in other words $S_0 = 0$. To achieve this, after the desorption sensor response is calculated, it is empirically fitted to a double

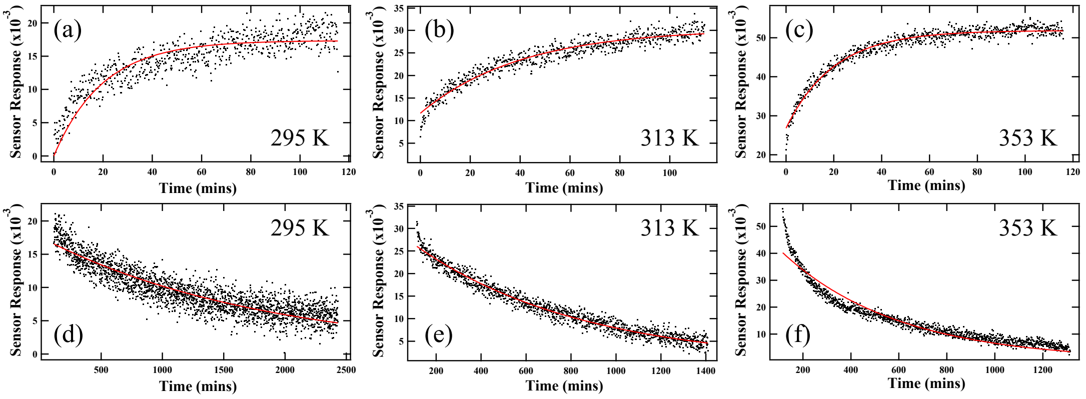

Figure 5.6: The sensor response characteristics of (a-c) adsorption and (d-f) desorption sensor response of graphene exposed to 3 ppm of NO_2 gas at 295, 313 and 353 K. The red fits correspond to equations (5.1) and (5.2) for adsorption and desorption respectively.

exponential and all the data is offset such that the maximum amplitude becomes 0. Figure 5.4 schematically shows the location of S_0 and S_∞ which corresponds to the graphene sensor in sorption equilibrium with the environment in the absence and presence of NO_2 molecules respectively.

Figure 5.6 shows the (a-c) adsorption and (e-f) desorption sensor responses of the three temperatures studied. The sensor response for each temperature set is determined by first calculating S_0 by empirically fitting the desorption data with a double exponential curve and determining ω_0 from the offset as $t \to \infty$. As a first approximation, the adsorption measurements are fitted with the solution to the unmodified Langmuir model (see equation (4.18) of chapter 4) as follows:

$$S_{ads}(t) = \frac{n_G k_{\mathrm{A,S}}}{k_{\mathrm{A,S}} + k_{\mathrm{D,S_\infty}}} \left(1 - e^{\left(-(n_G k_{\mathrm{A,S}} + k_{\mathrm{D,S_\infty}})(t-t_0)\right)}\right). \tag{5.1}$$

The desorption measurements, which do not depend on vacant adsorption sites, are fitted using the standard description of desorption [345, 348].

$$S_{des}(t) = Be^{-k_{\mathrm{D,S_0}} t}. \tag{5.2}$$

The t_0 term compensates an offset for the high temperature adsorption measurements, since the measurement does not start at sorption equilibrium. Interestingly, the desorption rate constants $k_{\mathrm{D,S}_\infty}$ and $k_{\mathrm{D,S}_0}$ corresponding to the adsorption and desorption fittings are an order of magnitude different. Therefore these parameters reflect two different desorption time scales. The implications of which are discussed further in this section.

The fittings of figure 5.6 clearly do not capture the rapid initial sensor responses. This is unsurprising since the previous work established in chapter 4 suggests that the sticking probability coefficient is non-constant during the adsorption process. Similarly, the desorption data suggests that the desorption constant is non-constant throughout the full desorption process. Regardless, these models provide a remarkably good first approximation describing the sorption interactions between graphene and NO_2. Particularly as the sensor reaches sorption equilibrium in the presence and absence of NO_2 for the adsorption and desorption measurements respectively. Figure 5.7 compares the pre-exponential factors of the adsorption and desorption measurements showing that the sensor response increases with the temperature. As mentioned above, from previous work it is expected that sensor response will decrease after reaching a threshold temperature [315, 343, 344, 345, 346].

The temperature measurements at 353 K are least well described by the sorption equations used to fit figures 5.6c and f. This is due to the initial rapid sorption slopes and the desorption constants differing by an order of magnitude when modeling the adsorption and desorption processes with equations (5.1) and (5.2) respectively. To visualise the extent of this disparity, figure 5.8 compares solutions to the (a) adsorption and (b) desorption response using a value of $k_{\mathrm{D,S}}$ that best fits adsorption (desorption) range given by the blue (red) fitted curves. Interestingly, using the value of the desorption constant that best describes the adsorption of NO_2 using equation (5.1)

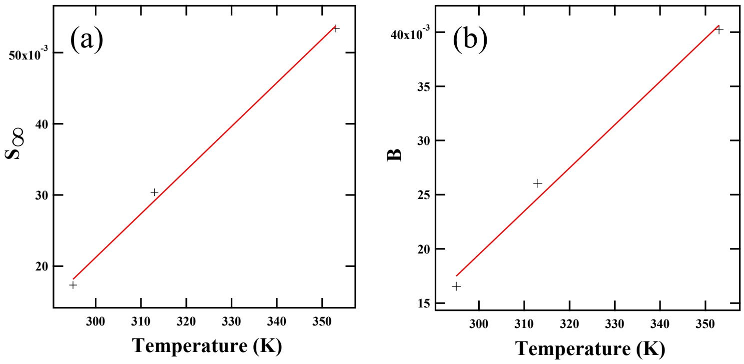

Figure 5.7: Comparison of the sensor response at sorption equilibrium with (a) the NO_2 environment and (b) the air environment corresponding to equations (5.1) and (5.2) respectively where $S_\infty = (n_G k_{\mathrm{A,S}})/(n_G k_{\mathrm{A,S}} + k_{\mathrm{D,S}_\infty})$. In both cases for this small temperature range, increasing the temperature increases the sensor responsivity.

(i.e. $k_{\mathrm{D,S}_\infty}$) into equation (5.2), it can be seen to capture the rapid initial desorption as shown in figure 5.8b. Similarly, the reverse also appears to give an equivalent result. Explicitly, using the value of the desorption constant that best describes the desorption of NO_2 using equation (5.2) (i.e. $k_{\mathrm{D,S}_0}$) into equation (5.1), it can be seen to capture the rapid initial adsorption characteristics as shown in figure 5.8a. In other words, using the value of the desorption constant appropriate to describe the sensor response as it approaches sorption equilibrium with the NO_2 environment where $S_{ads}(t) \rightarrow \infty$, the initial rapid decline in sensor response describing the desorption characteristics is approximated. Clearly the inverse can also be demonstrated, hence the assignment of the notation $k_{\mathrm{D,S}_\infty}$ and $k_{\mathrm{D,S}_0}$ to describe the adsorption and desorption characteristics as they approach sorption equilibrium with the NO_2 and ‘clean’ air environments respectively. It is suspected, that this is evidence towards a desorption constant that is dependent upon the surface coverage of NO_2 adsorbate species. This is akin to the previously established concept where the sticking probability decreases as the adsorption reaction proceeds. Moreover, the combined analysis of the adsorption and desorption characteristics and their two distinct desorption constants could be suggestive of why a double exponential provides a good empirical fit to the sorption

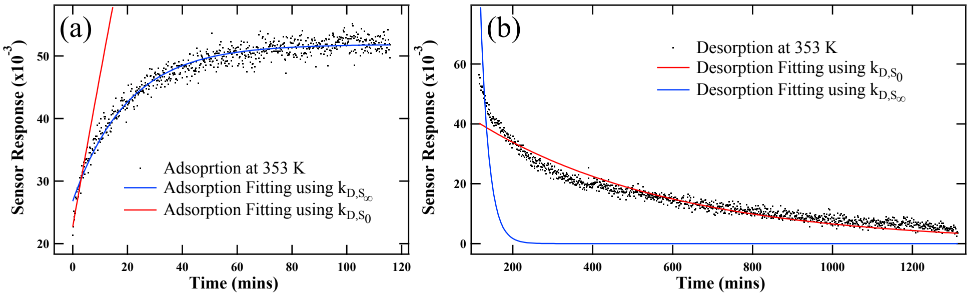

Figure 5.8: The sensor response of the (a) adsorption and (b) desorption of 3 ppm NO_2 gas at 353 K. The blue (red) curves correspond to solutions of equations (5.1) and (5.2) using the value $k_{\mathrm{D,S}_\infty}$ ($k_{\mathrm{D,S}_0}$) as the value used for both desorption constants.

processes. However, more temperature measurements and a more robust theoretical model are required to confirm this.

Further to this, using the Arrhenius relationship, the rate of sorption is proportional to some activation energy barrier where $k \propto exp(-E_a/(k_B T))$. Since the rate of adsorption and desorption is proportional to $k_{\mathrm{A,S}}$ and $k_{\mathrm{D,S}_0}$ respectively, an estimation of the activation energy barrier of adsorption and desorption as the system approaches equilibrium conditions provides a lower and upper limit respectively. Conceptually, a hotter surface provides more kinetic energy to the molecules promoting enhanced adsorption and desorption. However, if the surface becomes too hot, the molecules will acquire too much thermal energy such that the potential well will no longer be able to contain the molecule such that no adsorption is possible and only desorption will occur. Plotting $ln(k_{\mathrm{A,S}})$ and $ln(k_{\mathrm{D,S}_0})$ against the reciprocal temperature allows extraction of the adsorption and desorption barrier respectively. From figure 5.9b and c the adsorption energy barrier at sorption equilibrium is 0.190 ± 0.093 eV and the energy required to desorb from the surface is 0.193 ± 0.076 eV. The significance of producing similar barrier heights is due to both process describing equilibrium conditions i.e. $NO_2(ads) \rightleftharpoons NO_2(g)$ where the forwards reaction describes the desorption process and backwards reaction corresponds to the adsorption process.

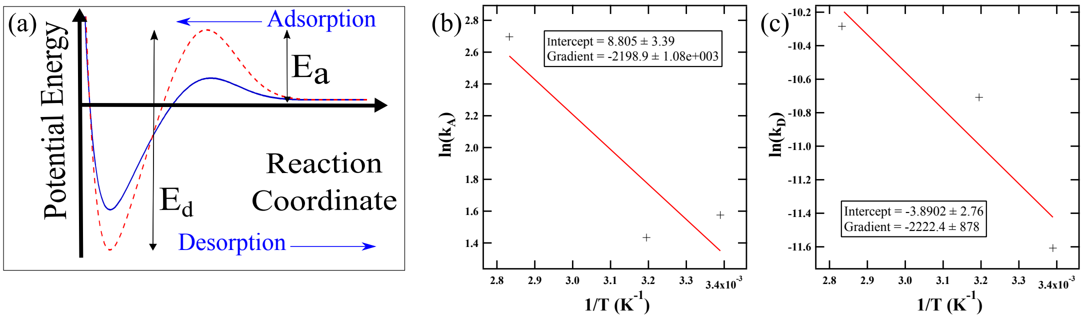

Figure 5.9: (a) A schematic of the adsorption and desorption reaction coordinate indicating the presence of an adsorption energy barrier. The heights of both are dependent upon surface occupancy. Plots of (b) $k_{A,S}$ and (c) k_{D,S_0} against reciprocal temperature are used to extract the barrier heights.

Figure 5.9a is a schematic of the sorption reaction co-ordinates describing the energy landscape encountered by a NO_2 molecule in the vicinity of a graphene surface. An approaching NO_2 molecule requires sufficient energy, E_a, to overcome some energy barrier in order to adsorb onto the graphene surface. A succesfully adsorbed species will be trapped in the potential well where the depth of the potential well is indicative of the surface binding energy. Therefore, for successful desorption a molecule must have sufficient energy, E_d, to escape the well. The dashed lines indicate the well and barrier heights are non-constant and it is expected that they change depending on surface coverage.

A final comment before the conclusion of this section is with respect to the sample integrity throughout the temperature measurements. Figure 5.10 shows the overall decline in conductivity (i.e. decreased linewidth) after the high temperature measurements by comparing the microwave gating characteristics at 295 K. A full discussion of electrical gating of the microwave set up is provided in the following section. The decrease in linewidth is suspected to be due to typical thermal annealing effects, whereupon the graphene better adheres to the substrate increasing graphene–substrate interactions and ultimately increasing the number of scattering centers a graphene

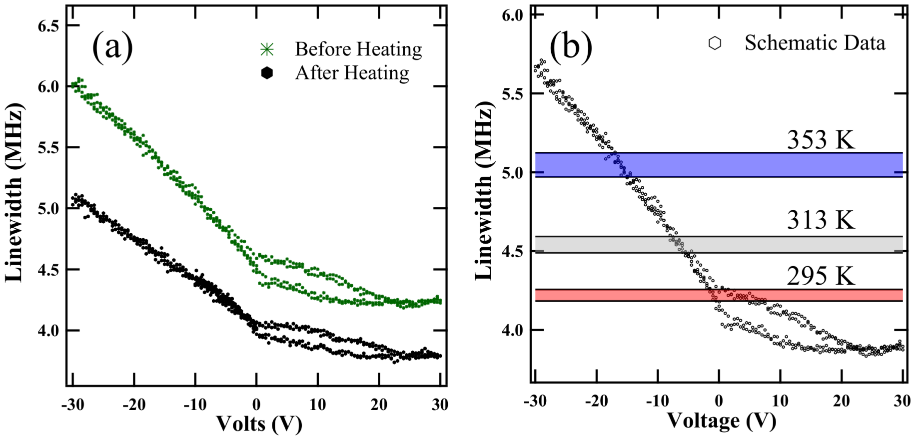

Figure 5.10: (a) The measured Dirac characteristics using the 3dB method before and after thermal treatments. (b) Schematic data points that correspond to the linewidth measured using the 3dB method (not the LSF Method) and are manually offset by 0.35 MHz, which is the offset required to match the 3dB and LSF measurements at 295 K. Since the gas sensing measurements use the LSF method and the gating measurements use the 3dB method, this figure is an approximate representation of how the change of linewidth during gas sensing matches the electrically gated slope. This figure is intended as a guide only, where the shaded areas correspond to the change in linewidth of the different measurements. See chapter 2.6.3 for a comparison of the 3dB and LSF methods.

electron encounters thus reducing the overall graphene conductivity [299]. However, figure 5.10a is measured using the 3dB method not the more accurate LSF method (see chapter 2 section 2.6.3 for details). Consequently, comparing the temperature gas sensing measurements to the gating measurements is not possible. Ideally, it would be interesting to evaluate how the temperature gas sensing measurements compare to the microwave 'Dirac' characteristics. Figure 5.10b uses schematic not real data to hypothetically suggest how the increased temperature excites the graphene electrons and how this thermal excitation changes the conductivity.

To conclude this section, these preliminary measurements provide a first approach to describe the sorption kinetics of NO_2 on graphene. Remarkably, equations (5.1) and (5.2) used to fit the adsorption and desorption data at various temperatures results in similar sorption barrier heights of $\sim$ 0.19 ev per molecule. This is consistent with the assignment that the models describe the relevant sorption processes as they approach equilibrium conditions. Therefore, providing a limit to the barrier heights. Following this, future work will include the sorption measurements at higher temperatures and the further development of an adsorption and desorption model which takes into account the variation of $k_{\mathrm{A,S}}$ and $k_{\mathrm{D,S}}$ during the sorpiton processes. From this work, the range of binding energies of NO_2 on graphene can be experimentally measured and compared to the many theoretically obtained values. More importantly, through the development of these sortpion models, a better description of the initial sensor response kinetics can be achieved which is of relevance to sensor applications. Finally, from a more robust temperature study, the optimum temperature of sensor operation for NO_2 sensing can be ascertained.

5.4 Preliminary Gas Gating Measurements

The following section demonstrates the gating functionality of the open cavity configuration. As stated previously, it is suspected that the sensor response is dependent on the charge transfer probability function such that $S(t) = c(n_c(t))\, n_c(t)$, where the subscript "$c$" explicitly denotes that the dependence of the NO_2 surface coverage on the function $c(n)$. As a consequence, the sticking and desorption coefficients are also dependent on $c(n)$ such that $k_A(n) \approx f(c(n))\, k_{\mathrm{A,S}}(c(n)\, n)$ and $k_D(n) \approx g(c(n))\, k_{\mathrm{D,S}}(c(n)\, n)$ (see supplementary section of ref. [89]).

In all gas sensing measurements it is assumed that $c(n) = 1$. However, a non-constant $c(n)$ function can be caused by the fact that the charge transfer per NO_2 molecule to graphene is reduced as more molecules adsorb and increase the electrostatic repulsion interactions between transferred electrons. Despite this, for all previous experiments considered in this thesis so far, the graphene is lightly p-doped prior to gas exposure

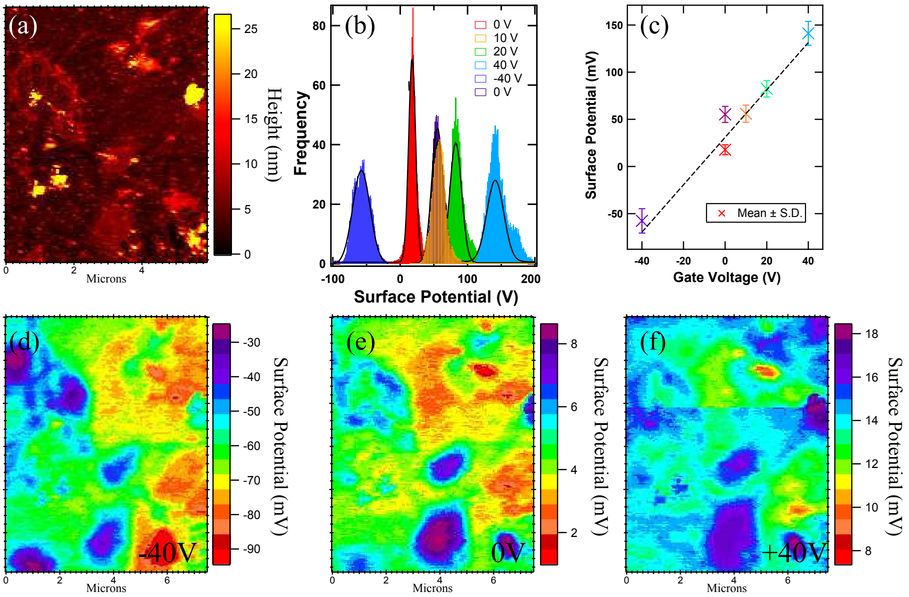

Figure 5.11: (a) AFM micrograph of graphene transferred onto a SiO_2/Si substrate. (b) Histograms of the surface potential of graphene at different gate voltages. Each histogram is fitted using a normal distribution where (c) plots the mean value ± one standard deviation, the dashed lines shows the linear relationship and the shift at zero is consistent with hysteresis effects. Representative KFM images with a back gate at (d) -40 V, (e) 0 V and (f) +40 V dropped across the dielectric of the same graphene area are compared.

such that this variation is small and continuous. The lowest possible range of $c(n)$ is set by the largest measured sensor response. From figure 4.7a in chapter 4, the maximum sensor response for 100 ppm NO_2 is around 0.26 such that $c(n) \geq 0.26$. Moreover, $S(t)$ appears to still be rising therefore it is expected that the maximum $c(n)$ is somewhat larger. The maximum $c(n)$ has to be of the order of one, which describes a system where the change in surface coverage leads to an equal change in sensor response.

Interestingly, figure 5.11 shows the linear relationship of the surface potential of CVD graphene on silicon with a 90 nm oxide with an applied gate voltage. Surface potential histograms of the same graphene region are acquired using KFM (figure 5.11b) . The mean of each distribution is plotted against the applied gate voltage in figure 5.11c, which is fitted by a line with a gradient of 0.0025 (dashed line). A cropped region of the representative KFM measurements at -40, 0 and 40 V (figures 5.11d-f) corresponding to the same region of the AFM micrograph (figure 5.11a). Since the measured surface potential scales to the difference in work function between the tip and sample, for this particular sample this gradient corresponds to 2.5 meV/V. As a result, the c(n) function should have a mild linear dependence upon the degree of graphene doping, since the work function is effectively a description of the energy required to 'transfer' an electron.

In addition to this, in the following work it is shown, by tuning the graphene work function via the electric field effect, the charge transfer affinity of graphene can be tuned to *enhance either the adsorption or desorption response of the graphene sensor*. The following section briefly describes the graphene/substrate requirements for successful microwave gating, parameters of the microwave measurements that are dependent on the gate voltage and finally the gas sorption measurements dependence on the gate voltage.

5.4.1 DC Gating Characterisation Measurements

To have a microwave compatible G-FET device, CVD graphene is transferred onto a high resisivity (> 10 kω cm) silicon substrate with a 100 nm thermally grown oxide to act as the dielectric gate. To prevent dielectric breakdown while gating a large area, it is found that a 100 nm oxide thickness is needed. Appendix A.8 discusses in detail these sample considerations. This G-FET configuration arose since Si/SiO$_2$ transistors are a well established research field, CVD graphene on silicon is a well studied graphene system and the fabrication procedure well established.

Using a two probe DC measurement, figure 5.12 shows the (a) the linear response of the probes in contact with graphene and (b) the silicon substrate response. In both cases

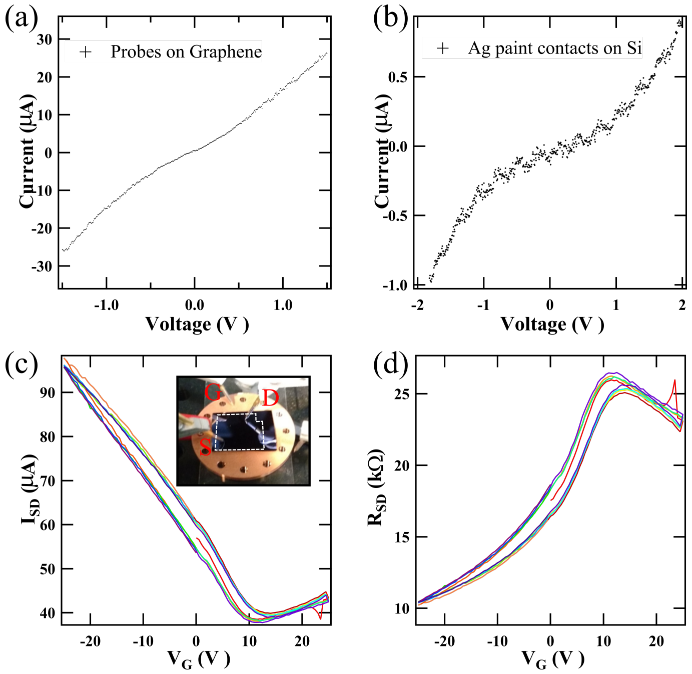

Figure 5.12: IV characteristics of (a) the graphene sheet (b) the silicon substrate via silver paint contacts. The slight Schottky behaviour is due to the silver silicon interface. FET characteristics of graphene showing (c) current and (d) calculated resistance. The current was driven at 1 V. The inset is the sample measurement configuration where the dashed white lines indicate the graphene area (approximately a 13 x13 mm square).

the 'S'-shape, more prominent in the latter, is due to contact resistance through the probes and silver paint respectively forming a Schottky barrier with pure silicon. Figure 5.12c and d show the FET characteristics in terms of the measured source drain current and calculated resistance respectively. Since the dimensions of the graphene sheet are approximately square (13 x 13 mm) the source drain resistance should approximate the graphene sheet resistance. Explicitly, since this measurement was determined using a two probe measurement, this poor geometry coupled with the probe contact resistances infers this is not an absolute measurement. However, it does show a functioning back gate and the location of the Dirac point at approximately 11.5-13.5 V. The measurement hysteresis is typical of Si/SiO$_2$ substrates (See appendix A.8 for details). Using equation (2.9) from chapter 2 ($\mu = (\partial I_{SD})/(\partial V_g) = L/(W C_g V_{SD})$) the hole and electron mobility is calculated to be 46.73 and 10.94 cm^{2}V^{-1} s^{-1} respectively. The large asymmetry between the hole and electron mobilities can be attributed to charge trap states and/or drift from charged impurities of the SiO_2 substrate [255, 205, 349].

5.4.2 Microwave Gating

After establishing the location of the charge neutrality point using DC measurements, the same sample is inserted into the open cavity set up as shown in figure 5.1. A gate voltage is swept back and forth between −25 and +30 V while continuously measuring the properties of the resonant peak. Figure 5.13 shows the resonant (a-c) frequency and (d-f) linewidth of the empty open cavity, bare substrate and graphene on substrate respectively. Unsurprisingly, after an initial drift of frequency, the resonant frequency and linewidth of the empty cavity are constant at approximately 9.2637 GHz and 3.17 MHz respectively. Interestingly, despite the silicon being lightly doped, the frequency (linewidth) increases (decreases) upon increasing the charge carrier concentration via electrical gating. The magnitude of the change in linewidth is $\approx$ 150 kHz. This is due to the increased concentration of charge carriers being driven by the electric field which broadens the lineshape due to losses. The symmetrical linear slopes of best fit around 0 V confirms that the sample is ever so slightly n-doped, since the symmetry is not quite at 0 V. The slight change in resonant frequency of $\sim$ 30 kHz is suspected to be the result of static charge build up at the dielectric interface.

Similar to Adabi et al. [337], the linewidth change of the graphene sample shows Dirac-like behaviour. Reporting a charge neutrality point around 20 V in contrast to the $\sim$ 12 V Dirac point measured in figure 5.12. This shows an increase in p-doping which is suspected to be due to environmental doping during transportation of the sample between measurements. However, to confirm this the sample will need to be remeasured using the probe station. Strikingly, the microwave measurement reproducibly captures the steep slope at negative gate voltages and the hysteresis

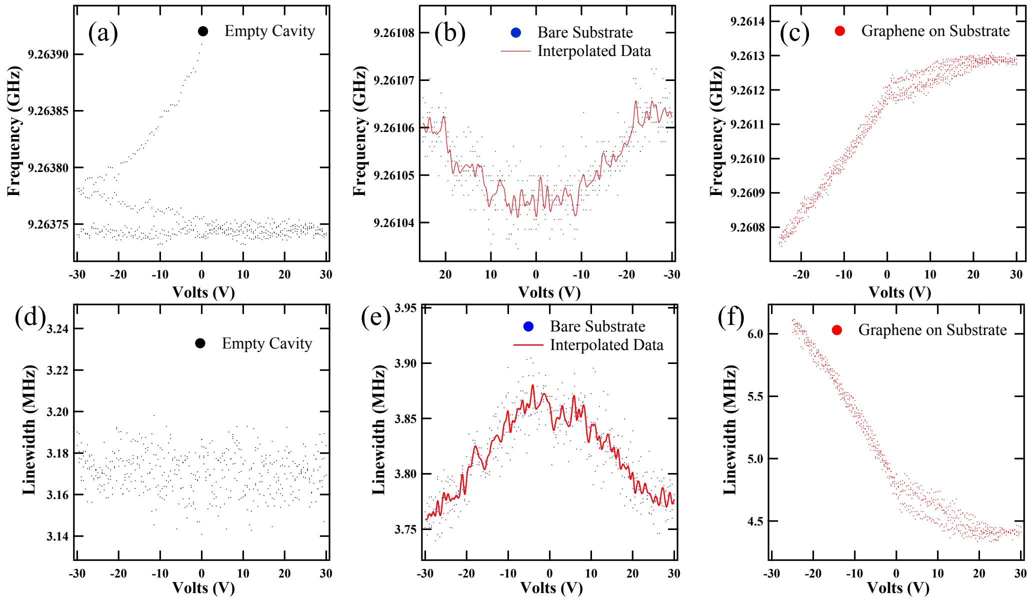

Figure 5.13: The gate induced microwave response of the (a-c) frequency and (d-f) linewidth of the resonant cavity mode. The initial decrease in the resonant frequency of the empty cavity (a) is an initial drift that settles at around 9.263745 GHz. The red line shows the averaged responses of the bare substrate (b, e). It should be noted that the graphene response is significantly larger than the bare substrate response.

at positive voltages. It is important to note that the shift in resonant frequency and linewidth of the graphene sample has a much larger gating response than that of the bare substrate. Unfortunately, the increase in resonant frequency is an artifact from the automatic 3dB measurement method inbuilt in the Anrtisu VNA not being able to correctly measure the peak of the resonant mode. Therefore, a least squares fit procedure is necessary not only to improve sensitivity for the gas sensing measurements, but to also accurately measure the resonant peak properties (see chapter 2 section 2.6.3 for more details).

Qualitatively, upon increasing gate voltage, the relative permittivity of SiO_2 is expected to decrease [350, 351] since, the relative permittivity depends upon the capacitance across the substrate i.e. $\epsilon' = (Ct_{ox})/(\epsilon_0 A) = (Qt_{ox})/(\epsilon_0 AV)$ where C is the capacitance of SiO_2, t_{ox} the oxide thickness, A the area of the dielectric layer, V the voltage and Q

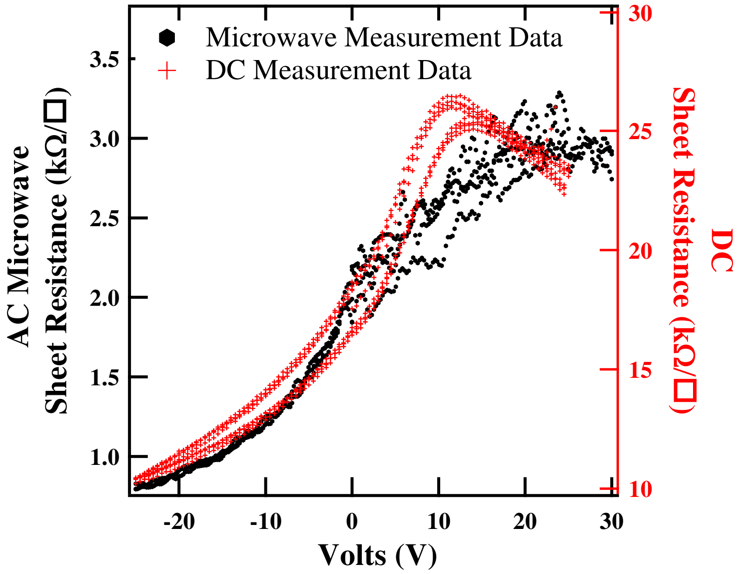

Figure 5.14: Comparison of the AC and DC measured sheet resistances of the same graphene sample. The Dirac point shifts between the DC and AC measurements primarily due to environmentally induced p-doping associated with sample transportation. The discrepancy between resistivity values is suspected to be due the AC impedance of the graphene sheet having a frequency dependence.

the charge accumulation at the dielectric interface. As a result, from equation (4.1) the resonant frequency should increase upon increasing voltage. This is seen with the more accurate LSF fit as shown in figure 2.17 in chapter 2. Therefore, all future measurements are more accurately measured using this methodology.

Using the interpolated frequency and linewidth data of the bare substrate measured from figure 5.13b and c, the graphene sheet resistance is calculated using equation (4.8). Figure 5.14 compares the AC and DC measured sheet restances from figure 5.12f and figure 5.12d. Although the absolute sheet resistivities measured differ by at least an order of magnitude, the comparison of the overall shape is useful for evaluating the position of the Dirac point, the gradient of the hole mobility slope and perhaps sensitivity issues of the microwave method at low carrier conductivities. The reason for the differences in sheet resistivity magnitudes for the AC and DC measurements can include the following: firstly, using a two contact approach to measure the DC sheet resistance means that contact resistances are not negligible. Secondly, this DC contact geometry results in a non-uniform electric field across the graphene sample, which could be resolved four terminal measurement (such as a Van der Pauw measurement) which would produce a more reliable result. Thirdly, AC measurements do not need the sample to be continuous, whereas in DC measurements the current is required to flow through high resistance paths such as wrinkles and grain boundaries.

Despite the discrepancies in resistivities, the Dirac behaviour has been adequately captured using the microwave method, where the DC measurement confirms the integrity of the dielectric oxide layer. Interestingly, figure 5.14 clearly shows that as the charge neutrality point is approached during the microwave measurements, at high positive gate voltages the signal becomes noisy. This is due to the sensitivity of microwave method decreasing as the conductivity decreases. Since the microwave method is the measurement of the change in linewidth, when the conductivity of graphene decreases (increases) the broadening of the linewidth is smaller (larger) and the measurement less (more) sensitive. One way to improve the sensitivity is to reduce insertion loss by improving resonator-microwave coupling by repositioning the coupling loops, reducing the length of the microwave cables and turning the sample upside down to improve graphene-resonator coupling. This was not tried in this study to prevent dielectric breakdown due to large contact area [352, 353]. However, appendix A.8 shows the preliminary control measurements that suggest a 100 nm dielectric thickness is robust enough for the microwave measurement configuration.

5.4.3 Initial Gate Modulated Gas Sensing Results

To conclude this section chapter, figure 5.15 shows the initial gate modulated graphene gas sensor measurements. Figure 5.15a compares the Dirac characteristics of the graphene sample before (blue crosses), during and after two hours of 3 ppm NO_2

exposure (green star) and after the sample recovered post NO_2 exposure (red triangles). Upon comparison of the linewidth before and during NO_2 exposure, there is an approximate 6 V shift at 5.85 MHz, $\Delta V_{P-Slope}$, due to the NO_2 p-doping the graphene. In addition to this, the minimum linewidth at the Dirac point decreases during gas exposure, indicative of a slight decrease in sheet conductivity. This is relatively minor and possibly due to the NO_2 adsorbates introducing additional scattering centers thus depressing the minimum conductivity value. However, this shift is minor and the sensitivity of the microwave measurement at the Dirac point is at its minimum. Consequently, no conclusive remarks can be made about the change in conductivity between the graphene before and during NO_2 exposure. More striking, is the hole slope shift between the sweep measurements post NO_2 exposure (red triangles), where the gate voltage is swept from 0 to -30 to plus 30 and back to 0 V. During this sweep, the 'post NO_2 exposure' curve (red triangles) is initially aligned well with the 'during NO_2 exposure' slope (green star) gas. However at a large negative bias, the curve shifts by $\sim \Delta V_{P-Slope}$ and aligns well with the initial response. This could correspond to gate stimulated desorption of residual NO_2 species. This implies that after recovery the graphene surface has not fully desorbed NO_2 species and perhaps the sweeping of the gate voltage to a high negative bias enhances desorption.

Figure 5.15b is a schematic representation of figure 5.15a exaggerating the measured $\Delta V_{P-Slope}$ shift, conductivity shift ($\Delta\sigma$) and the asymmetric hole/electron slopes for clarity before (blue) and during (green) 3 ppm NO_2 exposure. The reduction of the graphene conductivity combined with asymmetry of the hole/electron slopes results in a larger shift in the charge neutrality point (ΔV_{CNP}) compared to the hole slope shift. The interplay between the environmental and electrically stimulated doping of graphene, suggests three distinct doping regions of graphene. Where the hole (electron) slope of both the air ambient and NO_2 exposed graphene overlap, the graphene is

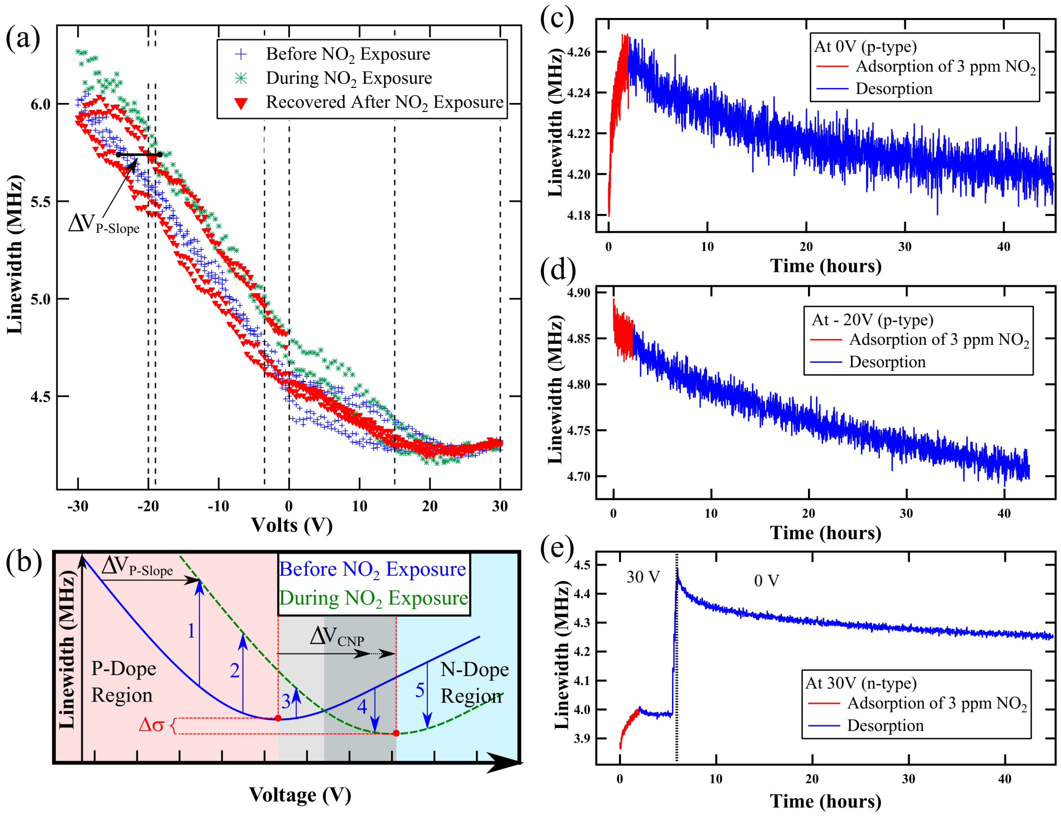

Figure 5.15: (a) Microwave measured linewidth (using the 3dB method) of the graphene gas sensor before (blue cross), during (green star) and after (red triangle) 3 ppm NO_2 gas exposure. (b) Exaggerated schematic of the Dirac point before (blue) and during (green) gas exposure showing the change in minimum conductivity ($\Delta\sigma$) where broader linewidths correspond to larger conductivities. The black horizontal arrows illustrates the difference in magnitude between the hole slope ($\Delta V_{P-Slope}$) and the Dirac point (ΔV_{CNP}). The blue arrows describe the electron charge transfer affinity from graphene in air to graphene with NO_2 adsorbates. The more positive the arrows correspond to conditions where the electron charge transfer affinity is higher. The pink (blue) region corresponds to graphene with and without the NO_2 adsorbates that is p- (n-) doped. The grey region corresponds to conditions where NO_2 adsorbate free graphene is n-type but when NO_2 adsorbates are present it is still p-type. The adsorption (red) and desorption (blue) curves of 3 ppm NO_2 at (c) 0 V gate voltage (d) -20 gate Voltage (e) 30 V gate voltage - where desorption only appears to be stimulated after the gate bias is reduced to 0 V.

clearly p-doped (n-doped) as shown by the pink (blue) region in figure 5.15b. The grey region, corresponds to graphene exposed to a high enough gate potential to shift the air doped graphene, but not the NO_2 doped graphene, from p-type to n-type.

Figures 5.15c-e shows the response of the sensor during (red) and after (blue) 3 ppm NO_2 exposure at 0, -20 and +30 applied gate voltage respectively. The response at 0 V bias unsurprisingly responds similar to all previous measurements as expected - the hole conductivity of graphene increases upon exposure to hole dopant molecules. At -20 V the sample is highly p-doped and the sensor response curve shows zero affinity for NO_2 adsorption. Instead, this gate voltage promotes the desorption of p-doping adsorbates from the graphene sheet which is evidenced by the seamless merging of the adsorption and desorption lineshape in figure 5.15c.

Interestingly, figure 5.15e shows the sample at 30 V, such that it is lightly n-doped during air ambient measurements and exhibits enhanced NO_2 adsorption (this enhancement is more clearly shown in figure 5.16 which is discussed further in this section). Remarkably, after NO_2 exposure, the sample shows zero affinity for desorption until the gate is returned to zero bias and the characteristic desorption curve is observed. Despite this sample being lightly n-doped via electrical gating, there is no evidence of the linewidth sharpening prior to broadening, which is normally suggestive of the graphene reducing electron conductivity prior to increasing hole conductivity. Two explanations are as follows: first the graphene is only lightly doped and the adsorption of NO_2 so rapid that there is no observable decline in the linewidth. Secondly, the graphene being lightly n-doped in air ambient is still p-doped in the NO_2 ambient, corresponding to the grey region in figure 5.15b.

This behaviour is further rationalized by considering the charge distribution and affinity of carriers at the graphene surface. By applying a large negative (positive) gate voltage, the graphene electrons redistribute to minimise the interaction induced by the charge accumulation at the dielectric interface; effectively p-doping (n-doping) the graphene material. As a result, the graphene is effectively psuedo positively (negatively) charged by increasing the density of holes (electrons). Therefore, an approaching NO_2 molecule, which is an electron acceptor/hole donor, is less able to successfully donate its positive charge when the graphene is p-doped for purely electrostatic reasons. Similarly the converse also holds true, it is easier for n-type graphene to donate an electron to an adsorbing NO_2 species that approaches the surface. Moreover, as evident in figure 5.15c, that charge is retained post NO_2 exposure indicating the n-type graphene adsorbate system is more energetically favourable.

This gate dependent adsorption behaviour is likely to depend upon the charge transfer affinity of graphene. Previous DC transport measurements have shown similar enhanced or diminished gas sensing properties using an electrical gate [354, 355, 356]. Moreover, Chen et al. [357] suggest that graphene heavily doped via an applied gate voltage causes ammonia adsorbates to bind to graphene either via the electronegative lone pair of the nitrogen atom or via the electropositive hydrogen plane. With this in mind, the blue vertical arrows in figure 5.15b describe the observed sensor responses in terms of electron transfer from the air ambient graphene to the NO_2 doped graphene; where the more positive arrows correspond to a higher electron transfer probability. In this representation the zero bias sensor response of figure 5.15c corresponds to arrow 2 and the sensor response of figure 5.15d corresponds to arrow 1. Arrow 1 suggests the heavily p-doped graphene has a high electron transfer affinity such that it is resistant to NO_2 adsorption. Whereas, arrow 2 corresponds to lightly p-doped graphene such that NO_2 adsorption still occurs and the hole conductivity increases. This implies that the graphene tends to a NO_2 adsorbate concentration equilibrium with a favourable energy which is consistent with previous work suggested by Singh et al. [358].

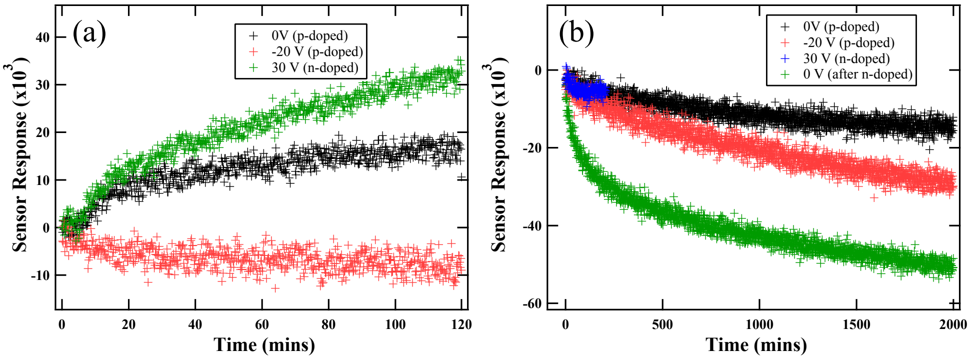

Figure 5.16: The sensor responses of the (a) adsorption and (b) desorption of the gas sensing measurements shown in figure 5.15c-e where $SR = (\omega - \omega_0)/\omega_0$ and ω_0 is the initial linewidth for each measurement. The desorption at 0V and 30 V from figure 5.15e are displayed separately. Although the electrical gating facilitates charge doping of the graphene sheet, the initial NO_2 adsorbate concentration prior to each adsorption measurement should be similar despite the widely different ω_0 values for the adsorption and desorption measurements. Therefore the comparison of these responses curves provide insight into the sorption rates.

Finally, arrows 3 and 4 in the grey region where graphene with and without adsorbates is p- or n- doped respectively. It is this region between the Dirac points where the sensor response of figure 5.15e is likely to be located. Unfortunately, since the sensitivity of microwave method is reduced close to the Dirac point is difficult to elucidate the mechanism. Furthermore, heavily n-type graphene wasn't reached such that arrow 5 of the n-doped graphene region was never reached. To verify this mechanism future measurements using NO_2 with highly n-type graphene and repeating the measurements with ammonia would be highly beneficial. As a final remark about the representation of figure 5.15b, during accumulation of NO_2 adsorbate species on the surface prior to saturation, there will be an interplay between regions of graphene that arewith and without adsorbates. Therefore, this representation, particularly in the grey region, better reflects this dynamic behaviour.

For completion, by comparing the sensor response curves of the data from figures 5.15c-e, figure 5.16 compares the sensor responses of the (a) adsorption and (b) desorption of graphene exposed to 3 ppm NO_2 at different gate potentials. Although the initial linewidth values are widely different, due to electrically modulating the carrier distribution in graphene; prior to each measurement, the graphene sample is recovered to equilibrium conditions at the 0 V bias. Consequently, the initial adsorbate coverage for each adsorption measurements is expected to be similar. Therefore, these sensor response curves provide a good visual comparison of the sensor response curve shapes and the rate of sorption. Figure 5.16a shows the rate of adsorption improves at high gate voltages where the air ambient graphene is n-doped. More strikingly, as before there appears to zero affinity for NO_2 adsorption when the sample is highly p-doped (at -20 gate voltage). Moreover, it appears that residual p-dopants on the surface are expelled. Figure 5.16b shows that the converse is true for the desorption, i.e. the desorption of the p-doping adsorbate is improved upon electrically p-doping the graphene sheet with the gate. Interestingly, the desorption at 30 V and 0 V from figure 5.15e (the blue and green curves respectively) are treated separately. As a consequence, it is clear that the desorption response is stunted at 30 V bias.

More interestingly, upon comparison of the 0 V desorption responses of both the 0 V bias adsorption and the 30 V biased adsorption measurements, the rate of desorption of the material that was previously lightly n-doped is significantly more rapid and 3.7 x larger than the 0 V adsorption-desorption measurement, implying more NO_2 molecules are liberated from the surface. Now, since the microwave method relies upon the measurement change in linewidth of loaded graphene gavity compared to the empty cavity; upon doping, as graphene approaches the Dirac point, the change in linewidth is smaller and the measurement is less sensitive. Moreover, due to graphene symmetry it is difficult to distinguish between hole and electron carriers. Therefore, it is possible that the n-doped graphene, close to the Dirac point, is adsorbing a large quantity of NO_2 but the microwave measurement lacks the sensitivity to distinguish this. For this reason it appears that the graphene desorbs more NO_2 species than was adsorbed (compare the green curves of figure 5.16).

Clearly it follows that the sensitivity is potentially a limiting factor for these measurements. Typical quality factors of the open resonator cavity achieved in this work ranged between 600-800. By comparison, Adabi et al. [337] showed much more sensitive AC transport measurements with Q values as high as 8000-8600. Therefore, in future work it is desirable to improve the resonator performance by improving the design by: using a dielectric material with a higher permitivity, improving the positioning of the microwave coupling loops to better interact with the resonator, reducing the amount ceramic spacer material and changing the geometry of the dielectric resonator or aperture/hole of the hosing. For example, using circular aperture with a puck resonator, instead of the square aperture which was used in this work, reduces the losses due to the otherwise sharp aperture edge [215]. Alternatively, a cubic resonator would improve the coupling of the TE_{011} mode with graphene. This arises from the electric field distribution of the cylindrical puck being "doughnut" shaped and interacting with the edges of the square graphene sample. Whereas, a square resonator would couple predominantly to the central graphene of the sample [359].

To summarise this section, as interesting consequence is that the charge transfer affinity of an adsorbing species appears to be dependent upon the degree of graphene doping. This is analogous to the electron affinity and ionization potential of the elements. Moreover, the adsorbate coverage dependence of the charge transfer affinity function $C(n)$ is perhaps more successfully described in terms of the chemical potential of graphene which will naturally have an adsorbate concentration dependence. To fully investigate this relationship, gas sensing measurements at different gate voltages at different temperatures could elucidate the binding energy variation at different voltages. However, it is important to assess where the equilibrium linewidth position is at each gate doped configuration. Although this changes the initial surface concentration of the graphene surface, measurements at equilibrium provide a more accurate determination of the overall sorption interactions. In addition to this, a sweep of gate voltages before, during and after each measurement is important to determine how the charge neutrality points shifts upon environmentally stimulated doping. Unfortunately, as mentioned before, the Dirac measurement of the linewidth for the voltage sweeps was achieved using the ‘3 dB method’ opposed to the ‘LSF method’ that was used during the gas sensing measurements (See chapter 2 section 2.6.3). However, this limitation has been resolved and now consistent measurements of the resonant response can be attained for all microwave measurements.

With consistent measurements, the change of linewidth of the graphene sensor can be related to a change in resisitivity and compared to position of the charge neutrality point. The dashed lines of figure 5.15 relate the change of linewidth of each gas sensing measurement to the charge neutrality point. Note that the equivalent 3dB values of figures 5.15c and d and the LSF values of figure 5.15e is used here. Therefore, this analysis is by no means rigorous and instead intended to provide a ‘ball park’ evaluation of the observed response. Upon comparison of the measured linewidths, it initially appears that the n-type graphene (in air ambient) is producing a p-type sensor response. It is suspected, this is due to the additional shift in the Dirac point achieved via environmental doping such that gate induced doping at 30 V produces a n-type response for the adsorbate free graphene but a p-type response for the adsorbate functionalised graphene. This is illustrated by the blue transition arrows in figure 5.15b in the grey region. To verify this, a larger voltage sweep range should be applied to access a heavily n-doped graphene state, such that it is far away from the CNP. Under such conditions it is expected that the sensor response will take the form of an initial rapid decrease in linewidth.

To conclude, tuning the doping of graphene via electronic gating, changes the charge transfer affinity of adsorbate species. Through this, the adsorption and more importantly the desorption, a current bottleneck to the commercialization of graphene sensors, can selectively be enhanced. This could lead to better sensitivity, improved desorption time scales and selective monitoring of gas species by tuning the graphene doping to best promote a charge transfer interaction. Clearly, there are still experimental hurdles to be overcome to fully understand the gate induced microwave response in addition to the gas sensing response. However, through this work these preliminary measurements show a promising start towards understanding the intrinsic chemical limitations of the graphene—NO_2 sensor response, while simultaneously providing alternate ways to enhance the response via tuning the chemical potential and thermodynamics via gating and temperature measurements.

5.5 Chapter Conclusion

To summarise, this chapter presents an alternative cavity design for gas sensing. This design enables a large variation of temperature control and electrical gating. The response of the cavity for the three sample configurations of the microwave method (empty, bare substrate and graphene on substrate) are measured at various temperatures and gate voltages. The initial adsorption and desorption measurements remarkably show similar sorption barrier values, indicating that the initial rudimentary models capture the equilibrium conditions of the graphene sensor. Clearly, the initial rapid response regime of the sensor is not fitted well, which is unsurprising since the previous chapter establishes that graphene sensor response can only be modeled by a non-constant sticking coefficient function. The next steps involve the design of an improved model to describe the adsorption and the desorption sensor response curves and repeating the measurements at more temperature values.

Similarly, the initial gating measurements show a comparison of the graphene sheet resistivity acquired using microwaves and a traditional DC circuit using the alternative cavity design. However, the initial gas-gating measurements show promise towards gas selective sensor response enhancement and stimulated desorption of the sensor. More remarkably, the adsorption of NO_2 can be prevented completely opening alternative applications in fields such as the ultra high vacuum, where non-evaporable getters and amorphous carbon thin films are materials designed to maintain ultra high vacuum in particle accelerators [360]. The major challenges of this work involved the implementation of a new cavity design, fabrication of a large 'gateable' graphene area and reducing the system noise. However, in addition to overcoming these practical difficulties, these preliminary measurements have allowed a more intuitive understanding of the NO_2—graphene sorption interactions. To elucidate the graphene—adsorbate charge transfer affinity, gas sensing measurements at different gate biases and temperatures would show the relationship between the binding energies of the gas species and the chemical potential of graphene. Ultimately, leading to a more informed evaluation of the best initial graphene conditions which result in the highest sensor sensitivity. Of course, the fundamental graphene—adsorbate interactions have relevance outside this single gas sensing platform.

Throughout all measurements the NO_2 sensor response can be modelled using a double exponential approximation. However, the response of other gases produce distinctly different sensor response curves [63]. Therefore, further work to investigate whether the NO_2 sensor response is truly 'characterisitc' since it appears to be consistent during non-steady state environmental conditions. To achieve this an extensive study into the response of other trace gases is needed. Gas sensing of ammonia would be an ideal candidate since, unlike NO_2, NH_3 is an electron donating gas and so produces a polar opposite sensor response curve. Therefore drastically different sticking and desorption coefficients should describe the sorption interactions and provide more insights into the tunable charge transfer affinity of graphene with trace gases.

Chapter 6

Conclusion

In this work two distinct graphene based molecular sensing platforms are explored: a G-SERS platform, comprised of graphene on a gold nanodisc array and a graphene coupled microwave dielectric resonator platform. The former measures the spectroscopic signal of graphene and the probe molecule and is limited to the spot size of the laser. Whereas, the latter measures the change in sheet resistivity upon the adsorption of gas molecules.

To summarise, it is shown that G-SERS platforms facilitate spectral enhancements through a variety of mechanisms which are explored through FTIR and Raman techniques. In addition to discussing the electromagnetic mechanism of enhancement, which is typical of traditional SERS platforms; the chemical enhancement mechanism, which manifests itself particularly strongly in graphene platforms, is instead the focus. To investigate the chemical enhancement mechanism of graphene; lightly, moderately and heavily p-doped graphene is fabricated through interfacing graphene with h-BN pacified, untreated (but wet transfered) and oxygen plasma treated AuND/SiO_2/Si substrates. Since the properties of CVD graphene vary spatially, Raman maps of the graphene surface are statistically analysed, which not only provides a robust characterisation technique for the comparison of the fabricated samples; but more generally demonstrates a more rigorous and complete approach to the Raman analysis of graphene. Consequently, chemically modifying graphene is shown to provide a small, yet non-negligible contribution to the overall enhancement of the graphene Raman peaks.

More interestingly, using Kelvin force microscopy to probe the surface potential variation of the graphene surface, it is shown that graphene can be optically doped via high power laser irradiation ((2.95±0.19)x10^5 Wcm^{-2}) over the AuNDs by $\sim -0.87 \pm 0.05$ meV and $\sim +0.75\pm$ 0.07 meV in air or nitrogen ambients respectively. Since the graphene sample used is transferred onto h-BN such that graphene is decoupled from charge interactions from the substrate, the laser induced doping is a surface chemical reaction. Through statistical Raman analysis, it is shown that at low power laser irradiation ((3.43±1.22)x10^4 Wcm^{-2}), where no doping is observed, there is no significant strain in the graphene lattice in the presence nor absence of the AuNDs. However, not only is there appreciable strain in the graphene lattice in the presence of the AuNDs after high power laser irradiation, but during measurements in the nitrogen ambient, a large number of sharp transient peaks are observed in the spectral region of largest electromagnetic enhancement, suggestive of near field optically induced excitation of molecular nitrogen. As a result, it is shown that Raman spectroscopy is not necessarily a non-invasive technique, nor is nitrogen an inert ambient, particularly in the characterisation of G-SERS platforms at certain laser irradiance.

In addition to this, it is shown that graphene coupled to a microwave dielectric resonator can be used as gas sensor. Upon adsorption, a gas molecule can donate an electron or hole into graphene which changes the graphene conductivity. This change in conductivity is non-invasively monitored by measuring the broadening or sharpening of the resonant linewidth of the TE_{011} mode. Using nitrogen dioxide as a p-dopant gas, a series of concentration measurements, spanning three orders of magnitude, confirm this platform as an alternative gas sensing platform. Moreover, through examination of the rate of adsorption at each concentration, the adsorption of NO_2 occurs in two distinct regimes. Consequently, the regime of rapid adsorption lasts $\sim$ 35 minutes which is a chemical limitation of the system. By contrast, the sensitivity limit reported suggests a minimum of 5 minutes is necessary to distinguish between the concentration. However, this is not a chemical limitation and can be improved via better graphene—resonator coupling and reduction of loss and noise.

More interestingly, the chemical adsorption kinetics of this system is explored using modified Langmuir models. The sensor response is described using a surface occupation model and an adsorption site model. Surprisingly, both models describe the sticking probability decreasing exponentially as it is exposed to more NO_2 adsorbates. However, the occupation model better captures the initial lineshape of the sensor response. Regardless, this behaviour is ascribed to an increase in the adsorption energy barrier with increased NO_2 surface coverage. Therefore, the binding sites of graphene vary continuously on the graphene opposed to discrete results which is in agreement with Raman and Kelvin probe surface measurements. Moreover, it is shown that the Langmuir modeled concentration slopes can be fitted to a double exponential equation, as is traditional in graphene based NO_2 sensors, which instead is an empirical fitting and does not reflect a surface with two distinct adsorption sites.

Further to this, an open cavity design with additional temperature and electrical gating properties is developed as an alternative gas sensing platform. The preliminary temperature measurements show that the adsorption and desorption responses, despite being fitted to two different models, have similar adsorption energy barrier values at equilibrium conditions. More strikingly, the initial gate modulated graphene gas sensing measurements show that the charge transfer affinity can enhance or hinder the sorption of gases on graphene. When the graphene is highly p-doped via electrical gating, it is shown that NO_2 has a negligible affinity for adsorption. Conversely, when graphene is lightly electrically n-doped using the gate, the desorption of NO_2 is prevented. These preliminary results suggest electrically gating graphene can improve the sticking factor of select gases which could have benefits in ultra high vacuum applications.

To summarise, two distinct gas sensing platforms have been explored in the work of this thesis. Using KFM and Raman spectroscopy, the graphene interactions with the SERS active substrate and its environment has been explored providing a baseline for future G-SERS applications. Of particular scientific benefit is the observation of optically stimulated doping, suggesting experimental conditions need to be carefully controlled when probing the graphene surface. On the other hand, the graphene microwave gas sensing platform enabled an investigation into the graphene—gas sorption interactions. The fundamental kinetic limits established here have relevance to all gas sensing platforms and are not limited to the microwave method. Consequently, a more informed approach towards graphene sensor optimisation can be achieved through understanding the system limitations and how they arise. Moreover, the systematic approach is general to all graphene—gas interactions and provide a platform to expand from. As such, extending this adsorption model to the optically induced non-equilibrium conditions, could provide new perspective to G-SERS platforms. Finally, in pursuing an alternative cavity design to explore sorption energies and the nature of the charge transfer affinity function, the preliminary measurements show promising selective sorption behaviors. Although this work is in its infancy, and further measurements are still needed, the ability to prevent molecular desorption and improve the 'stickiness' of a surface has interesting applications outside the field of gas sensing such as ultra high vacuum systems. In conclusion, these two drastically different molecular sensing platforms, have delivered unique insights both integral towards understanding the physical chemistry of graphene at both the solid and gas interfaces.

Chapter 7

Future Outlook

Both molecular sensing platforms studied have plenty of room to grow and develop beyond the work in this thesis. Naturally, the detection of further chemical species is of practical interest in the development of both sensing platforms. Assessments of the sensitivity, response time, recovery time, detection limit and selectivity in different environments is the most intuitive research direction to develop these sensors further. In this final chapter, different research directions including and beyond gas sensing is discussed based on these sensing platforms.

7.1 Future Outlook of G-SERS Platforms

7.1.1 Selective Molecular Enhancement

In chapter 3 a detailed study of the Raman characteristics of the nanodisc G-SERS platforms provides a baseline with respect to their properties. It has been shown that the Raman response of graphene and adsorbate species can be enhanced using an electrical gate [228, 229]. Moreover, chemical adsorbates have been shown to environmentally dope graphene in a similar manner [253]. More interesting is the reported GERS enhancement of particular vibrational modes upon electrical gating [252]. However, it is unclear whether this enhancement is due to favorable charge transfer modes, from graphene to the probe which can be enhanced by perturbing the graphene Fermi energy; or stray electric field effects permeating through graphene which has a negligible skin depth [313].

Therefore, it is of interest to understand the influence of the electric field-itself imposed by the gate voltage, in addition to the work function of graphene, as two distinct components influencing the chemical enhancement mechanism at the graphene-gas interface. To do this, a comparative study of the Raman peaks of well studied probe molecules (such as rhodamine 6G or porphyrins) where the Fermi energy of graphene is modulated either through electrical gating or chemical interactions with the substrate i.e. tailoring the graphene-solid interface. The latter can be achieved by interfacing graphene with different substrates treated with self assembled monolayers [257]. Through understanding the nature of the charge transfer mechanism, the selective stimulation of certain modes via chemical modulation can potentially lead to stereoselective surface reactions.

Similarly, where the chemical mechanism can induce vibrational mode specific enhancement, a G-SERS platform comprised of a fano-resonant nanostructure [361, 362] can be used to enhance both the incident and scattered light of certain Raman processes; where the scattered frequency is far from the pump frequency. In this way, a specific vibrational mode can be enhanced beyond others. As a result, using the statistical analysis techniques established in chapter 3 where the graphene response to G-SERS substrate is understood, the next step is to introduce molecular species. Through modulating the work function electrically or chemically the enhancement or diminishment of selective vibrational modes through electromagnetic and chemical enhancements from the G-SERS substrate can be tailored to allow spectral peak specific monitoring and potentially experimentally deconvolving the combination of broad similar frequency modes.

7.1.2 Optically Doping Graphene Domains

Moreover, from chapter 3 it is shown that doped domains could be optically induced through surface chemical reactions of G-SERS substrates. However, the exact nature of the chemical doping such as bond type and chemisorbed species is unknown. Techniques such as transmission electron microscopy, X-ray photoelectron spectroscopy and electron dispersive X-ray spectroscopy. Moreover, repeating the experiment at different laser wavelengths at a variety of laser powers and temperatures could provide information on activation energy barriers needing to be overcome for the surface chemistry to take place. In addition to this, repeating the experiment in different environments such as ammonia, nitrogen dioxide and a noble gas; which provides a highly electron donating, hole donating and inert atmospheres respectively could be interesting to see how big this chemical induced doping effect can be.

Moreover, laser writing doped domains in graphene can potentially provide a simple and versatile technique for future device fabrication. For example, a current hurdle to overcome in graphene functionalisation is controlling what percentage of the surface and location the material is functionalised [127, 335, 363]. This could facilitate preferential adsorption sites for gas sensors and the creation of p- and n-type domains for electronic device fabrication [364]. Finally, this near field enhanced doping mechanism can be used on non G-SERS platforms using a tip enhanced writing technique in different ambients; where instead of the nanoparticles facilitating near field enhancement, a scanning probe tip is used [365].

7.1.3 Hot Carrier Extraction

The optically induced surface chemical reactions on graphene is potentially a ‘hot-electron’ mediated reaction. Plasmons can decay into electron-hole pairs, where currently there is great interest in extracting them for various application including photochemical reactions [366]. Gold nanostructures thiolated with 4-nitrophenol (NTP), has been shown to facilitate the reduction reaction of NTP to 4-aminothiol (ATP) which requires an electron rich environment to proceed [295]. A drawback of these hot carrier mediated reactions is that they are limited to the region of the near field [4]. However, the charge carriers of graphene exhibit ballistic transport, with the potential to travel long distances [24, 25]. Moreover, hot carriers have already been observed in graphene [264, 274, 294]. As a result, G-SERS substrates can be used as a unique potential hot electron platform.

Unfortunately, since the most well studied hot carrier interactions take place at the SERS hot spot, it is impossible to detect the same NTP to ATP reduction reaction without the aid of SERS enhancement. However, Lee et al. [367] have shown the plasmon induced reduction of silver ions to silver atoms on a colloidal gold nanoparticle substrate. From this the silver precipitates can be measured using scanning electron microscopy. Incorporating graphene into this substrate, the distance the hot carriers travel could be assessed and potentially enhanced by passing a current through the graphene sheet. Moreover, through gating the graphene device, hot holes could be excited which could facilitate the oxidation process effectively returning the silver precipitates back to silver ions. In short, G-SERS platforms have potential applications beyond sensitive spectroscopic sensors.

7.2 Future Outlook of the Microwave Cavity Platform

7.2.1 Tuning the Charge Transfer Affinity of Graphene

The preliminary work detailed in chapter 5 is sill in the early stages. Similar to the adapted Langmuir model used in chapter 4, it is expected that modeling the graphene surface with a non-constant sticking probability which is dependent upon the adsorbate concentration, will better fit the adsorption data at different temperatures. From this, a picture of how the adsorption energy barrier evolves over time can be discerned.

In addition to this, the gate dependency of graphene clearly shows that charge transfer affinity can be perturbed. However, from the preliminary measurements, it is of interest to improve the graphene—resonator coupling in order to optimise the signal, which is partiularly poor at gating potentials close to the charge neutrality point. Although gate enhanced gas sensing has been reported before [354, 357], changing the sticking probability of a surface preventing either the adsorption or desorption process entirely hasn't been reported yet. However, since the skin depth of graphene is negligible, discerning whether this is simply a doping effect relating to the graphene work function, or an electrostatic effect is an area of future work. Finally, combining the temperature and gating measurements with NO_2 and other gases such as NH_3 will enable a quantitative description of sorption barriers and the charge transfer affinity.

7.2.2 Microwave Measurements Beyond CVD Graphene

The microwave method allows for the measurement of the graphene resistivity since it is an single atomically thin film, with highly conductive charge carriers which perturbs the cavity resonance depending on its conductivity. However, as is shown in this work, an absolute measurement of the graphene resistivity is not necessary for its use as a sensor. Instead the sensor response is a measurement in the change of graphene properties. As a result, alternative 2D materials can easily be integrated into this platform provided they are conductive and their properties can be tuned.

The microwave resonator platform is ideal for integration with liquid exfoliated conductive 2D materials [368]. For example, unlike CVD graphene, drop casted liquid exfoliated graphene forms a substrate comprised of graphene flakes that are not necessarily continuous. As a result, DC electrical measurements require thick films to ensure good electrical contact between the flakes [369]. With the microwave method, this restriction is not necessary since the electrons are driven electromagnetically. Therefore, liquid exfoliated graphene could lead to a cheap alternative material for this gas sensing platform.

In addition to this, the open cavity configuration lends itself well to optical integration, since the sample is not enclosed in the cavity - particularly since the graphene doesn't need to be facing into the resonator to interact with the microwaves. However, since the microwave technique is a large area measurement, narrow-band LEDs are ideal candidates to provide cheap and uniform large area irradience. Therefore, alternative 2D materials such as transition metal dichalcogenides, where molybdenum disulfide (MoS_2) which is an already proven gas sensor similar to graphene [370, 371], and quasi 2D thin film perovskites which have conductivity properties that can be enhanced through optical excitation [372, 373] and are sensitive to their environments, can easily be integrated into the microwave dielectric resonator sensing platform.

Finally, by adding large area optical capabilities to the microwave platform, it becomes compatible with large area colloidal nanoparticle based G-SERS platforms. Providing an unique platform to probe the large area doping of graphene upon large area optically induced environmental doping. Comparing nanoscale Raman and KFM based measurements the macroscale of the microwave measurements of the same process enables a unique non-invasive method to describe a nanoscale G-SERS platform.

Bibliography

[1] Myer. Kutz. *Handbook of materials selection*. J. Wiley, New York, 2002.

[2] National Research Council and others. *Expanding the vision of sensor materials*. National Academy Press, 1995.

[3] Philip D. Howes, Rona Chandrawati, and Molly M. Stevens. Colloidal nanoparticles as advanced biological sensors. *Science*, 346(6205):1247390, 2014.

[4] Emiliano Cortés, Wei Xie, Javier Cambiasso, Adam S Jermyn, Ravishankar Sundararaman, Prineha Narang, Sebastian Schlücker, and Stefan A Maier. Plasmonic hot electron transport drives nano-localized chemistry. *Nature Communications*, 8:14880, 2017.

[5] Adam B Taylor and Peter Zijlstra. Single-Molecule Plasmon Sensing: Current Status and Future Prospects. *ACS Sensors*, 2(8):1103–1122, 2017.

[6] Justin J. Gooding and Katerina Gaus. Single-Molecule Sensors:Challenges and Opportunities for QuantitativeAnalysis. *Angewandte Chemie*, 55(38):11354–11366, 2016.

[7] M A Mcevoy and N Correll. Materials that couple sensing, actuation, computation, and communication. *Science*, 347(6228):1261689, 2015.

[8] James G Bellingham and Kanna Rajan. Robotics in remote and hostile environments. *Science*, 318(5853):1098–102, 2007.

[9] Yoann Altmann, Stephen McLaughlin, Miles J Padgett, Vivek K Goyal, Alfred O Hero, and Daniele Faccio. Quantum-inspired computational imaging. *Science*, 361(6403):eaat2298, 2018.

[10] Thomas W. Hesterberg, William B. Bunn, Roger O. McClellan, Ali K. Hamade, Christopher M. Long, and Peter A. Valberg. Critical review of the human data on short-term nitrogen dioxide (NO2) exposures: Evidence for NO2 no-effect levels. *Critical Review in Toxicology*, 39(9):734–781, 2009.

[11] World Health Organisation. WHO Air quality guidelines for particulate matter, ozone, nitrogen dioxide and sulfur dioxide. Technical report, World Health Organisation, Geneva, 2005.

[12] World Health Organisation. WHO air quality guidelines for Europe, 2nd edition, 2000 (CD ROM version). Technical report, 2000.

[13] Anindya Nag, Arkadeep Mitra, and Subhas Chandra Mukhopadhyay. Graphene and its sensor-based applications: A review. *Sensors and Actuators A: Physical*, 270:177–194, 2017.

[14] Xiaowen Yu, Huhu Cheng, Miao Zhang, Yang Zhao, Liangti Qu, and Gaoquan Shi. Graphene-based smart materials. *Nature Reviews Materials*, 2(17046):1–23, 2017.

[15] Tao Wang, Da Huang, Zhi Yang, Shusheng Xu, Guili He, Xiaolin Li, Nantao Hu, Guilin Yin, Dannong He, and Liying Zhang. A Review on Graphene-Based Gas/Vapor Sensors with Unique Properties and Potential Applications. *Nano-Micro Letters*, 8(2):95–119, 2016.

[16] Seba S Varghese, Sunil Lonkar, K K Singh, Sundaram Swaminathan, and Ahmed Abdala. Recent advances in graphene based gas sensors. *Sensors and Actuators B: Chemical*, 218:160–183, 2015.

[17] Chaoyi Yan, Jiangxin Wang, and Pooi See Lee. Stretchable Graphene Thermistor with Tunable Thermal Index. *ACS Nano*, 9(2):2130–2137, 2015.

[18] John A Rogers, Takao Someya, and Yonggang Huang. Materials and mechanics for stretchable electronics. *Science*, 327(5973):1603–7, 2010.

[19] Shideh Kabiri Ameri, Myungsoo Kim, Irene Agnes Kuang, Withanage K Perera, Mohammed Alshiekh, Hyoyoung Jeong, Ufuk Topcu, Deji Akinwande, and Nanshu Lu. Imperceptible electrooculography graphene sensor system for human-robot interface. *npj 2D Materials and Applications*, 2:19, 2018.

[20] K S Novoselov, V I Fal, L Colombo, P R Gellert, M G Schwab, K Kim, V I Fal Ko, L Colombo, P R Gellert, M G Schwab, and K Kim. A roadmap for graphene. *Nature*, 490(7419):192–200, 2012.

[21] A K Geim. Graphene: status and prospects. *Science*, 324(5934):1530–4, 2009.

[22] Kin Fai Mak, Long Ju, Feng Wang, and Tony F. Heinz. Optical spectroscopy of graphene: From the far infrared to the ultraviolet. *Solid State Communications*, 152(15):1341–1349, 2012.

[23] R R Nair, P Blake, A N Grigorenko, K S Novoselov, T J Booth, T Stauber, N M R Peres, and A K Geim. Fine structure constant defines visual transparency of graphene. *Science*, 320(5881):1308, 2008.

[24] A H Castro Neto, F Guinea, Nuno M R Peres, Kostya S Novoselov, and Andre K Geim. The electronic properties of graphene. *Reviews of Modern Physics*, 81(1):109, 2009.

[25] Luca Banszerus, Michael Schmitz, Stephan Engels, Matthias Goldsche, Kenji Watanabe, Takashi Taniguchi, Bernd Beschoten, and Christoph Stampfer. Ballistic Transport Exceeding 28 μm in CVD Grown Graphene. *ACS Nano Letters*, 16(2):1387–1391, 2016.

[26] F Schedin, A K Geim, S V Morozov, E W Hill, P Blake, M I Katsnelson, and K S Novoselov. Detection of individual gas molecules adsorbed on graphene. *Nature materials*, 6(9):652–655, 2007.

[27] Alexander A. Balandin, Suchismita Ghosh, Wenzhong Bao, Irene Calizo, Desalegne Teweldebrhan, Feng Miao, and Chun Ning Lau. Superior Thermal Conductivity of Single-Layer Graphene. *Nano Letters*, 8(3):902–907, 2008.

[28] Insun Jo, Michael Thompson Pettes, Jaehyun Kim, Kenji Watanabe, Takashi Taniguchi, Zhen Yao, and Li Shi. Thermal Conductivity and Phonon Transport in Suspended Few-Layer Hexagonal Boron Nitride. *Nano Letters*, 13(2):550–554, 2013.

[29] Weigao Xu, Xi Ling, Jiaqi Xiao, Mildred S Dresselhaus, Jing Kong, Hongxing Xu, Zhongfan Liu, and Jin Zhang. Surface enhanced Raman spectroscopy on a flat graphene surface. *Proceedings of the National Academy of Sciences*, 109(24):9281–9286, 2012.

[30] Julian Gargiulo, Thomas Brick, Ianina L Violi, Facundo C Herrera, Toshihiko Shibanuma, Pablo Albella, Felix G Requejo, Emiliano Cortes, Stefan A Maier, and Fernando D Stefani. Understanding and Reducing Photothermal Forces for the Fabrication of Au Nanoparticle Dimers by Optical Printing. *Nano Letters*, 17(9):5747–5755, 2017.

[31] Xingang Zhang, Shuyao Si, Xiaolei Zhang, Wei Wu, Xiangheng Xiao, and Changzhong Jiang. Improved Thermal Stability of Graphene-Veiled Noble Metal Nanoarrays as Recyclable SERS Substrates. *ACS Applied Materials and Interfaces*, 9(46):40726–40733, 2017.

[32] I W Frank, D M Tanenbaum, A M Van Der Zande, and P L McEuen. Mechanical properties of suspended graphene sheets. *Journal of Vacuum Science & Technology B*, 25(6):2558–2561, 2007.

[33] Zainab Yunusa. Gas Sensors : A Review. *Sensors & Transducers*, 168(4):61–75, 2014.

[34] Xiao Liu, Sitian Cheng, Hong Liu, Sha Hu, Daqiang Zhang, and Huansheng Ning. A survey on gas sensing technology. *Sensors*, 12(7):9635–9665, 2012.

[35] Florian M Schwandner, Michael R Gunson, Charles E Miller, Simon A Carn, Annmarie Eldering, Thomas Krings, Kristal R Verhulst, David S Schimel, Hai M Nguyen, David Crisp, Christopher W O'Dell, Gregory B Osterman, Laura T Iraci, and James R Podolske. Spaceborne detection of localized carbon dioxide sources. *Science*, 358(6360):eaam5782, 2017.

[36] Dae-Sik Lee and Duk-Dong Lee. Environmental Gas Sensors. *Article in IEEE Sensors Journal*, 1(3):214–224, 2001.

[37] Simon M Sze and Kwok K Ng. *Physics of Semiconductor Devices*. John wiley & sons, 3 edition, 2007.

[38] Eric Bakker and Martin Telting-Diaz. Electrochemical Sensors. *Analytical Chemistry*, 74:2781–2800, 2002.

[39] Jane Hodgkinson and Ralph P Tatam. Optical gas sensing: a review. *Measurement Science and Technology*, 24(1):012004, 2013.

[40] A.A. Kosterev and F.K. Tittel. Chemical sensors based on quantum cascade lasers. *IEEE Journal of Quantum Electronics*, 38(6):582–591, 2002.

[41] Frank L Dorman, Joshua J Whiting, Jack W Cochran, and Jorge Gardea-Torresdey. Gas Chromatography. *Analytical Chemistry*, 82:4775–4785, 2010.

[42] Bryan P Sweeney, Paul G Quincey, David Green, and Gary W Fuller. Quantifying the impact of nitric oxide calibration gas mixture oxidation on reported nitrogen dioxide concentrations. *Atmospheric Environment*, 105:169–172, 2015.

[43] Nabil A. Abdel Ghany, Safaa A. Elsherif, and Hala T. Handal. Revolution of Graphene for different applications: State-of-the-art. *Surfaces and Interfaces*, 9:93–106, 2017.

[44] Robert Bogue. Nanophotonic technologies driving innovations in molecular sensing. *Sensor Review*, 38(2):171–175, 2018.

[45] Parikshit Sahatiya, Sampath Kumar Puttapati, Vadali V. S. S. Srikanth, and Badhulika.Sushmee. Graphene-based wearable temperature sensor and infrared photodetector on a flexible polyimide substrate. *Flexible and Printed Electronics*, 1(2):025006, 2016.

[46] Ke Xu, Chuhan Fu, Zhijun Gao, Fanan Wei, Yu Ying, Chong Xu, and Guojiang Fu. Nanomaterial-based gas sensors: A review. *Instrumentation Science & Technology*, 46(2):115–145, 2018.

[47] Arseniy I Kuznetsov, Andrey E Miroshnichenko, Mark L Brongersma, Yuri S Kivshar, and Boris Luk'yanchuk. Optically resonant dielectric nanostructures. *Science*, 354(6314):aag2472, 2016.

[48] Keith J Albert, Nathan S Lewis, Caroline L Schauer, Gregory A Sotzing, Shannon E Stitzel, Thomas P Vaid, and David R Walt. Cross-Reactive Chemical Sensor Arrays. *Chemical Reviews*, 100(7):2595–2626, 2000.

[49] Kinam Kim, Jae-Young Choi, Taek Kim, Seong-Ho Cho, and Hyun-Jong Chung. A role for graphene in silicon-based semiconductor devices. *Nature*, 479(7373):338–344, 2011.

[50] A Femius Koenderink, Andrea Alù, and Albert Polman. Nanophotonics: shrinking light-based technology. *Science*, 348(6234):516–21, 2015.

[51] Yotsarayuth Seekaew, Ditsayut Phokharatkul, Anurat Wisitsoraat, and Chatchawal Wongchoosuk. Highly sensitive and selective room-temperature NO_2 gas sensor based on bilayer transferred chemical vapor deposited graphene. *Applied Surface Science*, 404:357–363, 2017.

[52] Seyedeh Maryam Mortazavi Zanjani, Milo Holt, Mir Mohammad Sadeghi, Somayyeh Rahimi, and Deji Akinwande. 3D integrated monolayer graphene–Si CMOS RF gas sensor platform. *npj 2D Matierials and Applications*, 1(1):36, 2017.

[53] Shishir Kumar, Swati Kaushik, Rudra Pratap, and Srinivasan Raghavan. Graphene on paper: A simple, low-cost chemical sensing platform. *ACS Applied Materials and Interfaces*, 7(4):2189–2194, 2015.

[54] Fazel Yavari, Eduardo Castillo, Hemtej Gullapalli, Pulickel M Ajayan, and Nikhil Koratkar. High sensitivity detection of NO2 and NH3 in air using chemical vapor deposition grown graphene. *Applied Physics Letters*, 100(20):203120, 2012.

[55] Min Gyun Chung, Dai-Hong Kim, Dong Kyun Seo, Taewoo Kim, Hyeong Uk Im, Hyun Myoung Lee, Ji-Beom Yoo, Seong-Hyeon Hong, Tae June Kang, and

Yong Hyup Kim. Flexible hydrogen sensors using graphene with palladium nanoparticle decoration. *Sensors and Actuators B: Chemical*, 169:387–392, 2012.

[56] Juree Hong, Sanggeun Lee, Jungmok Seo, Soonjae Pyo, Jongbaeg Kim, and Taeyoon Lee. A highly sensitive hydrogen sensor with gas selectivity using a PMMA membrane-coated Pd nanoparticle/single-layer graphene hybrid. *ACS Applied Materials & Interfaces*, 7(6):3554–3561, 2015.

[57] G Ko, H.-Y Kim, J Ahn, Y.-M Park, K.-Y Lee, and J Kim. Graphene-based nitrogen dioxide gas sensors. *Current Applied Physics*, 10(4):1002–1004, 2010.

[58] Jong-Hyun Kim, Qin Zhou, Jiyoung Chang, Jong-Hyun Kim, Qin Zhou, and Jiyoung Chang. Suspended Graphene-Based Gas Sensor with 1 mW Energy Consumption. *Micromachines*, 8(2):44, 2017.

[59] Anderson D Smith, Karim Elgammal, Xuge Fan, Max C Lemme, Anna Delin, Råsander Mikael, Lars Bergqvist, Stephan Schröder, Andreas C Fischer, Frank Niklaus, and Mikael Östling. Graphene-based CO_2 sensing and its cross-sensitivity with humidity. *RSC Advances*, 7(36):22329–22339, 2017.

[60] Dejan Davidovikj, Paul H Scheepers, Herre S J Van Der Zant, Peter Gerard Steeneken, and Peter G Steeneken. Static capacitive pressure sensing using a single graphene drum. *ACS Applied Materials & Interfaces*, 9(49):43205–43210, 2017.

[61] Anderson D Smith, Sam Vaziri, Frank Niklaus, Andreas C Fischer, Mikael Sterner, Anna Delin, Mikael Östling, and Max C Lemme. Pressure sensors based on suspended graphene membranes. *Solid State Electronics*, 88:89–94, 2013.

[62] Stefan Goniszewski, Olena Shaforost, Norbert Klein, John Gallop, Ling Hao, and David Cox. Frequency readout of nanomechanical graphene drums via a microwave resonator coupling method. In *2014 44th European Microwave Conference*, pages 363–366. IEEE, 2014.

[63] Eric C. Nallon, Vincent P. Schnee, Collin J. Bright, Michael P. Polcha, and Qiliang Li. Chemical Discrimination with an Unmodified Graphene Chemical Sensor. *ACS Sensors*, 1(1):26–31, 2016.

[64] Sergey Rumyantsev, Guanxiong Liu, Michael S Shur, Radislav A Potyrailo, and Alexander A Balandin. Selective Gas Sensing with a Single Pristine Graphene Transistor. *ACS Nano LettersNanoLetters*, 12(5):2294–2298, 2012.

[65] Filiberto Ricciardella, Sten Vollebregt, Tiziana Polichetti, Mario Miscuglio, Brigida Alfano, Maria L. Miglietta, Ettore Massera, Girolamo Di Francia, and Pasqualina M. Sarro. Effects of graphene defects on gas sensing properties towards NO_2 detection. *Nanoscale*, 9(18):6085–6093, 2017.

[66] Qiuxia Feng, Xiaogan Li, and Jing Wang. Percolation effect of reduced graphene oxide (rGO) on ammonia sensing of rGO-SnO 2 composite based sensor. *Sensors and Actuators B*, 243:1115–1126, 2017.

[67] Indrani Choudhuri, Debopriya Sadhukhan, Priyanka Garg, Arup Mahata, and Biswarup Pathak. Lewis Acid–Base Adducts for Improving the Selectivity and Sensitivity of Graphene Based Gas Sensors. *ACS Sensors*, 1(4):451–459, 2016.

[68] Yung Ho Kahng, Sangchul Lee, Woojin Park, Sung-Soo Kim, Jeong-Yong Choi, Kwan Kim, Jia Zhang, Rongfu Zhang, Xiaona Wang, Wei Wu, Quanguo He, Hong Chen, Soo Min Kim, Allen Hsu, Yi-Hsien Lee, G Nandamuri, S Roumimov, R Solanki, Eli Sutter, Birol Ozturk, Peter Sutter, Enoch Nagelli, Rajesh Naik,

Yuhua Xue, Yunxiang Gao, Mei Zhang, and Liming Dai. Sensor arrays from multicomponent micropatterned nanoparticles and graphene. *Nanotechnology*, 24:444010, 2013.

[69] Alexey Lipatov, Alexey Varezhnikov, Peter Wilson, Victor Sysoev, Andrei Kolmakov, and Alexander Sinitskii. Highly selective gas sensor arrays based on thermally reduced graphene oxide. *Nanoscale*, 5:5426, 2013.

[70] Yong-Hui Zhang, Ya-Bin Chen, Kai-Ge Zhou, Jiayu Dai, Jianmin Yuan, Yongqing Cai, Miao Zhou, Minggang Zeng, Y G Zhou, X T Zu, P Yang, Martin Amft, Biplab Sanyal, Olle Eriksson, Ke-Feng Xie, Marek Gajdoš, Andreas Eichler, Jürgen Hafner, Yves Ferro, Nicolas Fernandez, Alain Allouche, Yun-Hao Lu, Yong-Qing Cai, Chun Zhang, and Yuan-Ping Feng. Adsorption of gas molecules on transition metal embedded graphene: a search for high- performance graphene-based catalysts and gas sensors. *Nanotechnology*, 22:385502, 2011.

[71] Yong-Hui Zhang, Ya-Bin Chen, Kai-Ge Zhou, Cai-Hong Liu, Jing Zeng, Hao-Li Zhang, and Yong Peng. Improving gas sensing properties of graphene by introducing dopants and defects: a first-principles study. *Nanotechnology*, 20(18):185504, 2009.

[72] Hui Zhang, Liwei Fan, Huilong Dong, Pingping Zhang, Kaiqi Nie, Jun Zhong, Youyong Li, Jinghua Guo, and Xuhui Sun. Spectroscopic Investigation of Plasma-Fluorinated Monolayer Graphene and Application for Gas Sensing. *ACS Applied Materials & Interfaces*, 8(13):8652–8661, 2016.

[73] Pablo Solís-Fernadez, Susumu Okada, Tohru Sato, Masaharu Tsuji, and Hiroki Ago. Gate-Tunable Dirac Point of Molecular Doped Graphene. *ACS Nano*, 10:2930–2939, 2016.

[74] R E Hill-Pearce, V Eless, A Lartsev, N A Martin, I L Barker Snook, J J Helmore, Rositsa Yakimova, J C Gallop, and L Hao. The effect of bilayer regions on the response of epitaxial graphene devices to environmental gating. *Carbon*, 93:896–902, 2015.

[75] Alexey Lipatov, Alexey Varezhnikov, Martin Augustin, Michael Bruns, Martin Sommer, Victor Sysoev, Andrei Kolmakov, and Alexander Sinitskii. Intrinsic device-to-device variation in graphene field-effect transistors on a Si/SiO 2 substrate as a platform for discriminative gas sensing. *Applied Physics Letters*, 104:013114, 2014.

[76] Jia Zhang, Rongfu Zhang, Xiaona Wang, Nantao Hu, Zhi Yang, Yanyan Wang, Ting Zhang, Syed Mubeen, Nosang V Myung, Ganhua Lu, Leonidas E Ocola, Junhong Chen, Rakesh Kumar, Deepak Varandani, B R Mehta, Quang Trung Tran, Tran My, Hoa Huynh, Duc Tai Tong, Christopher E Kehayias, Samuel Macnaughton, Sameer Sonkusale, and Cristian Staii. Kelvin probe microscopy and electronic transport measurements in reduced graphene oxide chemical sensors. *Nanotechnology*, 24:245502, 2013.

[77] Yang Yinxiao and Raghu Murali. Binding mechanisms of molecular oxygen and moisture to graphene. *Appl. Phys. Lett. Applied Physics Letters*, 98(93):093116, 2011.

[78] Igor A Pašti, Aleksandar Jovanovic, Ana S Dobrota, Slavko V Mentus, Börje Johansson, and Natalia V Skorodumova. Atomic adsorption on graphene with a single vacancy: systematic DFT study through the periodic table of elements. *Phys. Chem. Chem. Phys.*, 20:858–865, 2018.

[79] Y You, J Deng, X Tan, N Gorjizadeh, M Yoshimura, S C Smith, V Sahajwalla, and R K Joshi. On the mechanism of gas adsorption for pristine, defective and functionalized graphene. *Phys. Chem. Chem. Phys.*, 19(19):6051–6056, 2017.

[80] Geonyeop Lee, Gwangseok Yang, Ara Cho, Jeong Woo Han, and Jihyun Kim. Defect-engineered graphene chemical sensors with ultrahigh sensitivity. *Phys. Chem. Chem. Phys.*, 18(18):14198–14204, 2016.

[81] Alberto Cagliani, David Micheal, Angus Mackenzie, Lisa Katharina Tschammer, Filippo Pizzocchero, Kristoffer Almdal, and Peter Bøggild. Large-area nanopatterned graphene for ultrasensitive gas sensing. *Nano Research*, 7(5):743–754, 2014.

[82] Hongwei Gao and Zhijie Liu. DFT study of NO adsorption on pristine graphene. *RSC Advances*, 7:13082–13091, 2017.

[83] O Leenaerts, B Partoens, and F M Peeters. Adsorption of H_2O, NH_3, CO, NO_2, and NO on graphene: A first-principles study. *Physical Review B*, 77(12):125416, 2008.

[84] Tao Hu and Iann C Gerber. Theoretical Study of the Interaction of Electron Donor and Acceptor Molecules with Graphene. *Journal of Physical Chemistry C*, 117(5):2411–2420, 2013.

[85] T O Wehling, K S Novoselov, S V Morozov, E E Vdovin, M I Katsnelson, A K Geim, and A I Lichtenstein. Molecular Doping of Graphene. *Nano Letters*, 8(1):173–177, 2008.

[86] Indrani Choudhuri, Nandini Patra, Arup Mahata, Rajeev Ahuja, and Biswarup Pathak. B–N@ Graphene: Highly Sensitive and Selective Gas Sensor. *The Journal of Physical Chemistry C*, 119(44):24827–24836, 2015.

[87] Sadegh Mehdi Aghaei, M M Monshi, I Torres, S M J Zeidi, and I Calizo. DFT study of adsorption behavior of NO, CO, NO_2, and NH_3 molecules on graphene-like BC_3 : A search for highly sensitive molecular sensor. *Applied Surface Science*, 427:326–333, 2018.

[88] Nicola C G Black, CG Liu, Ruth Pearce, Bing Li, Stefan A Maier, Lesley F Cohen, John C Gallop, and Ling Hao. Graphene gas sensing using a non-contact microwave method. *Nanotechnology*, 28(39):395501, 2017.

[89] Nicola C. G. Black, I Rungger, B Li, S. A. Maier, L.F. Cohen, J. C. Gallop, and L. Hao. Adsorption dynamics of CVD graphene investigated by a contactless microwave method. *2D Materials*, 5(3):035024, 2018.

[90] Anindya Nag, Arkadeep Mitra, and Subhas Chandra Mukhopadhyay. Graphene and its sensor-based applications: A review. *Sensors and Actuators A: Physical*, 270:177–194, 2018.

[91] C Lin, J Gillespie, MD Schuder, W Duberstein, IJ Beverland, and MR Heal. Evaluation and calibration of aeroqual series 500 portable gas sensors for accurate measurement of ambient ozone and nitrogen dioxide. *Atmospheric Environment*, 100:111–116, 2015.

[92] PT Moseley. Solid state gas sensors. *Measurement Science and technology*, 8(3):223, 1997.

[93] Philip Peterson, Amrita Aujla, Kirsty Grant, Alex Brundle, Martin Thompson, Josh Vande Hey, and Roland Leigh. Practical use of metal oxide semiconductor gas sensors for measuring nitrogen dioxide and ozone in urban environments. *Sensors*, 17(7):1653, 2017.

[94] Aakash C Rai, Prashant Kumar, Francesco Pilla, Andreas N Skouloudis, Silvana Di Sabatino, Carlo Ratti, Ansar Yasar, and David Rickerby. End-user perspective of low-cost sensors for outdoor air pollution monitoring. *Science of The Total Environment*, 607:691–705, 2017.

[95] Ronan Baron and John Saffell. Amperometric gas sensors as a low cost emerging technology platform for air quality monitoring applications: A review. *ACS sensors*, 2(11):1553–1566, 2017.

[96] Sunho Kim, Dong-Ho Kim, and Sung-Gyu Park. Highly sensitive and on-site no 2 sers sensors operated under ambient conditions. *Analyst*, 143(13):3006–3010, 2018.

[97] Sukosin Thongrattanasiri, Frank H L Koppens, and F Javier García de Abajo. Complete optical absorption in periodically patterned graphene. *Physical review letters*, 108(4):47401, 2012.

[98] F H L MinovKoppensich, D E Chang, S Thongrattanasiri, and F J G de Abajo. Graphene Plasmonics: A Platform for Strong Light-Matter Interactions. *Optics and Photonics News*, 22(12):36, 2011.

[99] Caterina Cocchi, Deborah Prezzi, Alice Ruini, Marilia J Caldas, and Elisa Molinari. Electronics and Optics of Graphene Nanoflakes: Edge Functionalization and Structural Distortions. *Journal of Physical Chemistry C*, 116(33):17328–17335, 2012.

[100] Hans Riesen, Christian Wiebeler, and Stefan Schumacher. Optical Spectroscopy of Graphene Quantum Dots: The Case of C132. *The Journal of Physical Chemistry A*, 118(28):5189–5195, 2014.

[101] F Karimi and I Knezevic. Plasmons in graphene nanoribbons. *Physical Review B*, 96(12):125417, 2017.

[102] Yuan Zhao and Yanwu Zhu. Graphene-based hybrid films for plasmonic sensing. *Nanoscale*, 7(35):14561–14576, 2015.

[103] Hyeong Ryeol Park, Seon Namgung, Xiaoshu Chen, Nathan C. Lindquist, Vincenzo Giannini, Yan Francescato, Stefan A. Maier, and Sang Hyun Oh. Perfect Extinction of Terahertz Waves in Monolayer Graphene over 2-nm-Wide Metallic Apertures. *Advanced Optical Materials*, 3(5):667–673, 2015.

[104] M Khorasaninejad, S M Raeis-Zadeh, S Jafarlou, M J Wesolowski, C R Daley, J B Flannery, J Forrest, S Safavi-Naeini, and S S Saini. Highly enhanced Raman scattering of graphene using plasmonic nano-structure. *Scientific Reports*, 3:2936, 2013.

[105] H Graf, D Mele, M Rosticher, L Banszerus, D Stampfer, T. Taniguchi, K. Watanabe, E. Bocquillon, G. Féve, J. M. Berroir, E. H. T Teo, and B. Plaçais. Ultra-long wavelength Dirac plasmons in graphene capacitors. *JPhys Materials*, 1(1):01LT02, 2018.

[106] Alessandro Principi, Erik Van Loon, Marco Polini, and Mikhail I Katsnelson. Confining graphene plasmons to the ultimate limit. *Physical Review B*, 98(3):35427, 2018.

[107] Hai Hu, Xiaoxia Yang, Feng Zhai, Debo Hu, Ruina Liu, Kaihui Liu, Zhipei Sun, and Qing Dai. Far-field nanoscale infrared spectroscopy of vibrational fingerprints of molecules with graphene plasmons. *Nature Communications*, 7:12334, 2016.

[108] Yu Wu, Baicheng Yao, Caibin Yu, and Yunjiang Rao. Optical graphene gas sensors based on microfibers: A review. *Sensors*, 18(4):941, 2018.

[109] S Sridevi., K.S. Vasu, Navakanta Bhat, S. Asokan, and A.K. Sood. Ultra sensitive NO_2 gas detection using the reduced graphene oxide coated etched fiber Bragg gratings. *Sensors and Actuators B: Chemical*, 223:481–486, 2016.

[110] Anqi Zhang, Yu Wu, Baicheng Yao, and Yuan Gong. Optimization Study on Graphene-Coated Microfiber Bragg Grating Structures for Ammonia Gas Sensing. *Photonic Sensors*, 5(1):84–90, 2015.

[111] Baicheng Yao, Yu Wu, Yang Cheng, Anqi Zhang, Yuan Gong, Yun-Jiang Rao, Zegao Wang, and Yuanfu Chen. All-optical Mach–Zehnder interferometric NH_3 gas sensor based on graphene/microfiber hybrid waveguide. *Sensors and Actuators B: Chemical*, 194:142–148, 2014.

[112] Yu Wu, Baicheng Yao, Anqi Zhang, Yunjiang Rao, Zegao Wang, Yang Cheng, Yuan Gong, Weili Zhang, Yuanfu Chen, and K. S. Chiang. Graphene-coated microfiber Bragg grating for high-sensitivity gas sensing. *Optics Letters*, 39(5):1235, 2014.

[113] Fred Schedin, Elefterios Lidorikis, Antonio Lombardo, Vasyl G Kravets, Andre K Geim, Alexander N Grigorenko, Kostya S Novoselov, and Andrea C Ferrari. Surface-Enhanced Raman Spectroscopy of Graphene. *ACS Nano*, 4(10):5617–5626, 2010.

[114] Pu Wang, Wei Zhang, Owen Liang, Marcos Pantoja, Jens Katzer, Thomas Schroeder, and Ya-Hong Xie. Giant Optical Response from Graphene-Plasmonic System. *ACS Nano*, 6(7):6244–6249, 2012.

[115] Kannan Balasubramanian, Laura Zuccaro, and Klaus Kern. Tunable Enhancement of Raman Scattering in Graphene-Nanoparticle Hybrids. *Advanced Functional Materials*, 24(40):6348–6358, 2014.

[116] Xi Ling, Liming Xie, Yuan Fang, Hua Xu, Haoli Zhang, Jing Kong, Mildred S Dresselhaus, Jin Zhang, and Zhongfan Liu. Can Graphene be used as a Substrate for Raman Enhancement? *Nano Letters*, 10(2):553–561, 2010.

[117] Seung Min Song, Jong Kyung Park, Jae Sul, and Byung Jin Cho. Determination of Work Function of Graphene under a Metal Electrode and Its Role in Contact Resistance. *Nano Letters*, 12(8):3887–3892, 2012.

[118] G Giovannetti, P A Khomyakov, G Brocks, V M Karpan, J Van Den Brink, and P J Kelly. Doping graphene with metal contacts. *Physics Review Letters*, 101(2):026803, 2008.

[119] Eduardo J H Lee, Kannan Balasubramanian, Ralf Thomas Weitz, Marko Burghard, and Klaus Kern. Contact and edge effects in graphene devices. *Nature Nanotechnology*, 3(8):486–490, 2008.

[120] Quanfu Li, Weihua Liu, Guiming Cao, Xin Li, and Xiaoli Wang. A study of gas sensing behavior of metal-graphene contact with transfer length method. *Applied Physics Letters*, 108(22):221604–232105, 2016.

[121] Jian Zhang, Anthony Boyd, Alexander Tselev, Makarand Paranjape, and Paola Barbara. Mechanism of NO_2 detection in carbon nanotube field effect transistor chemical sensors. *Applied Physics Letters*, 88(12):123112, 2006.

[122] Kostya S Novoselov, Andre K Geim, S V Morozov, D Jiang, Y Zhang, S V Dubonos, I V Grigorieva, and A A Firsov. Electric Field Effect in Atomically Thin Carbon Films. *Science*, 306(5696):666–669, 2004.

[123] Lin Yuan, Jun Ge, Xianglin Peng, Qian Zhang, Zefei Wu, Yu Jian, Xiaolu Xiong, Hongxing Yin, and Junfeng Han. A reliable way of mechanical exfoliation of

large scale two dimensional materials with high quality. *AIP Advances*, 6:125201, 2016.

[124] A K Geim and I V Grigorieva. Van der Waals heterostructures. *Nature*, 499(7459):419–425, 2013.

[125] Ankur Gupta, Tamilselvan Sakthivel, and Sudipta Seal. Recent development in 2D materials beyond graphene. *Progress in Materials Science*, 75:44–126, 2015.

[126] Andrea C. Ferrari, Francesco Bonaccorso, Vladimir Fal'ko, Konstantin S. Novoselov, Stephan Roche, Peter Bøggild, Stefano Borini, Frank H. L. Koppens, Vincenzo Palermo, Nicola Pugno, José A. Garrido, Roman Sordan, Alberto Bianco, Laura Ballerini, Maurizio Prato, Elefterios Lidorikis, Jani Kivioja, Claudio Marinelli, Tapani Ryhänen, Alberto Morpurgo, Jonathan N. Coleman, Valeria Nicolosi, Luigi Colombo, Albert Fert, Mar Garcia-Hernandez, Adrian Bachtold, Grégory F. Schneider, Francisco Guinea, Cees Dekker, Matteo Barbone, Zhipei Sun, Costas Galiotis, Alexander N. Grigorenko, Gerasimos Konstantatos, Andras Kis, Mikhail Katsnelson, Lieven Vandersypen, Annick Loiseau, Vittorio Morandi, Daniel Neumaier, Emanuele Treossi, Vittorio Pellegrini, Marco Polini, Alessandro Tredicucci, Gareth M. Williams, Byung Hee Hong, Jong-Hyun Ahn, Jong Min Kim, Herbert Zirath, Bart J. van Wees, Herre van der Zant, Luigi Occhipinti, Andrea Di Matteo, Ian A. Kinloch, Thomas Seyller, Etienne Quesnel, Xinliang Feng, Ken Teo, Nalin Rupesinghe, Pertti Hakonen, Simon R. T. Neil, Quentin Tannock, Tomas Löfwander, and Jari Kinaret. Science and technology roadmap for graphene, related two-dimensional crystals, and hybrid systems. *Nanoscale*, 7(11):4598–4810, 2015.

[127] Bottari Giovanni, M Ángeles Herranz, Leonie Wibmer, Michel Volland, Laura Rodríguez-Pérez, Dirk M Guldi, Andreas Hirsch, Nazario Martín, Francis D'Souza,

and Tomás Torres. Chemical functionalization and characterization of graphene-based materials. *Chemical Society Reviews*, 46(15):4464, 2017.

[128] Sandip Niyogi, Elena Bekyarova, Jeongmin Hong, Sakhrat Khizroev, Claire Berger, Walt De Heer, and Robert C Haddon. Covalent Chemistry for Graphene Electronics. *Journal of Physical Chemistry Letters*, 2(19):2487–2498, 2011.

[129] Demetrios D. Chronopoulos, Aristides Bakandritsos, Martin Pykal, Radek Zbořil, and Michal Otyepka. Chemistry, properties, and applications of fluorographene. *Applied Materials Today*, 9:60–70, 2017.

[130] Ruitao Lv, Gugang Chen, Qing Li, Amber McCreary, Andres Botello-Mendez, SV Morozov, Liangbo Liang, Xavier Declerck, Nestor Perea-Lopez, David A Cullen, Simin Feng, Ana Laura Elias, Rodolfo Cruz-Silva, Kazunori Fujisawa, Morinobu Endo, Feiju Kang, Jean-Christophe Charlier, Vincent Meunier, Minghu Pan, Avetik R. Harutyunyan, Konstantin S. Novoselov, and Maurico Terrones. Ultrasensitive gas detection of large-area boron-doped graphene. *PNAS*, 112(47):14527–14532, 2015.

[131] Da Chen, Hongbin Feng, and Jinghong Li. Graphene Oxide: Preparation, Functionalization, and Electrochemical Applications. *Chemical Reviews*, 112(11):6027–6053, 2012.

[132] Dagmar Matochová, Miroslav Medved', Aristides Bakandritsos, Tomáš Steklý, Radek Zbořil, and Michal Otyepka. 2D Chemistry: Chemical Control of Graphene Derivatization. *Journal of Physical Chemistry Letters*, 9(13):3580–3585, 2018.

[133] Bruno De La Torre, Martin Švec, Prokop Hapala, Jesus Redondo, Ondřej Krejčí, Rabindranath Lo, Debashree Manna, Amrit Sarmah, Dana Nachtigallová, Jiří Tuček, Piotr Błoński, Michal Otyepka, Radek Zbořil, Pavel Hobza, and Pavel

Jelínek. Non-covalent control of spin-state in metal-organic complex by positioning on N-doped graphene. *Nature Communications*, 9(2831):1–9, 2018.

[134] F. Ricciardella, S. Vollebregt, T. Polichetti, B. Alfano, E. Massera, and P. M. Sarro. An innovative approach to overcome saturation and recovery issues of CVD graphene-based gas sensors. In *2017 IEEE SENSORS*, pages 1–3. IEEE, 2017.

[135] Ruitao Lv, Qing Li, Andrés R Botello-Méndez, Takuya Hayashi, Bei Wang, Ayse Berkdemir, Qingzhen Hao, Ana Laura Elías, Rodolfo Cruz-Silva, Humberto R Gutiérrez, Yoong Ahm Kim, Hiroyuki Muramatsu, Jun Zhu, Morinobu Endo, Humberto Terrones, Jean-Christophe Charlier, Minghu Pan, and Mauricio Terrones. Nitrogen-doped graphene: beyond single substitution and enhanced molecular sensing. *Scientific Reports*, 2:586, 2012.

[136] Min Yi and Zhigang Shen. A review on mechanical exfoliation for the scalable production of graphene. *Journal of Materials Chemistry A*, 3(22):11700–11715, 2015.

[137] Jinming Cai, Pascal Ruffieux, Rached Jaafar, Marco Bieri, Thomas Braun, Stephan Blankenburg, Matthias Muoth, Ari P Seitsonen, Moussa Saleh, Xinliang Feng, Klaus Müllen, and Roman Fasel. Atomically precise bottom-up fabrication of graphene nanoribbons. *Nature*, 466(7305):470–473, 2010.

[138] Pascal Ruffieux, Shiyong Wang, Bo Yang, Carlos Sánchez-Sánchez, Jia Liu, Thomas Dienel, Leopold Talirz, Prashant Shinde, Carlo A Pignedoli, Daniele Passerone, Tim Dumslaff, Xinliang Feng, Klaus Müllen, and Roman Fasel. On-surface synthesis of graphene nanoribbons with zigzag edge topology. *Nature*, 531(7579):489–493, 2016.

[139] Oliver Gröning, Shiyong Wang, Xuelin Yao, Carlo A Pignedoli, Gabriela Borin Barin, Colin Daniels, Andrew Cupo, Vincent Meunier, Xinliang Feng, Akimitsu Narita, Klaus Müllen, Pascal Ruffieux, and Roman Fasel. Engineering of robust topological quantum phases in graphene nanoribbons. *Nature*, 560(7717):209–213, 2018.

[140] Daniel J Rizzo, Gregory Veber, Ting Cao, Christopher Bronner, Ting Chen, Fangzhou Zhao, Henry Rodriguez, Steven G Louie, Michael F Crommie, and Felix Fischer. Topological band engineering of graphene nanoribbons. *Nature*, 560(7717):204–209, 2018.

[141] Sukang Bae, Hyeongkeun Kim, Youngbin Lee, Xiangfan Xu, Jae-Sung Park, Yi Zheng, Jayakumar Balakrishnan, Tian Lei, Hye Ri Kim, Young Il Song, and Others. Roll-to-roll production of 30-inch graphene films for transparent electrodes. *Nature Nanotechnology*, 5(8):574–578, 2010.

[142] S. Vollebregt, B. Alfano, F. Ricciardella, A. J.M. Giesbers, Y. Grachova, H. W. Van Zeijl, T. Polichetti, and P. M. Sarro. A transfer-free wafer-scale CVD graphene fabrication process for MEMS/NEMS sensors. Number January, pages 17–20, 2016.

[143] Mingguang Chen, Robert C Haddon, Ruoxue Yan, and Elena Bekyarova. Advances in transferring chemical vapour deposition graphene: a review. *Materials Horizons*, 4(4):1054–1063, 2017.

[144] Maria Kim, Ali Shah, Changfeng Li, Petri Mustonen, Jannatul Susoma, Farshid Manoocheri, Juha Rirkonen, and Harri Lipsanen. Direct transfer of wafer-scale graphene films. *2D Materials*, 4:035004, 2017.

[145] Zhikun Zhang, Jinhong Du, Dingdong Zhang, Hengda Sun, Lichang Yin, Laipeng Ma, Jiangshan Chen, Dongge Ma, Hui-Ming Cheng, and Wencai Ren. Rosin-enabled ultraclean and damage-free transfer of graphene for large-area flexible organic light-emitting diodes. *Nature Communications*, 8:14560, 2017.

[146] Jie Song, Fong-Yu Kam, Rui-Qi Png, Wei-Ling Seah, Jing-Mei Zhuo, Geok-Kieng Lim, Peter K H Ho, and Lay-Lay Chua. A general method for transferring graphene onto soft surfaces. *Nature Nanotechnology*, 8(5):356–362, 2013.

[147] Michael Her, Ryan Beams, and Lukas Novotny. Graphene transfer with reduced residue. *Physics Letters A*, 377(21):1455–1458, 2013.

[148] Xuelei Liang, Brent A Sperling, Irene Calizo, Guangjun Cheng, Christina Ann Hacker, Qin Zhang, Yaw Obeng, Kai Yan, Hailin Peng, Qiliang Li, Xiaoxiao Zhu, Hui Yuan, Angela R Hight Walker, Zhongfan Liu, Lian-mao Peng, and Curt A Richter. Toward Clean and Crackless Transfer of Graphene. *ACS Nano*, 5(11):9144–9153, 2011.

[149] Ji Won Suk, Alexander Kitt, Carl W Magnuson, Yufeng Hao, Samir Ahmed, Jinho An, Anna K Swan, Bennett B Goldberg, and Rodney S Ruoff. Transfer of CVD-Grown Monolayer Graphene onto Arbitrary Substrates. *ACS Nano*, 5(9):6916–6924, 2011.

[150] Xuesong Li, Yanwu Zhu, Weiwei Cai, Mark Borysiak, Boyang Han, David Chen, Richard D Piner, Luigi Colombo, and Rodney S Ruoff. Transfer of Large-Area Graphene Films for High-Performance Transparent Conductive Electrodes. *Nano Letters*, 9(12):4359–4363, 2009.

[151] Luca Banszerus, Michael Schmitz, Stephan Engels, Jan Dauber, Martin Oellers, Federica Haupt, Kenji Watanabe, Takashi Taniguchi, Bernd Beschoten, and

Christoph Stampfer. Ultrahigh-mobility graphene devices from chemical vapor deposition on reusable copper. *Science Advances*, 1(6):e1500222, 2015.

[152] C V Raman and K S Krishnan. A new class of spectra due to secondary radiation Part I. *Indian J. Phys*, 2:399–419, 1928.

[153] C. v. Raman and K. S. Krishnan. A new Type of Secondary Radiation. *Nature*, 121:501, 1921.

[154] Peter Vandenabeele. *Practical Raman spectroscopy : an introducti*. Wiley, 2013.

[155] Achxntya K Gangulyt and Joseph L Birman. Theory of Lattice Raman Scattering in Insulators*. *Physical Review*, 162(3):162–807, 1967.

[156] Ferraro John R Nakamoto Kazuo & Brown Chris W Ferraro John R. *Introductory Raman Spectroscopy*. Burlington : Elsevier Science, 2003.

[157] Manuel Cardona and Roberto Merlin. *Light scattering in solids I*. Springer-Verlag, 2 edition, 1983.

[158] Axel Eckmann. *Raman Spectroscopy of Graphene, its derivatives and graphene-based heterostructures*. PhD thesis, 2013.

[159] Robert C Maher. *Surface Enhancement of Raman Scattering*. PhD thesis, University of London, Imperial College, 2007.

[160] Mario González-Cardel, Pedro Arguijo, and Rufino Díaz-Uribe. Gaussian beam radius measurement with a knife-edge: a polynomial approximation to the inverse error function. *Applied Optics*, 52(16):3849–3855, 2013.

[161] Rufino Díaz-Uribe, Martha Rosete-Aguilar, and Roberto Ortega-Martínez. Position sensing of a Gaussian beam with a power meter and a knife edge. Technical Report 3, 1993.

[162] Walter Koechner. *Solid-State Laser Engineering*, volume 9. Springer, Atlanta, 6 edition, 1994.

[163] Ji Eun Lee, Gwanghyun Ahn, Jihye Shim, Young Sik Lee, and Sunmin Ryu. Optical separation of mechanical strain from charge doping in graphene. *Nature Communications*, 3:1024, 2012.

[164] L M Malard, M A Pimenta, G Dresselhaus, and M S Dresselhaus. Raman spectroscopy in graphene. *Physics Reports*, 473(5–6):51–87, 2009.

[165] E Kogan and V U Nazarov. Symmetry classification of energy bands in graphene. *Physical Review B*, 85(11):115418, 2012.

[166] Andrea C Ferrari and Denis M Basko. Raman spectroscopy as a versatile tool for studying the properties of graphene. *Nature Nanotechnology*, 8(4):235–246, 2013.

[167] M S Dresselhaus, G Dresselhaus, R Saito, and A Jorio. Raman spectroscopy of carbon nanotubes. *Physics Reports*, 409(409):47–99, 2005.

[168] R Saito, A Jorio, A G Souza Filho, G Dresselhaus, M S Dresselhaus, and M A Pimenta. Probing Phonon Dispersion Relations of Graphite by Double Resonance Raman Scattering. *Physical Review Letters*, 88(2), 2002.

[169] Anindya Das, S Pisana, B Chakraborty, S Piscanec, S K Saha, U V Waghmare, K S Novoselov, H R Krishnamurthy, A K Geim, A C Ferrari, and Others. Monitoring dopants by Raman scattering in an electrochemically top-gated graphene transistor. *Nature Nanotechnology*, 3(4):210–215, 2008.

[170] Martin Kalbac, Alfonso Reina-Cecco, Hootan Farhat, Jing Kong, Ladislav Kavan, and Mildred S Dresselhaus. The Influence of Strong Electron and Hole Doping

on the Raman Intensity of Chemical Vapo Deposition Graphene. *ACS Nano*, 4(10):6055–6063, 2010.

[171] D L Mafra, G Samsonidze, L M Malard, D C Elias, J C Brant, F Plentz, E S Alves, and M A Pimenta. Determination of LA and TO phonon dispersion relations of graphene near the Dirac point by double resonance Raman scattering. *Physical Review B*, 76(23):233407, 2007.

[172] D M Basko, S Piscanec, and A C Ferrari. Electron-electron interactions and doping dependence of the two-phonon Raman intensity in graphene. *Physical Review B*, 80(16):165413, 2009.

[173] Michele Lazzeri and Francesco Mauri. Nonadiabatic Kohn Anomaly in a Doped Graphene Monolayer. *Physics Review Letters*, 97(26):266407, 2006.

[174] M Mohr, J Maultzsch, and C Thomsen. Splitting of the Raman 2D band of graphene subjected to strain. *Physical Review B*, 82(20):201409, 2010.

[175] A C Ferrari, J C Meyer, V Scardaci, C Casiraghi, M Lazzeri, F Mauri, S Piscanec, D Jiang, K S Novoselov, S Roth, and A K Geim. Raman Spectrum of Graphene and Graphene Layers. *Physics Review Letters*, 97(18):187401, 2006.

[176] Xiaochen Dong, Dongliang Fu, Wenjing Fang, Yumeng Shi, Peng Chen, and Lain-Jong Li. Doping Single-Layer Graphene with Aromatic Molecules. *Small*, 5(12):1422–1426, 2009.

[177] Axel Eckmann, Alexandre Felten, Artem Mishchenko, Liam Britnell, Ralph Krupke, Kostya S Novoselov, and Cinzia Casiraghi. Probing the Nature of Defects in Graphene by Raman Spectroscopy. *Nano Letters*, 12:3925–3930, 2012.

[178] W Richard Bowen and Nidal Hilal. *Atomic Force Microscopy in Process Engineering: An Introduction to AFM for Improved Processes and Products*. Butterworth-Heinemann, first edition, 2009.

[179] Nader Jalili and Karthik Laxminarayana. A review of atomic force microscopy imaging systems: application to molecular metrology and biological sciences. *Mechatronics*, 14(8):907–945, 2004.

[180] Khaled Kaja. *Development of nano-probe techniques for work function and assessment and application to materials for microelectronics*. PhD thesis, University of Grenoble, 2010.

[181] José Manoel Balthazar, Angelo Marcelo Tusset, Atila Madureira Bueno, and Bento Rodrigues de Pontes Junior. *On an overview of nonlinear and chaotic behavior and their controls of an atomic force microscopy (afm) vibrating problem*. INTECH Open Access Publisher, 2012.

[182] Sascha Sadewasser and Thilo Glatzel. *Kelvin probe force microscopy: measuring and compensating electrostatic forces*, volume 48. Springer Science & Business Media, 2011.

[183] Wilhelm Melitz, Jian Shen, Andrew C Kummel, and Sangyeob Lee. Kelvin probe force microscopy and its application. *Surface Science Reports*, 66(1):1–27, 2011.

[184] Wilford N Hansen and Galen J Hansen. Standard reference surfaces for work function measurements in air. *Surface science*, 481(1):172–184, 2001.

[185] Y Park, V Choong, Y Gao, B R Hsieh, and C W Tang. Work function of indium tin oxide transparent conductor measured by photoelectron spectroscopy. *Citation: Appl. Phys. Lett*, 68(19):295, 1996.

[186] H O Jacobs, H F Knapp, and A Stemmer. Practical aspects of Kelvin probe force microscopy. *Review of Scientific Instruments*, 70(3):1168, 1999.

[187] H O Jacobs, P Leuchtmann, O J Homan, and A Stemmer. Resolution and contrast in Kelvin probe force microscopy. *Journal of Applied Physics*, 84(3):1756, 1998.

[188] Young-Jun Yu, Yue Zhao, Sunmin Ryu, Louis E Brus, Kwang S Kim, and Philip Kim. Tuning the Graphene Work Function by Electric Field Effect. *Nano Letters*, 9(10):3430–3434, 2009.

[189] Rui Wang, Ruth Pearce, John Gallop, Trupti Patel, Fang Zhao, Andrew Pollard, Norbert Klein, Richard Jackman, Amaia Zurutuza, and Ling Hao. Surface Topography: Metrology and Properties Investigation of CVD graphene topography and surface electrical properties Related content Investigations of the effect of SiC growth face on graphene thickness uniformity and electronic properties. *Surface Topography: Metrology and Properties*, 4(2):025001, 2016.

[190] Fei Long, Poya Yasaei, Raj Sanoj, Wentao Yao, Petr Kraí, Amin Salehi-Khojin, and Reza Shahbazian-Yassar. Characteristic Work Function Variations of Graphene Line Defects. *ACS Applied Materials and Interfaces*, 8(28):18360–18366, 2016.

[191] Vishal Panchal, Arseniy Lartsev, Alessandra Manzin, Rositza Yakimova, Alexander Tzalenchuk, and Olga Kazakova. Visualisation of edge effects in side-gated graphene nanodevices. *Scientific Reports*, 4:5881, 2014.

[192] Jeremy T. Robinson, James Culbertson, Morgann Berg, and Taisuke Ohta. Work Function Variations in Twisted Graphene Layers. *Scientific Reports*, 8(1):2006, 2018.

[193] Sujit S Datta, Douglas R Strachan, E J Mele, and A T Charlie Johnson. Surface potentials and layer charge distributions in few-layer graphene films. *Nano Letters*, 9(1):7–11, 2008.

[194] D Ziegler, P Gava, J Güttinger, F Molitor, L Wirtz, M Lazzeri, A M Saitta, A Stemmer, F Mauri, and C Stampfer. Variations in the work function of doped single- and few-layer graphene assessed by Kelvin probe force microscopy and density functional theory. *Physical Review B*, 83(23):235434, 2011.

[195] Xin He, Ning Tang, Xiaoxiao Sun, Lin Gan, Fen Ke, Tao Wang, Fujun Xu, Xinqiang Wang, Xuelin Yang, Weikun Ge, and Bo Shen. Tuning the graphene work function by uniaxial strain. *Applied Physics Letters*, 106(4):043106, 2015.

[196] Yumeng Shi, Xiaochen Dong, Peng Chen, Junling Wang, and Lain-Jong Li. Effective doping of single-layer graphene from underlying SiO 2 substrates. *Physical Review B*, 79(11):115402, 2009.

[197] Rajni Garg, Naba K Dutta, and Namita Roy Choudhury. Work Function Engineering of Graphene. *Nanomaterials*, 4(2):267, 2014.

[198] Tani Tadaaki. Analysis of Work Functions of Noble Metals in Ambient Atmosphere in Commemoration of Journal Award. Technical Report 1, 2015.

[199] Jining Xie and James P. Spallas. Different Contrast Mechanisms in SEM Imaging of Graphene Application Note. *Agilent Technologies Report*.

[200] Jaesung Lee, Xuqian Zheng, Robert C. Roberts, and Philip X.-L. Feng. Scanning electron microscopy characterization of structural features in suspended and non-suspended graphene by customized CVD growth. *Diamond and Related Materials*, 54:64–73, 2015.

[201] S J Haigh, A Gholinia, R Jalil, S Romani, L Britnell, D C Elias, K S Novoselov, L A Ponomarenko, A K Geim, and R Gorbachev. Cross-sectional imaging of individual layers and buried interfaces of graphene-based heterostructures and superlattices. *Nature Materials*, 11(9):764–767, 2012.

[202] Hugh D. Young and Roger A. Freedman. *University Physics: with Modern Physcis*. Pearson Addison Wesley, San Francisco, 12 edition, 2008.

[203] Werner Herres and Joern Gronholz. Understanding FT-IR Data Processing. 1985.

[204] K S A Novoselov, Andre K Geim, S V Morozov, D Jiang, M I Katsnelson, I V Grigorieva, S V Dubonos, and A Firsov. Two-dimensional gas of massless Dirac fermions in graphene. *Nature*, 438(7065):197–200, 2005.

[205] Y. W. Tan, Y. Zhang, K. Bolotin, Y. Zhao, E. H. Hwang, S. Das Sarma, H. L. Stormer, and P. Kim. Measurement of Scattering Rate and Minimum Conductivity in Graphene. *Physics Review Letters*, 99:246803, 2007.

[206] Frank Schwierz. Graphene Transistors. *Nature Nanotechnology*, 5(7):487–496, 2010.

[207] Nuno JG Couto, Davide Costanzo, Stephan Engels, Dong-Keun Ki, Kenji Watanabe, Takashi Taniguchi, Christoph Stampfer, Francisco Guinea, and Alberto F Morpurgo. Random strain fluctuations as dominant disorder source for high-quality on-substrate graphene devices. *Physical Review X*, 4(4):041019, 2014.

[208] S Engels, B Terrés, A Epping, T Khodkov, K Watanabe, T Taniguchi, B Beschoten, and C Stampfer. Limitations to carrier mobility and phase-coherent transport in bilayer graphene. *Physical review letters*, 113(12):126801, 2014.

[209] Mailadil T Sebastian. *Dielectric materials for wireless communication*. Elsevier, 2010.

[210] Hesham A. Auda, Allen W. Glisson, Pierre Guillon, Donald F. Hanson, Darko Kajfez, Amarpal S. Khanna, and Kryzystof A. Michalski. *Dielectric Resonators*. Noble Publishing Corporation, Tucker, Georgia, 2 edition, 1986.

[211] Aldo Petosa and Apisak Ittipiboon. Dielectric resonator antennas: A historical review and the current state of the art. *IEEE antennas and Propagation Magazine*, 52(5):91–116, 2010.

[212] Jerzy Krupka. Frequency domain complex permittivity measurements at microwave frequencies. *Measurement Science and Technology*, 17(6):R55, 2006.

[213] Jerzy Krupka, Martin Klinger, Matthias Kuhn, A Baryanyak, Michael Stiller, Johann Hinken, and Jozef Modelski. Surface resistance measurements of hts films by means of sapphire dielectric resonators. *IEEE Transactions on Applied Superconductivity*, 3(3):3043–3048, 1993.

[214] N Klein, U Dähne, U Poppe, N Tellmann, K Urban, S Orbach, S Hensen, G Müller, and H Piel. Microwave surface resistance of epitaxial yba 2 cu 3 o 7 thin films at 18.7 ghz measured by a dielectric resonator technique. *Journal of superconductivity*, 5(2):195–201, 1992.

[215] O. Shaforost, K. Wang, S. Goniszewski, M. Adabi, Z. Guo, S. Hanham, J. Gallop, L. Hao, and N. Klein. Contact-free sheet resistance determination of large area graphene layers by an open dielectric loaded microwave cavity. *Journal of Applied Physics*, 117(2):024501, 2015.

[216] N Klein, H Chaloupka, G Müller, S Orbach, H Piel, B Roas, L Schultz, U Klein, and M Peiniger. The effective microwave surface impedance of high t c thin films. *Journal of Applied Physics*, 67(11):6940–6945, 1990.

[217] Katrin Kneipp, Martin Moskovits, and Harald Kneipp. *Surface-Enhanced Raman Scattering. Physics and Applications*. 2006.

[218] Paul L Stiles, Jon A Dieringer, Nilam C Shah, and Richard P Van Duyne. Surface-enhanced Raman spectroscopy. *Annu. Rev. Anal. Chem.*, 1:601–626, 2008.

[219] Tuan Vo-Dinh. Surface-enhanced Raman spectroscopy using metallic nanostructures. *TrAC Trends in Analytical Chemistry*, 17(8):557–582, 1998.

[220] A Otto, I Mrozek, H Grabhorn, and W Akemann. Surface-enhanced Raman scattering. *Journal of Physics: Condensed Matter*, 4(5):1143–1212, 1143.

[221] Xi Ling, Shengxi Huang, Shibin Deng, Nannan Mao, Jing Kong, Mildred S Dresselhaus, and Jin Zhang. Lighting Up the Raman Signal of Molecules in the Vicinity of Graphene Related Materials. *Accounts of Chemical Research*, 48(7):1862–1870, 2015.

[222] Xi Ling, L G Moura, Marcos A Pimenta, and Jin Zhang. Charge-Transfer Mechanism in Graphene-Enhanced Raman Scattering. *Physical Review C*, 116(47):25112–25118, 2012.

[223] Kostiantyn Turcheniuk, Rabah Boukherroub, and Sabine Szunerits. Gold-graphene nanocomposites for sensing and biomedical applications. *Journal of Materials Chemistry B*, 3(21):4301–4324, 2015.

[224] Qingzhen Hao, Bei Wang, Jeremy A Bossard, Brian Kiraly, Yong Zeng, I-Kao Chiang, Lasse Jensen, Douglas H Werner, and Tony Jun Huang. Surface-Enhanced Raman Scattering Study on Graphene-Coated Metallic Nanostructure Substrates. *The Journal of Physical Chemistry C*, 116(13):7249–7254, 2012.

[225] Dmitry K Polyushkin, James Milton, Salvatore Santandrea, Saverio Russo, Monica F Craciun, Stephen J Green, Laureline Mahe, C Peter Winolve, and William L

Barnes. Graphene as a substrate for plasmonic nanoparticles. *Journal of Optics*, 15(11):114001–114007, 2013.

[226] Leilei Kang, Jiayu Chu, Hongtao Zhao, Ping Xu, and Mengtao Sun. Recent progress in the applications of graphene in surface-enhanced Raman scattering and plasmon-induced catalytic reactions. *Journal of Material Chemistry C*, 3(35):9024–9037, 2015.

[227] E B Barros and M S Dresselhaus. Theory of Raman enhancement by two-dimensional materials: Applications for graphene-enhanced Raman spectroscopy. *Physical Review B*, 90(3):035443, 2014.

[228] Hua Xu, Liming Xie, Haoli Zhang, and Jin Zhang. Effect of Graphene Fermi Level on the Raman Scattering Intensity of Molecules on Graphene. *ACS Nano*, 5(7):5338–5344, 2011.

[229] C Casiraghi. Doping dependence of the Raman peaks intensity of graphene close to the Dirac point. *Physical Review B*, 80(23):233407, 2009.

[230] O Ochedowski, G Begall, N Scheuschner, M El Kharrazi, J Maultzsch, and M Schleberger. Graphene on Si(111)7x7. *Nanotechnology*, 23(40):405708, 2012.

[231] Krzysztof Gajewski, Stefan Goniszewski, Anna Szumska, Magdalena Moczala, Piotr Kunicki, John Gallop, Norbert Klein, Ling Hao, and Teodor Gotszalk. Raman Spectroscopy and Kelvin Probe Force Microscopy characteristics of the CVD suspended graphene. *Diamond & Related Materials*, 64:27–33, 2016.

[232] Martin Fleischmann, Patrick J Hendra, and A J McQuillan. Raman spectra of pyridine adsorbed at a silver electrode. *Chemical Physics Letters*, 26(2):163–166, 1974.

[233] David L Jeanmaire and Richard P Van Duyne. Surface Raman Spectroelectrochemistry Part I: Heterocyclic, aromatic, and aliphatic amines adsorbed on the anodized silver electrode. *Journal of electroanalytical chemistry and interfacial electrochemistry*, 84(1):1–20, 1977.

[234] Grant M. Albrecht and Alan J. Creighton. Anomalously intense Raman spectra of pyridine at a silver electrode. *J. Am. Chem. Soc*, 99(15):5215–5217, 1977.

[235] M Moskovits. Surface roughness and the enhanced intensity of Raman scattering by molecules adsorbed on metals. *The Journal of Chemical Physics*, 69(9):4159–4161, 1978.

[236] Meikun Fan, Gustavo F. S. Andrade, and Alexandre G. Brolo. A review on the fabrication of substrates for surface enhanced Raman spectroscopy and their applications in analytical chemistry. *Analytica Chmica Acta*, 693(1):7–25, 2011.

[237] Pamela A Mosier-Boss. Review of SERS Substrates for Chemical Sensing. *Nanomaterials*, 7(6):142, 2017.

[238] Pablo. Le Ru E. & Etchegoin. *Principles of Surface-Enhanced Raman Spectroscopy and Related Plasmonic Effects.* Elsevier Science & Technology, Amsterdam, 1 edition, 2009.

[239] Stefan Alexander Maier. *Plasmonics: fundamentals and applications*. Springer Science & Business Media, 2007.

[240] Xiayan Wu, Esa Jaatinen, Sarina Sarina, Judith Langer, Sergey M Novikov, Luis M Liz-Marzán, Vincenzo Amendola, Roberto Pilot, Marco Frasconi, Onofrio M Maragò, and Maria Antonia Iatì. Surface plasmon resonance in gold nanoparticles: a review. *Journal of Physics: Condensed Matter*, 29(20):203002, 2017.

[241] Martin Moskovits. Surface-enhanced Raman spectroscopy: a brief retrospective. *Journal of Raman Spectroscopy*, 36(6-7):485–496, 2005.

[242] Shuming Nie and Steven R. Emroy. Probing Single Molecules and Single Nanoparticles by Surface-Enhanced Raman Scattering. *Science*, 275(5303):1102–1106, 1997.

[243] Martin Moskovits. Surface-enhanced spectroscopy. *Reviews of Modern Physics*, 57(3):783–826, 1985.

[244] E C Le Ru and P G Etchegoin. Rigorous justification of the| E| 4 enhancement factor in surface enhanced Raman spectroscopy. *Chemical Physics Letters*, 423(1):63–66, 2006.

[245] Igor Zori, Michael Z€ Ach, Bengt Kasemo, and Christoph Langhammer. Gold, Platinum, and Aluminum Nanodisk Plasmons: Material Independence, Subradiance, and Damping Mechanisms. *ACS Nano*, 5(4):2535–2546, 2011.

[246] David G W Goad and M Moskovits. Colloidal metal in aluminum-oxide Nickel pigmented anodic aluminum oxide for selective absorption of solar energy Colloidal metal in aluminum-oxide. *Journal of Applied Physics*, 49(5):2929–1173, 1978.

[247] Y Y Wang, Z H Ni, Z X Shen, H M Wang, and Y H Wu. Interference enhancement of Raman signal of graphene. *Applied Physics Letters*, 92(4):043121, 2008.

[248] Libo Gao, Wencai Ren, Bilu Liu, Riichiro Saito, Zhong-Shuai Wu, Shisheng Li, Chuanbin Jiang, Feng Li, and Hui-Ming Cheng. Surface and Interference Coenhanced Raman Scattering of Graphene. *ACS Nano*, 3(4):933–939, 2009.

[249] Nicholas Valley, Nathan Greeneltch, Richard P Van Duyne, and George C Schatz. A Look at the Origin and Magnitude of the Chemical Contribution to the Enhance-

ment Mechanism of Surface-Enhanced Raman Spectroscopy (SERS): Theory and Experiment. *Journal of Physical Chemistry Letters*, 20(16):9, 2013.

[250] E S Brandt, T M. ; B W Cotton, R C Rossiter, J Baetzold ; Ivanecky, C M Child, A Campion, J R Lombardi, R L Birke, L A Sanchez, I Bernard, and S C Sun. Communications to the Editor On the Mechanism of Chemical Enhancement in Surface-Enhanced Raman Scattering. Technical Report 2, 1995.

[251] Won-Hwa Park and Zee Hwan Kim. Charge Transfer Enhancement in the SERS of a Single Molecule. *Nano Letters*, 10(10):4040–4048, 2010.

[252] Shengxi Huang, Xi Ling, Liangbo Liang, Yi Song, Wenjing Fang, Jin Zhang, Jing Kong, Vincent Meunier, and Mildred S Dresselhaus. Molecular Selectivity of Graphene-Enhanced Raman Scattering. *Nano Letters*, 15(5):2892–2901, 2015.

[253] Hua Xu, Yabin Chen, Weigao Xu, Haoli Zhang, Jing Kong, Mildred S Dresselhaus, Jin Zhang, H Xu, Y B Chen, W G Xu, J Zhang, Gers H L Zhang, J Kong, and M S Dresselhaus. Modulating the Charge-Transfer Enhancement in GERS using an Electrical Field under Vacuum and an n/p-Doping Atmosphere. *Small*, 7(20):2945–2952, 2011.

[254] P Blake, E W Hill, A H Castro Neto, K S Novoselov, D Jiang, R Yang, T J Booth, and A K Geim. Making graphene visible. *Applied Physics Letters*, 91(6):063124, 2007.

[255] Viktoryia Shautsova, Adam M Gilbertson, Nicola C G Black, Stefan A Maier, and Lesley F Cohen. Hexagonal Boron Nitride assisted transfer and encapsulation of large area CVD graphene. *Scientific Reports*, 6:30210, 2016.

[256] S Goniszewski, M Adabi, O Shaforost, S M Hanham, L Hao, and N Klein. Correlation of p-doping in CVD Graphene with Substrate Surface Charges. *Scientific Reports*, 6:22858, 2016.

[257] Nathan Cernetic, Daniel O Hutchins, Hong Ma, and Alex K-Y Jen. Influence of self-assembled monolayer binding group on graphene transistors. *Applied Physics Letters*, 106(2):84312, 2015.

[258] Wi Hyoung Lee, Jaesung Park, Youngsoo Kim, Kwang S. Kim, Byung Hee Hong, and Kilwon Cho. Control of Graphene Field-Effect Transistors by Interfacial Hydrophobic Self-Assembled Monolayers. *Advanced Materials*, 23(30):3460–3464, 2011.

[259] Stehane Berciaud, Xianglong Li, Han Htoon, Louis E Brus, Stephen K Doorn, and Tony F Heinz. Intrinsic Line Shape of the Raman 2D-Mode in Freestanding Graphene Monolayers. *Nano Letters*, 13(8):3517–3523, 2013.

[260] Stéphane Berciaud, Sunmin Ryu, Louis E Brus, and Tony F Heinz. Probing the Intrinsic Properties of Exfoliated Graphene: Raman Spectroscopy of Free-Standing Monolayers. *Nano Letters*, 9(1):346–352, 2009.

[261] Yung-Chang Lin, Chun-Chieh Lu, Chao-Huei Yeh, Chuanhong Jin, Kazu Suenaga, and Po-Wen Chiu. Graphene Annealing: How Clean Can It Be? *Nano Letters*, 12(1):414–419, 2011.

[262] Joshua D Wood, Gregory P Doidge, Enrique A Carrion, Justin C Koepke, Joshua A Kaitz, Isha Datye, Ashkan Behnam, Jayan Hewaparakrama, Basil Aruin, Yaofeng Chen, Hefei Dong, Richard T Haasch, Joseph W Lyding, and Eric Pop. Annealing free, clean graphene transfer using alternative polymer scaffolds. *Nanotechnology*, 26:055302, 2015.

[263] K Nagashio, T Yamashita, T Nishimura, K Kita, and A Toriumi. Electrical transport properties of graphene on SiO 2 with specific surface structures. *Journal of Applied Physics*, 110(2):024513, 2011.

[264] Zheyu Fang, Yumin Wang, Zheng Liu, Andrea Schlather, Pulickel M Ajayan, Frank H L Koppens, Peter Nordlander, and Naomi J Halas. Plasmon-induced doping of graphene. *Acs Nano*, 6(11):10222–10228, 2012.

[265] Barun Das, Rakesh Voggu, Chandra Sekhar Rout, and C N R Rao. Changes in the electronic structure and properties of graphene induced by molecular charge-transfer. *Chem. Commun*, 4(41):55–71, 2008.

[266] Hyun Ho Kim, Yoonyoung Chung, Eunho Lee, Seong Kyu Lee, and Kilwon Cho. Water-Free Transfer Method for CVD-Grown Graphene and Its Application to Flexible Air-Stable Graphene Transistors. *Advanced Materials*, 26(20):3213–3217, 2014.

[267] Yingbo He, Guowei Lu, Hongming Shen, Yuqing Cheng, and Qihuang Gong. Strongly enhanced Raman scattering of graphene by a single gold nanorod. *Applied Physics Letters*, 107(5):053104, 2015.

[268] C R Dean, a F Young, I Meric, C Lee, L Wang, S Sorgenfrei, K Watanabe, T Taniguchi, P Kim, K L Shepard, and J Hone. Boron nitride substrates for high-quality graphene electronics. *Nature Nanotechnology*, 5(10):722–726, 2010.

[269] Min Gao, Andrey Lyalin, and Tetsuya Taketsugu. Oxygen activation and dissociation on h-BN supported Au atoms. *International Journal of Quantum Chemistry*, 113(4):443–452, 2013.

[270] J Sławińska, P Dabrowski, and I Zasada. Doping of graphene by a Au(111) substrate: Calculation strategy within the local density approximation and a semiempirical van der Waals approach. *Physical Review B*, 83(24):245249, 2011.

[271] Jingang Wang, Fengcai Ma, and Mengtao Sun. Graphene, hexagonal boron nitride, and their heterostructures: properties and applications. *RSC Advances*, 7(27):16801–16822, 2017.

[272] David Alcaraz Iranzo, Sébastien Nanot, Eduardo J C Dias, Itai Epstein, Cheng Peng, Dmitri K Efetov, Mark B Lundeberg, Romain Parret, Johann Osmond, Jin-Yong Hong, Jing Kong, Dirk R Englund, Nuno M R Peres, and Frank H L Koppens. Probing the ultimate plasmon confinement limits with a van der Waals heterostructure. *Science*, 360(6386):291–295, 2018.

[273] Xuanye Wang, Jason W Christopher, and Anna K Swan. 2D Raman band splitting in graphene: Charge screening and lifting of the K-point Kohn anomaly. *Scientific Reports*, 7(13539), 2017.

[274] Adam M Gilbertson, Yan Francescato, Tyler Roschuk, Viktoryia Shautsova, Yiguo Chen, Themistoklis P H Sidiropoulos, Minghui Hong, Vincenzo Giannini, Stefan A Maier, Lesley F Cohen, and Rupert F Oulton. Plasmon-Induced Optical Anisotropy in Hybrid Graphene–Metal Nanoparticle Systems. *Nano Letters*, 15(5):3458–3464, 2015.

[275] Guillaume Baffou and Romain Quidant. Thermo-plasmonics: using metallic nanostructures as nano-sources of heat. *Laser & Photonics Review*, 7(2):171–187, 2013.

[276] Guillaume Baffou, Romain Quidant, and Christian Girard. Thermoplasmonics modeling: A Green's function approach. *Physical Review B*, 82(16):165424, 2010.

[277] S D Costa, J Ek Weis, O Frank, M Fridrichová, Fridrichov Fridrichová, and M Kalbac. Monitoring the doping of graphene on SiO$_2$/Si substrates during the thermal annealing process. *RSC Advances*, 6(76):72859, 2016.

[278] Sunmin Ryu, Li Liu, Stephane Berciaud, Young-Jun Yu, Haitao Liu, Philip Kim, George W Flynn, and Louis E Brus. Atmospheric Oxygen Binding and Hole Doping in Deformed Graphene on a SiO 2 Substrate. *Nano Letters*, 10(12):4944–4951, 2010.

[279] a Tiberj, M Paillet, P Landois, M Mikolasek, S Contreras, E Dujardin, Laboratoire Charles, M Rubio-Roy, J-R Huntzinger, J-L Sauvajol, and a-a Zahab. Reversible optical doping of graphene. *Scientific Reports*, 3:1–23, 2013.

[280] L Ju, J Velasco Jr, E Huang, S Kahn, C Nosiglia, Hsin-Zon Tsai, W Yang, T Taniguchi, K Watanabe, Y Zhang, G Zhang, M Crommie, A Zettl, and F Wang. Photoinduced doping in heterostructures of graphene and boron nitride. *Nature Nanotechnology*, 9(5):348–352, 2014.

[281] Christoph Neumann, Leo Rizzi, Sven Reichardt, Bernat Terre, Timofiy Khodkov, Kenji Watanabe, Takashi Taniguchi, Bernd Beschoten, and Christoph Stampfer. Spatial Control of Laser-Induced Doping Profiles in Graphene on Hexagonal Boron Nitride. *ACS Applied Materials & Interfaces*, 8(14):9377–9383, 2016.

[282] Young Duck Kim, Myung-Ho Bae, Jung-Tak Seo, Yong Seung Kim, Hakseong Kim, Jae Hong Lee, Joung Real Ahn, Sang Wook Lee, Seung-Hyun Chun, and

Yun Daniel Park. Focused-Laser-Enabled p-n Junctions in Graphene Field-Effect Transistors. *ACS Nano*, 7(7):5850–5857, 2013.

[283] Christopher Coleman, Rudolph Erasmus, and Somnath Bhattacharyya. Investigation of electron irradiation-induced magnetism in layered MoS_2 single crystals. *Applied Physics Letters*, 109(25):253110, 2016.

[284] B Krauss, T Lohmann, D.-H Chae, M Haluska, K Von Klitzing, and J H Smet. Laser-induced disassembly of a graphene single crystal into a nanocrystalline network. *Physical Review B*, 79(16):165428, 2009.

[285] Ting Huang, Jiangyou Long, Minlin Zhong, Juan Jiang, Xiaohui Ye, Zhe Lin, and Lin Li. The effects of low power density CO_2 laser irradiation on graphene properties. *Applied Surface Science*, 273:502–506, 2013.

[286] Adam Roberts, Daniel Cormode, Collin Reynolds, Ty Newhouse-Illige, Brian J Leroy, and Arvinder S Sandhu. Response of graphene to femtosecond high-intensity laser irradiation. *Citation: Appl. Phys. Lett*, 99(5):51912, 2011.

[287] Zhen Hua Ni, Hao Min Wang, Zhi Qiang Luo, Ying Ying Wang, Ting Yu, Yi Hong Wu, and Ze Xiang Shen. The effect of vacuum annealing on graphene. *Journal of Raman Spectroscopy*, 41(5):479–483, 2009.

[288] Hossein Sojoudi, Jose Baltazar, Clifford Henderson, and Samuel Graham. Impact of post-growth thermal annealing and environmental exposure on the unintentional doping of CVD graphene films. *Journal of Vacuum Science & Technology B*, 30(4):41213, 2012.

[289] Christos Melios, Alba Centeno, Amaia Zurutuza, Vishal Panchal, Cristina E. Giusca, Steve Spencer, S. Ravi P Silva, and Olga Kazakova. Effects of humidity

on the electronic properties of graphene prepared by chemical vapour deposition. *Carbon*, 103:273–280, 2016.

[290] Efraín Ochoa-Martínez, Mercedes Gabás, Laura Barrutia, Amaia Pesquera, Alba Centeno, Santiago Palanco, Amaia Zurutuza, and Carlos Algora. Determination of a refractive index and an extinction coefficient of standard production of CVD-graphene. *Nanoscale*, 7(4):1491, 2014.

[291] Kevin Brenner and Raghu Murali. In situ doping of graphene by exfoliation in a nitrogen ambient. *Applied Physics Letters*, 98(11):113115, 2011.

[292] En Cao, Mengtao Sun, Yuzhi Song, and Wenjie Liang. Exciton-plasmon hybrids for surface catalysis detected by SERS. *Nanotechnology*, 29(37):372001, 2018.

[293] Anneli Hoggard, Lin-Yung Wang, Lulu Ma, Ying Fang, Ge You, Jana Olson, Zheng Liu, Wei-Shun Chang, Pulickel M Ajayan, and Stephan Link. Using the Plasmon Linewidth To Calculate the Time and Efficiency of Electron Transfer between Gold Nanorods and Graphene. *ACS Nano*, 17(12):11209–11217, 2018.

[294] Mark L Brongersma, Naomi J Halas, and Peter Nordlander. Plasmon-induced hot carrier science and technology. *Nature Nanotechnology*, 10(1):25–34, 2015.

[295] Wei Xie and Sebastian Schlücker. Hot electron-induced reduction of small molecules on photorecycling metal surfaces. *Nature Communications*, 6:7570, 2015.

[296] Wei Wu Yupeng Zhang Lei Liao Shishang Guo Jianjian Ying Chongxin Shan Mengtao Sun Zhigao Dai Xiangheng Xiao and Changzhong Jiang. Plasmon-driven reaction controlledby the number of graphene layers and localized surface plasmon distribution during optical excitation. *Light: Science & Applications*, 4(10):e342, 2015.

[297] Woosuk Choi, Muhammad Arslan Shehzad, Sanghoon Park, and Yongho Seo. Influence of removing PMMA residues on surface of CVD graphene using a contact-mode atomic force microscope. *RSC Advances*, 7(12):6943, 2017.

[298] Haiqing Zhou, Jixin Zhu, Zheng Liu, Zheng Yan, Xiujun Fan, Jian Lin, Gunuk Wang, Qingyu Yan, Ting Yu, Pulickel M. Ajayan, and James M. Tour. High thermal conductivity of suspended few-layer hexagonal boron nitride sheets. *Nano Research*, 7(8):1232–1240, 2014.

[299] Lene Gammelgaard, Jose M. Caridad, Alberto Cagliani, David M. A. Mackenzie, Dirch H. Petersen, Timothy J. Booth, and Peter Bogglid. Graphene transport properties upon exposure to PMMA processing and heat treatments. *2D Materials*, 1(3):035005, 2014.

[300] C Neumann, S Reichardt, P Venezuela, M Drögeler, L Banszerus, M Schmitz, K Watanabe, T Taniguchi, F Mauri, B Beschoten, S V Rotkin, and C Stampfer. Raman spectroscopy as probe of nanometre-scale strain variations in graphene. *Nature Communications*, 6:8429, 2015.

[301] Haiqing Zhou, Caiyu Qiu, Fang Yu, Huaichao Yang, Minjiang Chen, Lijun Hu, Yanjun Guo, and Lianfeng Sun. Raman scattering of monolayer graphene: the temperature and oxygen doping effects. *Journal of Physics D: Applied Physics*, 44(18):185404, 2011.

[302] Weigao Xu, Jiaqi Xiao, Yanfeng Chen, Yabin Chen, Xi Ling, and Jin Zhang. Graphene-veiled gold substrate for surface-enhanced raman spectroscopy. *Advanced Materials*, 25(6):928–933, 2013.

[303] L. Hao, J. Gallop, S. Goniszewski, O. Shaforost, N. Klein, and R. Yakimova. Non-contact method for measurement of the microwave conductivity of graphene. *Applied Physics Letters*, 103(12):123103, 2013.

[304] Sang-Zi Liang, Gugang Chen, Avetik R Harutyunyan, Milton W Cole, and Jorge O Sofo. Analysis and optimization of carbon nanotubes and graphene sensors based on adsorption-desorption kinetics. *Applied Physics Letters*, 103(23):233108, 2013.

[305] Winadda Wongwiriyapan, Satoshi Inoue, Shin-ichi Honda, and Mitsuhiro Katayama. Adsorption kinetics of NO2 on single-walled carbon nanotube thin-film sensor. *Japanese Journal of Applied Physics*, 47(10):8145, 2008.

[306] H H Pu, S H Rhim, M Gajdardziksa-Josifovska, C J Hirschmugl, M Weinert, and J H Chen. A statistical thermodynamics model for monolayer gas adsorption on graphene-based materials: implications for gas sensing applications. *RSC Advances*, 4(88):47481, 2014.

[307] Y Hajati, T Blom, S H M Jafri, S Haldar, S Bhandary, M Z Shoushtari, O Eriksson, B Sanyal, and K Leifer. Improved gas sensing activity in structurally defected bilayer graphene. *Nanotechnology*, 23(50):505501, 2012.

[308] N Pompeo, K Torokhtii, and E Silva. Dielectric Resonators for the Measurements of the Surface Impedance of Superconducting Films. *Measurement Science Review*, 14(3):164–170, 2014.

[309] Jerzy Krupka. Contactless methods of conductivity and sheet resistance measurement for semiconductors, conductors and superconductors. *Measurement Science and Technology*, 24(6):062001, 2013.

[310] Jerzy Krupka, Danh Nguyen, and Janina Mazierska. Measurement of the complex permittivity of metal nanoislands and the surface resistance of thin conducting films at microwave frequencies. *Measurement Science and Technology*, 19(6):65701, 2008.

[311] J Krupka and W Strupinski. Measurements of the sheet resistance and conductivity of thin epitaxial graphene and SiC films. *Citation: Appl. Phys. Lett*, 96(8):82112, 2010.

[312] Jerzy Krupka, Wlodek Strupinski, and Norbert Kwietniewski. Microwave Conductivity of Very Thin Graphene and Metal Films. *Journal of Nanoscience and Nanotechnology*, 11(4):3358–3362, 2011.

[313] Ling Hao, John Gallop, Quan Liu, and Jie Chen. Microwave method for high-frequency properties of graphene. *IET Circuits, Devices & Systems*, 9(6):397–402, 2015.

[314] Jesse D Fowler, Matthew J Allen, Vincent C Tung, Yang Yang, Richard B Kaner, and Bruce H Weiller. Practical Chemical Sensors from Chemically Derived Graphene. *ACS Nano*, 3(2):301–306, 2009.

[315] Haifen Xie, Keke Wang, Zhiqiang Zhang, Xiaojing Zhao, Feng Liu, and Haichuan Mu. Temperature and thickness dependence of the sensitivity of nitrogen dioxide graphene gas sensors modified by atomic layer deposited zinc oxide films. *RSC Advances*, 5(36):28030, 2015.

[316] S Novikov, N Lebedeva, A Satrapinski, J Walden, V Davydov, and A Lebedev. Graphene based sensor for environmental monitoring of NO_2. *Sensors & Actuators: B. Chemical*, 236:1054–1060, 2016.

[317] Md W K Nomani, Razib Shishir, Muhammad Qazi, Devendra Diwan, V B Shields, M G Spencer, Gary S Tompa, Nick M Sbrockey, and Goutam Koley. Highly sensitive and selective detection of NO_2 using epitaxial graphene on 6H-SiC. *Sensors and Actuators B*, 150(1):301–307, 2010.

[318] Tsung-Cheng Chen, Yu-Cheng Yang, Hui-Ling Liu, Chia-Ming Yang, M. Meyyappan, and Chao-Sung Lai. The Effect of Monolayer Graphene on the UV Assisted NO_2 Sensing and Recovery at Room Temperature. In *Proceedings. EUROSENSORS 2017*, volume 1, page 461, Paris, 2017.

[319] Andrzej Wilczak and Thomas M Keinath. Kinetics of sorption and desorption of copper (II) and lead (II) on activated carbon. *Water Environment Research*, 65(3):238–244, 1993.

[320] Hui Qiu, Lu Lv, Bing-cai Pan, Qing-jian Zhang, Wei-ming Zhang, and Quan-xing Zhang. Critical review in adsorption kinetic models. *Journal of Zhejiang University Science A*, 10(5):716–724, 2009.

[321] Nathalie Chiron, Richard Guilet, and Eric Deydier. Adsorption of Cu (II) and Pb (II) onto a grafted silica: isotherms and kinetic models. *Water Research*, 37(13):3079–3086, 2003.

[322] D C Johnston. Stretched exponential relaxation arising from a continuous sum of exponential decays. *Physical Review B*, 74(18):184430, 2006.

[323] Min Zhong, R J Loy, and Robert S Anderssen. Approximating the Kohlrausch function by sums of exponentials. *The ANZIAM Journal*, 54(04):306–323, 2013.

[324] Egor A Kolesov, Mikhail S Tivanov, Olga V Korolik, Olesya O Kapitanova, Xiao Fu, Hak Dong Cho, Tae Won Kang, and Gennady N Panin. The effect of atmo-

spheric doping on pressure-dependent Raman scattering in supported graphene. *Beilstein Journal of Nanotechnology*, 9:704–710, 2018.

[325] F W Clarke and BY Irving Langmuir. Constitution of solids and liquids. *JACS*, 38(11):2221–2295, 1916.

[326] Irving Langmuir. Adsorption of gases on glass, mica and platinum. *JACS*, 40(9):1361–1403, 1918.

[327] K W Kolasinski. *Surface Science - Foundation of Catalysis and Nanoscience*. John Wiley & Sons, Ltd., 2 edition, 2012.

[328] Hasselbrink and Lundqvist. *Handbook of Surface Science*. Elsevier, Oxford, 3 edition, 2008.

[329] Bing Huang, Zuanyi Li, Zhirong Liu, Gang Zhou, Shaogang Hao, Jian Wu, Bing-Lin Gu, and Wenhui Duan. Adsorption of gas molecules on graphene nanoribbons and its implication for nanoscale molecule sensor. *The Journal of Physical Chemistry C*, 112(35):13442–13446, 2008.

[330] Arthur W. Adamsam and Alice P. Gast. *Physical Chemistry of Surfaces*. John Wiley & Sons, Inc., 6 edition, 1997.

[331] FRANK M WANLASS and HENRY EYRING. *Sticking Coefficients*, chapter 16. American Chemical Society, 1961.

[332] Samuel Glasstone, Keith J. Laidler, and Henry Eyring. *The Theory of Rate Processes*. McGraw-Hill Book Company, Inc., New York and London, 1941.

[333] Le-Sheng Zhang, Wei D Wang, Xian-Qing Liang, Wang-Sheng Chu, Wei-Guo Song, Wei Wang, and Zi-Yu Wu. Characterization of partially reduced graphene oxide as room temperature sensor for H_2. *Nanoscale*, 3(6):2458–2460, 2011.

[334] Fazel Yavari and Nikhil Koratkar. Graphene-Based Chemical Sensors. *Physical Chemistry Letters*, 3(13):1746–1753, 2012.

[335] See Lee, Qing Tang, Zhen Zhou, and Zhongfang Chen. Graphene-related nanomaterials: tuning properties by functionalization. *Nanoscale*, 5(11):4519–5130, 2013.

[336] See Martin Pumera, Zdeněk Sofer, Martin Pumera, and Zdeně K Sofer. Towards stoichiometric analogues of graphene: graphane, fluorographene, graphol, graphene acid and others. *Chemical Society Reviews*, 46(15):4450, 2017.

[337] Mohammad Adabi, Johannes Lischner, Stephen M. Hanham, Andrei P. Mihai, Olena Shaforost, Rui Wang, Ling Hao, Peter K. Petrov, and Norbert Klein. Microwave Study of Field-Effect Devices Based on Graphene/ Aluminum Nitride/Graphene Structures. *Scientific Reports*, 7:44202, 2017.

[338] Shengke Zhang, Hasan Sahin, Engin Torun, Francois Peeters, Dinesh Martien, Tyler DaPron, Neil Dilley, and Nathan Newman. Fundamental mechanisms responsible for the temperature coefficient of resonant frequency in microwave dielectric ceramics. *Journal of the American Ceramic Society*, 100(4):1–9, 2017.

[339] Jerome A. Cuenca, Daniel R. Slocombe, and Adrian Porch. Temperature Correction for Cylindrical Cavity Perturbation Measurements. *IEEE Transactions on Microwave Theory and Techniques*, 65(6):2153–2161, 2017.

[340] Yong Guan and Yoshio Nikawa. Measurement of temperature-dependent complex permittivity for materials using cylindrical resonator under microwave irradiation. *Electronics and Communications in Japan (Part II: Electronics)*, 90(11):1–8, 2007.

[341] Jian-Hao Chen, Chaun Jang, Shudong Xiao, Masa Ishigami, and Michael S Fuhrer. Intrinsic and extrinsic performance limits of graphene devices on SiO_2. *Nature Nanotechnology*, 3(4):206–209, 2008.

[342] Jürgen Schiefele, Fernando Sols, and Francisco Guinea. Temperature dependence of the conductivity of graphene on boron nitride. *Physical Review B*, 85(19):195420, 2012.

[343] S Ahlers, G Müller, and T Doll. A rate equation approach to the gas sensitivity of thin film metal oxide materials. *Sensors and Actuators B*, 107(2):587–599, 2005.

[344] Shubhda Srivastava, Kiran Jain, V. N. Singh, N. Vijayan, Nita Dilawar, Govind Gupta, and T. D. Senguttuvan. Faster response of NO_2 sensing in graphene-WO_3 nanocomposites. *Nanotechnology*, 23(20):205501, 2012.

[345] Madhav Gautam and Ahalapitiya H. Jayatissa. Ammonia gas sensing behavior of graphene surface decorated with gold nanoparticles. *Solid-State Electronics*, 78:159–165, 2012.

[346] Madhav Gautam and Ahalapitiya H Jayatissa. Adsorption kinetics of ammonia sensing by graphene films decorated with platinum nanoparticles. *Journal of Applied Physics*, 111(9):094317, 2012.

[347] Matthias Kühne, Federico Paolucci, Jelena Popovic, Pavel M Ostrovsky, Joachim Maier, and Jurgen H Smet. Ultrafast lithium diffusion in bilayer graphene. *Nature Nanotechnology*, 12(9):895–901, 2017.

[348] P A Redhead. Thermal Desorption of Gases. *Vacuum*, 12(4):203–211, 1962.

[349] Lay-Lay Chua, Jana Zaumsell, Jui-Fen Chang, Eric C.W. Ou, Peter K. H. Ho, Henning Sirringhaus, and Richard H. Friend. General observation of n-type field-effect behaviour in organic semiconductors. *Nature*, 434:194–199, 2005.

[350] A. Tataroğlu. Frequency and voltage dependence of the electrical and dielectric properties of Au/n-Si Schottky diodes with SiO_2 insulator layer. *Journal of Optoelectronics and Advanced Materials*, 13(8):940–945, 2011.

[351] S. Demirezen, A. Kaya, S.A. Yerişkin, M. Balbaşı, and İ. Uslu. Frequency and voltage dependent profile of dielectric properties, electric modulus and ac electrical conductivity in the PrBaCoO nanofiber capacitors. *Results in Physics*, 6:180–185, 2016.

[352] D.W. Ormond C. M. Osburn. Dielectric Breakdown in Silicon Dioxide Films on Silicon. *Journal of electrochemical Society: Solid-state science and Technology*, 119(5):591–597, 1972.

[353] Haomin Wang, Yihong Wu, Chunxiao Cong, Jingzhi Shang, and Ting Yu. Hysteresis of Electronic Transport in Graphene Transistors. *ACS Nano*, 4(12):7221–7228, 2010.

[354] Guiming Cao, Xiaorong Liu, Weihua Liu, Quanfu Li, Xin Li, and Xiaoli Wang. Chemical environment dominated Fermi level pinning of a graphene gas sensor. *Carbon*, 124:57–63, 2017.

[355] Yuya Murata, Arrigo Calzolari, and Stefan Heun. Tuning Hydrogen Adsorption on Graphene by Gate Voltage. *Journal of Physical Chemistry C*, 112(21):111591–11597, 2018.

[356] Shun Mao, Jingbo Chang, Haihui Pu, Ganhua Lu, Qiyuan He, Hua Zhang, and Junhong Chen. Two-dimensional nanomaterial-based field-effect transistors for chemical and biological sensing. *Chemical Society Reviews*, 46:6872, 2017.

[357] Shanshan Chen, Weiwei Cai, David Chen, Yujie Ren, Xuesong Li, Yanwu Zhu, Junyong Kang, and Rodney S. Ruoff. Adsorption/desorption and electrically controlled flipping of ammonia molecules on graphene. *New Journal of Physics*, 12:125011, 2010.

[358] A K Singh, M A Uddin, J T Tolson, H Maire-Afeli, N Sbrockey, G S Tompa, M G Spencer, T Vogt, T S Sudarshan, and G Koley. Electrically tunable molecular doping of graphene. *Applied Physics Letters*, 102(4):043101, 2013.

[359] H Yoo and A Gopinath. Plane wave scattering induced resonant modes of cubic resonator. *Electronics Letters*, 49(13):793–795, 2013.

[360] P Chiggiato and P Costa Pinto. Ti-Zr-V non-evaporable getter films: From development to large scale production for the Large Hadron Collider. *Thin Solid Films*, 515(2):382–388, 2006.

[361] Naresh K Emani, Ting-Fung Chung, Alexander V Kildishev, Vladimir M Shalaev, Yong P Chen, and Alexandra Boltasseva. Electrical Modulation of Fano Resonance in Plasmonic Nanostructures Using Graphene. *Nano Letters*, 14(1):37, 2014.

[362] Han Yu, Quan Sun, Kosei Ueno, Tomoya Oshikiri, Atsushi Kubo, Yasutaka Matsuo, and Hiroaki Misawa. Exploring Coupled Plasmonic Nanostructures in the Near Field by Photoemission Electron Microscopy. *ACS Nano*, 18(11):10373–10381, 2016.

[363] Demetrios D. Chronopoulos, Aristides Bakandritsos, Martin Pykal, Radek Zbořil, and Michal Otyepka. Chemistry, properties, and applications of fluorographene. *Applied Materials Today*, 9:60–70, 2017.

[364] Jeroen E. Scheerder, Shuanglong Liu, Vyacheslav S. Zharinov, Nicolas Reckinger, Jean-François Colomer, Hai-Ping Cheng, Joris Van de Vondel, and Ewald Janssens. Electronic Detection of Oxygen Adsorption and Size-Specific Doping of Few-Atom Gold Clusters on Graphene. *Advanced Materials Interfaces*, 5(19):1801274, 2018.

[365] Zhenglong Zhang, Shaoxiang Sheng, Rongming Wang, and Mengtao Sun. Tip-Enhanced Raman Spectroscopy. *Analytical Chemistry*, 88(19):9328–9346, 2016.

[366] Emiliano Cortés. Activating plasmonic chemistry. *Science*, 362(6410):28–29, 2018.

[367] Seung Joon Lee, Brian D Piorek, Carl D Meinhart, and Martin Moskovits. Photoreduction at a Distance: Facile, Nonlocal Photoreduction of Ag Ions in Solution by Plasmon-Mediated Photoemitted Electrons. *Nano Letters*, 10(4):1329–1334, 2010.

[368] V. Nicolosi, M. Chhowalla, M. G. Kanatzidis, M. S. Strano, and J. N. Coleman. Liquid Exfoliation of Layered Materials. *Science*, 340(6139):1226419–1226419, 2013.

[369] Shuai Wang, Priscilla Kailian Ang, Ziqian Wang, Ai Ling, Lena Tang, John T L Thong, and Kian Ping Loh. High Mobility, Printable, and Solution-Processed Graphene Electronics. *Nano Letters*, 10(1):52, 2010.

[370] Dae-Hyun Baek and Jongbaeg Kim. MoS_2 gas sensor functionalized by Pd for the detection of hydrogen. *Sensors and Actuators B: Chemical*, 250:686–691, 2017.

[371] Aliasghar Shokri and Nadia Salami. Gas sensor based on MoS_2 monolayer. *Sensors and Actuators B: Chemical*, 236:378–385, 2016.

[372] Zhaohua Zhu, Qian Sun, Zhipeng Zhang, Jie Dai, Guichuan Xing, Shaozhou Li, Xiao Huang, and Wei Huang. Metal halide perovskites: stability and sensing-ability. *Journal of Material Chemistry C*, 6(38):10121, 2018.

[373] Letian Dou, Andrew B Wong, Yi Yu, Minliang Lai, Nikolay Kornienko, Samuel W Eaton, Anthony Fu, Connor G Bischak, Jie Ma, Tina Ding, Naomi S Ginsberg, Lin-Wang Wang, A Paul Alivisatos, and Peidong Yang. Atomically thin two-dimensional organic-inorganic hybrid perovskites. *Science*, 349(6255):1518–21, 2015.

[374] Stephanie Reich and Christian Thomsen. Raman spectroscopy of graphite. *Philosphical Transactions of the Royal Society of London A: Mathematical, Physical and Engineering Sciences*, 362(1824):2271–2288, 2004.

[375] D. L. Rousseau, R. P. Bauman, and S. P. S. Porto. Normal mode determination in crystals. *Jounal of Raman Spectroscopy*, 10(1):253–290, 1981.

[376] F Tuinstra and J L Koenig. Raman Spectrum of Graphite. *The Journal of Chemical Physics*, 53(3):1126–32183, 1970.

[377] Gene Dresselhaus Ado Jorio Riichiro Saito and Mildred S Dresselhaus. *Raman Spectroscopy in Graphene Related Systems*. WILEY-VCH Verlag GmbH & Co. KGaA, 2011.

[378] P Josgi, H. E. Romero, A. T. Neal, V. K. Toutam, and S. A. Tadigadapa. Intrinsic doping and gate hysteresis in graphene field effect devices fabricated on SiO_2 substrates. *Journal of Physics: Condensed Matter*, 22(33):334214, 2010.

[379] Young Gon Lee, Chang Goo Kang, Jin Jung, Jin Ju Kim, Jun Hwang, Hyun-Jong Chung, Sunae Seo, Rino Choi, and Byoung Hun Lee. Hysteresis reversion in graphene field-effect transistors. *The Journal of Chemical Physics*, 98(18):44703, 2011.

Appendices

A.1 Semi-Classical Raman Scattering in a Lattice

The incident electromagnetic field $\mathbf{E}(\mathbf{r}, t)$ at position $\mathbf{r}$ at time t can be described as follows $\mathbf{E}(\mathbf{r}, t) = \mathbf{E}(\mathbf{k}, \omega)e^{-i(\mathbf{k}\cdot\mathbf{r}-\omega t)}$, where $\mathbf{k}$ is its wave vector and ω the frequency. As the incident radiation approaches and interacts with the material's surface a local polarization is induced, $\mathbf{P}(\mathbf{r}, t) = \mathbf{P}(\mathbf{k}, \omega)e^{-i(\mathbf{k}\cdot\mathbf{r}-\omega t)}$. The relationship between the polarizability of the material and the incident light is

$$\mathbf{P}(\mathbf{k}, \omega) = \chi(\mathbf{k}, \omega, \mathbf{Q})\mathbf{E}(\mathbf{k}, \omega)\,, \tag{A.1}$$

where χ is the electric susceptibility of the material which has a dependence on the lattice displacement $\mathbf{Q}$. Lattice vibrations through atomic crystals behave like standing waves with boundaries at the Brillouin zones. Therefore, the atomic displacements are described analogous to electromagnetic waves such that $\mathbf{Q}(\mathbf{r}, t) = \mathbf{Q}(\mathbf{q}, \omega_\nu)e^{\pm i(\mathbf{q}\cdot\mathbf{r}-\omega_\nu t)}$. Since the response of the material to electromagnetic radiation is dependent upon the displacement of atomic positions, which can be considered as small perturbations around a point, the susceptibility can be Taylor expanded as follows

$$\chi(\mathbf{k}, \omega, \mathbf{Q}) = \chi_0(\mathbf{k}, \omega) + \left(\frac{\partial \chi}{\partial Q}\right)\mathbf{Q}(\mathbf{r}, t) + \frac{1}{2}\left(\frac{\partial^2 \chi}{\partial Q^2}\right)\mathbf{Q}^2(\mathbf{r}, t) + \ldots \tag{A.2}$$

Each partial derivative terms of the expansion in equation (A.2) define the first- and second-order Raman tensor. Considering only the first-order effect, substituting equation (A.2) in to equation (A.1) the polarization becomes:

$$\begin{aligned}\mathbf{P}(\mathbf{r},t) =& \chi_0(\mathbf{k},\omega)\mathbf{E}(\mathbf{k},\omega)e^{-i(\mathbf{k}\cdot\mathbf{r}-\omega t)}+\\ &\left(\frac{\partial\chi}{\partial Q}\right)\mathbf{Q}(\mathbf{k},\omega)\mathbf{E}(\mathbf{k},r)e^{-i(\mathbf{q}\cdot\mathbf{r}-\omega_\nu t)}e^{\pm i(\mathbf{k}\cdot\mathbf{r}-\omega t)}.\end{aligned} \tag{A.3}$$

Finally using the cosine product to sum trigonometry identity equation A.3 can be expanded to

$$\begin{aligned}\mathbf{P}(\mathbf{r},t) =& \chi_0(\mathbf{k},\omega)\mathbf{E}(\mathbf{k},\omega)e^{-i(\mathbf{k}\cdot\mathbf{r}-\omega t)}+\\ &\left(\frac{\partial\chi}{\partial Q}\right)\mathbf{Q}(\mathbf{k},\omega)\mathbf{E}(\mathbf{k},r)exp\Big\{-i\big((\mathbf{q}\pm\mathbf{k})\cdot\mathbf{r}-(\omega\pm\omega_\nu)t\big)\Big\}.\end{aligned} \tag{A.4}$$

Equation (A.4) shows that the polarizabilty varies according to three distinct frequencies, ω, $\omega \pm \omega_\nu$ the Rayleigh and Stokes shifts respectively. The Stokes (Anti-Stokes) scattered light corresponds to the system were energy is gained (lost) by amount ω_ν. The first term, the Rayleigh term, corresponds to the ‘static’ part of the expanded susceptibility where the polarization is in phase with the incident radiation. The second term, relevant to first order Raman scattering, requires that there is a change in lattice displacement. Specifically that the material is polarizable such that $\partial\chi/\partial Q \neq 0$.

The intensity of the scattered light is proportional to the first order Raman tensor along the displacement unit vector $\hat{\mathbf{Q}} = Q/|Q|$ such that

$$I_R \propto \left|\hat{\mathbf{e}}_\mathrm{i}\cdot\left(\frac{\partial\chi}{\partial Q}\right)\hat{\mathbf{Q}}\cdot\hat{\mathbf{e}}_\mathrm{s}\right|, \tag{A.5}$$

where $\hat{\mathbf{e}}_\mathrm{i}$ and $\hat{\mathbf{e}}_\mathrm{s}$ are the unit vectors of the polarized incoming and scattered light. Therefore, for a scattering event to be "Raman active", the scattered phonon must have the same symmetry as the first-order Raman tensor. The Raman active vibrational modes are determined by referencing the character table associated with the point or space group.

A.1.1 Raman Scattering Kinematics

For wavelengths appreciable to visible light, the excitation source usually used in Raman measurements, the wave vector $\mathbf{k} = 2\pi/\lambda$ is much smaller than the wave vector associated with the phonon, which is on the order of $2\pi/a$ where a is the lattice spacing. To conserve energy and momentum in the scattering process, the phonon's wave vector must equal the difference between the incident and scattered photon $\mathbf{q} = \mathbf{k}_i - \mathbf{k}_s$. From equation A.5 there must be overlap between the phonon direction with the incident and scattered light. Therefore for a single phonon process $\mathbf{q}$ can only equal 0. A corollary of this is that for two phonon scattering processes the scattered phonons must be the same but in opposite directions. As a result two phonon processes are not confined to the first Brillouin zone.

Therefore for a single first order phonon process $\mathbf{q} = 0$ and Raman scattering is confined to the center of the Brillouin zone. The only phonons that carry momentum are optical phonons (figure 2.6). Therefore an electronic excitation to a virtual state, comparable to the energy of the optical phonons, is necessary to allow a scattering event to occur. The Stokes Raman process is as follows: first the absorption of an incident photon with energy ω_i excites an electron from its initial state $|i\rangle$ to a virtual excited state $|m\rangle$. The electron loses energy and falls to an energy state $|n\rangle$ due to interacting with a phonon of energy, $\hbar\omega_p h$. Finally the electron returns to its initial state by emitting a photon $\hbar\omega_s$. The Anti-Stokes Raman process requires that the initial electronic state is already an excited. Finally if the absorption of the initial photon results in a transition to a real energy state, this process is considered Resonant and the intensity of the Raman scattering process is enhanced by several orders of magnitude.

A.1.2 Rigorous Description of the Graphene Raman peak positions

Interestingly the G peak is the only Raman peak of graphene that is due to a first order single phonon scattering event- where $\mathbf{q} = 0$ at the Γ point located at the centre of the Brillouin zone. The D_{6h} space group describes the symmetry at the Γ point [164]. The irreducible representation at the Brillouin zone center is given by $A_{2u} + B_{2g} + E_{1u} + E_{2g}$ [166, 374]. Upon consultation of the character table in reference [375], only the E_{2g} symmetry operation is Raman active. The E_{2g} mode arises from out of phase vibrations of the two inequivalent atoms that make up the unit cell. This mode corresponds to the doubly degenerate iTO and iLO phonons [164] (see figure 2.6b of chapter 2). The 2D and D peak arise from a breathing mode associated with the six member carbon ring with symmetry a A_{1g} at the K point [172, 376, 166]. The 2D peak requires two iTO phonons of opposite wave vectors ($\mathbf{q}$ and $-\mathbf{q}$) to conserve momentum where $\mathbf{q} \simeq 2\mathbf{k}$. The 2D peak arises due to an inter-valley scattering process between the K and K' Dirac cones is K-space.

Unlike the G peak which requires a virtual transition state, both electronic transitions involved in the 2D peak mechanism are between the π and π^* bands are to real energy states. As a result there are two resonant process enhancing the intensity of the Raman peak. This process is referred to as the double resonance mechanism and is the main reason why the D peak overtone process leads to a Raman peak roughly twice the height of the first order G peak scattering. To finish discussing the origins of the observed Raman peaks, defect activated peaks need to be considered. The D and D' peak both require defects to be Raman active. The D peak requires a single iTO phonon scattering event such that $\mathbf{q} \simeq \mathbf{k}$ whereas the 2D peak, being an overtone, requires two iTO phonons of opposite wave vectors ($\mathbf{q}$ and $-\mathbf{q}$) where $\mathbf{q} \simeq 2\mathbf{k}$. Clearly a D band scattering event does not conserve momentum, therefore it requires a defect in the crystal structure to be Raman active [164, 166, 376]. As a result only the 2D peak is observed in pristine graphene. Similarly the D' Peak also requires defect to become active however where the D peak is a double resonant intervally scattering process, the D' peak arises due to intravalley scattering with an iLO phonon [164, 172, 177].

A.1.3 Origin in the Raman peak intensities

The Raman intensity is proportional to the probability of an electronic transition taking place which is encompassed by Fermi's Golden Rule [157, 377, 167].

$$I_G(\omega_{ph(G)}, E_L) \propto \left| \sum_{m,n} \frac{\langle f | H_{eR} | n \rangle \langle n | H_{ep} | m \rangle \langle m | H_{eR} | i \rangle}{(E_L - (E_m - E_i) - i\gamma_G)(E_L - \hbar\omega_{ph(G)} - (E_n - E_i) - i\gamma_G)} \right|^2 \tag{A.6}$$

$$\begin{aligned} I_{2D}(\omega_{ph(2D)}, E_L) \propto \Bigg| \sum_{m,n'} & \frac{\langle f | H_{eR} | l' \rangle \langle l' | H_{ep} | n' \rangle}{(E_L - \hbar\omega_{ph(+D)} - \hbar\omega_{ph(-D)} - (E_{l'} - E_i) - i\gamma_{2D})} \\ & \cdot \frac{\langle n' | H_{ep} | m \rangle \langle m | H_{eR} | i \rangle}{(E_L - (E_m - E_i) - i\gamma_{2D})(E_L - \hbar\omega_{ph(D)} - (E_{n'} - E_i) - i\gamma_{2D})} \Bigg|^2 \end{aligned} \tag{A.7}$$

The numerators from equations (A.6) and (A.7) describe probability of wave functions overlapping between the various energy states involved in the scattering process. The Hamiltonian H_{eR} describes the interaction of an electron with electromagnetic radiation whereas H_{ep} describes the energy interaction between the electron and phonon. The denominator describes the density of the final energy states where E_L is the energy of the laser. It is clear at resonance, when $E_L = E_m - E_i$ the denominator becomes small and the intensity is at its largest. Additionally since the all transitions are real the 2D peak denominator terms approach zero [158]. The γ corresponds to the inverse lifetime of the photoexcited carrier and corresponds to the full width at half maximum of the Raman peak. Clearly $I_G \propto 1/\gamma_G$ and $I_{2D} \propto 1/\gamma_{2D}$. It turns out that $\gamma_{2D} = 2\gamma_G$ [158] which leads to the intensity ratio of the G and 2D peak = 0.5 for pristine graphene. Conceptually, due to the equivalent dispersion around the K and K' points, an exciton has twice the probability to stay in the excited state as it spends half its time in each cone.

A.2 Examples of Graphene Raman Spectra

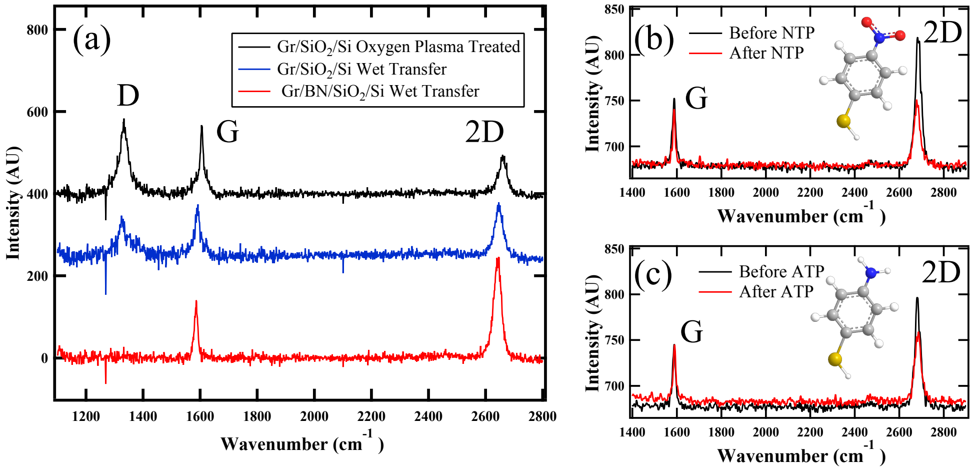

Figure A.1: Representative graphene Raman spectra of (a) differently prepared and therefore doped CVD graphene spectra. The three spectra correspond to the 'SERS' samples discussed in detail in chapter 3 where the least to most doped sample is the h-BN pacified sample, wet transferred graphene and oxygen plasma treated sample. The Raman spectra of CVD graphene in the presence and absence of (b) 4-aminothiophenol (ATP) and (c) 4-nitrothiophenol (NTP), where the amino and nitro groups on the aromatic ring are electron donating and withdrawing respectively. Despite the aromatic molecules not being strong Raman scatterers, their presence clearly perturbs the graphene spectrum.

For context, figure A.1 compares some very differently treated CVD graphene samples either with substrate treatments, or external graphene doping. Clearly the differently treated substrates of figure A.1a shows some very different representative graphene peaks. Where the bottom (red) h-BN spectrum demonstrates lightly doped and good quality graphene. The middle (blue) wet transferred graphene spectrum shows defects as indicated by the emergence of a D peak and broadening of the 2D peak. The top spectrum (black) shows the highly doped and defected oxygen plasma treated substrate graphene spectrum, as indicated by the very intense D peak, shallow 2D peak and the most blue shifted G and 2D bands. These spectra are discussed in detail in section 3.3.1 of chapter 3. For contrast, figures A.1b and c compare the Raman spectrum of graphene doped with 4-aminothiophenol and 4-nitrothiophenol. In both cases, the Raman cross section of both molecules are too weak to be observed without SERS enhancement. However, the graphene spectrum itself is altered predominantly by $\pi - \pi$ interactions between the graphene and the molecules reducing the intensity of the 2D peak.

A.3 Raman Background Removal

All spectral peak fitting procedures are made on spectra after background removal. The background is removed by either fitting a gaussian distribution as shown in figure A.2 or by taking a line fit of the peak and fitting either a peak shape after. Most fittings of the map data were taken using the latter method.

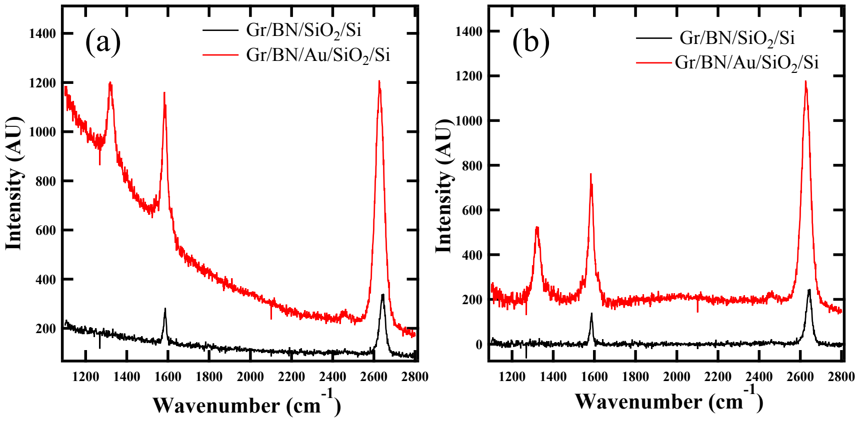

Figure A.2: Spectra of graphene in the presence and absence of the gold nanodiscs (a) before and (b) after background removal. The large slope is primarily due to fluorescence from the gold nanoparticles.

A.4 Raman Fitting for Table 3.1

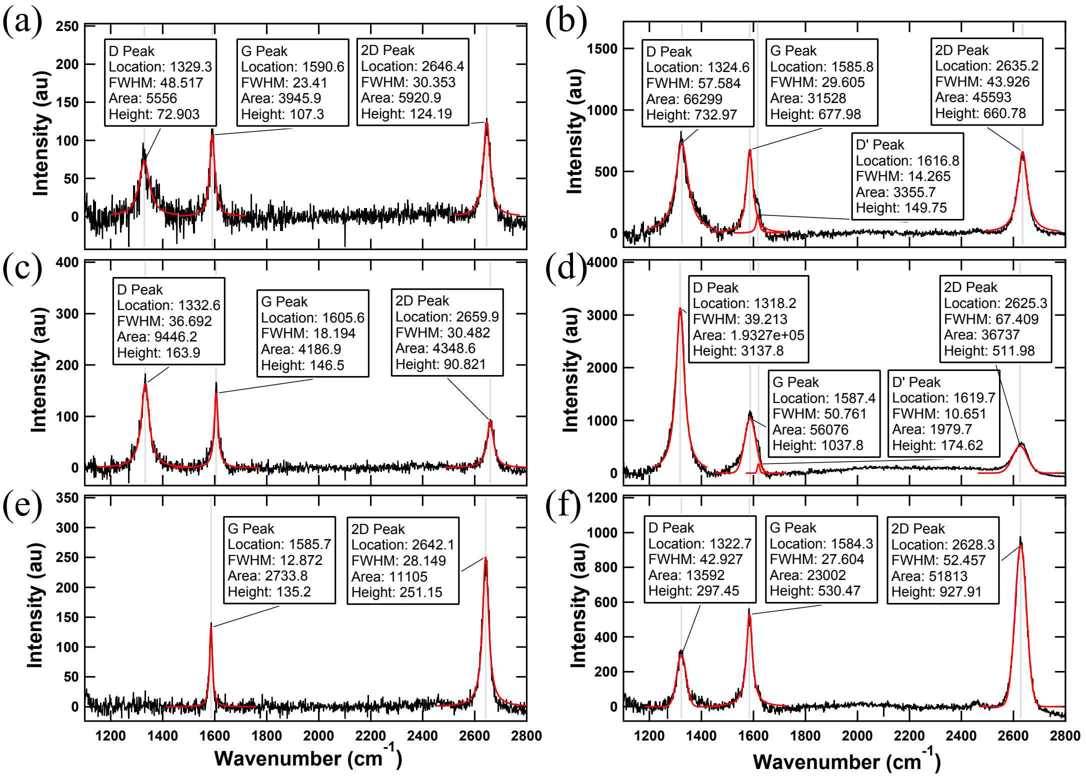

Figure A.3: Fitted curves corresponding to (a,b) wet transferred graphene, (c,d) oxygen plasma treated substrate and (e,f) h-BN pacified substrate in the absence and presence of AuND of G-SERS platforms.

Figure A.3 details the spectral curve fittings of figure 3.3 and table 3.1 using Gaussian and Lorentzian peak shape described as follows.

$$f_{Gauss}(x) = y_0 + A\left\{exp - \left(\frac{x - x_0}{width}\right)^2\right\} \tag{A.8}$$

$$f_{Lor}(x) = y_0 + \frac{A}{(x - x_0)^2 + B} \tag{A.9}$$

where A is the peak amplitude, and y_0 the offset. The FWHM from the Gaussian peak from is $2\sqrt{ln(2)}width$ and from the Lorentzian is $2\sqrt{B}$. The curve fittings were performed using IgorPro version 6.37 where the fitted coefficients chi-squared error is minimised using an Levenberg-Marquardt algorithm which is a non-linear least-squares fitting procedure.

A.5 Transport measurements for equivalently fabricated samples

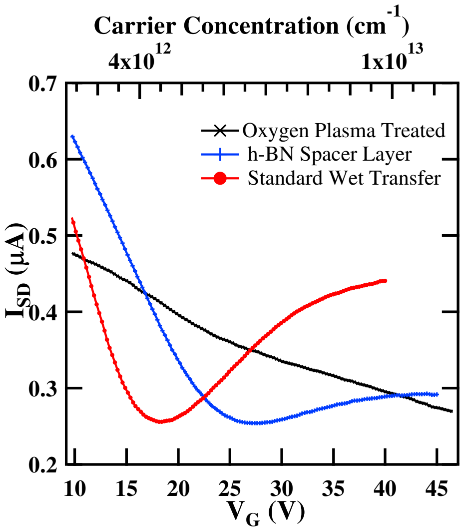

Figure A.4: Dirac characteristics of graphene transferred onto differently prepared substrates. All samples are p-doped. These measurements were taken by Dr Shautsova.

Figure A.4 compare the transport properties of differently treated substrates. Unsurprisingly, the oxygen plasma treated substrate agressively dopes the graphene such that the charge neutrality point cannot be reached without dielectric break down. Interestingly, the h-BN layer is shown to be more p-doped than the wet transferred graphene. Shautosova et al. [255] showed that this is due to surface doping of the graphene not substrate interactions. The Raman peaks of pristine graphene shift in the same direction from electron and hole doing effects. Therefore, figure A.4 confirms that all samples fabricated using our method will be p-doped.

A.6 KFM images of graphene/AuNDs/SiO_2/Si

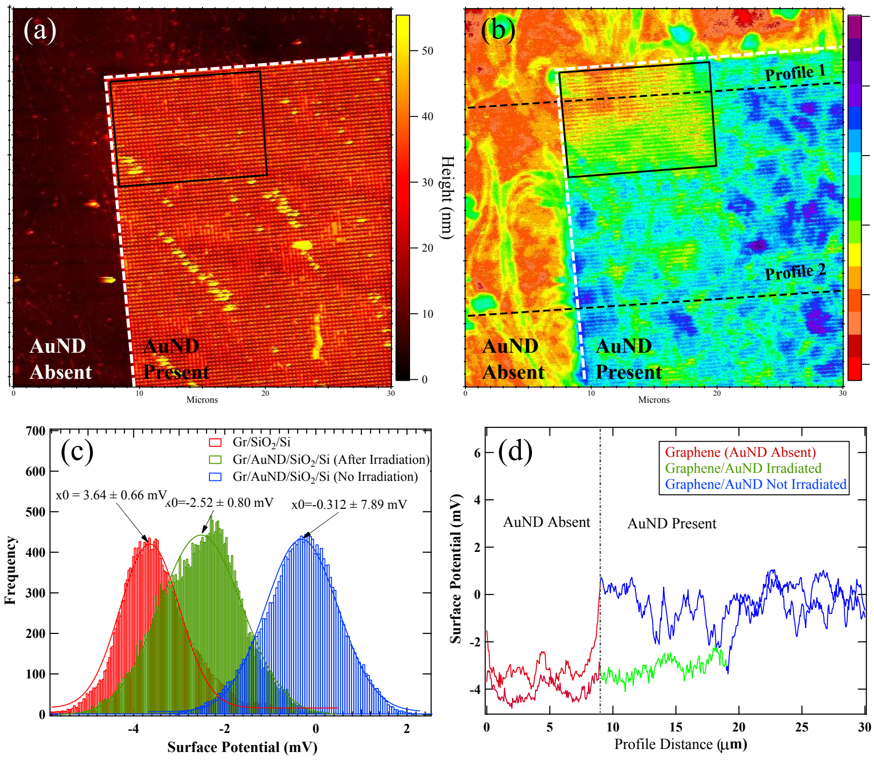

Figure A.5: (a) AFM and (b) KFM micrographs of graphene wet transferred onto a AuND substrate. The dashed lines mark the edge of the AuND array and the black box marks the region of AuNDs that were illuminated. (c) Surface potential histograms showing variations between graphene not interfaced with the AuNDs and the regions of graphene interfaced with AuNDs that have and have not been laser irradiated.(d) The surface profiles corresponding to the dashed black lines of (b) showing the variation at the interface of AuND irradiated (Profile 1) and untampered (Profile 2).

Figure A.5 is the AFM and KFM micrographs of graphene wet transferred on to a AuND array (radius 50 nm periodicity 300 nm). Compared to the h-BN pacified sample of studied in chapter 3, the graphene in contact with the AuND array is clearly distinguishable from the graphene only in contact with bare substrate with approximately 3 mV difference. Since the laser induced doping of graphene in the presence of the h-BN layer is in the order of 0.1 mV, the h-BN is effectively screening the graphene from substrate interactions and the results in chapter 3 is primarily due to surface interactions.

A.7 Plasmonic Nanoparticle Enhanced Heating

The heat deposited into graphene, Q_{Gr}, in the absence of nanostructures upon illumination is described as follows [275, 276]:

$$Q_{Gr} = \sigma_{abs,Gr} \frac{n_S c \epsilon_0}{2} |\mathbf{E_0}|^2, \tag{A.10}$$

where $\sigma_{abs,Gr}$ is the absorption cross section of graphene, $n_s = \sqrt{\epsilon_s}$ where ϵ_s is the real part of the surrounding permitivity and $|\mathbf{E_0}|$ the incident electric field. In the vicinity of nanostructures, the electric field amplitude at each particle position is considered. Therefore, as an approximation the heat deposited into graphene coupled to AuNDs is:

$$Q_{AuND} = \sigma_{abs,AuND} \frac{n_S c_0 \epsilon_0}{2} g^2 |\mathbf{E_0}|^2, \tag{A.11}$$

where absorption cross section of the gold nanodiscs $\sigma_{abs,AuND}$ and the enhancement factor g^2 describe the heating augmentation.

Despite this, the high thermal conductivity of graphene is effective at dissipating thermal heat from plasmonic hot spots [30]. In addition to this, despite being a 2D insulator, h-BN has high lateral thermal conductivity [298]. As a consequence, despite the SERS active nanostructured platform augmenting the heat generated at the resonant frequency (figure 3.20a), it is uncertain how big the magnitude of this thermal enhancement is. Moreover, since the 2D material integrated system is expected to be good at dissipating heat away from the hot spots, it is unclear how much thermal effects are expected to play a role in the overall laser induced doping of graphene, since the measurement of such a temperature is the focus of future work.

A.8 Graphene Sample Optimisation for Microwave Gating

The microwave method in short is a measurement of the losses induced by the graphene electrons. Therefore, the best substrate materials are insulators with low losses such as sapphire and quartz. However, dropping a voltage across a thick dielectric substrate requires large voltages in order to achieve an appreciable response in graphene. Therefore, high resistivity silicon with a thin thermally grown oxide layer is an ideal substrate material for microwave compatible field effect measurements. The high resistance silicon substrate is low loss enough to not overtly dampen the graphene response but conductive enough to drop a voltage across the thin film oxide layer.

In the main text, a 100 nm oxide layer is used, however, initially graphene is transferred onto a 50 nm thick oxide layer. The thinner dielectric results in a more sensitive graphene response to the applied back gate as shown in Figure A.6a. Here, the DC IV curve characteristics of graphene show the typical hysteresis associated with using a silicon dioxide dielectric due to charge traps and substrate effects [353, 378, 379], where the Dirac point drifts from 10-3 V. Note that the sample is being gated via a probe in contact with the freshly cleaved silicon side. Unfortunately, probes alone made it difficult to consistently achieve good contact with graphene, therefore silver paint is the preferred method to ensure good contact. Although a thin dielectric layer allows the charge neutrality point to be reached at relatively low gate voltages, A.6b shows that dielectric breakdown can occur at low voltages too. In this sub-figure, the horizontal signal close to zero is the initial voltage sweep measuring the noise due

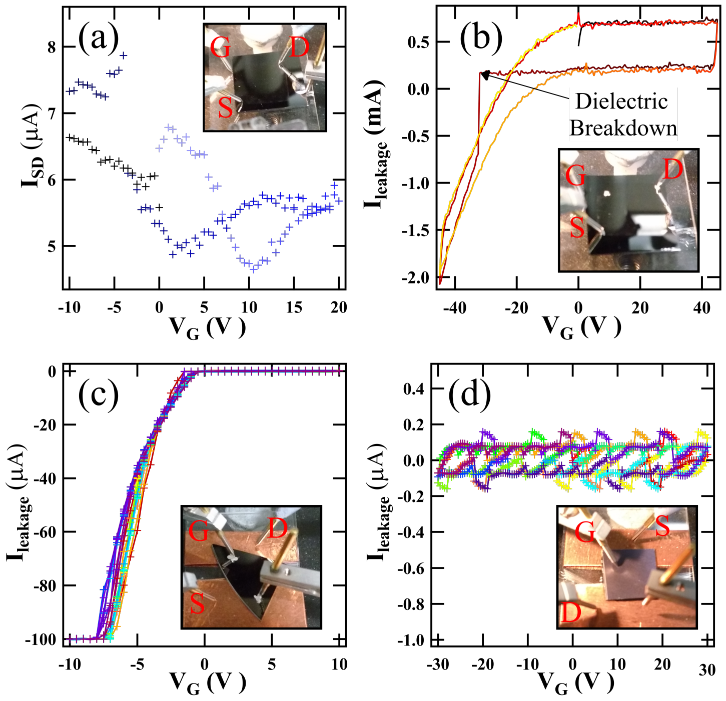

Figure A.6: (a) IV characteristics of graphene on high resistivity silicon with a 50 nm thermally grown oxide. Inset is the probe station configuration where the gate is a side contact. The leakage current through the dielectric of (b) a graphene sample in a similar configuration which breaks down at -35 V, (c) of an equivalent 50 nm substrate using large contacts similar to microwave rig where break down occurs between 5 and 10 V (d) a 90 nm oxide sample which doesn't break down as indicated by the noise signal at 0 V.

to zero current leakage. After -35 V the dielectric breaks down and there is a linear response. The horizontal line around 0.5 mA between 0-15 gate voltage is due to the Keithley power supply unit reaching a pre-determined 'compliance' value and diverting current though the ground.

Figure A.6c demonstrates a representative silicon sample where the probes are connected to large area contacts mimicking the gap of the microwave cavity. Interestingly, regardless of sample dielectrics showing no leakage using the silver paint and probe contacts only. The moment a voltage is dropped across the same sample using large area contacts, the dielectric break down voltage is reduced to as little as 5 V. By comparison, figure A.6d demonstrates a low resistivity silicon sample with a 90 nm thermally grown oxide, whereupon there is no leakage current detected (only noise). From this mini/control experiment it is clear that the contact size does impact the probability of a dielectric break down through the oxide. This is suggested to be due to large area contacts being more likely to be positioned over a defect in the silicon crystal which are known to promote low gate voltage breakdown events [352, 353]. Therefore, although thin oxide layers of 50 nm is compatible for micro- and nano- electronic devices that typically have small area contacts, for large area gating measurements thicker oxides are necessary.

A.9 Copyright Permissions

All copyrighted material adapted or otherwise used in this thesis is clearly cited.

1. LICENSE #: 4458811317431
    - Order Date: 10/30/2018
    - *Physics Reports*
    - Malard et al. [164]
    - Title: Raman spectroscopy in graphene
    - Used in Figure 2.6
2. LICENSE #: RNP/18/OCT/008984
    - Order Date 10/30/2018
    - *Physical Review B*
    - Kogan et al. [165]
    - Title: Symmetry classification of energy bands in graphene
    - Used in Figure 2.6
3. LICENSE #: 4460291443608
    - Order Date: 11/01/2018
    - *Mechatronics*
    - Jalili et al. [179]
    - Title: A review of atomic force microscopy imaging systems: application to molecular metrology and biological sciences
    - Used in Figure 2.8
4. LICENSE #: 4460331417692
    - Order Date: 11/01/2018
    - *Surface Science Reports*
    - Melitz et al. [183]
    - Title: Kelvin probe force microscopy and its application
    - Used in Figure 2.9
5. LICENSE #: 4462030192218
    - Order Date: 11/04/2018
    - *Nature*
    - Novoselov et al. [204]
    - Title: Two-dimensional gas of massless Dirac fermions in graphene
    - Used in Figure 2.15
6. LICENSE #: 4444731250607
    - Order Date: 10/09/2018
    - *Nanotechnology*
    - Black et al. [88]
    - Title: Graphene gas sensing using a non-contact microwave method
    - Used in Chapter 4 Figures 4.2 and 4.3

7. LICENSE #: 4444730912729
    - Order Date: 10/09/2018
    - *2D Materials*
    - Black et al. [89]
    - Title: Adsorption dynamics of CVD graphene investigated by a contactless microwave method
    - Used in Chapter 4 Figures 4.4,4.5, 4.7, 4.8, 4.9, 4.10, 4.11, 4.12, 4.13, 4.14, 4.15, 4.16 and 4.17